SURGE DYNAMICS AND UNSTEADY FLOW PHENOMENA IN CENTRIFUGAL COMPRESSORS

by

DAVID ALLAN FINK

B.S., Massachusetts Institute of Technology (1975)
S.M., Massachusetts Institute of Technology (1984)

SUBMITTED IN PARTIAL FULFILLMENT OF THE REQUIREMENTS FOR THE DEGREE OF DOCTOR OF PHILOSOPHY

at the

MASSACHUSETTS INSTITUTE OF TECHNOLOGY

May 1988

Signature of Author _____
Department of Aeronautics and Astronautics April 29, 1988

Certified by _____
Professor Edward M. Greitzer
Thesis Supervisor, Director of Gas Turbine Laboratory and Professor of Aeronautics and Astronautics

Certified by _____
Dr. Nicholas A. Cumpsty
Lecturer, Whittle Laboratory, Cambridge University

Certified by _____
Professor Jack L. Kerrebrock
Maclaurin Professor of Aeronautics and Astronautics and Associate Dean of Engineering

Certified by _____
Dr. Choon S. Tan
Research Associate of Aeronautics and Astronautics

Accepted by _____
Professor Harold Y. Wachman
Chairman, Department Graduate Committee

SURGE DYNAMICS AND UNSTEADY FLOW PHENOMENA

IN

CENTRIFUGAL COMPRESSORS

by

DAVID ALLAN FINK

Submitted to the Department of Aeronautics and Astronautics on April 29, 1988 in partial fulfillment of the requirements for the Degree of Doctor of Philosophy

ABSTRACT

Detailed time resolved measurements of centrifugal compressor surge has been obtained on an automotive turbocharger for two very different compression systems one with a large downstream volume and one with a much smaller downstream volume. These measurements show impeller stall at the inducer tips to be a key phenomena in initiating surge. The inducer tip stall, which is dominant over other types of stall in the compressor, is observed to be non-rotating and asymmetric due to the presence of an asymmetric downstream volute. The most severe stalling of the impeller occurs at a circumferential position nearest the volute tongue position and is due to a circumferential flow distortion set up by the volute. The vaneless diffuser is seen to be destabilizing but does not initiate surge by abrupt stalling. Rotating stall was found to be unimportant in surge initiation.

New evidence is presented concerning the dynamic behavior of the compressor characteristics in surge operation. Instantaneous compressor characteristics in surge when operating in a large volume(large B-parameter) system are found to be flatter than the time averaged ones for a small volume(small B-parameter) stabilized system. A physical mechanism accounting for the difference between the two measured characteristics is the slow development time and differing circumferential extent of the inducer stall present. The flatness of the large B characteristic contrasts with the characteristic of an axial compressor operating in surge and leads to slow growth of the surge massflow instability.

A dynamic model has been developed which includes effects of speed variations, compressibility, and time lags. The inclusion of speed variations changes the time domain behavior of the compression system substantially from the results obtained with constant speed. A precursor period of mild surge whose length depends on the amount of throttling is shown to be present before deep surge and is due to the speed variations. Both speed variations and time lags in compressor behavior are shown to introduce a stabilizing effect on compressor behavior in mild surge. The results of this model agree qualitatively as well as quantitatively with the measured experimental system dynamic behavior.

The dynamic behavior observed has some properties of importance for the new field of active control of surge instabilities in centrifugal compressors. The flatness of the instantaneous compressor characteristic, the existence of a mild surge precursor period, and slow growth of the surge instability are favorable conditions for a relatively simple active control strategy to stabilize the compression system and eliminate surge. Also the dynamic model developed may be useful for exploring alternative active control strategies.

Thesis Supervisor: Dr. Edward M. Greitzer
Title: Professor of Aeronautics and Astronautics
and Director of Gas Turbine Laboratory

ACKNOWLEDGEMENTS

I would most like to thank my advisor, Prof. Greitzer for his continued guidance, stimulating discussions, understanding, patience, nervous energy, and enthusiasm over the course of this project and my years at the lab. His technical excellence, uncanny ability to find the "nuggets" in raw data, and ability to motivate were a constant presence as the project evolved. In addition, his interest in my educational development during several critical phases of the doctoral program have been instrumental in my successful completion. As both colleague and friend, I am grateful for his support.

I would also like to thank Prof. Cumpsty, whose intuition, constructive criticism, and useful suggestions were a positive force in the research and helped focus my efforts in the experimentation. His insight, continuing interest, and enthusiasm over the long haul are deeply appreciated.

I wish to also thank Prof. Kerrebrock, whose intuition, probing questions, and interest in the "big" picture were refreshing and a source of inspiration. Despite a hectic schedule, he always had time to listen and give advice for which I am indebted.

I must also acknowledge the continuous help, advice, and support of Dr. Tan. He was instrumental in unshrouding the mysteries of computerized data acquisition hardware and software, served as a sounding board during various phases of the project, and also taught me about "real" Chinese food. His advice, sense of humor, and friendship have helped to smooth my stay at the Institute and are greatly appreciated.

This work was supported by the Cummins Engine Company under the direction of Dr. H.G. Weber and their interest and support is gratefully appreciated. I am also very grateful to the U.S. Air Force which provided financial assistance in the form of an AFRAPT traineeship which allowed me to pursue the doctoral program at the Institute.

Thanks are also in order to several fellow experimentalists or "comrades in arms", whose discussions, assistance, and advice during the experimentation have been enlightening and whose friendship has made my experience at G.T.L. a rewarding one. I wish to thank Capt. R. Gamache for his practical advice in the early stages of my research. I am indebted to P. Lavrich for his many helpful suggestions concerning

"computerese", filtering techniques, etc. and also his assistance when it was time to play "DEC repairman". I wish to thank V. Filipenco not only for his technical advice but also for the many lively discussions of turbochargers, CD's, watches, swatches, RC planes, cars, transmissions, etc. and for teaching me the pleasures and relaxation of unintended aerobatics and "augering in" on Brigg's Field.

Thanks are also due to Prof. Martinez-Sanchez, for his constructive criticism and suggestions on the initial draft of the thesis, Prof. Epstein, who was a wealth of information in data acquisition and experimental techniques, Dr. J. Guenette, whose equipment I was constantly borrowing, R. Haimes, who performed numerous feats of software black magic which kept the lab computers sane, and A. Shaw, who always had just what I was looking for. In addition, I would like to thank G. Chen, for his help in running the Chue code, Prof. B. Jery, for the use of his electronic filters, N. Lee, P. Kotidis, and Y. Qui for their camaraderie, and G. Haldemann and J. Pinsley for the use of the speaker and amplifier equipment.

As with any experimental effort at the lab, the project would not have been possible without the support of many additional G.T.L. "team" members. The author is indebted to W. Cook for his electronic wizardry, V. Dubrowski for machine shop support, expertise, and continued enthusiasm, J. Nash and R. Andrews for technical support during the experiments and help in the infernal regions of the lab, and H. Rathbun, who kept the funds flowing smoothly at critical times in the project.

I would also like to acknowledge the teaching excellence and influence of Prof. Wilson, who first sparked my interest in turbomachinery through his graduate turbomachinery design course and also the guidance and support of R. Raymond of the Thermo Electron Corporation, who as my mentor and friend, has had a strong and positive influence on me.

Finally, no words can really describe the understanding, unceasing patience, and love my wife, Barbara, has shown during my stay at the Institute. Her stamina combined with the continuing wisdom, encouragement, and emotional support of my mother, Ruth, has given me the strength to continue my education. I am indeed fortunate and grateful.

To my wife, my mother, and in memory of my father, Allan Fink, an aeronautical engineer from whom I probably inherited my romance of aviation.

TABLE OF CONTENTS

Abstract i
Acknowledgements iii
Table of Contents vii
List of Figures ix
List of Photographs xiii
Nomenclature xv

1.0 Introduction and Background 1
1.1 Introduction 1
1.2 Background 4
1.3 Research Questions 5
1.4 Literature Review and Discussion 6
1.4.1 Basic System Model for Surge 6
1.4.2 The Effect of the B-Parameter 7
1.4.3 Actuator Characteristic Types and Surge Triggering 10
1.4.4 Surge Initiation Phenomena and Actuator Behavior in Centrifugal Compressors 12
1.5 Review of Gas Turbine Laboratory Experimental Work 16
1.6 Experimental Approach and Objectives 18

2.0 Facility and Experimental Apparatus 29
2.1 Overall Facility Description 29
2.2 Turbocharger Description 30
2.3 Inlet Instrumentation 31
2.4 Compressor Case Instrumentation 32
2.5 System Natural Frequency Measurement Apparatus 34
2.6 Inlet Calibration 34
2.7 Inlet Hotwire Calibration 35
2.8 Miscellaneous Calibration and Testing 38

3.0 Large B System Experimental Results and Discussion 51
3.1 Compressor Map 51
3.2 Method of Determining the Instantaneous Compressor Actuator Characteristic 52
3.3 System Inductance Measurement and B-Parameter Calculation 53
3.4 Reduced Frequency Calculation 54
3.5 Nondimensionalization of Data 55
3.6 Large B System Behavior during Throttling 56
3.7 Surge Initiation Discussion 59
3.8 Reverse Flow Calculation of Surge Operation 59
3.9 Inertially Corrected Compressor Head Coefficient in Deep Surge 61
3.10 The Approach to Deep Surge for Axial and Centrifugal Compressors . . 67
3.11 Time Resolved Compressor Component Pressure Results 67
3.12 Compressor Component Behavior in Surge 69
3.12.1 Impeller Behavior 69
3.12.2 Stall Cell Observations 73
3.12.3 Diffuser Behavior 75
3.13 Summary 77

4.0 Small B Experimental Results and Discussion 107
4.1 Stability Argument for a Small B System and System Stabilization . . 107
4.2 Natural Frequency Measurement and B-Parameter Calculation 108
4.3 Compressor Map and Overall Efficiency 109
4.4 Large B vs Small B Overall Compressor Performance. 109
4.5 Small B System Behavior during Throttling 110
4.6 Small B System Compressor Component Measurement Description . . . 111
4.7 Discussion of Small B Stalling Phenomena in the Compressor Components 111
4.7.1 Impeller Stalling Phenomena. 111
4.7.2 Diffuser Stalling Phenomena. 119
4.8 Influence of the Volute Match Point on Compressor Stalling Behavior . 121
4.9 Calculation of Circumferential Variation of Flow Coefficient 125
4.10 Flow Distortion Corrected Vaneless Diffuser Cp Results. 126
4.11 Summary 127

5.0 System Dynamic Model 165
5.1 Introduction and Assumptions. 165
5.2 Governing Equations 166
5.3 Compressor Characteristics 170
5.4 Constant Drive Torque Stability Analysis 172
5.5 Constant Drive Torque System Response Numerical Results 177
5.6 Quasisteady Model Comparison of Theory with Experimental Results. . 179
5.7 Effects of Drive Characteristic on Deep Surge Results 179
5.8 Effect of Time Lags on System Response 180
5.9 Time Lag Stability Analysis 181
5.10 Time Lag System Response Numerical Results 183
5.11 Time Lag Model Comparison of Theory with Experimental Results. . . 183
5.12 External System Effects 184
5.13 Summary 184

6.0 Summary and Conclusions 207
6.1 Centrifugal Compressor Surge Initiation Flow Phenomena Summary . . 207
6.2 Summary of Centrifugal Compressor Surge Dynamics. 210
6.3 Summary of Contributions 213
6.4 Implications for Active Control of Surge 213
6.5 Recommendations for Future Research 215

References 217
Photographs 221
Appendix A Compression System Electrical Analog. 227
Appendix B Turbocharger Laboratory Drive 237
Appendix C Compressor Hardware for Pressure Distortion Measurement 239
Appendix D Data Acquisition Hardware 241
Appendix E Instrumentation and Calibration. 245
Appendix F Calculation of the Slip Parameter. 257
Appendix G Calculation of Impeller Exit Mach Number 265
Appendix H Estimate of Inducer Recovery Loss 269

LIST OF FIGURES

Fig. 1.1 Compressor Instability Modes, from [25] 21
Fig. 1.2 Cummins Diesel-Turbocharger Map, from [20] 22
Fig. 1.3 B-Parameter Effect on Compressor Surge Cycle Behavior, from [25] . . 23
Fig. 1.4 Compressor Actuator Characteristic Types 24
Fig. 1.5 Performance Map of Test Compressor, from [37] 25
Fig. 1.6 Comparison of Pressure Signals with and without Stall, from [37]. . . 25
Fig. 1.7 Points of Occurence of Rotating Stall on Compressor Map, from [1] . . 26
Fig. 1.8 Compressor Time Resolved Pressure Signals, from [1] 26
Fig. 1.9 Overall Pressure Ratio and Throat Total Pressure Characteristic, from [52] 27
Fig. 1.10 Pressure Variation During the Surge at 85% Speed, from [52] 27
Fig. 1.11 Total Pressure at the Initiation Point of Surge, from [52] 28
Fig. 1.12 Compressor Characteristic and Limit Cycle Oscillation, from [12]. . . . 28

Fig. 2.1 Overall Turbocharger Test Facility 39
Fig. 2.2 Large B Turbocharger Drive Arrangement 40
Fig. 2.3 Small B Turbocharger Drive Arrangement 41
Fig. 2.4 Turbocharger Cutaway. 42
Fig. 2.5 Inlet Instrumentation 43
Fig. 2.6 Reverse Flow Probe 44
Fig. 2.7 Compressor Case 1 Instrumentation Meridional Positions 45
Fig. 2.8 Compressor Case 1 Instrumentation Circumferential Positions. 46
Fig. 2.9 High Response Thermocouple Cross Section and Response 47
Fig. 2.10 Compressor Case 2 Instrumentation Meridional Positions 48
Fig. 2.11 Compressor Case 2 Instrumentation Circumferential Positions. 49
Fig. 2.12 System Natural Frequency Measurement Equipment 50

Fig. 3.1 Large B Compressor Map. 79
Fig. 3.2 Large B System Natural Frequency Measurement Results 80
Fig. 3.3 Large B Compressor Head Coefficient vs Cx/U. 81
Fig. 3.4 Large B System Parameters in Non-Surge Operation(ϕ = .275) 82
Fig. 3.5 Large B System Parameters in Mild Surge(ϕ = .23) 82
Fig. 3.6 Large B System Parameters in Deep Surge(ϕ = .225). 83
Fig. 3.7 Large B System Parameters in Deep Surge(ϕ = .19) 84
Fig. 3.8 Large B System Parameters in Deep Surge(ϕ = .16) 85
Fig. 3.9 Comparison of Hotwire Measured and Plenum π_p Derived Cx/U 86
Fig. 3.10 Time Resolved Rotor Inlet and Exit Temperature in Deep Surge(Mto = .92, ϕ = .225) 87
Fig. 3.11 Comparison of Reverse Flow Probe and Hotwire Measured Cx/U(Mto = .92) 88
Fig. 3.12 System Parameters in Deep Surge(Mto = .92, ϕ = .225) 89
Fig. 3.13 Smoothing and Numerical Differentiation Results 90
Fig. 3.14 Inertially Corrected Compressor Head Coefficient vs Cx/U in Deep Surge 91
Fig. 3.15 System Parameters in Deep Surge(Mto = .63, ϕ = .16) 92
Fig. 3.16 Comparison of Inertially Corrected Compressor Head Coefficients vs Cx/U in Deep Surge 93

Fig. 3.17 Axial vs Centrifugal in Deep Surge Approach 94
Fig. 3.18 Compressor Static Head Coefficients vs Time in Deep Surge(Mto = .92). 95
Fig. 3.19 Detail of Deep Surge Event(Mto = .92) 96
Fig. 3.20 Compressor Static Head Coefficients vs Time in Deep Surge(Mto = .63). 97
Fig. 3.21 Detail of Deep Surge Event(Mto = .63) 98
Fig. 3.22 Non-Rotating Circumferential Distortion Effect on Pressure Phase Measurements 99
Fig. 3.23 Impeller Head Coefficient vs Cx/U(Mto = .92). 100
Fig. 3.24 Impeller Head Coefficient vs Cx/U(Mto = .63). 101
Fig. 3.25 Vaneless Diffuser Head Coefficient vs Cx/U(Mto = .92) 102
Fig. 3.26 Vaneless Diffuser Head Coefficient vs Cx/U(Mto = .63) 103
Fig. 3.27 Overall Diffuser Head Coefficient vs Cx/U(Mto = .92). 104
Fig. 3.28 Overall Diffuser Head Coefficient vs Cx/U(Mto = .63). 105

Fig. 4.1 Small B System Natural Frequency Measurement Results. 129
Fig. 4.2 Compressor Map 130
Fig. 4.3 Compressor Head Coefficient vs Cx/U 131
Fig. 4.4 Compressor Efficiency vs Cx/U 132
Fig. 4.5 Small B Time Averaged vs Large B Time Resolved Characteristic Data 133
Fig. 4.6 Small B System Parameters vs Time at Various Throttle Settings(Mto = .92) 134
Fig. 4.7 Small B Head Coefficients vs Cx/U 135
Fig. 4.8 Impeller and Overall Compressor Efficiency vs Cx/U 136
Fig. 4.9 Impeller Head Coefficient vs Theta at High Mean Cx/U(Mto = .63). . 137
Fig. 4.10 Impeller Head Coefficient vs Theta at Low Mean Cx/U 138
Fig. 4.11 Volute Induced Head Distortion, from [44] 139
Fig. 4.12 Impeller Head Coefficients vs Cx/U 140
Fig. 4.13 Circumferentially Averaged Impeller and Overall Compressor Efficiency vs Cx/U 141
Fig. 4.14 Estimated Circumferential Variation in Inducer Flow Coefficient at High Mean Flow Coefficients(Mto = .63) 142
Fig. 4.15 Estimated Circumferential Variation in Inducer Flow Coefficient at Low Mean Flow Coefficients. 143
Fig. 4.16 Estimated Inducer Tip Incidence Angle vs Cx/U. 144
Fig. 4.17 Compressor Head Coefficients vs Time(Mto = .92, ϕ = .20) 145
Fig. 4.18 Compressor Head Coefficients vs Time(Mto = .92, ϕ = .10) 146
Fig. 4.19 Compressor Head Coefficients vs Time(Mto = .92, ϕ = .05) 147
Fig. 4.20 Compressor Head Coefficients vs Time(Mto = .92, Shutoff). 148
Fig. 4.21 Inducer Kulite FFT Results at Low Mean Flow Coefficients(Mto = .92) 149
Fig. 4.22 Inducer Kulite FFT Results at Throttle Point of Maximum Stall Cell Pressure Amplitude(Mto = .63). 150
Fig. 4.23 Circumferential Variation in Vaneless Diffuser Cp at High Flows(Mto = .63). 151
Fig. 4.24 Circumferential Variations in Vaneless Diffuser Cp at Low Flows . . 152
Fig. 4.25 Circumferentially Averaged Vaneless Diffuser Cp vs Cx/U 153
Fig. 4.26 Circumferentially Averaged Vaneless Diffuser Cp vs $1/\lambda$ 154
Fig. 4.27 Component Circumferentially Averaged Head Coefficients vs Cx/U . . 155
Fig. 4.28 Volute Matching Conditions 156

Fig. 4.29 Volute Head Coefficients vs Cx/U 157
Fig. 4.30 Estimated Axisymmetric Curve of Impeller Cp vs Cx/U(Mto = .63) . 158
Fig. 4.31 Estimated Axisymmetric Curve of Impeller Cp vs Cx/U(Mto = .92) . 159
Fig. 4.32 Circumferential Variation in Impeller Flow Coefficient at High Mean Flow Coefficients(Mto = .63). 160
Fig. 4.33 Circumferential Variation in Impeller Flow Coefficient at Low Mean Flow Coefficients. 161
Fig. 4.34 Distortion Corrected vs Non Corrected Variation in Circumferential Vaneless Diffuser Cp at High Mean Flow Coefficients(Mto = .63) . . 162
Fig. 4.35 Distortion Corrected vs Non Corrected Variation in Circumferential Vaneless Diffuser Cp at Low Mean Flow Coefficients(Mto = .63) . . 163
Fig. 4.36 Distortion Corrected and Non Corrected Circumferentially Averaged Vaneless Diffuser Cp vs Cx/U(Mto = .63) 164

Fig. 5.1 Compression System Model, from [51]. 187
Fig. 5.2 Compressor Pumping Characteristic 188
Fig. 5.3 Compressor Torque Characteristic. 189
Fig. 5.4 Instability Cx/U vs B-Parameter for Quasisteady Model(A=constant). . 190
Fig. 5.5 Instability Cx/U vs A-Parameter for Quasisteady Model(B=constant). . 191
Fig. 5.6 Quasisteady Model Large B System Parameters vs Time(ϕ = .24). . . 192
Fig. 5.7 Quasisteady Model Large B System Parameters vs Time(ϕ = .2398) . 193
Fig. 5.8 Quasisteady Model Large B System Parameters vs Time(ϕ = .2397). . 194
Fig. 5.9 Quasisteady Model Large B System Parameters vs Time(ϕ = .235) . . 195
Fig. 5.10 System Response with and without Speed Fluctuations(ϕ = .235) . . 196
Fig. 5.11 Quasisteady Model Large B System Parameters vs Time(ϕ = .23). . . 197
Fig. 5.12 Quasisteady Model Large B System Parameters vs Time(ϕ = .20). . . 198
Fig. 5.13 Quasisteady Model Large B System Parameters vs Time(ϕ = .1) . . . 199
Fig. 5.14 Quasisteady Model Simulation Results vs Experimental Results(ϕ = .235) 200
Fig. 5.15 Constant Drive Torque vs Choked Turbine System Response(ϕ = .235). 201
Fig. 5.16 Instability Cx/U vs B-Parameter with Compressor Time Lags 202
Fig. 5.17 Quasisteady Model Results vs Time Lag Model Results. 203
Fig. 5.18 Time Lag Model Results vs Experimental Results in Non-Surge(ϕ = .275) 204
Fig. 5.19 Time Lag Model Results vs Experimental Results in Mild Surge(ϕ = .236) 205
Fig. 5.20 Time Lag Model Results vs experimental Results in Deep Surge(ϕ = .235) 206

Fig. A.1 Compression System Electrical Analog 235
Fig. B.1 Small B System Drive Schematic 237
Fig. C.1 Compressor Case 2 for Circumferential Pressure Distortion Measurement 239
Fig. C.2 Diffuser Plate 2 for Circumferential Pressure Distortion Measurement 240
Fig. D.1 Data Acquisition Schematic 243
Fig. D.2 Direct to Disc Data Translation A/D System Schematic 244
Fig. E.1 Speed Sensor Probe Fixture 245

Fig. E.2 Transient Speed Electronics Schematic 246
Fig. E.3 Photo Optic Speed Probe Calibration 247
Fig. E.4 Speed Sensor F/V Step Response 248
Fig. E.5 Speed Probe Filter Transfer Function 249
Fig. E.6 High Response Thermocouple Conditioner and Amplifier Schematic . . 250
Fig. E.7 Typical High Response Thermocouple Calibration Curve 251
Fig. E.8 Typical Reverse Flow Probe Calibration Curve 252
Fig. E.9 Reverse Flow Probe Amplifier Schematic 253
Fig. E.10 Typical Hotwire Calibration Curve 254
Fig. E.11 Typical Kulite High Response Pressure Transducer Calibration Curve . 255
Fig. F.1 Vaneless Diffuser Velocity Triangle. 259
Fig. F.2 Compressor Work Coefficient vs Cx/U 260
Fig. F.3 Control Volume of Compressor. 261
Fig. F.4 Compressor Torque Coefficient vs Cx/U. 262
Fig. F.5 Compressor Slip Factor vs Cx/U 263
Fig. H.1 Inducer Tip Velocity Diagram 273

LIST OF PHOTOGRAPHS

Photo. 1 Overall Facility 221
Photo. 2 Small B Throttling Arrangement 221
Photo. 3 Impeller 223
Photo. 4 Inlet Tongue Region Oil Streaks 223
Photo. 5a Inlet Flow Visualization, No Swirl(ϕ =.125 @ 33K) 225
Photo. 5b Inlet Flow Visualization, Onset of Tip Swirl 225
Photo. 5c Inlet Flow Visualization, Severe Overall Swirl(ϕ =.1 @ 33K) 225

NOMENCLATURE

Symbols

A = dimensionless turbospool inertia parameter; defined in Eq. 5.7

A(ℓ) = normal flow area at position ℓ along flow path

a = speed of sound

Ac = equivalent duct area in compressor-duct model

Aref = reference area equivalent to inducer eye flow area

A = volute flow area cross section at angular position

At = throttle throat area

B = dimensionless parameter; defined in Eq. 1.1

C′ = slope of compressor pressure rise characteristic

$= \delta \Delta\widetilde{Pco} \;/\; \delta \bar{\Phi}_c$

$\widetilde{C}$ = dimensionless compression system capacitance, defined in Eq. 1.2

cp = gas specific heat

Cp = nondimensional pressure rise coefficient; defined in Eq. 3.12
for impeller, defined in Eq. 4.5 and 4.12 for vaneless diffuser

Cx = mean axial velocity in compressor impeller eye

f = frequency

f_H = Helmholtz frequency

$\tilde{f}$ = reduced frequency

k = ratio of specific heats
= Cp/Cv

K = dimensionless constant; used in Eq. 2.3 and 2.4

I = turbospool polar moment of inertia

Lc = equivalent length of compressor-duct model

Lt = compressor throughflow length

$\widetilde{L}$ = dimensionless inductance of compression system, defined in Eq. 1.3

l = length along flowpath

$(L/A)_c$ = compression system equivalent inductance, defined in Eq. 3.2

$\dot{m}$ = compressor massflow

$\dot{m}_{cor}$ = compressor corrected massflow
$= \dot{m}\sqrt{\theta}/\delta$

$\dot{m}^*$ = choked flow through reference area Aref at ambient Po, To

$$= \frac{P_o A_{ref}}{\sqrt{T_o}} \sqrt{\frac{k}{R}} \left(\frac{2}{k+1} \right)^{\frac{(k+1)}{2(k-1)}}$$

Mx = flow Mach number in equivalent duct of area Aref
= Cx/a

Mt = flow Mach number in throttle throat

Mto = impeller tip Mach index with respect to ambient temperature
$= U/(kRTo)^{.5}$

Mtp = impeller tip Mach index with respect to plenum temperature
$= U/(kRTp)^{.5}$

N_{cor} = corrected RPM
$= N/\sqrt{\theta}$

$\widetilde{P}$ = static pressure

$\widetilde{\Delta Pco}$ = nondimensional compressor pressure rise coefficient(total to static)
$= (Pc - Po)/(.5\rho_o U^2)$

$\widetilde{\Delta Ppo}$ = plenum pressure rise coefficient(total to static)
= (Pp - Po)/(.5$\rho_o U^2$)
Q_θ = volume flowrate through area A_θ
r, R = compressor radius
r_T = compressor impeller tip radius
R = specific gas constant
= 53.3 ft-lbf/lbm F(287 Nm/(Kg K)) for air
Rex = inlet tube Reynolds number
= CxX/ν
s = meridional casing length of impeller
T = temperature
T' = slope of throttle characteristic
= $\delta \widetilde{\Delta Ppo} / \delta \Phi_T$
t = time
$\tilde{t}$ = nondimensional time
= $\omega_H t$
$\tilde{T}$ = ratio of throughflow times; defined in Eq. 2.5
U = impeller blade tip velocity
Uss = steady state free stream velocity component over flat plate
Uus = unsteady free stream velocity component over flat plate
U = free stream velocity over flat plate
Vc = volume of compressor flow area
Vp = volume of compression system plenum
X = distance from inlet entrance
$\widetilde{\Gamma_o}$ = nondimensional torque coefficient
= $\Gamma/(\rho_o Acr_T U^2)$
$\widetilde{\Gamma_f}$ = nondimensional friction torque coefficient
δ = nondimensional pressure
= P/Pref
δ^* = inlet tube displacement thickness
ε = unsteady velocity parameter; defined in Eq. 2.2
= Uus/Uss
Θ = nondimensional temperature
= T/Tref
λ = vaneless diffuser inlet swirl parameter
= $C_{\theta 2}/Cr_2$
ν = kinematic viscosity
π = pi
π_c = compressor pressure ratio(static exit/total ambient)
π_p = plenum pressure ratio(static plenum/total ambient)
ρ = density
σ = slip parameter, defined in Eq. F.1
τ_c = compressor total temperature ratio
= Tex/To
τ_p = plenum total temperature ratio
= Tp/To
τ = characteristic time
τ_H = Helmholtz resonator period
Φ_c = compressor flow coefficient
= $\dot{m}/(\rho AcU)$
ϕ = compressor flow coefficient; defined in Eq. 3.9

ψ_{is} = compressor isentropic head coefficient; defined in Eq. 3.10
ψ_{work} = compressor work coefficient
= $(\tau_c - 1)/((k - 1)Mto^2)$
ω = flow change frequency, compressor angular rate of rotation
ω_H = Helmholtz angular frequency
= $2\pi f_H = 1/\tau_H$

Subscripts
amb = at ambient conditions
b = backflow
c = compressor, change
char = characteristic value
cor = corrected value
D = diffuser
d = drive
duct = related to difference measured across duct ends
f = forward flow
H = Helmholtz
I = impeller
Inlet = inlet of compressor
p = with respect to plenum conditions
ref = reference condition value
rel = in relative rotating frame
ss = steady value
T = turbine
t = throttle, thoughflow
us = unsteady value
X = characteristic length of X
0 = at or relative to ambient condition
1 = inducer eye position
2 = impeller tip diameter position
3 = vaneless diffuser exit position
4 = volute discharge position
Θ = at angular position Θ
∞ = free stream value

Other
$|\ |$ = absolute value of
$\widetilde{(\ )}$ = non-dimensional quantity
$(\ )'$ = derivative of quantity
$d(\ )/dt$ = time derivative of quantity
$\delta(\ )$ = perturbation quantity
$\Delta(\ )$ = difference or uncertainty of quantity

CHAPTER 1

INTRODUCTION AND BACKGROUND

1.1 Introduction

Centrifugal compressors are used for a range of applications due to their potential combination of high pressure ratio per stage, reasonable efficiency, large stable flow range, and low cost. In smaller aviation applications, for example, such as helicopter engines, where the maximum massflow/frontal area ratio is less critical, centrifugals and axi-centrifugals are the most common form and are currently under extensive development. In the automotive, motorcycle, and trucking industry, turbocharging is becoming popular in improving an engine's maximum specific power output and efficiency and centrifugal compressors are used almost exclusively for these applications. Future applications, such as adiabatic diesels, will also require high pressure ratio turbocharger components.

It is often desirable to operate centrifugal compressors over a wide flow range. When throttled to low flowrates, however, stable operation of the centrifugal compression system is limited by the occurence of surge. Surge is a self-excited global instability characterized by large oscillations in system annulus averaged massflow and pressure rise. It occurs in both centrifugal and axial compression systems. A second type of self excited instability which may occur during low flow operation is rotating stall where a localized non-axisymmetric regime of periodic flow disturbances propagates around the compressor case. Both surge and rotating stall instability modes for an axial machine are shown in Fig. 1.1. These two instability phenomena were observed by Emmons[16] in the early 1950's in both a centrifugal and an axial machine and were then first clearly recognized as two distinctly different behaviors.

Over the years, substantial gains in understanding the stability aspects of axial compressors have been made. This includes knowledge of both the dynamic

behavior and details of the surge triggering mechanism. There is reasonably general agreement that the dynamics of surge behavior in axial compressors is controlled by the magnitude of the B-parameter as defined in Greitzer[25] and that the occurence of rotating stall is the triggering mechanism for surge. When B exceeds a critical value, the onset of rotating stall will trigger the global instability of surge.

Since B is a system parameter which is a measure of the ratio of system compliance to inductance, its influence on overall system behavior is independent of compressor type. Hence a centrifugal compressor's overall surge behavior must also depend on this parameter. There are however several issues dealing with surge behavior in centrifugal machinery which are considerably less understood than for axial compressors.

The first, perhaps most controversial, issue is tne considerable disagreement over the mechanism which "triggers" the overall flow reversal of deep surge. The earliest evidence for rotating stall in the inducer as a precursor to surge was seen in the pioneering work of Emmons[16]. Since then, great progress has been made in the field of data acquisition and experimental measurement, which has enabled a number of researchers to investigate the surge behavior of the centrifugal compressor by means of time resolved data. Of these the data of Toyama, Runstadler, and Dean[52] is perhaps the most well known example. In their results, it was concluded that flow reversal in the stage was preceeded by stall of the inlet region of the diffuser. They did not observe rotating stall to occur prior to the overall flow reversal as was observed by Emmons. More recent time resolved data[1],[37] has presented evidence of rotating stall in both the impeller and the diffuser. Despite the large amount of new detail observable with the time resolved data, however, no consensus of opinion could be reached on the dominance of any one component on the surge initiation process.

A second area of controversy, considered by Dean and Young[12],[13] arose out of the Toyama results which concerns the behavior of the instantaneous compressor characteristics. The Toyama results showed a mild surge limit cycle behavior when the compressor was throttled to a point near the deep surge line of the compressor. An attempt to model this behavior using the compression system model of Taylor[51] and a two valued slope compressor characteristic succeeded only when a much flatter characteristic than the time averaged one was used. Three possible reasons were

given for this result. Among them were:

- The time mean characteristic is steeper than the instantaneous characteristic.
- Other inertias such as the rotor wheel inertia are present.
- The compressor is time dependent and does not remain instantaneously on a unique "actuator" characteristic.

In this thesis, both issues; stall initiation and behavior of the centrifugal compressor actuator characteristics, were investigated experimentally in a turbocharger compressor utilizing high and low response instrumentation. With regard to the first issue, stall of the impeller at the inducer tips was found to be dominant over other types of stall in the compressor. New evidence will be presented that shows the inducer stall to be non-rotating and asymmetric due to the presence of the downstream volute. The most severe stalling of the impeller occurs at a circumferential position nearest the volute tongue position and is due to a circumferential flow distortion set up by the volute. The tongue stall in the impeller increased in severity at higher values of compressor Mach index(i.e. tip speed) when the compressor was operated away from the volute design point.

New evidence will also be presented concerning the dynamic behavior of the compressor characteristics in surge operation. The compressor instantaneous trajectory in deep surge for a large B-parameter system will be shown to be much flatter than and to lag the time averaged value in a low B-parameter(stable) system during the initial approach to reverse flow. A physical mechanism accounting for the difference between these two measured characteristics is the differing circumferential extent of the inducer stall present in the two measurements. The flatness of this characteristic also contrasts with the characteristic of an axial compressor operating in surge and leads to slow growth of the surge massflow instability.

A compression system dynamic model which includes the effect of variable speed, i.e. variable B-parameter will also be presented. In this system model, two types of compressor characteristic behavior were investigated. Initially, the compressor was assumed to operate quasisteadily on a unique time independent actuator characteristic. The results of the quasisteady model show a stabilizing effect on mild surge oscillations. Results that compare closely with experimental data show that speed fluctuations play a significant role in the surge "triggering" behavior

commonly observed in many practical centrifugal compression systems. A variable length precursor period of mild surge before deep surge is shown to be present due to the speed variation.

In a second type of compressor behavior, the quasisteady compressor characteristic assumption was relaxed by the inclusion of a small first order time lag(of the order of the compressor throughflow time) to simulate the formation time of inducer stall. The inclusion of the time lag is found to have a stabilizing effect on mild surge oscillations and to considerably improve the qualitative and quantitative agreement with the experimental measurements.

The dynamic behavior observed in the centrifugal compressor system studied in this thesis has a number of properties of practical significance to the new field of active control of surge instabilities. The flatness of the instantaneous actuator compressor characteristic and slow growth of the surge instability observed should allow a relatively simple active control strategy to be successfully implemented to stabilize the system. The mild surge precursor period observed due to speed fluctuations also increases the chances that an implementation of active control will be successful in the stabilization process. The dynamic model developed here may also be useful as a compressor model for the development of active surge control algorithms.

1.2 Background

Surge can be classified as either "mild" or "deep", depending on the amplitude of the massflow fluctuation. Mild surge refers to system instability in which the compressor annulus averaged massflow is oscillating but remains in forward flow at all instants of time. The massflow oscillation frequency is usually of the order of the Helmholtz resonator frequency of the system. With low response instrumentation, the compressor appears to be operating stably at constant speed and pressure rise although some additional noise may be present. Deep surge refers to system instability in which the compressor annulus averaged massflow is oscillating and will for some period of time be reversed. A compression system operating in deep surge generally undergoes a large self excited oscillation in massflow which is a type of relaxation oscillation. Surge behavior of this type is typified by reverse massflows through the compressor, large pressure variations in the connecting plenum, and

sub-Helmholtz massflow oscillation frequencies of order of the plenum blowdown and fill time. The onset of this violent instability usually terminates the useful range of the compressor. The surge line on a compressor performance map typically denotes the lefthand limit of the usable flow range and is the locus of compressor operating "points" at which the compression system enters deep surge[1].

The matching of turbochargers to diesel engines is one example of the problems created by the onset of deep surge. A central objective of the matching process is to avoid surge altogether in the engine operating range[a]. It is essential to have a compressor performance map that is sufficiently broad so that an engine can operate over its entire rpm and throttle range without compressor surge and/or choking. It is also desirable to run the compressor in the region of highest compressor thermal efficiency. A performance map of a current Cummins turbocharger centrifugal compressor overlaid on a set of typical diesel engine air demand lines is shown in Fig. 1.2 and illustrates some of the problems an engineer is faced with in the matching process [20]. From this diagram, one can see that the current compressor map width represents a constraint on engine drivability in the 1200 rpm upper power region (compressor surge) and the 2100 rpm upper power region (low compressor efficiency). Since the ratio of surge massflow to low compressor efficiency massflow for turbocharger centrifugal compressors is often too large, there is much incentive to lower this ratio. This can be accomplished by moving the surge line left relative to the low efficiency line towards shutoff.

1.3 Research Questions

Research questions addressed in this work are subdivided into two broad categories. The first category concerns the fluid mechanic details of component

---

(1) The word "points" is somewhat of a misnomer in that each point may in fact represent some type of average value of instantaneous compressor operation occurring in a region around the average point.

---

(2) It is interesting to note that, in direct contrast to this, in military aircraft(axial) gas turbine engines, surge is preferred over rotating stall since it creates a more favorable atmosphere for stall recovery, a reversal in design goals.

stall in the centrifugal compressor prior to and during surge which define its compressor characteristics. The second category concerns the time dependence of the compressor characteristics and the effect of system parameters. These details are important when modeling the compression system dynamic behavior in surge.

Questions of category 1 include:

- Which component, impeller, diffuser, volute, etc. is most significant in the stage stalling that initiates deep surge?
- What are the time resolved details of flow breakdown in the stalling component?(axisymmetric?, rotating stall?, progressive?, abrupt? etc.)
- How does an asymmetric scroll influence surge behavior?
- What non-dimensional parameters govern the impeller and/or diffuser stall behavior?
- What do the "hidden" low flow and backflow characteristics of the compressor look like?
- How does compressibility influence the stall process?

Questions of category 2 include:

- What are the critical system parameters associated with surge in centrifugal compressors?
- How does the variation of system parameters effect the position of the surge line?
- Does the actuator characteristic exhibit appreciable hysteresis?
- How is the compressor's instantaneous operation in surge described on a compressor map?
- How significant are real time lags associated with such unsteady fluid mechanic phenomena such as stall cell growth?
- How significant are apparent time lags associated with speed fluctuations?
- What degree of complication is required in a system model to properly predict the system surge behavior?

1.4 Literature Review and Discussion

1.4.1 Basic System Dynamic Model for Surge

For a compressor with a known actuator characteristic running at constant speed, the basic overall dynamic behavior of a compression system in surge is reasonably

well understood. A simple compression system which contains all the essential elements necessary for surge is described in Taylor[51]. This system consisted of a compressor operating in a duct attached to a single plenum with an exit throttle valve. The stability of this system was investigated using a linearized quasi-steady compressible analysis. In this analysis, it was assumed that the compressor characteristic are unaffected by transient massflow changes (quasi-steady assumption) and also that massflow at all points in the compressor duct are constant. Two criteria of stability are derived which depend on both the throttle and compressor slope characteristics and two characteristic time parameters associated with the compressor, the plenum, and system duct geometry. An interesting point brought out is that, as plenum size becomes large, dynamic stability is only assured on the negatively sloped part of the pressure ratio curve. Compressor stability also required the compressor slope to be less positive than the throttle characteristic.

1.4.2 The Effect of the B-Parameter

Much of the dynamic behavior of a compression system in surge was illuminated by Greitzer[25], who considered low pressure ratio axial compression systems. In the analysis presented, the flow was assumed incompressible except in the connecting plenum and the compressor was also assumed to run at constant speed. While the details of the compressor characteristics are different from centrifugal machines, the dynamical equations used in the analysis are independent of compressor type. In a break from previous work, Greitzer also modeled the instantaneous actuator compressor characteristic as a first order system (i.e., with a time lag). A significant time constant in the compressor was time associated with the formation of stall cells in the compressor. The non-linear computation, which is verified by experiment, demonstrated the dependence of system behavior on the B-parameter, defined as

$$B = \frac{U}{2\omega_H L_c} = \frac{U}{2a_p}\sqrt{\frac{V_p}{A_c L_c}} \tag{1.1}$$

The B-parameter is the major influencing system parameter on surge cycle dynamic

behavior. In analogy with electric circuits, B controls the ratio of capacitance and inductance in the compression system. The details of this analog are shown in App. A. The capacitance relates the derivative of pressure in the volume with the net flowrate into the volume(unsteady mass continuity equation in plenum) and is due to the compressibility of gas in the system plenum which adds compliance to the system. In nondimensional terms, the capacitance is quantified simply as

$$\tilde{C} = B \tag{1.2}$$

The inductance relates the derivative of flowrate in the compression system ducting to the difference in pressure across the ducting(1-D unsteady momentum equation). The inductance is due to the inertia of the fluid present in the compression system ducting. In nondimensional terms, the inductance is

$$\tilde{L} = \frac{1}{B} \tag{1.3}$$

The B-parameter is then physically a measure of the ratio of capacitance to inductance in the compression system since

$$B = \left(\frac{\tilde{C}}{\tilde{L}}\right)^{1/2} \tag{1.4}$$

The 1-D unsteady momentum equation for incompressible flow in a duct can be nondimensionalized and written then as

$$\left(\frac{1}{B}\right)\frac{d\Phi}{d\tilde{t}} = \tilde{\Delta P}_{Duct} \tag{1.5}$$

Flow velocity is nondimensionalized by wheel tip speed U to form a flow coefficient, pressure differences at the ends of the compression system ducting are nondimensionalized by $1/2\rho_0 U^2$, and time is non-dimensionalized by $1/\omega_H$, the Helmholtz resonator period. As B increases, the system inductance decreases and then for a given amplitude sinisoidal variation in $\widetilde{\Delta P}$, the amplitude of the sinisoidal variation in Φ will increase. Large B systems then can necessarily produce large variations in Φ.

Wheel speed plays a direct role in the physics of the instability when quantified in terms of the B-parameter. This was not the case for the two characteristic time constants derived in the Taylor analysis discussed previously. This is a result of the fact that compressor pressure rise scales directly with the square of wheel speed and depends on the value of Cx/U for incompressible flow.

For a compressor with a smooth time independent actuator characteristic[3], small perturbations in compressor flow coefficient $\delta\Phi_c$ from an operating equilibrium point satisfy the second order differential equation given by

$$\frac{d^2\delta\Phi_c}{d\tilde{t}^2} + \left(\frac{1}{BT'} - BC'\right)\frac{d\delta\Phi_c}{d\tilde{t}} + \left(1 - \frac{C'}{T'}\right)\delta\Phi_c = 0 \qquad (1.6)$$

Conditions required for stability of the compression system naturally follow from this equation to give

$$C' < T' \qquad (1.7)$$

and

---

(3) The term actuator characteristic refers to an equivalent characteristic to be used when modeling the compressor as an actuator disc in a 1-D duct flow. It is an average characteristic which ignores all internal compressor flow details.

$$C' < \frac{1}{B^2 T'} \tag{1.8}$$

where C' is the compressor characteristic slope, T' is the throttle slope, and B is the B-parameter. These stability conditions are derived in App. A. Of the two stability conditions, Eq. 1.8 is usually the more critical for surge initiation. Since T' is always positive, Eq. 1.8 insures that instability will only occur when the compressor characteristic slope is positive. When the compressor slope is positive, the instability point of the compressor is determined by the magnitude of B. For large B, the instability point approaches the point on the compressor characteristic where the slope is zero. When B is small, the instability point moves towards the point of zero flow(shutoff) where the characteristic is more positively sloped.

For operation on the positively sloped part of the compressor characteristic, the magnitude of B controls the surge behavior. The dramatic effect of the B-parameter on compression system behavior due to a throttle perturbation is illustrated in Fig. 1.3. While the quantitative behavior of compression systems is also compressor dependent as well as B dependent, qualitatively the compression system behavior is chiefly governed by the relative magnitude of B. For small B values, the axial compressor operating point, when perturbed past the stall limit, settles on a new stable operating point on the rotating stall characteristics. Surge does not occur.

For larger values of B, the compression system no longer settles on a stable operating point, but instead exhibits a mild surge oscillation with frequency of the order of the Helmholtz frequency. At very large values of B, the system undergoes a limit cycle deep surge or relaxation oscillation. In this limit cycle, the system operating point traces a portion of the steady state compressor operating characteristic.

1.4.3 Actuator Characteristic Types and Surge Triggering

It must be emphasized that the model behavior presented in [25] depends on the shape of the compressor actuator characteristics as well as B. Two typical types of compressor actuator characteristics are shown in Fig. 1.4. The first is a smooth

characteristic continuous in slope while the second has a large discontinuity at the peak pressure rise of the primary(unstalled) characteristic and also a separate distinct secondary(stalled) characteristic. For compressors with the continuous relatively flat actuator characteristic, deep surge is "triggered" via a growing oscillatory type of instability when Eq. 1.8 has been violated.

Compressors with discontinuous actuator characteristics of the second type have a quality missing from those of the first. This quality may be best described as one of "abruptness". Provided B is large enough, deep surge can be "triggered" by the compressor operating point shifting from its primary to secondary characteristic [4]. Again this behavior is dependent on the magnitude of B. If the transition to the secondary characteristic occurs without a time lag, the discontinuity in the compressor characteristic is roughly equivalent to a system step input that creates instantaneously a large pressure imbalance on the duct fluid which can then decelerate the flow into deep surge.

When a compressor with a time independent actuator characteristic(such as shown in Fig. 4a) operates in a simple compression system, surge onset will occur when the overall compressor characteristic slope reaches a critical positive value as given by Eq. 1.8. The overall compressor characteristic slope is naturally the sum of its separate component static pressure rise coefficient slopes. Hence the potential for surge exists when one component(inducer, impeller, or diffuser) has a positively sloped characteristic of sufficient size to overwhelm the negatively sloped stable components such that the overall slope exceeds the critical value. The offending component, termed the stalling component and the flow phenomena present in that stalled component are then credited for initiating surge.

When the compressor actuator characteristic is discontinuous(such as shown in Fig. 4b), the component and flow phenomena responsible for creating the hysteresis is then considered the stalling mechanism which can initiate surge. For multistage axial compressors, rotating stall formation in the compressor is generally regarded

---

(4) If B is not sufficiently large, deep surge will not occur and the mild surge produced will not be sustainable. Instead the system response will decay to steady state operation on the secondary characteristic. Such behavior occurs when aircraft engines enter stagnation stall. See Greitzer[25] for a discussion of this.

as the physical stalling mechanism that can trigger surge in the manner described in Fig. 4b. However surge can only be triggered by rotating stall formation when B is sufficiently large.

1.4.4 Surge Initiation Phenomena and Actuator Behavior in Centrifugal Compressors

Much is known about the surge initiation and dynamic behavior of axial compressor in surge because of their extensive development since World War II, but this is not the case for centrifugal compressors. The role of rotating stall as a key element to surge initiation in axial compressors is well recognized but this view is not universally held for centrifugal compressors.

Emmons, Pearson, and Grant[16] provided the earliest evidence that the occurance of rotating stall might be a precursor to the onset of surge in centrifugal compressors. In a landmark paper, they reported a thorough experimental and analytical investigation of surge and stall in both an axial and centrifugal machine. They first clearly differentiated the non-axisymmetric rotating stall from the annulus averaged oscillating massflow of surge. With their hotwire anemometer installed in the axial gap behind the rotating inducer section, they discovered groups of 3 to 5 stall cells rotating around the compressor case at about 25% of the wheel speed. Two regions of surge oscillations were reported, a mild surge region occurring on the positively sloped portion of the compressor characteristic near the peak at 10.5 Hz, and a deep surge region of lower frequency at 9.5 Hz. At low speeds, these two surge regions were separated by a surge-free region but, at higher speeds, the surge regions coalesced, thereby eliminating the surge-free zone. In the mild surge region, it was also observed that inducer stall cells would form in bursts during the diminishing positive flow part of the oscillation. The report also presents a mathematical surge model which predicts that surge will occur when the compressor useful work per unit mass curve slope vanishes. It was a linearized analysis, and thus only predicted the surge onset point.

An important point was brought out in Emmons, Kronauer, and Rockett [17] which explained the relation between rotating stall and surge. The order (or orders) of magnitude difference in frequency between surge and rotating stall are such that it is generally agreed that rotating stall disturbances cannot drive surge oscillations

directly. They stated: "Thus there is no connection between stall propagation and surge except that the falling pressure characteristic which is necessary for surge excitation may originate in the stall propagation regime."

Kammer and Rautenberg[37] reported rotating stall to be occuring during surge but only near the peak of the characteristic. A performance map of their compressor and time traces at several throttling positions of the map are shown in Fig. 1.5 and 1.6. A phase measurement is also done to compute stall cell number and speed. One area of uncertainty in the results is that no distinction is drawn between surge and rotating stall frequencies. System information such as plenum and ducting sizes are not mentioned so that an estimate of the Helmholtz frequency can be made. The strongest frequency observed near the peak of the compressor characteristic at 211 Hz is said to be a rotating stall frequency. The argument would be strengthened considerably if the system frequency were known to be much lower.

More recently, Abdel-Hamid, Haupt, and Rautenberg[1] report similar rotating stall like disturbances for a centrifugal compressor with a vaned diffuser. They note that no rotating stall was observed until one entered the mild surge regime. A map showing the throttling condition at which these frequencies develop is shown in Fig. 1.7. A set of time traces of the compressor operating presumably in a mild surge oscillation is shown in Fig. 1.8. As in [37], the distinction between rotating stall and surge frequencies is not clearly visable in the results presented.

Flynn and Weber [20] investigate experimentally the effects of various impeller modifications on the surge line and axisymmetric impeller stalling rather than rotating stall is seen as being the prime cause of surge. Because the inducer section of an impeller is made up of thin relatively straight axial blades, the flow in this section can remain attached to the blading only over a very limited range of flow coefficients. Once this stall range is exceeded, the inducer stalls and separated flow regions appear in the inducer tip region. At low throttle values, actual tip reverse flows have been measured [37]. Along the flowpath region downstream of the inducer, these separated flows may reattach or not, depending on the pressure gradients present. Further back meridionally in the impeller, very low pressure surface velocities are present at low throttle conditions. Flynn and Weber contend that as the compressor is throttled down sufficiently, the stalled region at the inducer tip and the expanding suction surface wake region coalesce. This causes

a major flow reversal in the impeller which then precipitates surge.

Implied in this reasoning is that surge is precipitated by a drop in the overall compressor pressure rise characteristic due to local axisymmetric flow reversal in the impeller. The three wide range impeller compressor maps presented also all exhibited nearly flat or negatively sloped characteristics in the low flow regimes, a general requirement of system stability [5]. Flynn and Weber hypothesize that the surge instability is initiated in the impeller. They conclude that a successful prediction of the deep surge limit on a centrifugal compressor map also depends on other unspecified parameters (i.e., system parameters).

Other researchers believe that the surge initiation is dominated by the diffuser performance. Jansen [33] presented both a 2-D theoretical analysis of flow in a radial vaneless diffuser which predicted the occurrence of instability and also experimental data documenting the occurrence of diffuser rotating stall. He found that, as the diffuser inlet flow vector moved toward the tangential during throttling at constant speed, the basically axisymmetric 2-D steady flow changed to an unsteady 3-D flow where stagnant stalled areas of fluid rotated tangentially in the diffuser at some fraction of wheel speed. Later, Frigne and Braembussche[22],[4] documented various types of vaneless diffuser stall present in their test compressor. Senoo and Kinoshita [45] derived a critical diffuser inlet swirl angle for the developement of rotating stall cells in a vaneless diffuser. They found that the ratio of width to radius of the diffuser inlet had a strong effect on the critical angle.

Toyama, Runstadler, and Dean [52] conducted experimental work on a 9:1 pressure ratio centrifugal stage with a vaned diffuser and showed evidence that stalling of the diffuser inlet was a key item in surge initiation. They obtained time-resolved data of the surge event which was an extremely important advance from previous work. As throttling of the stage proceeded towards the surge line, they reported large oscillating massflows of approximately 16% in the steady, "stable" region (mild surge) and then deep surge. From time averaged measurements of the compressor when

---

(5) This is a consequence of the large amount of backsweep they employed in the impeller design modifications as discussed in [31] and [36]. This backsweep also tends to move the diffuser inlet swirl toward the radial direction which, for vaneless radial diffusers, enhances the diffuser's flow stability.

operating in mild surge, a compressor characteristic was estimated in the region of the map near the surge line. As shown in Fig. 1.9, the characteristic appears to change slope discontinuously at the mild surge point. It was not clear whether this effect represented the real characteristic of the compressor or was just a result of time averaging. If the massflow oscillations are large, the compressor may be operating instantaneously for a time much further to the left on the map where the stage is more stalled. The time averaging would then tend to underestimate the level of the instantaneous characteristic.

One additional area of uncertainty in the results presented concerns the level of speed fluctuations present during the surging. Toyama postulates that surge is "triggered" by diffuser inlet stall based on a comparison of calculated mixed out impeller exit total pressure and measured diffuser throat total pressure. This conclusion is quite sensitive to the magnitude of any unresolved and unaccounted for speed differences which might exist between the calculated and measured impeller total pressure. During a deep surge cycle, the compressor torque varies widely although the effect on speed can be minimal if the overall rotary inertia is large and the drive motor changes torque continuously to hold the compressor speed constant. Evidence of speed changes of order $\pm$1.3%(RPM=29500$\pm$350) shown in Fig. 1.10 are roughly equivalent to changes in pressure ratio of roughly $\pm$2%(PR=5.75$\pm$.12) which are of the same order of magnitude as the variation they measured. However the speed variations may be more severe than this if the speed measurement instrumentation frequency response is low. As seen in Fig. 1.11, a comparison of calculated mixed out impeller exit total pressure at their defined surge initiation point shows that there appears to be a loss in total pressure indicative of diffuser inlet stall. However this apparent total pressure deficit could also be a result of larger than measured speed fluctuations present during deep surge.

Dean and Young[12],[13] analyzed some of the main features of the Toyama data and provided additional evidence that the compressor characteristics in the oscillatory regime are not nearly as steep as the time-averaged characteristic would indicate. A modified form of Taylor's analysis was performed which seemed to explain the observed massflow oscillation in the Toyama data. Using a two-valued slope compressor characteristic, the calculation exhibited a steady limit cycle behavior like that in the mild surge regions of Toyama's compressor. However, more

importantly, the calculation only duplicated the 16% massflow oscillation when the positive compressor characteristic slope in the unstable region was much less than the time averaged as measured by Toyama. When the measured value was used, the calculation diverged. Three reasons were given for this result. Among them were the following:

- The time mean actuator characteristic is steeper than the instantaneous characteristic.
- Other inertias such as the rotor wheel inertia are present.
- The compressor is time dependent and does not remain instantaneously on a unique "actuator" characteristic.

To properly measure the compressor actuator characteristics in the low flow regime, Dean suggested that the rig should be stabilized in some fashion so that the "hidden" characteristics could be measured. As an alternative to rig stabilization, the compressor actuator characteristic can be measured transiently if one knows the inductance of the system, the instantaneous massflow vs time, and the instantaneous pressure in the downstream plenum. Then one can subtract out the pressure forces which accelerate the duct fluid in a so called inertial correction technique. Such a proceedure was used by Koff[40] and others to analyze transient data of axial compressors. The inductance required for the inertial correction can be estimated by calculation of an equivalent L/A or measured experimentally by finding the Helmholtz frequency in a duct-plenum system containing a large and well defined plenum.

1.5 Review of Gas Turbine Laboratory Experimental Work

With the goal of increasing the range of centrifugal compressors, a research program was started to provide a more fundamental understanding of centrifugal compressor surge. In the first phase of the project under Capece[5], a turbocharger test facility was designed and built. Essential features of the hardware construction included the design and testing of an air ejector to drive the turbocharger using the oil-free air supply and steam ejector, installation of steady and unsteady pressure instrumentation in the compressor casing, construction of a high response amplifier for Kulite probes, and loop plumbing.

A steady state performance map was constructed, and a surge line was defined. Some high response static pressure data was obtained as the compressor was throttled.

FFT results of these traces, taken at a corrected speed of 51000 rpm, indicated that several subsynchronous frequencies predominated, consisting of the mild surge frequency of 28 Hz and several possible rotating stall frequencies ranging from 94 Hz to 269 Hz. No phase information was then available to determine the number of stall cells occurring in this regime but the results seemed to indicate that rotating stall in the impeller was present prior to surge. Another significant point was that the surge line appeared to depend on system parameters.

In the second phase of work, described in Fink[19], a new facility was constructed. This new facility featured a very large plenum chamber downstream of the compressor. There were several reasons for increasing the compression system volume to create a large B system. Among these, it was desirable to:

- Lower Helmholtz(surge) frequency so that the slow repetitive stalls generated can be studied in the time domain via high response instrumentation.
- When the large B system is in mild surge, the reduced frequency of the compressor is much less than one and therefore its operation is essentially quasisteady.
- Decouple(i.e. lower) the surge frequency from the rotating stall frequency.
- Observe the effect of changing plenum size on the position of the surge line on the compressor map.
- Measure the backflow characteristic of the compressor which during deep surge is accessed transiently by the compressor.

Several types of stall were found in this second phase. The fact that surge point was associated with a critical diffuser swirl parameter seemed to suggest that the vaneless diffuser was the dominant factor in the stage stalling event. Rotating stall while present seemed to be of very low amplitude and confined only to the inducer rather than existing through the whole compressor. This appeared to be different from the behavior of multistage axial compressors where the rotating stall extends through a whole set of closely coupled stages.

The main conclusions reached in the second phase of work were the following:

- The surge line is substantially affected by the B-parameter
- Large massflow oscillations are present in the apparently stable compression system operation close to the surge line.
- Surge induced by large changes in B-parameter can cause large changes in the time averaged vaneless diffuser Cp at equal operating points.

- Diffuser flow is degraded and non-axisymmetric in the oscillatory region close to the surge line for the large B system.
- A critical average diffuser inlet swirl angle appears to be associated with the onset of deep surge for the large B system.
- The flow reversal of deep surge is a consequence of a slow growing dynamic system instability and is influenced by stall in the vaneless diffuser.
- A single inducer stall cell, which is present at the inducer at both large and small flows, does not appear to precipitate deep surge.
- Some circumferential flow distortion was present.

1.6 Experimental Approach and Objectives

To answer the questions posed in Sec. 1.3, a primarily experimental approach was taken. The turbocharger compressor was instrumented with low and high response instrumentation to perform 3 major experimental tasks. These are described as follows:

1) Acquire time resolved and steady data of surge in the large B system and use the results to derive the inertially corrected compressor characteristic.
2) Obtain time resolved and steady data of surge in a small B system.
3) Measure the circumferential distortion present in the small B system.

The goal of the first experiment was to obtain an accurate time history of events occuring in both the compressor and the system during the surge process. The data would answer many of the questions of Sec 1.3, in both categories. The time history was obtained in the large B system. High response instrumentation was used to measure instantaneous mass flow, speed, and pressures in the compressor and downstream plenum during surge. Details of the facility and instrumentation are discussed in Chap. 2. The results and analysis of this experiment are presented in Chap. 3.

In the second experiment, a throttle valve was closely coupled downstream of the compressor thus creating a low B system. The main goals were to obtain low flow characteristics and time resolved data for a comparison with the results of experiment 1 and to stabilize the system to very low flow coefficients. The results of this experiment are discussed in Chap. 4.

In the third experiment, the goal was to determine the asymmetry of the flow

during stall. This was only done on the small B stabilized system. The results of this experiment are described in Chap. 4. To assess asymmetry in the flow and overall flow reversal, the distortion data of experiment 3 was also used to calculate the variation in flow coefficient around the impeller. This is also discussed in Chap. 4.

In addition to the data analysis of the 3 experiments, a variable speed dynamic system model was developed in an effort to explain some of the measured large B system dynamic behavior. This model is described in detail in Chap. 5. A summary of the main conclusions of the experiments and modeling and recommendations for future work are found in Chap. 6.

ROTATING STALL

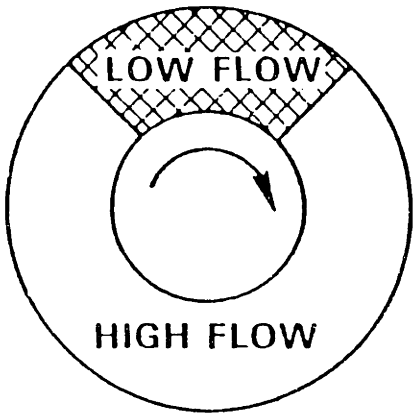

CIRCUMFERENTIALLY
NONUNIFORM FLOW

SURGE

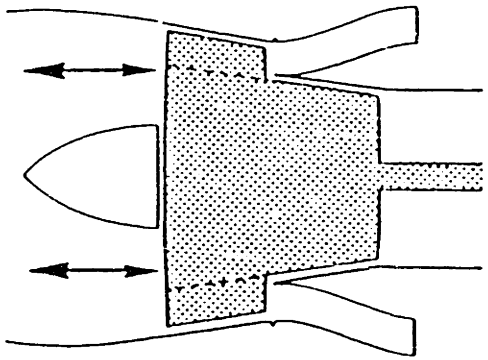

AXIALLY OSCILLATING FLOW

Fig. 1.1 Compressor Instability Modes
(From Greitzer[25])

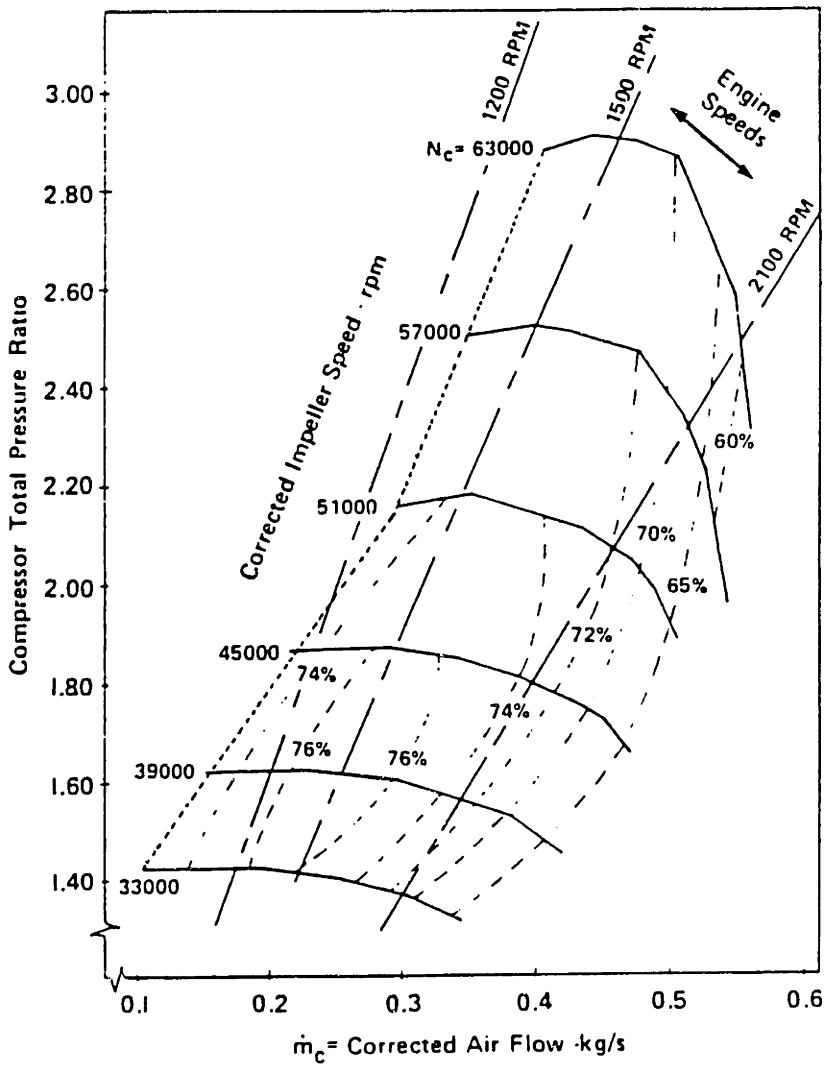

Fig. 1.2 Cummins Diesel-Turbocharger Map
(From Flynn and Weber[20])

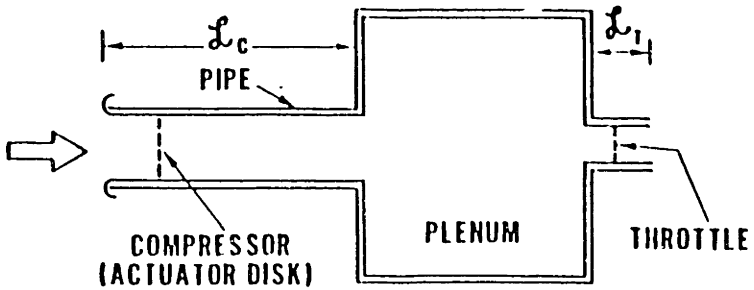

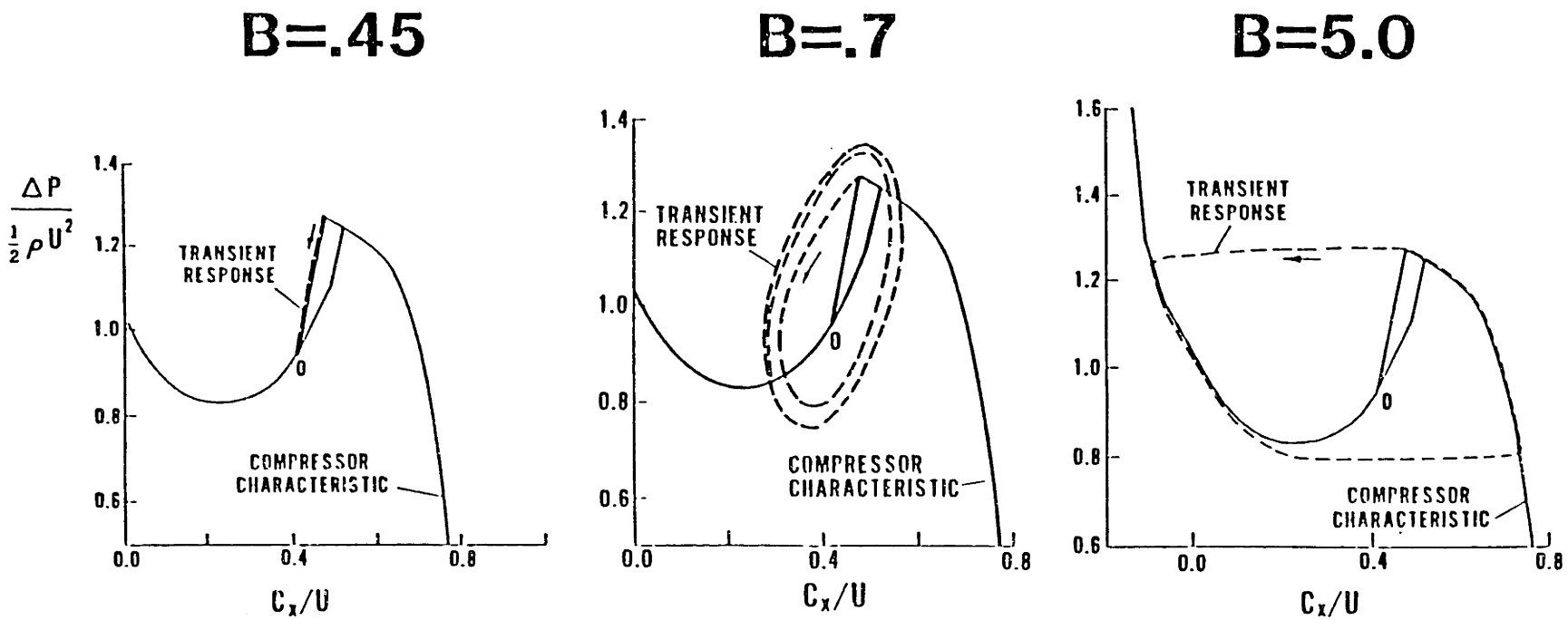

Fig. 1.3 B-Parameter Effect on Compressor Surge Cycle Behavior (From Greitzer[25])

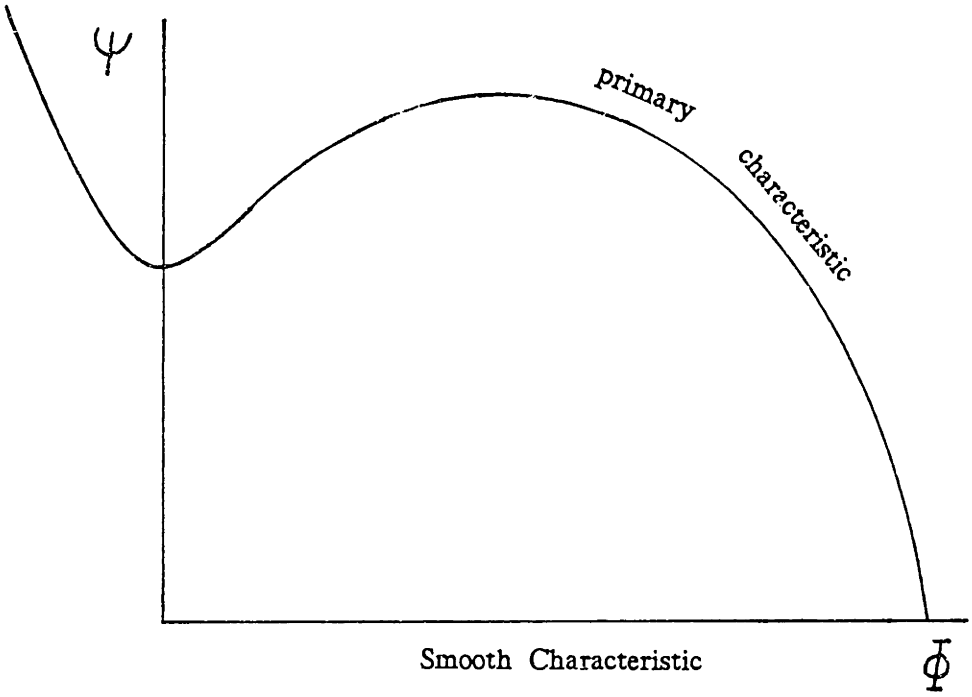

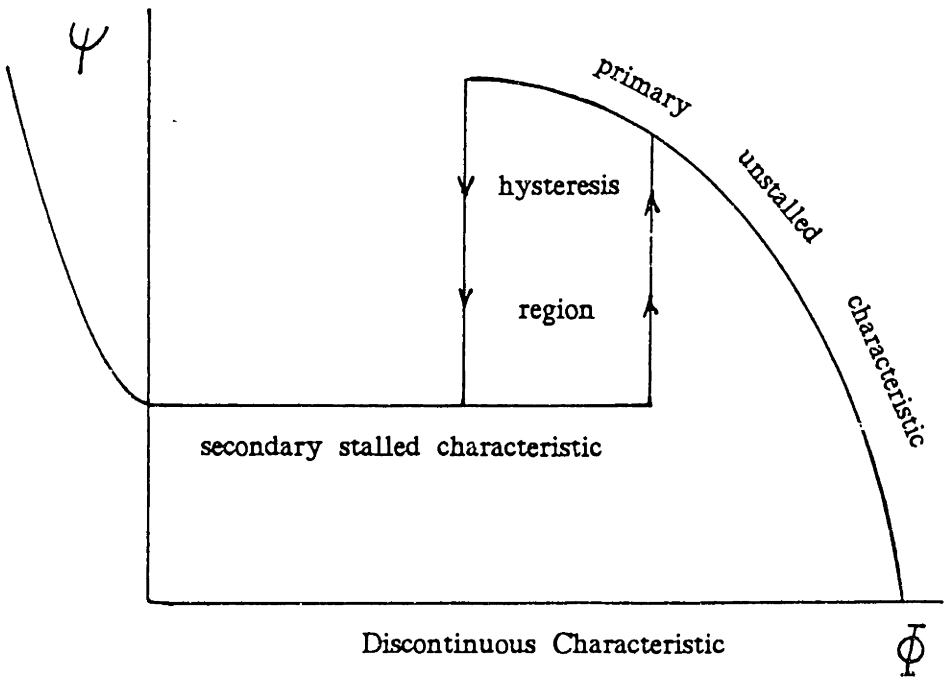

Fig. 1.4 Compressor Actuator Characteristic Types

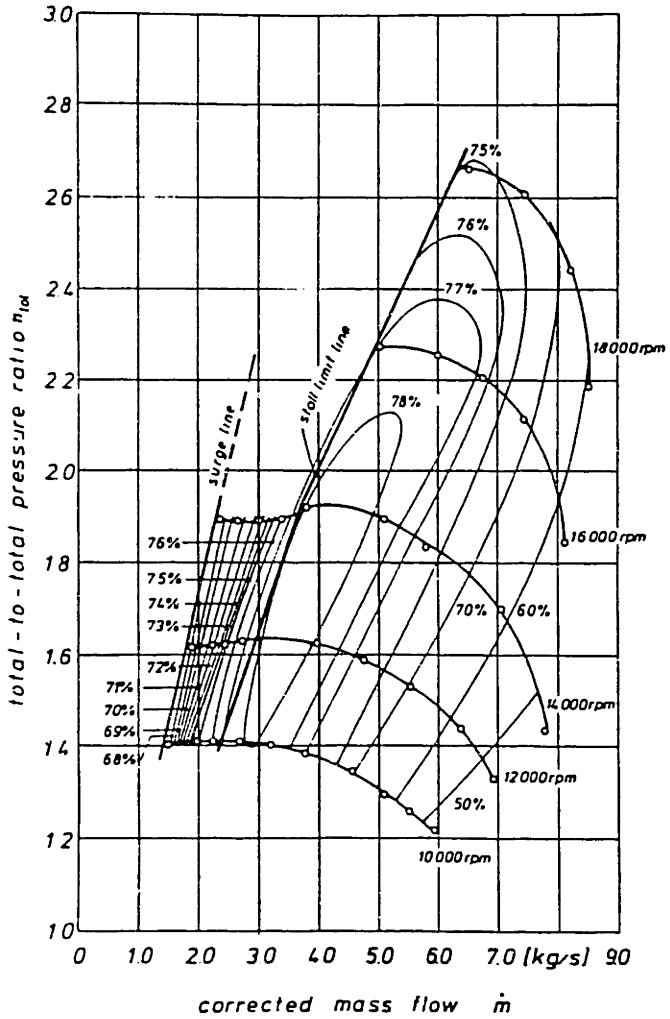

Fig. 1.5 Performance Map of Test Compressor

(From Kammer and Rautenberg[37])

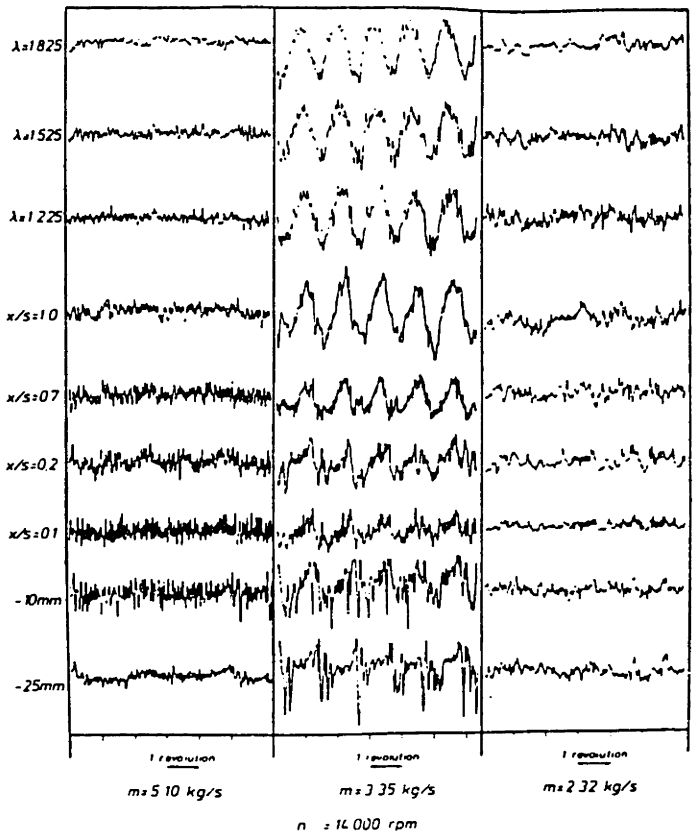

Fig. 1.6 Comparison of Pressure Signals with and without Stall

(From Kammer and Rautenberg[37])

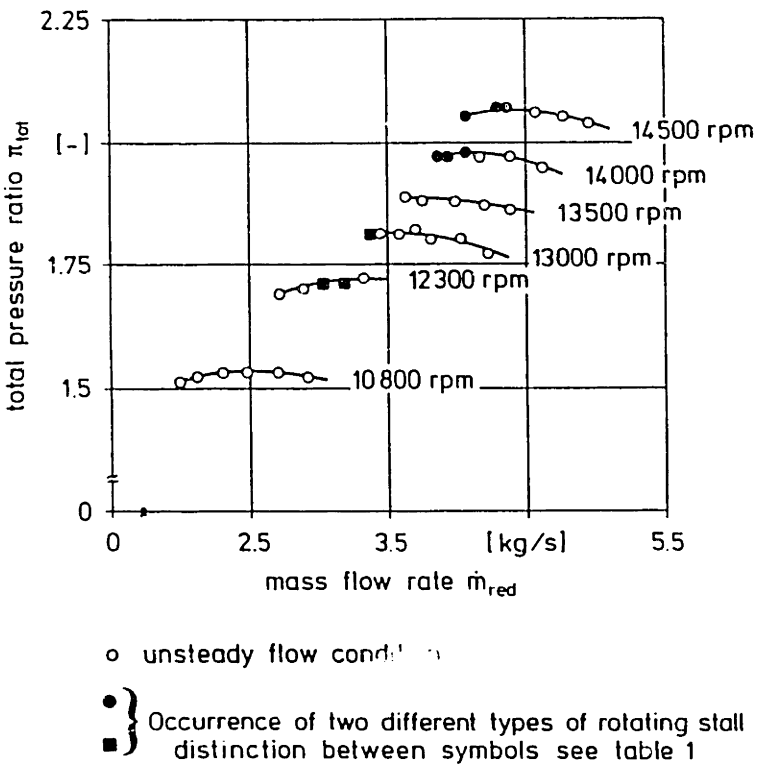

Fig. 1.7 Points of Occurence of Rotating Stall on Compressor Map

(From Abdel-Hamid[1])

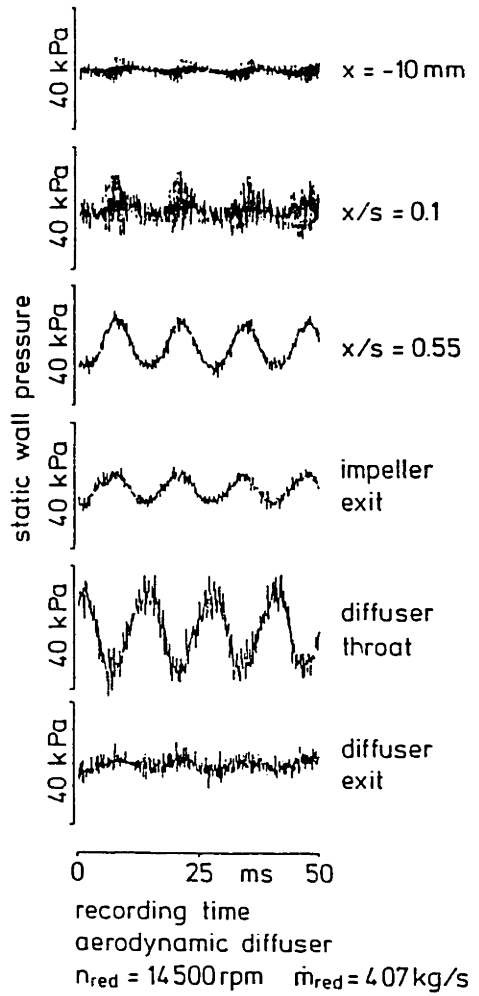

Fig. 1.8 Compressor Time Resolved Pressure Signals

(From Abdel-Hamid[1])

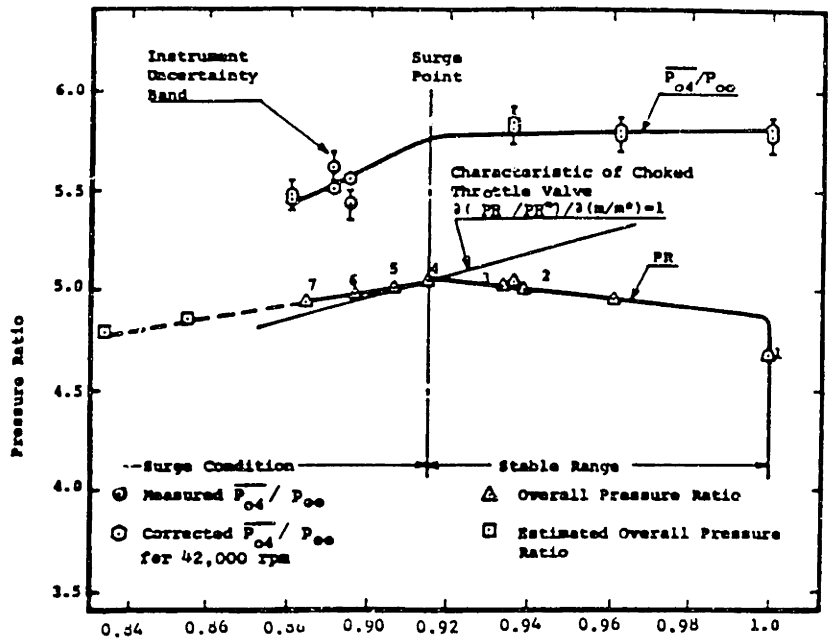

Fig. 1.9 Overall Pressure Ratio and Throat Total Pressure Characteristics

Total Pressure Characteristics
Uncertainties: pr = ± 0.14,
m/m* = ± 0.01, p_{o4}/p_{oo} = ± 0.14

(From Toyama[52])

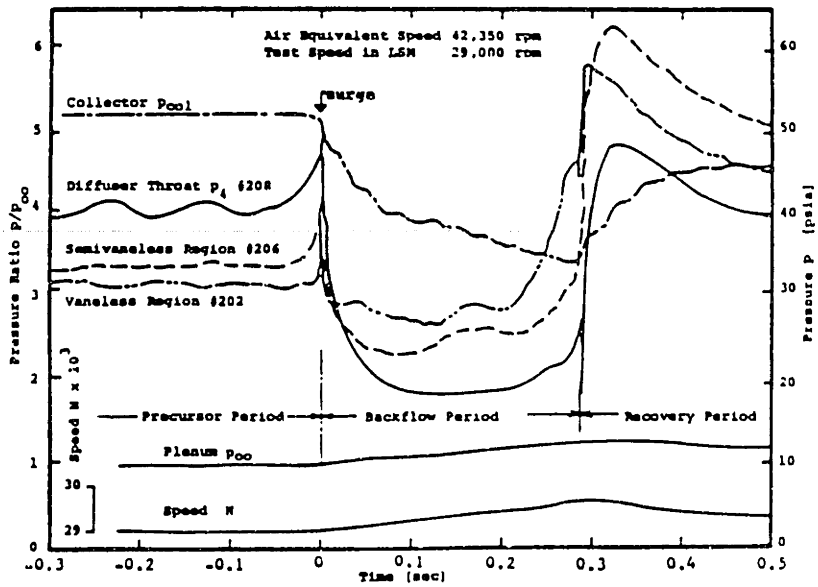

Fig. 1.10 Pressure Variation During the Surge at 85% Speed

(1 psia = 6.89 kPa)
Uncertainties: p = ± 2 psi,
t = ± 0.005 sec, N = ± 50 rpm,
p/p_{oo} = ± 0.14

(From Toyama[52])

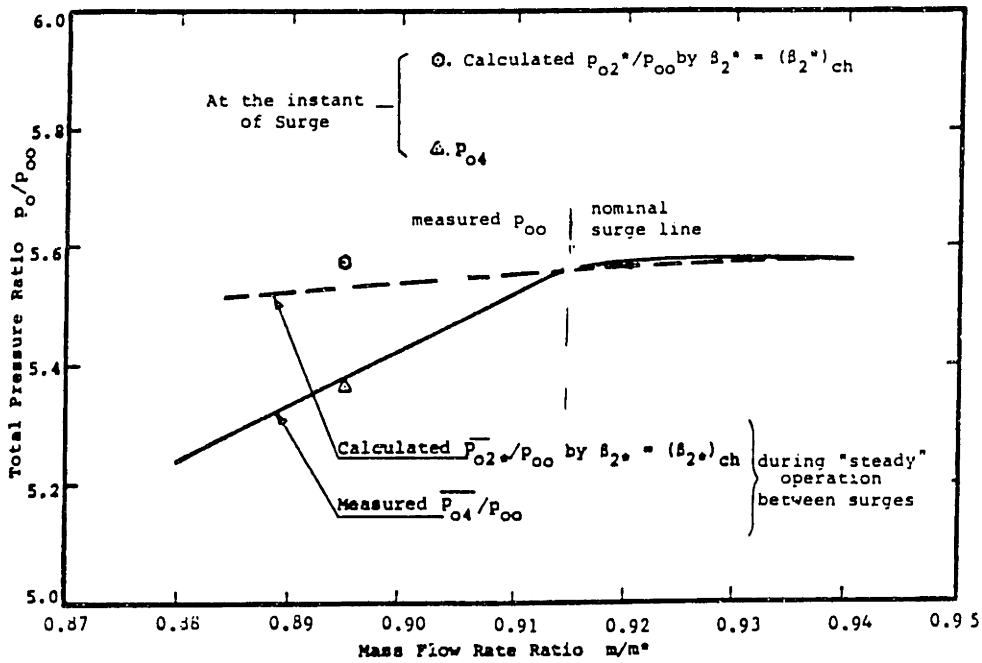

Fig. 1.11 Total Pressure at the Initiation Point of Surge
(m^* = choked mass flow)
Uncertainties: $p_o/p_{oo} = \pm 0.14$,
$m/m^* = \pm 0.01$

(From Toyama[52])

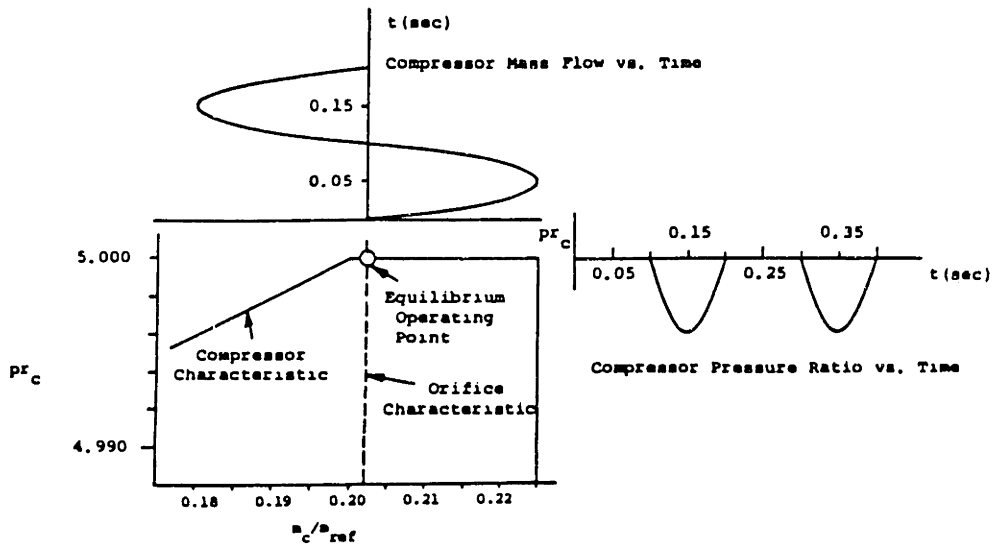

Fig. 1.12 Compressor Characteristic and Limit Cycle Oscillation
(From Dean[12])

CHAPTER 2

FACILITY AND EXPERIMENTAL APPARATUS

2.1 Overall Facility Description

An overhead view of the turbocharger test facility built at the Gas Turbine Laboratory for the experiments in this report is shown in Fig. 2.1. This facility provides a means for driving the test turbocharger without a combustor using the various sources of compressed air available in the laboratory. The details of the design and construction of this facility are discussed in Fink[19]. The air ejector design and design of several other mechanical parts from the original facility are discussed in Capece[5]. The essential features of this facility include:

- Turbocharger mounted on a vibration isolated Unistrut stand.
- Air ejector for driving the turbocharger turbine.
- Capability to operate the turbocharger compressor in large or small B mode by the connection of a large or small volume downstream of the compressor ahead of a throttle valve.
- Three motorized valves and actuators for throttling the compressor, controlling the steam ejector vacuum at the turbocharger turbine exit.
- Oil system with tank, cooler, pump, and filter for turbocharger bearing lubrication. lubrication.
- Manual high pressure air and steam ejector valves for emergency shutdown and backup control.

A photograph of the facility as built is shown in Photo 1.

The turbocharger drive arrangement when operated in the large B mode is shown in Fig. 2.2. In this mode of operation, the turbocharger compressor discharges into a large plenum of approximately 7.3 ft^3. The air in the plenum then empties through a motorized throttle valve and enters the secondary side of an air ejector. In the air ejector, this air mixes with air entering the ejector primary side which is supplied

by the lab oil-free air supply. The ejector provides a several psi boost in total pressure to the secondary flow entering from the throttle valve. The combined primary and secondary air streams mixes out in the ejector mixing tube and then enters the turbocharger turbine inlet. After flowing through the turbocharger drive turbine, the flow exhausts into a pipe of subatmospheric pressure which leads to the laboratory steam ejector.

When the turbocharger compressor is operated in the small B mode, several changes are made in the plumbing of the large B system. These changes are shown in Fig. 2.3. A new valve closely coupled to the discharge tube of the turbocharger compressor volute acts as the throttle valve in the small B arrangement. The turbocharger compressor air that flows through this valve is discharged outside the laboratory via a length of marine hose. The secondary air stream for the air ejector is supplied by a second compressor located in the wind tunnel building. In this arrangement, the air ejector shown in Fig. 2.3 serves to mix the flows provided by both the oil-free compressor and the wind tunnel compressor(Nash compressor). The combined airstream of these two compressors emerges from the air ejector mixing tube, enters the turbocharger turbine, and drives the turbine in an identical manner as was described for the large B system. A schematic of the required air flowpaths from the two laboratory compressors when operating in the small B mode is shown in App. B. The small B throttle valve arrangement is shown in Photo 2.

2.2 Turbocharger Description

The turbocharger compressor studied in the experiments is a Cummins ST-50 centrifugal compressor with a no. 3002729 vaneless diffuser case. A cutaway of the entire turbocharger showing the major features of its mechanical construction is shown in Fig. 2.4. There are no inlet guide vanes and the impeller has 20 blade passages that are unsplit at the inducer and have no backsweep at exit. Tip diameter is 5.035 inches(12.8 cm) and the inlet hub to tip ratio is .428. Vaneless diffuser parameters include a width/inlet radius ratio of 0.092 and an outer/inner radius ratio of 1.619. The compressor is designed to operate at speeds up to 70000 RPM at pressure ratios of over 3. A photograph of the impeller is shown in Photo 3.

2.3 Inlet Instrumentation

The inlet instrumentation is shown in detail in Fig. 2.5. When the inlet is calibrated, measured static wall pressure provides a steady state measure of the compressor massflow. The static wall pressure is monitored through two opposing static wall taps 1.5 inlet tube diameters downsteam from the inlet entrance. These taps are read by two Dwyer flow manometers with ranges of 0-10 inches (0-25.4 cm) and 0-6 inches (0-15.2 cm) H_2O.

To measure unsteady velocity in the inlet tube during surge, a single platinum hotwire(TSI no. 1210T1.5) is mounted approximately 2.6 inlet diameters downstream from the inlet entrance. It is approximately 6.3 impeller inducer diameters upstream of the inducer leading edge and thus out of the local region of unsteadiness which exists in front of the inducer. The inlet hotwire was excited with a DISA type 55D01 amplifier without linearizer. The hotwire output was amplified in separate signal amplifier of 1 - 10 gain and then filtered with a 6-pole Butterworth filter set at a 1KHz cutoff frequency (1/rev frequency = .8 KHz at 48K corrected speed) before sampling by the lab A/D system.

As a hotwire does not distinguish forward from reverse flow, a reverse flow probe was constructed to detect overall reversed flow in the inlet tube. The probe as constructed consists of two pitot tubes oriented 180° relative to each other. This is shown in Fig. 2.6. This probe was mounted at the same axial location in the inlet tube as the hotwire but 180° from it. The reverse flow probe is connected to a Setra Systems Model 237 differential pressure probe with a full scale range of 0 - .5 psi. Damping which is required for following transients with this probe is achieved by the introduction of small lengths of yarn in the plastic tubing connecting the probe to the transducer. The transducer is excited by a 24 VDC supply with its ground offset seven volts below the normal instrumentation ground. The conditioning circuit for the Setra transducer is shown in App. E. This circuit contains a 2-pole Bessel filter with cutoff set at approximately 110 Hz. The amplified and filtered output of this conditioning circuit is sampled on the laboratory A/D system.

The inlet air temperature was measured with a type K thermocouple mounted 1.5 inlet tube diameters downstream of the inlet tube entrance. The total temperature is read via an Analog Devices microprocessor controlled μMAC-4000 temperature multiplexer.

2.4 Compressor Case Instrumentation

To measure unsteady static wall pressures in the compressor during surge, eight high response pressure transducers were installed in the compressor case. The transducers used for the time resolved pressure measurements were Kulite model XT-140-50 semiconductor pressure probes with a full scale of 50 psi. Fig. 2.7, which is a scale drawing of the compressor flowpath, shows the meridional location of the Kulite transducers in the compressor case. The circumferential location of the Kulites relative to the volute tongue position is shown in Fig. 2.8. The tongue location of the compressor volute is defined as the zero degree reference position. There are 4 Kulite transducers denoted by K1-K4 in each of 2 planes on the case located at 27.5° and 117.5° from the the volute tongue. The 4 Kulites at 27.5° are designated the "near tongue" Kulites while those at 117.5° are designated the "far tongue" Kulites.

The Kulite transducers were excited via a 5 volt regulated Ni-Cad battery source. The outputs were amplified by "GTL-Epstein Standard" amplifiers and then filtered with Measurements Group 2310 signal conditioning amplifiers containing 6-pole Butterworth filters. Since it was desired to observe phenomena exhibiting frequencies below the rotational 1/rev frequency such as rotating stall and surge, the filters were set for a cutoff of 1 KHz(1/rev is .8 KHz at 48K). The filtered output was sampled by the laboratory A/D at 3.125 KHz/channel(Nyquist frequency = 1.56 KHz).

The instantaneous rotor speed was detected by a Dolan-Jenner EY2772 reflective scanner fiber optic probe which senses blade passing frequency. The probe is held in position over the inducer region of the impeller in a probe holder. Its angular position is shown in Fig. 2.8. A drawing of the scanner probe holder required is shown in App. E.

The source, detector, and amplifier circuit for the reflective scanner probe was designed and constructed by W. Cook for this application. The essential electronics are shown in App. E.1. Two outputs are provided in this circuit, a 1/blade pulsed output for direct input into the HP counter and a second DC voltage output proportional to blade passing frequency. This circuit also employs an Analog Devices AD4516 frequency to voltage conversion chip to convert the blade passing frequency pulse into a DC voltage. The DC output is directly sampled by the A/D system. The

frequency response of this output was found by measuring the overall speed sensor device response to a frequency step alternating between 10 and 20 KHz. A first order time constant of 5 milliseconds was found for a both a positive and negative step. The results of this test are also shown in App. E.

To measure the instantaneous temperature during surge, a model 300 high response micro-miniature K-type thermocouple manufactured by the Paul Beckman Company was positioned mid-span immediately in front of the impeller inducer at a 16.25 circumferential position. Its position is shown in Fig. 2.7 and 2.8. This thermocouple has a time constant of approximately 1 millisecond or equivalently a frequency response of approximately 160 Hz. A cross section of the probe and the probe's response in a sample test are shown in Fig. 2.9. The thermocouple signal was then amplified in a circuit based on an Analog Devices AD597 conditioning chip. A schematic of this circuit as constructed is shown in App. E. The output of this conditioning circuit was then sampled by the lab A/D.

To measure the impeller total exit pressure, a single low response Kiel head probe KL1 is located at the impeller exit 152.5° from the tongue and oriented in the flow direction. The probe is oriented in the flow direction at a fixed angle of 70° from the radial direction. This angle was calculated as the average flow direction for the diffuser entrance near the large B surge line. For an estimated impeller exit Mach number range 0.6 to 0.8, the Kiel probe is insensitive to flow yaw angles up to ± 40°. The flow yaw angle was estimated to range from -23°($\dot{m}\sqrt{\Theta}/\delta$ = 59.6 lbm/min or .45 Kg/sec @ 33K) to +20° at shutoff thus falling in the range requiring no correction. The effects of local flow unsteadiness was not corrected for in the Kiel probe measurements.

A second compressor case of identical geometry was used for the circumferential pressure distortion measurement. This contains two sets of 16 static pressure taps equally spaced around the circumference at 22.5° at the impeller inlet and exit meridional positions. In addition to these 32 taps, three additional sets of 16 equally spaced static pressure taps are positioned on a vaneless diffuser backplate to measure the static pressure distortion field in the diffuser. The meridional position of these static pressure taps is shown in Fig. 2.10 and their circumferential position is shown in Fig. 2.11. Drawings of the compressor and diffuser plate used for these distortion measurements is shown in App. C.

At the compressor exit, an additional pipe section contains two Kiel probes for total exit pressure measurement, a K-type low response thermocouple, four static pressure taps, and a second Beckman high response K-type thermocouple. The second high response thermocouple was used downstream of the impeller so that the instantaneous temperature ratio across the impeller could be measured. Further downstream in the plenum a single Kulite pressure transducer(K5) was installed to measure unsteady plenum pressure.

Steady state and low response pressure data are taken by a 48-channel Scanivalve with a 0-50 psi (0-3.45x10^{5} N/m^{2}) precision transducer. The compressor exit total pressure as measured by the exit Kiel probes was indicated by a 0-60 inch(0-1.524 m) mercury manometer. All low response thermocouples are read by the MAC-4000 multiplexer. The operation of this and other data acquisition hardware is covered in App. D.

2.5 System Natural Frequency Measurement Apparatus

The equipment necessary to find the system natural frequencies are shown in Fig. 2.12. The periodic noise source of the HP3582A spectrum analyzer served as input to a Harmon/Kardon hk ultrawideband monophonic DC amplifier and channel A of the analyzer. The output of this amplifier drove a Radio Shack 40-1015 6 inch diameter woofer which was placed at the inlet entrance. The amplifier and speaker equipment was provided by G. Haldemann and J. Pinsley. The Setra differential pressure probe used for the reverse flow probe described previously was connected to the downstream plenum. The output of the Setra conditioner amplifier serves as the input to channel B of the spectrum analyzer. Connected as described, the amplitude transfer function of the channel B relative to channel A was measured using the analyzer.

2.6 Inlet Calibration

Measured static wall pressure in the inlet provides a steady state measure of inlet massflow when the inlet tube is properly calibrated. The calibration essentially requires a measurement of the average displacement thickness δ^* of the tube wall boundary layer. To accomplish this, a small 3-hole cobra probe mounted on a traverse was used to measure the total pressure at various radial stations in the

inlet tube. The total pressure measurement combined with a measurement of wall static pressure then determines the radial variation of axial velocity in the inlet if the static pressure across the inlet diameter is constant. Integration of the measured axial velocity profile then determines the displacement thickness. For the calibration, the traverse was mounted approximately 1.5 inlet diameters downstream of the inlet entrance. The traverse could be positioned radially in one of two circumferential orientations 90° apart. This allowed traversing of the inlet at each of 4 circumferential locations 90° apart. The static wall pressure is monitored through the two opposing static wall taps at this location. Additional details and results of the inlet calibration are discussed in Fink[19].

The results of the inlet massflow calibration generates a calibration curve of corrected massflow vs manometer head. To determine the maximum massflow error of the inlet calibration, an uncertainty analysis was performed. For typical uncertainties of ± 0.05 in(± 1.27 mm) H_2O in the panel flow manometer, ± 0.01 mm in the alcohol micromanometer, ± 0.001 in ($\pm 2.54 \times 10^{-2}$ mm) Hg in the mercury barometer, $\pm 1^{\circ}$ R($\pm 0.56^{\circ}$ K) for the MAC-4000, and ± 0.001 in($\pm 2.54 \times 10^{-2}$ mm) for the traverse position, the absolute uncertainty in massflow was calculated. For flows of 20 lbm/min(0.15 Kg/sec) and higher, the uncertainty is roughly equal or less than .1 lbm/min($\simeq \pm 0.5\%$). At lower flowrate of 15 lbm/min(0.11 Kg/sec), massflow uncertainty increased to .15 lbm/min($\simeq \pm 1\%$).

2.7 Inlet Hotwire Calibration

The inlet hotwire whose position is shown in Fig. 2.5 was calibrated in steady state Since δ^* is known from the inlet calibration, compressor massflow can be determined directly via the hotwire. During unsteady massflow surge oscillations, the hotwire provides an approximate measure of the oscillation amplitudes provided that the unsteady δ^* in the inlet is of similar size as the steady state value. A typical calibration curve relating massflow to hotwire output voltage is shown in App. E. Utilizing a second order curvefit, the massflow measured by the hotwire is within $\pm 6\%$ of the calibrated value for the relevant range of flows from zero to approximately 43 lbm/min(0.33 Kg/sec).

The error associated with this method of massflow measurement when the duct flow is not steady is dependent mainly on the unsteady behavior of δ^* in the tube. If we

consider a simple oscillating unsteady laminar flow over a flat plate, one can by an approximate analysis, evaluate the ratio of magnitudes of the steady and unsteady δ^* values. If the freestream velocity over the plate is

$$U_\infty = U_{ss}(1 + \varepsilon \cos \omega t) \tag{2.1}$$

where

$$\varepsilon = \frac{U_{us}}{U_{ss}} \tag{2.2}$$

then for a laminar flow(Rex ~ (O)10^5), the steady state value of the displacement thickness is

$$\delta^*_{ss} \simeq K\sqrt{\nu\, t_{ss}} \tag{2.3}$$

and the unsteady value is

$$\delta^*_{us} \simeq K\sqrt{\nu\, t_{us}} \tag{2.4}$$

where t_{ss} and t_{us} are respectively the steady and unsteady flow time for a freestream fluid particle from 0 to position x on the plate. The ratio of displacement thickness is then given by

$$\frac{\delta^*_{us}}{\delta^*_{ss}} = \sqrt{\frac{t_{us}}{t_{ss}}} = \sqrt{\tilde{T}} \tag{2.5}$$

It can be shown by integration that the ratio of t_{us} to t_{ss} ($= \tilde{T}$) is related to the reduced frequency parameter $\tilde{f}$($= \omega$ x/Uss) and oscillation amplitude ε by

$$\tilde{T} + \frac{\varepsilon}{\tilde{f}}\left[\sin(\omega t)\left(\cos(\tilde{T}\tilde{f}) - 1\right) + \cos(\omega t)\sin(\tilde{T}\tilde{f})\right] - 1 = 0 \qquad (2.6)$$

For forward flow $\varepsilon < 1$ and for $\tilde{f} \gg 1$, Eq. 2.6 reduces to $\tilde{T} = 1$. For very small values of $\tilde{f}$, $\tilde{T} = 1/(1 + \varepsilon \cos \omega t)$. For $\tilde{f} = 1$, the solution depends on the magnitude of ε. For $\varepsilon \ll 1$, $\tilde{T} = 1$. For a severe oscillation of $\varepsilon = 1$. one finds that $\tilde{T}$ can vary in a range of $0.50 < \tilde{T} < 3.00$.

The reduced frequency parameter $\tilde{f}$ can be evaluated for the inlet with ω being the Helmholtz oscillation frequency, x the distance to the hotwire from the inlet entrance, and Uss the average freestream velocity. For a typical value of corrected flow $\simeq$ 25 lbm/min(0.19 Kg/sec) then Uss = 50 ft/sec(15.2 m/sec), x = 1 ft(0.305 m), and $\omega = 42\ \text{sec}^{-1}$. Then $\tilde{f} = 42./50. = .84 \simeq 1$. For a large oscillation $\varepsilon = 1$, then

$$\sqrt{.5} \leq \sqrt{\tilde{T}} \leq \sqrt{3} \qquad (2.7)$$

or

$$.707 \leq \frac{\delta^*_{us}}{\delta^*_{ss}} \leq 1.732 \qquad (2.8)$$

Expressed in terms of absolute uncertainty in δ *ss ($\Delta\ \delta$ *ss), this is equivalently $-0.293\ \delta$ *ss $< \Delta\ \delta$ *ss $< 0.732\ \delta$ *ss. Conservatively then, the absolute uncertainty in the value of displacement thickness from unsteadiness($\Delta\ \delta$ *ss) must be less than the steady state value(δ *ss). By using the measured value of δ *ss at the traverse location and assuming

$$\delta^*_{ss} = 1.7208 \left(\frac{\nu x}{U_\infty}\right)^{1/2} \qquad (2.9)$$

δ^*_{ss} in the tube at the hotwire location is then 0.037 inches(0.94 mm). Then from the approximate analysis result, the absolute uncertainty in δ^* at the hotwire axial position is $\Delta\delta^* < +$ 0.037 in(0.94 mm). This uncertainty in δ^* is equivalent to a ±3.4% uncertainty in massflow.

2.8 Miscellaneous Calibration and Testing

The Scanivalve transducer was calibrated with the 0-60 inch(0-1.52 m) mercury manometer with 0.1 inch(2.54 mm) divisions. Maximum non-repeatable error and nonlinearity were small and found to be within ± 0.05 inch(±1.27 mm) of Hg or ±0.025 psi(±1.72x10^2 N/M^2). The 4 MAC-4000 was also checked against a precision laboratory thermometer at several temperatures ranging from 32° F to 212° F(273° K to 373° K) and found to be accurate to within ±0.5% or ±1° F(+0.56° K). The speed counter was checked with a strobotac and accuracy is roughly ±0.2% or ±1 revolution/sec. The Kulites were calibrated with the mercury manometer in the same manner as the Scanivalve transducer. Non-repeatable error and nonlinearity for the transducers averaged ±0.5% over the manometer range of 0-29.5 psi(0-2.034x10^5 N/M^2). A typical Kulite calibration curve is shown in App. E.5. The Beckman thermocouples were calibrated in steady state by immersion in a temperature controlled oil bath. A typical calibration curve for the thermocouple is shown in App. E.2. Uncertainty in the temperature measurement was less than approximately ±5° F(±2.8° K).

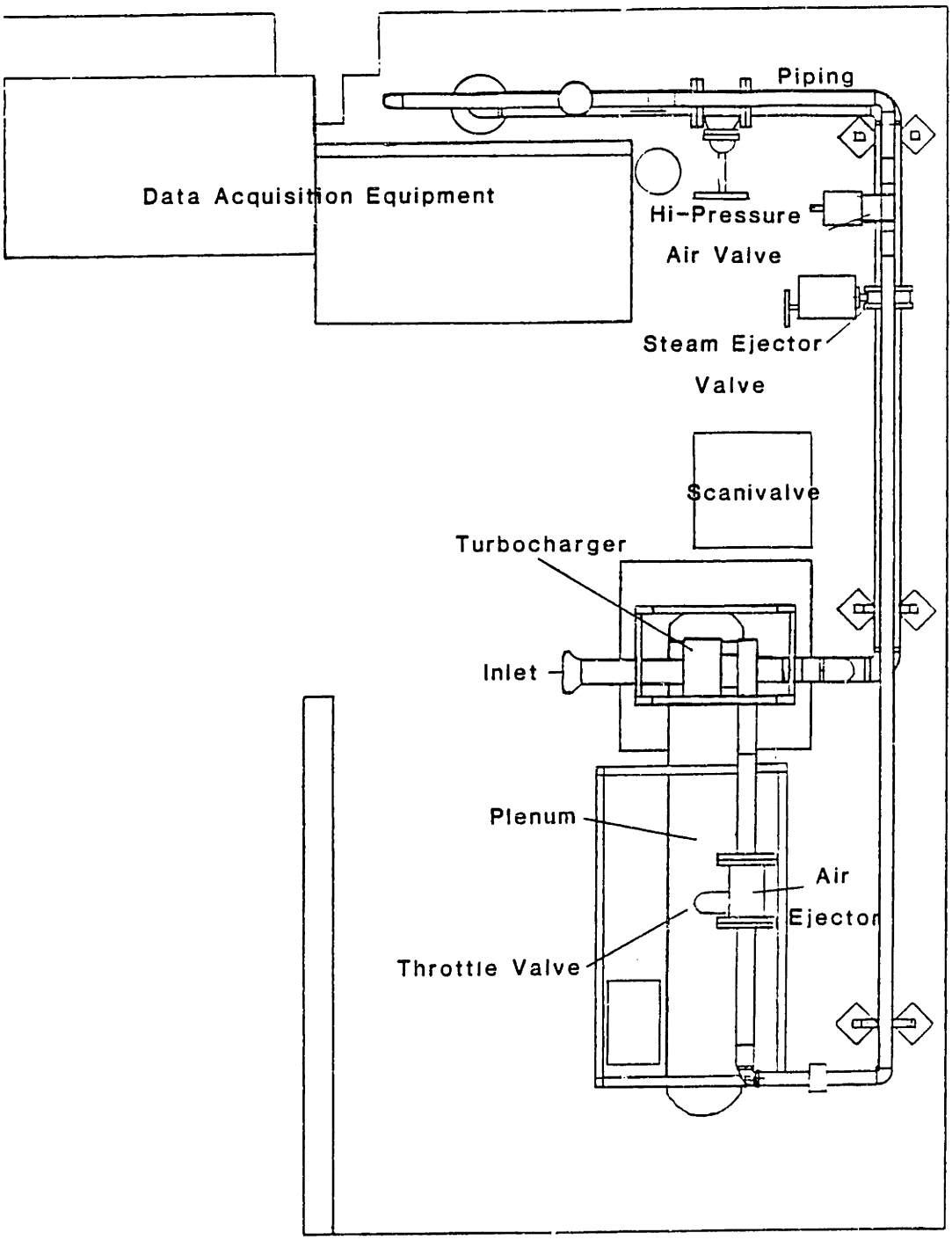

Fig. 2.1 Overall Turbocharger Test Facility

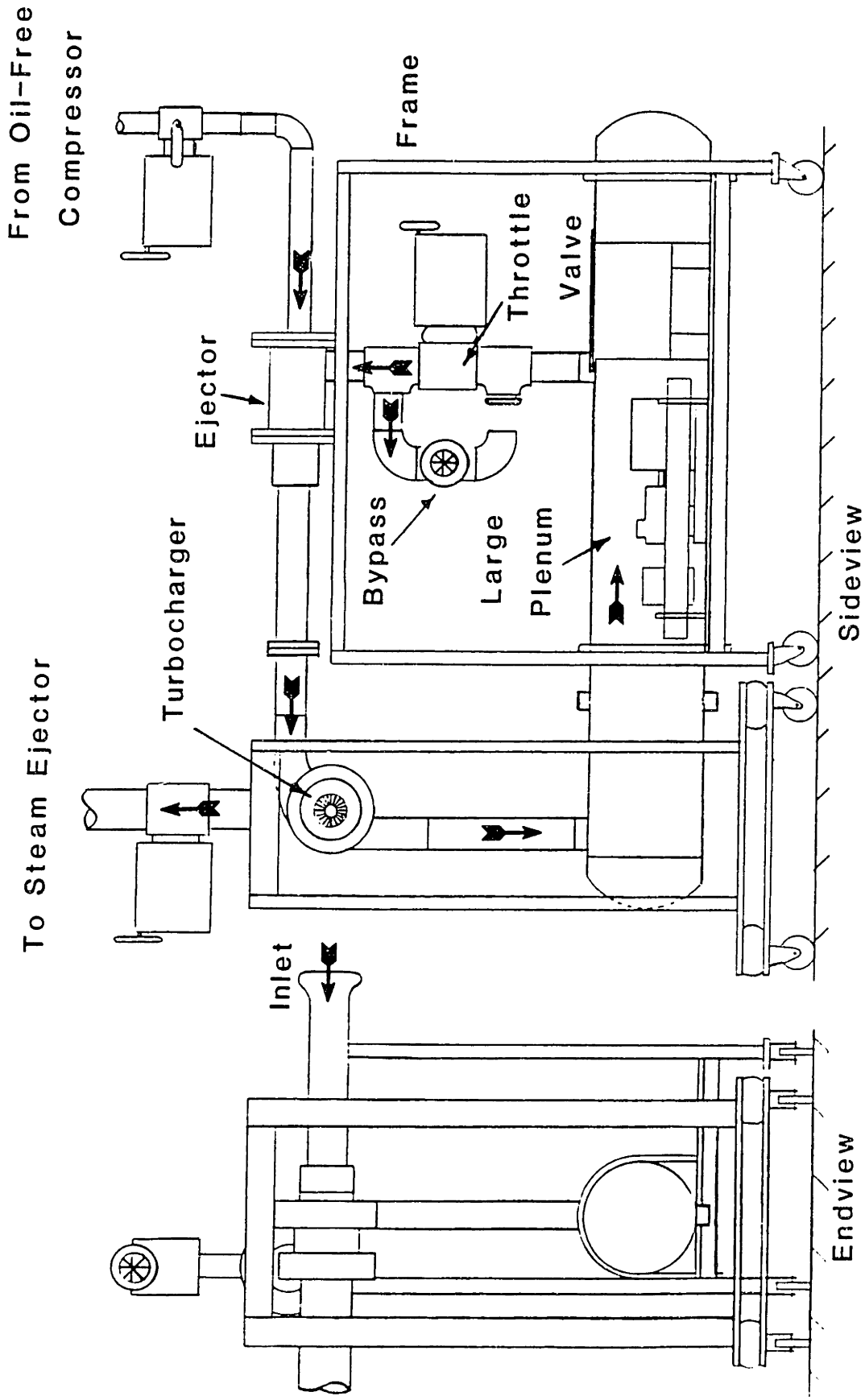

Fig. 2.2 Large B Turbocharger Drive Arrangement

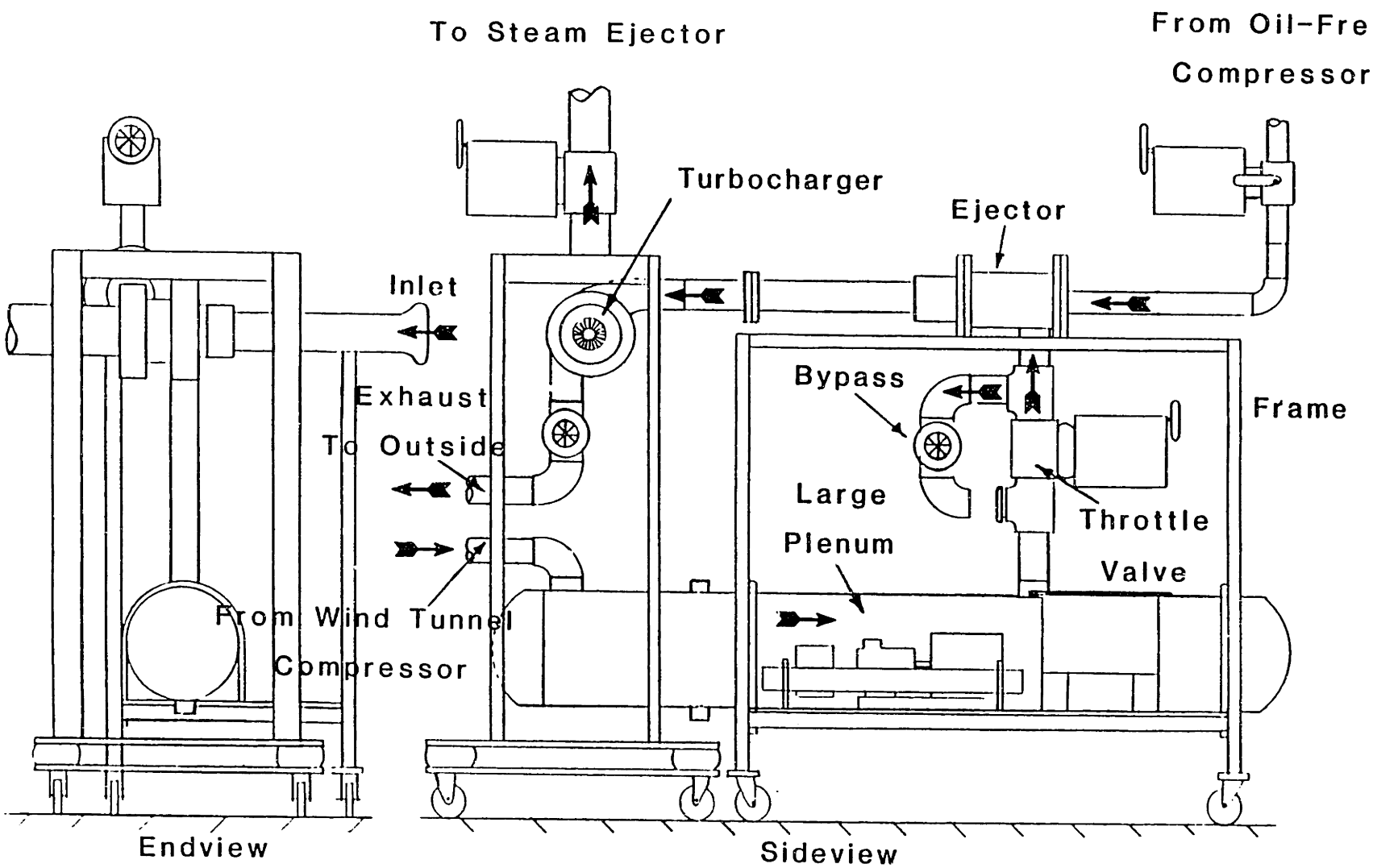

Fig. 2.3 Small B Turbocharger Drive Arrangement

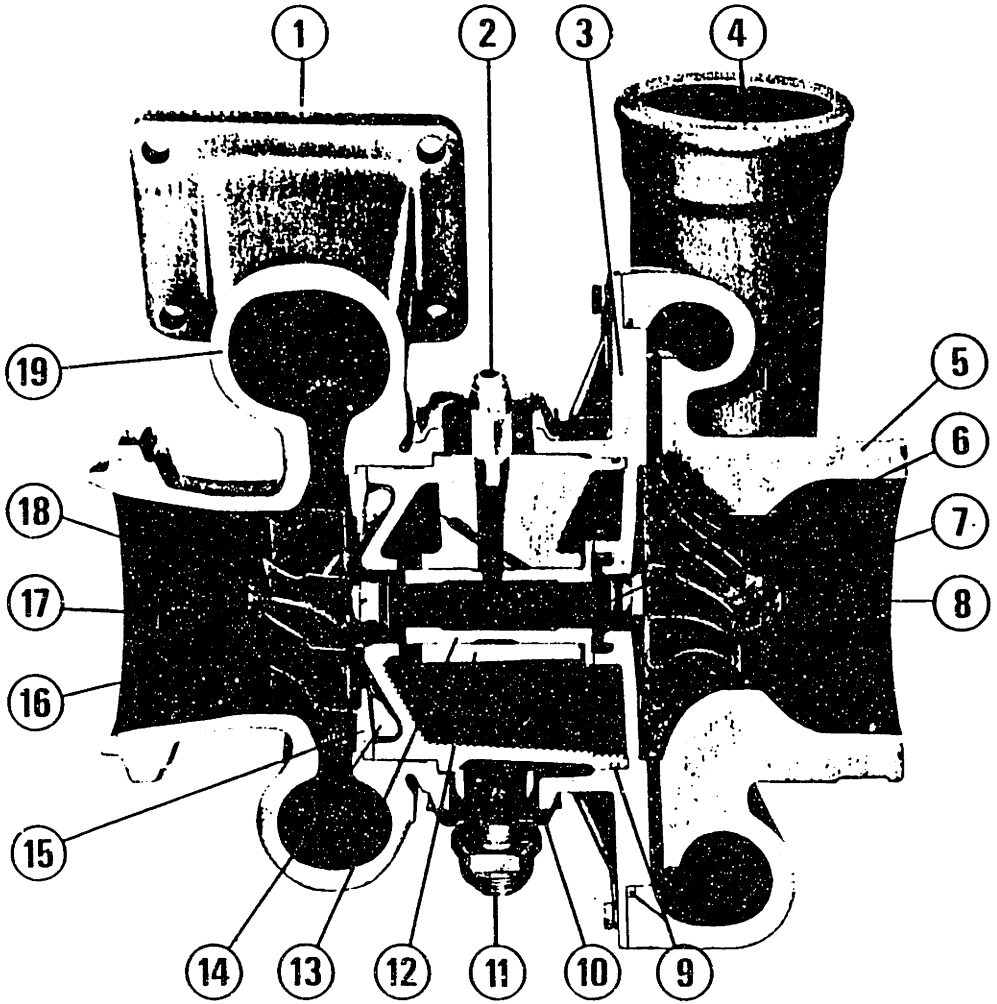

1. EXHAUST IN
2. OIL IN
3. DIFFUSER PLATE
4. AIR TO ENGINE
5. COMPRESSOR CASING
6. OIL SEAL SLEEVE
7. COMPRESSOR WHEEL
8. AIR IN
9. "O" RING SEAL
10. "V" BAND CLAMP
11. OIL OUT
12. BEARING HOUSING
13. FLOATING BEARING
14. INSULATION BATT
15. HEAT SHIELD
16. SEALING RING
17. EXHAUST OUT
18. TURBINE WHEEL AND SHAFT
19. TURBINE CASING

Fig. 2.4 Turbocharger Cutaway

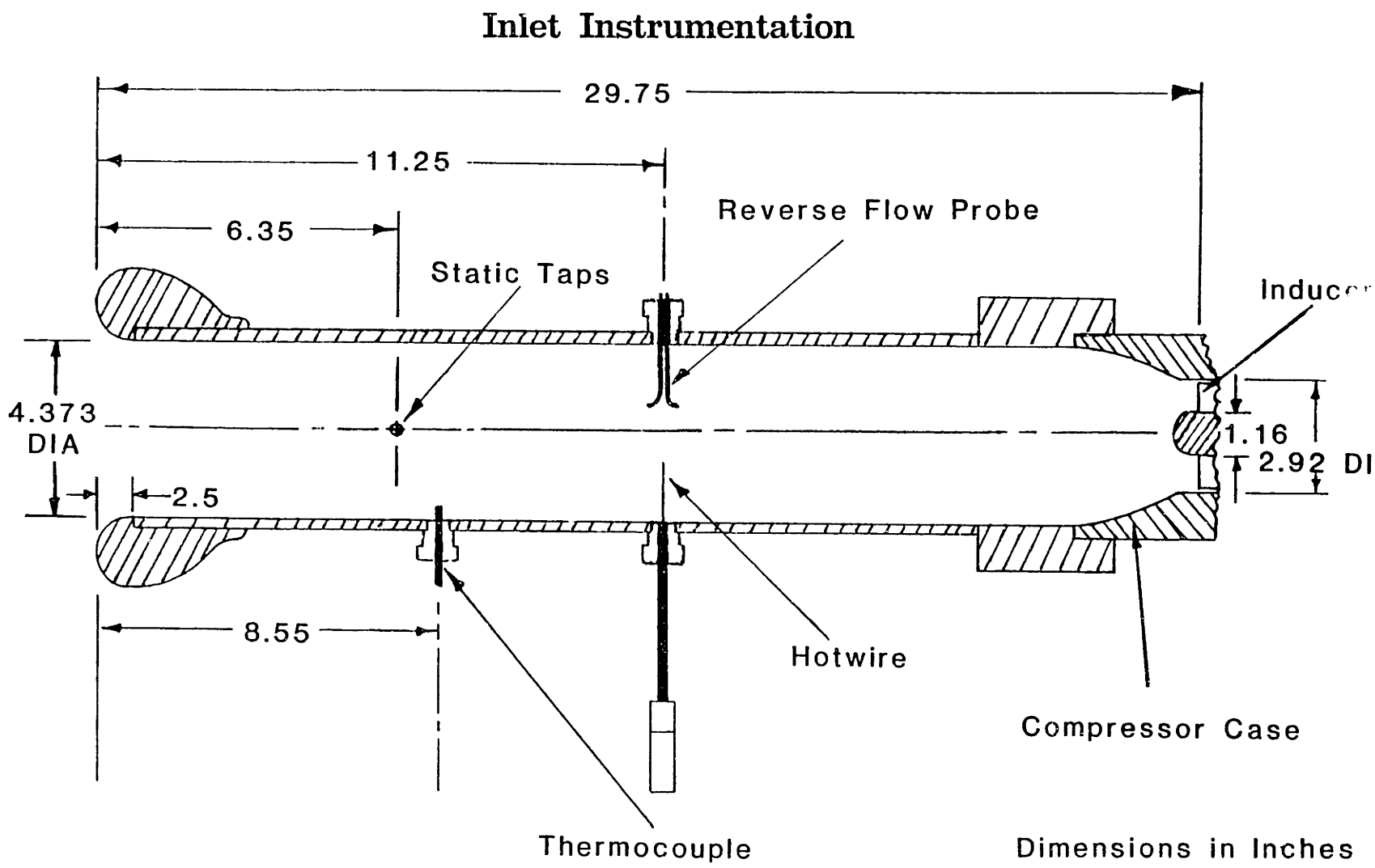

Fig. 2.5 Inlet Instrumentation

Reverse Flow Probe

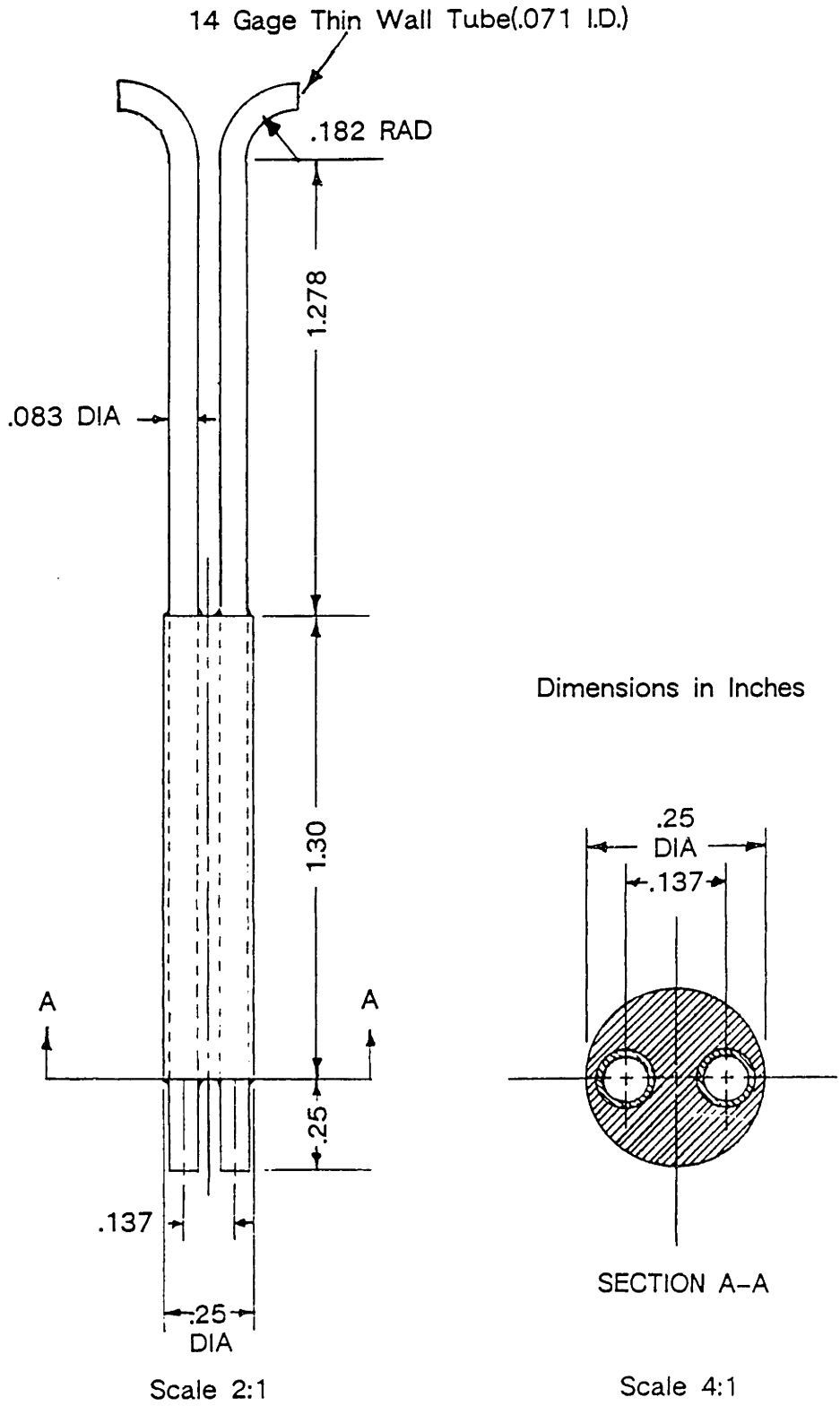

Fig. 2.6 Reverse Flow Probe

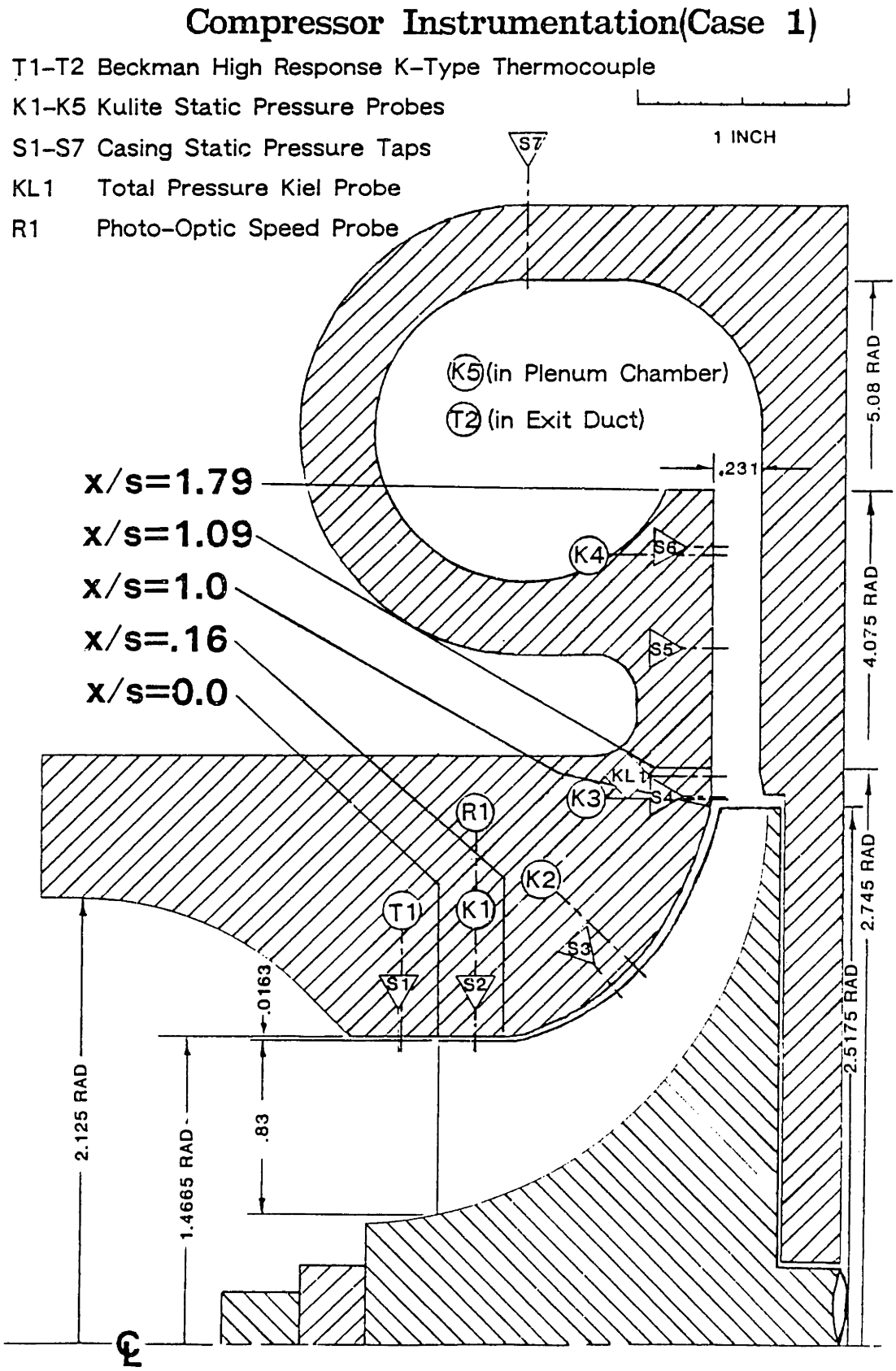

Fig. 2.7 Compressor Case 1 Instrumentation Meridional Positions

Compressor Instrumentation(Case 1)

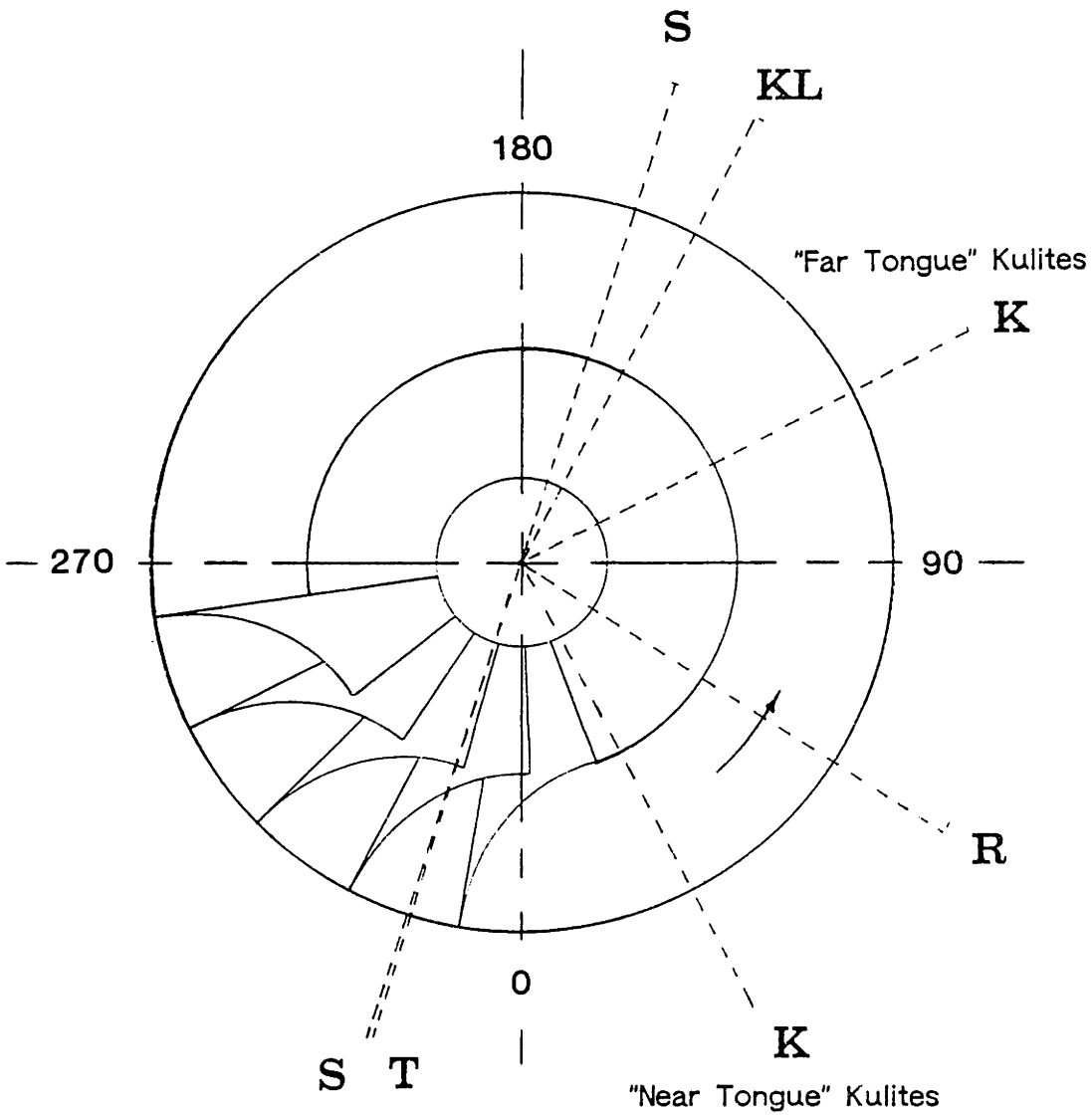

Volute Tongue Position = 0°

T	Beckman High Response K-Type Thermocouple at 343.75°
K	Kulite Static Pressure Probes at 27.5°, 117.5°
S	Casing Static Pressure Taps at 162.5°, 342.5°
KL	Total Pressure Kiel Probe at 152.5°
R	Photo-Optic Speed Probe at 57.5°

Fig. 2.8 Compressor Case 1 Instrumentation Circumferential Positions

Beckman High Response Thermocouple Probe

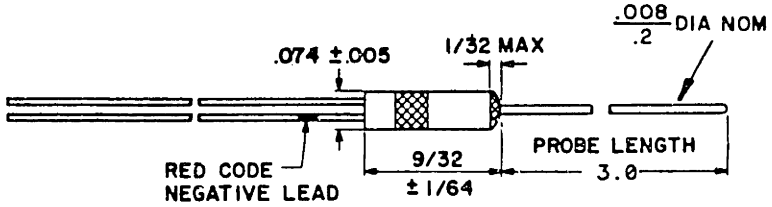

K-Type Micro-Disc Exposed Junction

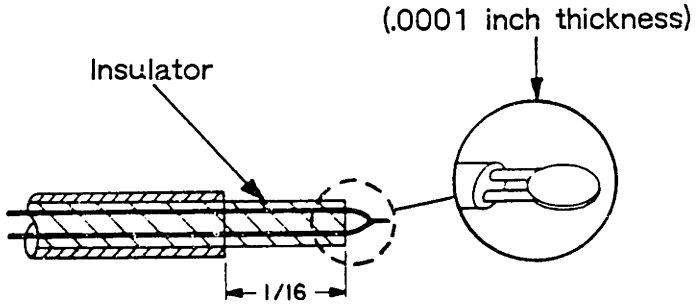

Response in Automotive Exhaust Valve Test

(Test Results from Paul Beckman Company)

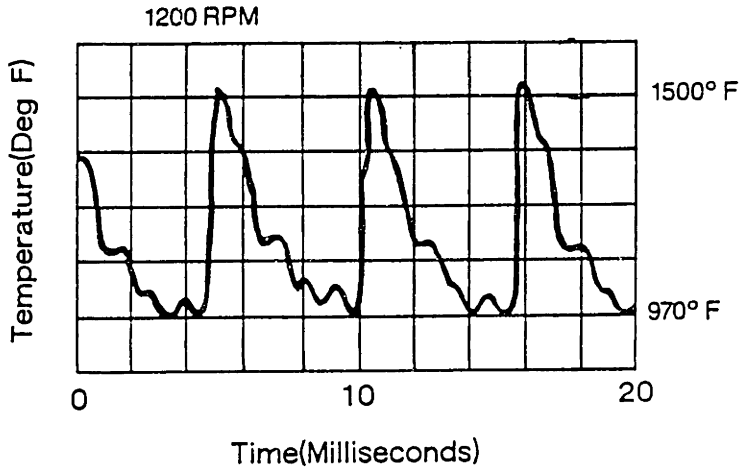

Fig. 2.9 High Response Thermocouple Cross Section and Response

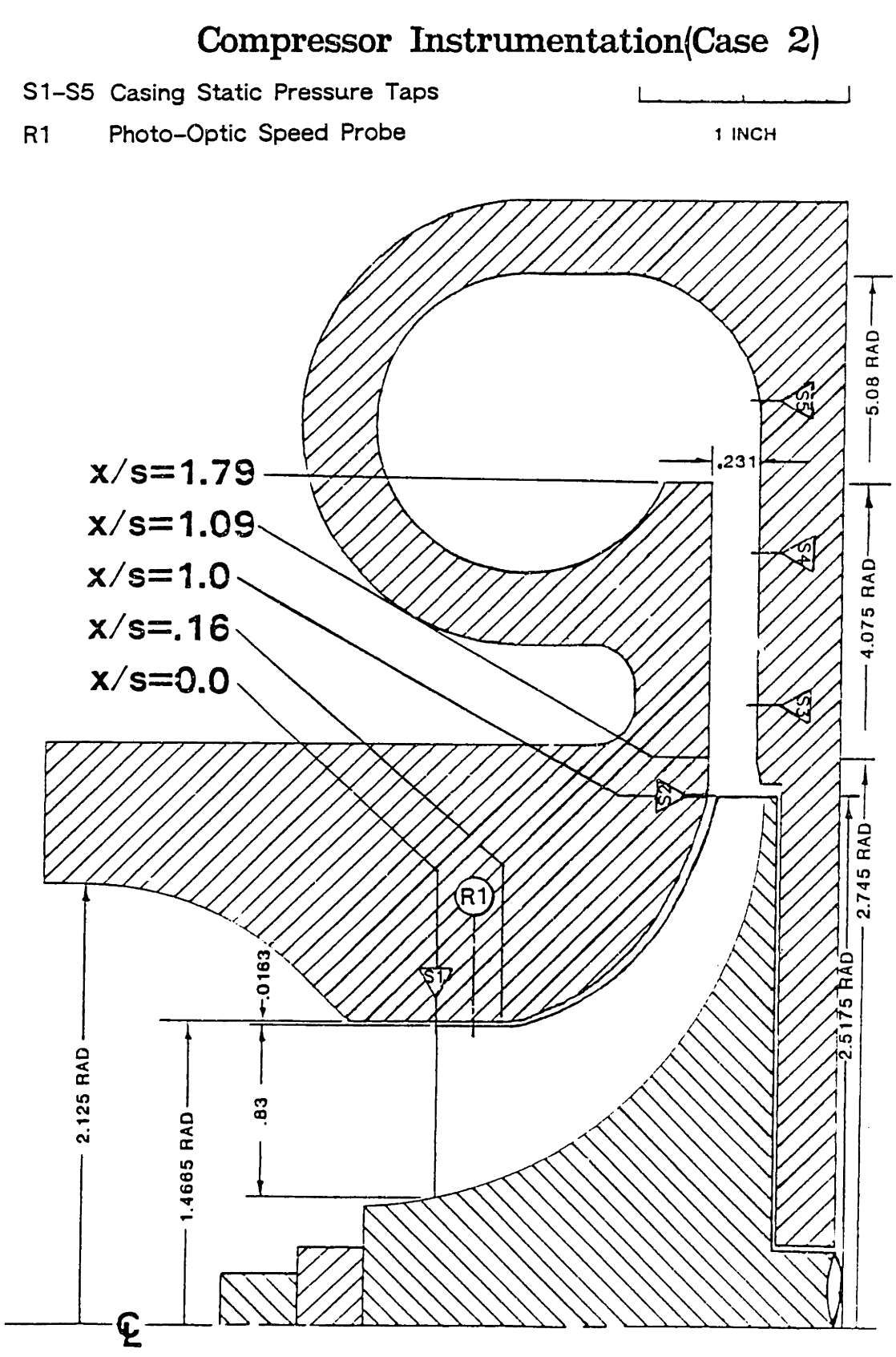

Fig. 2.10 Compressor Case 2 Instrumentation Meridional Positions

Compressor Instrumentation(Case 2)

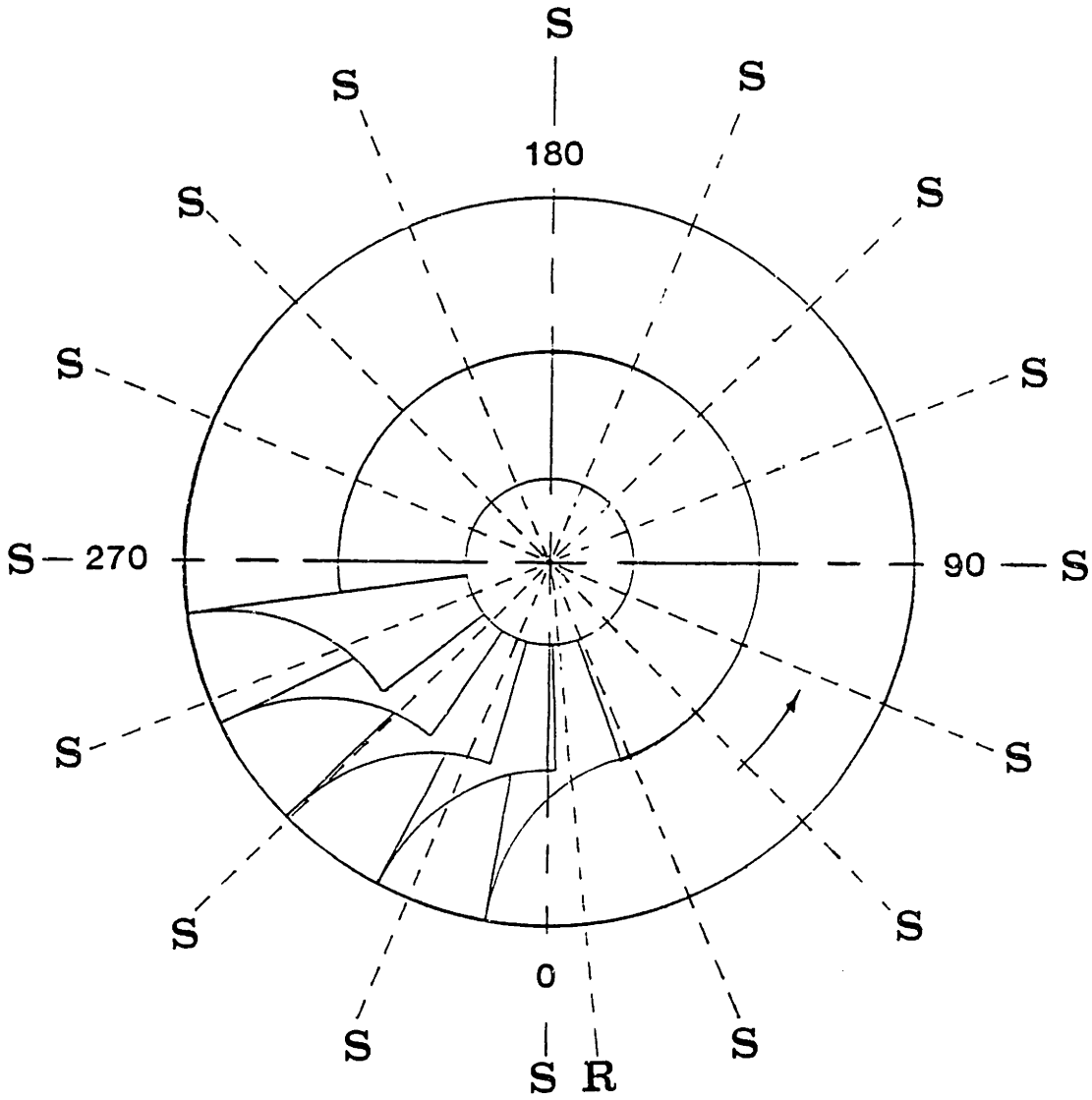

Volute Tongue Position = 0

S Casing Static Pressure Taps at 0°, 22.5°, 45.0°, . . . , 315°, 332.5°

R Photo-Optic Speed Probe at 6.25°

Circumferential angle measured with respect to a reference blade whose trailing edge is aligned with the volute tongue.

Fig. 2.11 Compressor Case 2 Instrumentation Circumferential Positions

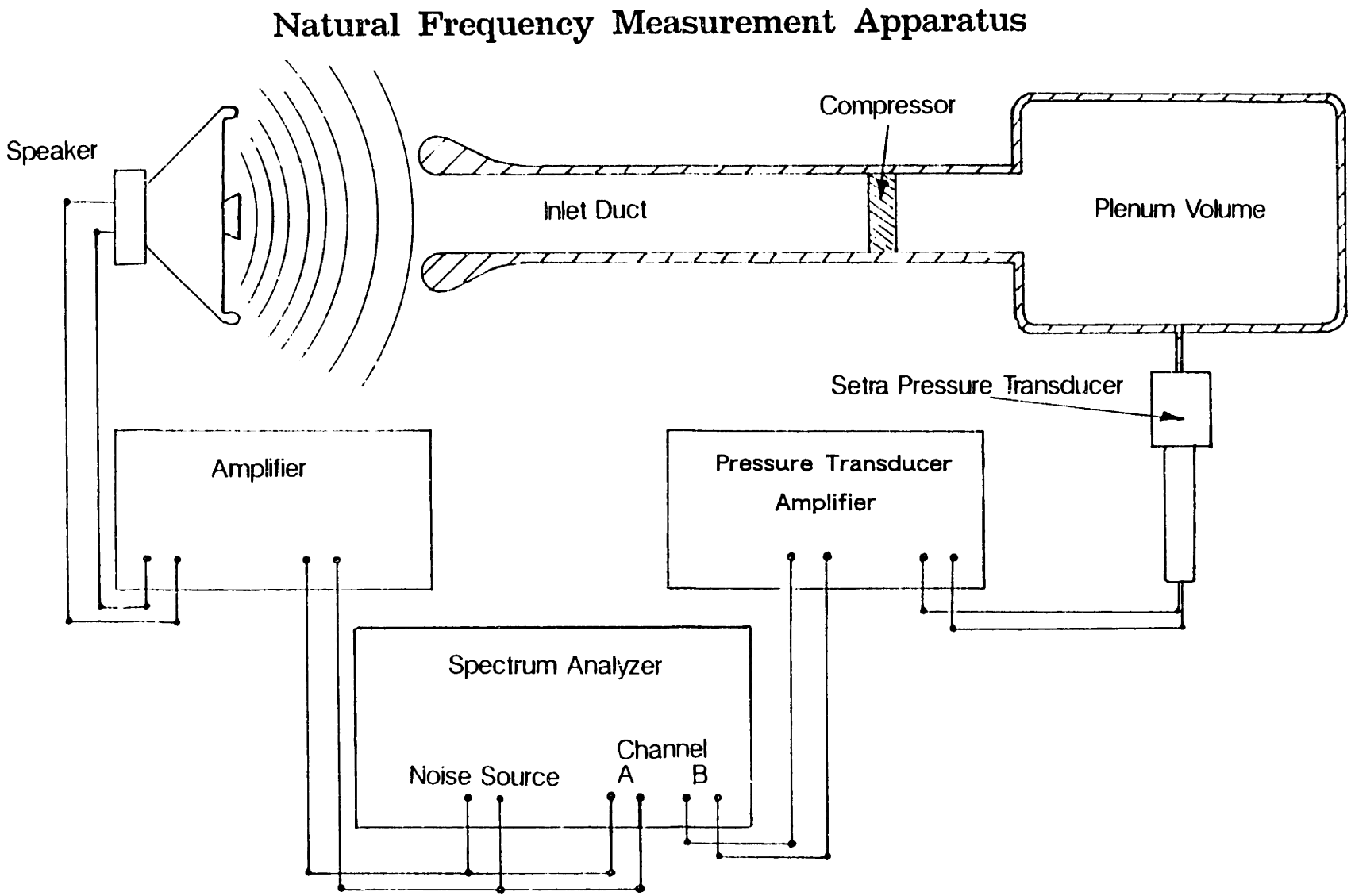

Fig. 2.12 System Natural Frequency Measurement Equipment

CHAPTER 3

LARGE B SYSTEM EXPERIMENTAL RESULTS AND DISCUSSION

3.1 Compressor Map

The performance map of total pressure ratio vs $\dot{m}/\dot{m}^*$ are shown in Fig 3.1. The abscissa $\dot{m}/\dot{m}^*$ is the compressor corrected flow nondimensionalized by the calculated choke flow through the impeller eye reference area at reference conditions(= 111.4 lbm/min @ 545°R, 14.69 psia). Compressor exit pressure for this map is measured directly by the mercury manometer. Corrected flow is determined by the calibrated inlet flowrate manometer pressure drop. At 33K, the maximum error of the pressure ratio is approximately ±.25% of the measured value for a ±0.1 in(±2.54 mm) Hg uncertainty in the manometer. At high flowrates, however, unsteadiness in the pressure reading considerably increases maximum error to typically ±0.2 in (±5.08 mm) Hg giving a ±0.1 psi (±6.89x10 N/m^2) accuracy or approximately ±0.5% for pressure ratio.

The speedlines obtained at lower speeds were obtained utilizing the compressor bypass valve shown in Fig. 2.2. The right point of each speedline is the facility dependent maximum power point. To the left of the surge line, compressor operation was a deep surge cycle of varying period depending on speed and amount of throttling. At the 48K corrected speed, the features of the surge cycle obtained included a very audible plenum blowdown with reverse flow in the inlet, a several thousand RPM drop in compressor speed, and large plenum pressure variations. The surge line was well defined and repeatable at each RPM. A mild surge oscillation of approximately 6-7 Hz begins immediately to the right of the compressor pressure peak very near the surge line shown in Fig. 3.1(deep surge line). With slightly more throttling, the amplitude of the mild surge oscillation increases as the mean operating point approaches the surge line. Time resolved data of the unsteady behavior when in surge will be discussed in detail in Sec. 3.6.

3.2 Method of Determining the Instantaneous Compressor Actuator Characteristic

A major goal of the experimental work as discussed in Chap. 1 was to determine the behavior of the compressor's instantaneous actuator characteristic during surge. When a compression system such as shown in Fig. 1.3 is operating in surge, the massflow is unsteady and in general the instantaneous compressor pressure ratio(total to static) will be different than the plenum pressure ratio. The difference is due to the acceleration of fluid in the equivalent compression system duct of length L and area A. For one dimensional, unsteady, incompressible flow, the momentum equation relates the instantaneous compressor actuator total to static pressure ratio π_c to the plenum total to static pressure ratio π_p by

$$\pi_c = \pi_p + \frac{1}{P_o}\left(\frac{L}{A}\right)_c \frac{d\dot{m}}{dt} \tag{3.1}$$

The right hand term of this equation is the inertial correction applied to the plenum pressure ratio to calculate the compressor actuator pressure ratio. The term (L/A)c in Eq. 3.1 is the equivalent compression system inductance which can be calculated from the compression system flowpath geometry by

$$\left(\frac{L}{A}\right)_c = \int_0^{\ell=\ell_0} \frac{d\ell}{A(\ell)} \tag{3.2}$$

Hence by knowing the stage inductance (L/A)c, $\dot{m}$, $d\dot{m}/dt$, and P_o, the inertial correction term necessary to find the compressor actuator characteristic pressure ratio can be determined.

For a compression system with a large well defined plenum volume(large B system), the stage inductance is also related to the Helmholtz resonator frequency by

$$\left(\frac{L}{A}\right)_c = \frac{a_{po}^2}{4\pi^2 f_H^2 V_p} \tag{3.3}$$

where f_H is the measured Helmholtz frequency, apo is the plenum chamber speed of sound, and Vp is the plenum volume. Hence if the system Helmholtz frequency is known, the compression system inductance can also be determined by application of Eq. 3.3.

3.3 System Inductance Measurement and B-Parameter Calculation

To find the system inductance (L/A)c required for an inertial correction, the natural frequency of the large B system was found experimentally by exciting the duct-plenum system with a random noise source driving an amplifier-speaker setup as shown in Fig. 2.12. The amplitude transfer function of the pressure signal from a transducer located in the plenum chamber with the noise source signal as reference was found utilizing the HP-3582A spectrum analyzer. The results of this measurement is shown in Fig. 3.2 and indicates a resonator natural frequency of 6.48 Hz @ 88°F(31°C).

For measured natural frequency of 6.48 Hz, a plenum temperature of 88°F(31°C), ap0 = 1150 ft/sec(349 m/sec), and Vp = 7.34 ft^3(2.08E-02 m^3), the equivalent system inductance (L/A)c via Eq. 3.3 is equal to 108 ft^{-1}(354 m^{-1}). The calculated (L/A)c from the detailed internal flow geometry was found by application of Eq. 3.2 to be 104.5 ft^{-1}(343 m^{-1}). Hence the experimentally derived (L/A)c was found to be within 3.3 % of the calculated value. Using as the reference area the impeller eye area defined by the annulus area of the compressor inducer with Rtip = 1.467 in(3.7 cm) and Rhub = .620(1.6 cm), A = Aref = 3.85E-02 ft^2 (35.8 cm^2). Then for an (L/A)c of 108 ft^{-1}(354 m^{-1}), the equivalent length is L = 4.16 ft(1.27 m).

The B-parameter is found from Eq. 1.1 for operation at the 48K corrected speed with an impeller tip radius of Rtip = 2.518 in(6.40cm) and Utip = 1055 ft/sec(322 m/sec). At reference conditions, the natural frequency is 6.46 Hz @ 545°R(29.6°C). Since the natural frequency scales directly with sound speed in the plenum or the squareroot of temperature, for a temperature ratio of 1.29, the natural frequency becomes 7.35 Hz. Using the values given above in Eq. 1, the B-parameter is calculated and found to be equal to 2.74.

3.4 Reduced Frequency Calculation

A central objective in the use of the large plenum, was to observe the compressor in essentially quasisteady operation while operating in surge. The nondimensional parameter which is a measure of the importance of unsteadiness in a flow is the reduced frequency or Strouhal Number defined as

$$\tilde{f} = \frac{\omega L}{C_x} \tag{3.4}$$

For quasisteady operation, $\tilde{f} \ll 1$. The reduced frequency can be rewritten as

$$\tilde{f} = \frac{\left(\frac{L}{C_x}\right)}{\left(\frac{1}{\omega}\right)} = \frac{\tau_{throughflow}}{\tau_{change}} \tag{3.5}$$

which is the ratio of two time constants, the compressor throughflow time constant and the flow change time. The compressor throughflow time is given approximately by

$$\tau_{throughflow} = \frac{\rho_o V_c}{\left(\frac{\dot{m}}{\dot{m}^*}\right) \dot{m}^*} \tag{3.6}$$

where Vc is the volume of flow area in the compressor impeller and diffuser. The flow change time for the compressor when operating in mild surge is on the order of the Helmholtz resonator period or

$$\tau_{change} = \frac{1}{2\pi f_H} \tag{3.7}$$

Substituting Eq. 3.6 and Eq. 3.7 into Eq. 3.5 then gives the expression for the reduced frequency which is

$$\tilde{f} = \frac{\rho_o V_c 2\pi f_H}{\left(\frac{\dot{m}}{\dot{m}^*}\right) \dot{m}^*} \tag{3.8}$$

Typical values for operation in mild surge at the 48K surge line are then $\dot{m}^*$ = 111.4 lbm/min = 5.771E-02 slug/sec(.842 Kg/sec), $(\dot{m}/\dot{m}^*)$ = .35, $\rho o = \rho amb$ = 2.263E-03 slug/ft^3 (1.166 Kg/m^3), Vcomp = 9.552E-03 ft^3 (2.70E-04 m^3), and f_H = 6.48 Hz. Then using Eq. 3.8, the reduced frequency $\tilde{f}$ = .044 and the compressor operation may be expected to approach quasisteady operation in mild surge(In deep surge, non quasisteady operation occurs when $\dot{m} \longrightarrow 0$). Since $\tilde{f} << 1$, the expected inertial correction calculated by Eq. 3.1 should be small.

3.5 Nondimensionalization of Data

The steady and transient data in surge was nondimensionalized in terms of flow coefficient and isentropic headrise coefficient. The following discussion explains the reason for changing from the nondimensionalization of Fig. 3.2. Flow coefficient is defined as

$$\phi = \frac{C_x}{U} \tag{3.9}$$

where Cx is the 1-D compressible flow velocity through the impeller eye and U is the impeller tip velocity. The isentropic headrise coefficient is defined as

$$\psi = \frac{\pi^{\frac{K-1}{K}} - 1}{(K-1) M_{TO}^2} \tag{3.10}$$

where π is the compressor pressure ratio, k is the ratio of specific heats, and Mto is the Mach index defined as

$$M_{TO} = \frac{U}{\sqrt{KRT_o}} \tag{3.11}$$

Since the instantaneous rotor speed varies over the course of a cycle, the flow and head coefficient were calculated using the instantaneous speed data from the photo optic probe. The steady state compressor map data of Fig. 3.1 replotted in terms of flow coefficient and isentropic head rise coefficient is shown in Fig. 3.3. When plotted in terms of head coefficients defined by Eq. 3.10, the data nearly collapses into a single curve. Such is not the case when plotted as Cp defined as

$$C_p = \frac{P_4 - P_0}{\frac{1}{2} \rho_0 U^2} \tag{3.12}$$

because of compressibility effects. If the work coefficient is independent of Mach index(a good assumption for a centrifugal compressor with radial exit blades), and the efficiency is only dependent on Cx/U as defined in Eq. 3.9, then the isentropic headrise coefficient would be a single valued curve independent of Mach index. This is true even when the flow is compressible. If efficiency is dependent mainly on Cx/U, and relatively insensitive to Mach index, then the transient data can be presented in terms of the two main variables, flow and head coefficient. Deviations from a single curve reflect the effect Mach number has on the compressor efficiency at fixed values of inlet Cx/U. All the time resolved data that follows in this chapter will be presented in terms of flow coefficient, head coefficient, and Mach index as defined by Eq. 3.9, 3.10, and 3.11.

3.6 Large B System Behavior during Throttling

The behavior of the system parameters, compressor flow coefficient, Mach index, and system isentropic head coefficient at various throttle settings along a 48K corrected speedline is shown in Fig. 3.4 through Fig. 3.8. These parameters are calculated from measurements taken with the inlet hotwire, photo optic speed sensor, and plenum Kulite. In Fig. 3.4, the system parameters vs time are shown at a throttle point of Cx/U $\simeq$ .275. There is some unsteadiness in massflow but the system head coefficient and compressor Mach index are essentially flat.

As shown in Fig. 3.5, changing throttle position to Cx/U $\simeq$ .23, which is just to the right of the surge line(deep surge point), causes the system to enter a mild

surge oscillation of 7.3 Hz. An audible chugging noise accompanies operation in this mode. The amplitude of the roughly sinusoidal massflow oscillation is approximately 18% of the mean flow. This is the type of stable limit cycle phenomena that Toyama et al[52] and Dean[12] reported previously. As Dean showed by calculation, mild surge limit cycle behavior can occur when the compressor characteristic exhibits curvature(Dean's two slope linear characteristic was the simplest one exhibiting curvature). The limit cycle was also found at other corrected speeds when the compressor was throttled very near the deep surge line. The plenum pressure clearly lags the massflow by 90 deg as is observed in Fig. 3.5.

Spectra of the hotwire and phase between the hotwire and the plenum Kulite from Fink[19] showed the frequency of the mild surge oscillation to have a speed dependence. At 33K, the mild surge oscillation occurs at 6.2 Hz and at 48K, the surge oscillation increases in frequency to 7.3 Hz. These frequencies are reasonably close to the measured Helmholtz frequency of 6.48 Hz.

Several effects can cause the mild surge oscillation frequency to vary with speed. One effect which will increase the frequency above that measured at zero rotor speed is simply due to the temperature ratio across the compressor. For a fixed $(L/A)_c$ from Eq. 3.3, the Helmholtz frequency varies directly with sound speed in the plenum which increases with the square root of absolute temperature. If we assume that the frequency of oscillation of the limit cycle observed is roughly of Helmholtz order, then this frequency will depend on the compressor temperature ratio. For example, when the compressor is operating in mild surge at 48K, the temperature ratio across the compressor is approximately 1.3. Then the expected frequency is then equal to $6.48 \times (1.3)^{.5} = 7.4$ Hz which is within 1 % of the measured 7.3 Hz.

At 33K however, the temperature ratio argument does not appear to predict the trend properly. Operating in mild surge at 33K, the temperature ratio is 1.14 and then the expected frequency is equal to $6.48 \times (1.14)^{.5} = 6.9$ Hz. This is over 11% above the actual observed value of 6.2 Hz. This discrepancy may be a consequence of speed variations in the system. However speed fluctuations are smaller at 33K than at 48K. Speed fluctuations will effect the system natural frequency but the trend depend on characteristics of the driving element in the system. This will discussed more fully when the variable speed model in Chap. 5 is presented.

A deep surge cycle can be initiated by a slight throttle closing while the

compression system is operating in mild surge. After the throttle transient, the system enters the deep surge mode of operation shown in Fig. 3.6. There are two distinctly different frequencies seen in Fig. 3.6, a Helmholtz order oscillation of approximately 7 Hz and a much lower frequency of approximately 1/3 Hz. There are roughly four distinctly different regimes of flow in the full 3 second period of the deep surge cycle. First a "quiet period" in flowrate exists where Mach index is increasing and flow coefficient is decreasing slightly. In this phase, the compressor is moving left on its compressor characteristic towards the surge line. In the second phase, fluctuations tend to grow to a large amplitude. During this period, the compressor is operating in mild surge. In the 3rd phase, the surge changes from mild to deep. The plenum pressure collapses in a blowdown phase during which the compressor massflow is reversed. The inlet hotwire is insensitive to flow direction in the inlet tube and registers a high flowrate during the backflow phase. Accompanying this blowdown phase is a violent report from the inlet duct(which made the author very nervous the first time it was heard!!). The blast of hot plenum air at the inlet duct could be felt with a hand placed near it. In the last regime, the blowdown finishes and the flow recovers to the forward direction by first accelerating rapidly to high flow and then decreasing gradually to the "quiet" flowrate. After this, the deep surge cycle repeats.

As seen in Fig. 3.7, further throttling to $Cx/U \simeq .19$ produces the same qualitative system response as in Fig. 3.6 except that the period between blowdowns is reduced to approximately 1.3 seconds and the quiet period has disappeared. With additional throttling to $Cx/U \simeq .16$ as is seen in Fig. 3.8, the quiet phase is gone, the instability growth phase is extremely short, but blowdown and recovery phases remain nearly identical to the less throttled situations of Fig 3.6 and 3.7.

A model of the dynamic behavior that has been observed in Fig. 3.4 through 3.8 will be discussed in Chap. 5. In this system model, the compressibility, speed dynamics, and time lags are shown to have an important effect on the system behavior in time. The speed variations are shown to be a factor in "triggering" the compressor reverse flow seen in the blowdown phase. Abrupt compressor stalls are not necessary to produce the observed periodic blowdown behavior.

3.7 Surge Initiation Discussion

The conditions required to initiate surge as seen in Fig. 3.5 are a result of the violation of the stability criterion given by Eq. 1.8. When $C' > 1/(B^2 x\ T')$ a self excited oscillation or dynamic instability in Ψ will begin to develop. As B $\rightarrow \infty$, then Eq. 1.8 reduces to $C' < 0$. Then for large B, instability will be initiated when the characteristic slope becomes positive and its frequency will be equal to the Helmholtz oscillator frequency. Hence instabilities will develop around the peak of the compressor characteristic. This was generally seen in the system behavior of Fig. 3.5.

3.8 Reverse Flow Calculation for Surge Operation

The hotwire does not distinguish forward from reverse flow so the backflow region for deep surge transient data was calculated by utilizing the mass continuity equation applied to the plenum volume. The massflow in the reverse flow region can be estimated by considering the 1-D unsteady mass continuity equation in the plenum:

$$\frac{d}{dt}\left(\rho_p V_p\right) + \dot{m}_t - \dot{m}_c = 0 \tag{3.13}$$

If we assume the plenum process is isentropic,

$$\frac{d\rho}{dt} = \frac{\rho}{kP}\frac{dP}{dt} \tag{3.14}$$

Substituting Eq. 3.14 into Eq. 3.13 and performing some algebraic manipulation, the compressor corrected flow can be written as

$$\frac{\dot{m}_c\sqrt{\theta}}{\delta} = \left\{\frac{\dot{m}_t\sqrt{T_p/T_{ref}}}{P_p/P_{ref}}\right\}\frac{\pi_p}{\sqrt{\tau_p}} + \frac{V_p P_{ref}}{a_{ref}^2\sqrt{\theta}\,\tau_p}\frac{d\pi_p}{dt} \tag{3.15}$$

where the quantity in brackets { } is the throttle parameter, and τp is the plenum temperature ratio = $\tau po(\pi p/\pi po)^{\frac{\kappa-1}{\kappa}}$ for an isentropic process from an initial equilibrium gas state given by pressure ratio = πpo and temperature ratio = τpo. If the throttle parameter, πpo, τpo, $\pi p(t)$, and its time derivative $d\pi p/dt$ are known, the compressor corrected flow can be calculated from equation 3.15.

The time derivative $d\pi_p/dt$ was obtained by a two step proceedure performed on the plenum pressure ratio time trace. First, the data was smoothed by a moving average taken over approximately 1/5 of a Helmholtz cycle. Then the averaged pressure ratio was numerically differentiated over approximately 1/10 of a Helmholtz cycle. Smaller moving average windows were tried bu failed to produce a reasonably smooth trace of compressor flow. The throttle parameter was assumed fixed since all flow leaving the plenum through the throttle valve passes through the turbine which is nearly choked. Measured total to static pressure ratio in the turbine nozzle were 1.74 @ 33K and 1.64 @ 48K at the surge line operating point. For a 1-D nozzle operating with a total to static π of 1.64(choke π = 1.89) across it, the massflow is 98% of the choked flowrate. Assuming choked flow therefore only incurs a small 2 % error in massflow. The high turbine nozzle π is a result of the sub-atmospheric back pressure created at the turbine exit by the steam ejector.

With these assumptions, the corrected flow was calculated by Eq. 3.15 and compared with the value obtained by the inlet hotwire measurement for 33K and 48K operation in the deep surge cycle mode. The comparison is shown in Fig. 3.9. There is good agreement in the early Helmholtz oscillations with some rounding of the sharp edges due to the "smoothing" moving average proceedure. In the final large oscillation before blowdown, there is excellent agreement in the magnitude and slope. The negative flow region is clearly shown in the figure. In transition back to forward flow, the calculated flow leads the hotwire measured value and is less steeply sloped. The calculated value peaks at a much higher flow and then returns to general agreement with the measured value.

The backflow region was confirmed independently with high response thermocouple mounted immediately upstream and downstream of the rotor. The output is shown in Fig. 3.10 for a similar 48K deep surge cycle. The reverse flow probe output shown in Fig. 3.11 indicates the backflow region but probe "ringing" from underdamping prevented accurate tracking of the transient.

3.9 Inertially Corrected Compressor Head Coefficient in Deep Surge

To determine the instantaneous compressor head coefficient in deep surge, Eq. 3.1 was used to correct transient plenum pressure data. The transient data used for this calculation is seen in Fig. 3.12 which shows flow coefficient(corrected for backflow), Mach index, and plenum head coefficient for system operation in deep surge at an average Mach index $\simeq$ .92(corrected speed 48K). Use of Eq. 3.1 to inertially correct the measured plenum pressure requires the time derivative of massflow $d\dot{m}/dt$. The slope was calculated in an identical two step proceedure as for the time derivative $d\pi p/dt$ discussed previously. First the massflow was calculated from Eq. 3.15, smoothed by a moving average over approximately 1/10 of a Helmholtz cycle. Then the averaged massflow was numerically differentiated by averaging over aprroximately 1/20 of a Helmholtz cycle. The results of the smoothing and numerical differentiation proceedure are shown for the critical transition regions in Fig. 3.13. Also shown for comparison is the hotwire flow measurement data. For the forward to reverse transition, the maximum correction in pressure ratio occurs at the zero flow crossing points.

For example, the magnitude of the inertial pressure ratio correction to be applied to the plenum Kulite data at the forward to reverse flow shutoff point is found by using Eq. 3.1 and typical values of $(L/A)c$ = system (L/A) = 108^{-1} ft (354 m^{-1}), Po = 14.69 lbf/in^2 = 2115 lbf/ft^2 (1.013E+05 N/m^2), and peak slope from Fig. 3.13 for forward to reverse flow of $d\dot{m}/dt$ = -1.8 lbm/(min msec) = .932 slug/sec^2 (13.6 Kg/sec^2). Using these values in Eq. 3.1 gives a correction in pressure ratio = .048. This is a rather small correction and indicates that the compressor and plenum pressure are nearly equal throughout the surge cycle even in the transition regimes where $d\dot{m}/dt$ is highest.

The inertially correct overall compressor head as calculated from Eq. 3.1 using the plenum Kulite data is shown plotted vs instantaneous flow coefficient in Fig. 3.14 along with the large B steady state data. This plot presents a trajectory of compressor instantaneous operating point over 1 complete deep surge cycle. The points are 3.2 msec apart in time or approximately, at 48K corrected speed, 2.6 rotor revolutions. As shown in Sec. 3.4, the reduced frequency in mild surge is much less than 1, so the compressor may be considered to be in essentially quasisteady operation over most of the entire deep surge cycle shown.

There are 5 basic regimes of compressor operation shown in Fig. 3.14. Region 1 is the instability growth phase as shown by the cloud of data centered roughly around $\phi \simeq .225$. From this one sees that oscillations develop around a characteristic pressure curve peak, a consequence of the very large B-parameter of the system. Region 2 is the forward to backflow transition region. In a small interval around $\phi = 0$ given by $-.1 < \phi < +.1$, the compressor is not quasisteady because the through flow time becomes large and the reduced frequency falls in the interval given by $.1 < \tilde{f} < \infty$. However much of the transition is outside this region so may be considered quasisteady. For $\phi > 0$ the data indicates a characteristic which is downward sloping and fairly flat. Region 3, which is the backflow region, is again essentially quasisteady except during the transient to forward flow at the end of blowdown. The significance of the quasisteady blowdown is that the compressor must be operating on its steady state backflow characteristic. In region 4, the transition to forward flow, the compressor reingests the hot gas residing in the inlet duct from the previous blowdown of region 3 and proceeds back towards its forward flow characteristic. In region 5, the plenum fill phase, the compressor operates quasisteadily manner along its forward flow characteristic. At the end of this phase, the compressor reenters the instability growth phase to complete the deep surge cycle.

The shutoff points defined by $\phi = 0$(shown as shutoff 1 and shutoff 2 in Fig 3.14) are of interest because they are different. There is a large hysteresis in compressor pressure ratio over the course of deep surge operation. If one assumes the flow is axisymmetric, then the compressor static pressure rise from ambient conditions at shutoff is just the radial equilibrium value for the fluid inside the impeller channels. By an analysis similar to that in Kerrebrock[39], radial equilibrium requires

$$\frac{dP}{dr} = \rho \omega^2 r \tag{3.16}$$

where ω is the rotor rotation angular frequency. For isentropic flow in the impeller channel, then the density and pressure at any radius is related to the inlet

density and pressure by

$$\rho = \left(\frac{\rho}{\rho_1}\right)^{1/k} \rho_1 \tag{3.17}$$

Substituting Eq. 3.17 into Eq. 3.16 for ρ, integrating both sides, and evaluating at inlet and impeller exit radius R_1 and R_2 respectively gives the following relationship for pressure ratio

$$\pi = \left\{\frac{1}{2}(k-1) M_{T_1}^2 \left(1 - \left[\frac{R_1}{R_2}\right]^2\right) + 1\right\}^{\frac{k}{k-1}} \tag{3.18}$$

where

$$M_{T_1} = \frac{\omega R}{\sqrt{kRT_1}} \tag{3.19}$$

Rewritten in terms of the head coefficient ψ, Eq. 3.18 is then

$$\psi = \frac{1}{2}\left(1 - \left[\frac{R_1}{R_2}\right]^2\right) \tag{3.20}$$

For $R_1/R_2 \ll 1$, this reduces to $\psi = .5$. The data shows a crossing at $\psi = .56$(shutoff 1 in Fig. 3.14) which is close to this value. Physically a crossing from forward to backflow requires a ψ near .5(assuming isentropic flow and zero diffuser contribution).

In backflow, the data of Fig. 3.14 shows a lower crossing of $\psi = .37$(shutoff 2 in Fig. 3.14). However in the data of Fig. 3.14, the Mach index used to calculate the trajectory uses the freestream ambient temperature at all points in the cycle.

From a dynamic point of view, this is the relevant reference since one cares about how well the compressor pumps fluid drawn at ambient pressure Po and temperature To. If one however uses the transient inlet measured temperature such as from Fig. 3.10 to calculate the Mach index, the head coefficient for the characteristic is then

$$\psi_{char} = \frac{\pi^{\frac{\kappa-1}{\kappa}} - 1}{(\kappa-1)\frac{U^2}{\kappa R T_1}} = \frac{\pi^{\frac{\kappa-1}{\kappa}} - 1}{(\kappa-1) M_{To}^2 \left(\frac{T_o}{T_1}\right)} \qquad (3.21)$$

or simply

$$\psi_{char} = \psi_{data} \left(\frac{T_1}{T_o}\right) \qquad (3.22)$$

The data as shown in Fig. 3.14 must be corrected by Eq. 3.22 to arrive at the characteristic value. Correcting using the temperature measurement of Fig 3.10, Tin/To = 1.27 at the end of plenum blowdown and then ψ char = .37 x 1.27 = .47 which is within 6% of the radial equilibrium value of .5. The main point to be observed in the temperature correction is that a significant portion of the pressure collapse seen between shutoff 1 and shutoff 2, where ψ goes from ψ = .57 to .37, is a temperature effect alone. In shutoff 1, the inlet density is ρ o, the ambient value. In shutoff 2, the inlet density is reduced by the temperature ratio(τ = 1.27 from measurement in Fig 3.10) since the pressure is still ambient i.e. ρ = P/(R x T) = Po / (R x τ in x To).

The timing of the collapse in compressor head coefficient where ψ goes from .57 to .37 is also very significant. The collapse occurs after ϕ becomes negative not before. This behavior contrasts with that of a multistage axial where the collapse in actuator head coefficient occurs while the overall mass averaged flow is still positive. Both the timing and the hysteresis mechanism are different between axial and centrifugal compressor surge behavior. These differences have ramifications for the active control of surge behavior which will be discussed in Chap. 6.

The region 4 hot gas reingestion or recovery phase is also of interest. In this phase of the surge cycle, the low density air residing in the inlet duct from the previous plenum blowdown is reingested by the compressor. Since the density is much lower, the compressor pressure rise will also be proportionately lower. The time of reingestion can be estimated as roughly the time it takes to empty the inlet tube or

$$\tau_{reingest} = \frac{\rho V_{inlet}}{\dot{m}} \tag{3.23}$$

The inlet density of air at this point was estimated from the temperature measurement shown in Fig. 3.10., which shows an inlet temperature ratio above ambient conditions of approximately 1.27 at the end of the plenum blowdown phase when the flow changes direction from back to forward flow. Pressure in the tube at this time is essentially ambient. Then the density of air = ρ amb or 1.81E-03 slug/ft^3 (.933 Kg/m^3). The massflow for the estimate was taken to be the average one in the transition or 38.5 lbm/min = 1.99E-02 slug/sec(.29 Kg/sec). For a tube volume of .210 ft^3 (5.94E-03 m^3), the time of hot gas reingestion from Eq. 3.23 is then equal to 19.1 msec. The data shows this phase to take 2.5 times longer or roughly 45 msec. Clearly temperature effects alone do not explain behavior in the transition phase and some other as yet unidentified lagging process must be present in the compressor. This will be discussed further when the transient pressure data is presented in the next section.

After the hot gas from the previous blowdown has been reingested, the inlet temperature returns to ambient as seen by Fig. 3.10. and operation returns to the forward flow characteristic. The transient data however does not appear to reach the steady state data shown. The reason for this is probably because the steady state data is for a much lower Mach index. As seen in Fig. 3.12, the transient data speed peaks at about 51K during the start of recovery and then drops rapidly to 45K. The 45K-51K high flow steady state characteristic data could not be obtained because drive power limitations prevented running in this regime in steady state.

When operating at lower average values of Mach index, the compression system exhibits similar surge behavior but with some differences. Fig. 3.15 shows the

system parameters in surge operation at 33K average corrected speed. As in the 48K data of Fig. 3.12, the overall surge cycle consists of flow oscillations with two different characteristic periods. The shorter period oscillation is a Helmholtz order resonator period and the longer one, the time between blowdowns is associated with speed changes. However, the magnitude of the massflow oscillation in mild surge as a percentage of the mean flow is much larger on the order of 60 % of the mean flow. Also no "quiet" period of oscillation-free flow is seen in the 33K data which was clearly present in the 48K data of Fig. 3.12. This is perhaps due to the smaller percentage change in speed observed in the deep surge cycle for 33K compared to the 48K data. The speed fluctuations were on the order of $\pm$ 3 % for 33K vs $\pm$ 5.5 % at 48K.

The inertially corrected compressor characteristic trajectory for operation in deep surge at 33K is shown in Fig 3.16 along with the previous 48K results for comparison. There appears to be a speed dependence in the characteristic peaks. For the 33K data, the peak of the compressor head occurs at a lower ϕ = .19 and is higher in magnitude(ψ = .67 vs .63) than at 48K. The dependence of the peak location on speed is a compressibility effect. Physically, this may be a result of the effect compressibility has on the volute matching condition. Additional evidence of this behavior will be discussed in Chap. 4.

In Fig. 3.16, the surge oscillations are also seen to develop around the trajectory peak as was the case at 48K. Both shutoff points 1 and 2 are higher than those of 48K data. This is not an effect of temperature induced transducer drift. The zero of the transducer when in the hot state is recorded with each set of transient data and is used in the data reduction process. For axisymmetric and isentropic conditions of flow and density in the impeller, the forward cross points 1 should be speed independent and approximately equal to .5 as given by Eq. 3.20 for $R_1/R_2 << 1$. However Eq. 3.20 assumes that flow entering the inducer from freestream does so without losses(isentropic) and that the flow is axisymmetric. As will be shown in Sec. 3.12, the flow is strongly asymmetric due to a local flow reversal in the impeller at the inducer tip location nearest the volute tongue. The large losses present in the stalled inducer tips combined with the volute induced asymmetry of stalled flow can result in deviations of overall head coefficient from the .5 predicted by Eq. 3.20. The backward cross points 2 are different between 33K

and 48K because the inlet gas temperature depends on the compressor temperature ratio prior to surge and its backflow value(i.e. speed dependent).

3.10 The Approach to Deep Surge for Axial and Centrifugal Compressors

The differences in the surge approach between an axial and a centrifugal for a large B system are shown qualitatively in Fig. 3.17. This shows both an axial and a centrifugal compressor being perturbed from an equilibrium point to a point just to the left of the deep surge line of the compressor. For an axial, the onset of rotating stall causes compressor performance to fall within several rotor revolutions to its secondary part of its actuator characteristic. The resulting sudden finite pressure imbalance on duct fluid between the compressor and plenum via conservation of linear momentum results in a sudden deceleration in flow in the duct. With a large enough B-parameter, the pressure imbalance will be sufficient to decelerate flow to negative values(deep surge). This surge process grows in a non-oscillatory manner toward backflow(deep surge) as Fig. 3.17 shows. The speed with which reverse flow is approached depends on both B, the size of the step, and the time lag associated with the fall to the secondary characteristic.

In the centrifugal, as we have seen in the data, the surge approach is more slowly growing due to the flatness of the instantaneous compressor characteristic. The slow growth may be understood qualitatively by considering the damping term of Eq. 1.6 which for large B is essentially $-B \times C'$ since the throttle slope is large. The magnitude of the damping term controls the growth rate of the instability. Higher negative values of the damping term create a faster growing instability. Since the instantaneous inertially corrected compressor characteristic seen in Fig. 3.14 is quite flat, C' is also a small positive quantity, but eventually the oscillations in flow grow to the point of flow reversal(deep surge) as Fig. 3.17 shows.

3.11 Time Resolved Compressor Component Pressure Results

Up until now, the focus has been on the dynamics of the overall compression system in surge, and on the behavior of the compressor actuator characteristic. Now some of the details of flow field inside the compressor which define the compressor's

instantaneous actuator characteristic behavior in surge will be discussed. When the system operated in the deep surge mode as shown in Fig. 3.12 and 3.15, wall static pressure Kulite data was taken to examine the stage time history before and after flow reversal. The data was taken at both 33K and 48K corrected speed. An inertial correction was applied to all the Kulite static pressure data by using an estimated (L/A) for each probe from freestream to the probe location in the compressor. These corrections are extremely small since the reduced frequency $\tilde{f} << 1$ and since (L/A) to each of the Kulites from freestream is appreciably smaller than the system (L/A) value of 108.0 ft^{-1} (354 m^{-1}).

The static head coefficients vs time in the compressor during one surge cycle at ~48K are shown are shown in Fig. 3.18. The time interval around overall flow reversal is shown in expanded scale in Fig. 3.19. The upper set of traces(marked 1 through 4) shows the Kulite pressures located 27.5 ° in the rotor rotation direction from the scroll tongue circumferential position(0 °). These are designated the "near tongue" Kulites. The plenum Kulite is shown as the top trace(marked 5). The middle set traces shows the Kulites located 117.5 ° away from the tongue(marked 1 through 4). These are designated the "far tongue" Kulites. The plenum Kulite is also shown here(marked 5). The bottom two traces shows compressor flow in terms of flow coefficient and speed in terms of Mach index. The time period of the flow reversal region is approximately .15 seconds and is clearly shown. In Fig. 3.18, each time block represents .1 seconds or 80 rotor revolutions for an average corrected speed of 48K. In Fig. 3.19, a time block is 20 milliseconds or approximately 16 rotor revolutions. The data was sampled at 3.125 KHz per channel with anti-aliasing filtering cutoff set at 1 KHz. As was done for the system parameters, the instantaneous speed was used to calculate the flow and head coefficients.

The static head coefficients vs time in the compressor during one surge cycle at a lower corrected speed ~33K are shown are shown in Fig. 3.20 and in expanded scale in Fig. 3.21. In Fig. 3.20, a time block is equivalent to .1 sec or 55 rotor revolutions. In the expanded detail of Fig. 3.21, one time block is 20 milliseconds or approximately 11 rotor revolutions. The time traces shown in Fig. 3.18 through 3.21 are discussed in detail in the next section.

3.12 Compressor Component Behavior in Surge

3.12.1 Impeller Behavior

Evidence linking surge with impeller stalling from local flow reversal at the inducer tips is shown in Fig. 3.18 thru Fig. 3.21. In these figures, the inducer tips are observed to stall and unstall at the Helmholtz frequency during the mild surge precursor period to deep surge. At the flow coefficient maxima during the mild surge period, the inducer inlet head(trace 1) has a negative value which would indicate forward inducer flow. At the flow coefficient minima, on the other hand, the inducer inlet static head is observed to be well above ambient for both "near tongue" and "far tongue" circumferential locations. Such behavior is indicative of local reverse flow at the inducer tips. These local flow reversals occur well in advance of deep surge in both the time traces of Fig. 3.18 and 3.20.

In the 48K time traces shown in the expanded scale of Fig. 3.19, evidence of inducer tip flow reversal occurs first at the "near tongue" position approximately 120 milliseconds or roughly 96 rotor revolutions before overall flow reversal and approximately 90 milliseconds or 72 rotor revolutions at the "far tongue" position. The instantaneous value of overall mass averaged flow coefficient at which the local flow reversals occur at the inducer tip is approximately .26 for the tongue and .225 away from the tongue. This corresponds approximately with the 48K overall peak in the compressor characteristic shown in Fig. 3.3 at approximately $\phi \simeq .225$. This suggests that the characteristic peak is in fact the point on the map where the onset of tip inducer stall begins. The physical phenomena initiating surge(which creates a positively sloped overall compressor characteristic necessary for surge onset) in this compressor appears to be impeller stall associated to the onset of inducer tip stall.

At a lower corrected speed of 33K, the time traces of Fig. 3.21 shows similar behavior as those of Fig. 3.19. The "near tongue" inducer inlet Kulite(trace 1) moves above ambient at 103 milliseconds or 57 rotor revolutions before overall flow reversal. At the "far tongue" inlet Kulite(trace 1) ambient pressure is exceeded later at 95 milliseconds or 52 rotor revolutions. Again as at 48K, the above ambient pressure indicative of inducer tip reverse flow occurs when the overall flow coefficient lies in the range of $.225 < \phi < .25$.

A significant feature evident in the time resolved data of Fig. 3.18 is the 180° phasing of the "near tongue" traces at the mid-impeller and impeller exit meridional position relative to the "far tongue" pressure traces. This was also observed in the FFT phase measurements done in Fink[19] during mild surge. Is this out of phase disturbance rotating stall? If so then this would correspond to two stall cells rotating around the annulus at 3.6 rev/sec. This is 3.6/800 or less than .5% of rotor speed which is extremely low. Stall cells generally propagate faster usually from 10 to 40 % of rotor speed. A more realistic explanation is that this is not a rotating stall but a stationary distortion associated with the asymmetry of the volute. A similar non-rotating pressure distortion in an incompressible pump is discussed in detail in Lorett and Gopalakrishnan[44].

The effect of non-rotating circumferential distortion on phase measurements when the mean annulus averaged flow is oscillating is seen more clearly if one considers the somewhat exagerated situation shown in Fig. 3.22. The distortion in pressure around the impeller varies with the average overall flowrate and then introduces a phase among the two sets of Kulites. Again 0° in Fig. 3.22 is the volute tongue position. At design point, the volute distortion is minimum and represented by the straight line. At high flow and low flow, the distortions are flipped in sign. The phase between the two probe signals depends on where around the circumference the probes are located. In the situation as drawn which corresponds closely to the situation in the test setup, probe 1 is near the tongue(27.5°) and probe 2 is 90° from that at 117.5°. A large mild surge oscillation in massflow around the design Cx/U where circumferential volute induced pressure distortion is small will(for quasisteady operation) result in the 180° phase difference in probe output. It is thus incorrect to always interpret phase outputs of the Kulites as rotating stall if there is a stationary, circumferential, flowrate dependent distortion. Data concerning this circumferential distortion will be shown in Chap 4. when the small B distortion data is presented.

Asymmetric inducer tip flow reversal related to the stationary flow distortion present is also clearly seen to be most severe at the circumferential position corresponding to the volute tongue. In Fig. 3.18, the pressure recovery of the inducer shown by the head difference between trace 1 and 2 at the tongue circumferential position diminishes when the overall massflow oscillations reach

their minima. Away from the tongue there is some evidence of "clipping" behavior in the final few cycles of mild surge but it is much less severe than at the tongue location. In Fig. 3.19 an almost complete loss in pressure rise in the impeller inducer at the tongue circumference occurs approximately 13 milliseconds or 10 rotor revolutions before overall reverse flow at t = 3.815 seconds. The overall flow coefficient does not drop rapidly to negative values until after the collapse in inducer pressure rise occurs at the tongue.

Strong evidence that the impeller tip flow is reversed at the tongue circumferential position while the overall average flow is still forward can also be seen by comparing the "near tongue" pressure trace levels(trace 1, 2, and 3) at the flow minima during the mild surge precursor to deep surge with their levels when the overall massflow has reversed. They are observed to be practically the same in level. For example, the impeller head levels at t = 3.815 seconds in Fig. 3.19 (the instant in the precursor period to deep surge when the tongue inducer pressure recovery is seen to collapse completely) are virtually the same as a later instant of t = 3.885 seconds when the plenum is blowing down and the overall compressor massflow is reversed. Such is definitely not the case for the "far tongue" traces at the same instants of time.

The data of Fig. 3.20 and 3.21 for 33K operation is similar to the 48K data shown in Fig 3.18 and 3.19 and provides additional evidence of inducer tip stalling. The inducer pressure recovery as seen by the difference between traces 1 and 2 at the tongue diminishes when the instantaneous value of ϕ drops to .1. Away from the tongue, pressure recovery is much higher at the ϕ = .1 valleys. The inducer Kulite(trace 1) at "near tongue" and "far tongue" positions is mostly above atmosphere and is indicative of tip backflow. The asymmetry in flow appears less extreme than at 48K as seen by the smaller difference in impeller head(trace 3) between "near tongue" and "far tongue" Kulites. At impeller exit(trace 3), the "near tongue" Kulite pressure is again very roughly 180° out of phase with the "far tongue" Kulite and slightly depressed in head. However there is less difference in head between the two circumferential positions.

The asymmetric stalling of the impeller at the volute tongue circumferential location and its link to the onset of deep surge is seen more clearly if the impeller total to static head coefficient from the Kulite data of Fig. 3.18 is replotted vs

overall flow coefficient instead time. This is shown in Fig. 3.23 for 48K and in Fig. 3.24 for 33K at both the "near tongue" and "far tongue" position. Also marked in these plots are the throttle point values of flow coefficient at which the overall system enters deep surge. At 48K, the impeller head at the "near tongue" circumferential location clearly peaks at ϕ = .25 which is higher than the approximate deep surge throttle point of ϕ = .225. A similar trend is seen at 33K where the head at the tongue peaks at ϕ = .2 and the deep surge point occurs at ϕ = .190. The data shows a connection between the local stalling of the impeller at the tongue and the onset of deep surge in the compression system.

Additional evidence of impeller stall at the tongue circumferential location is seen by an examination of the crossing points(ϕ = 0) labeled 1 and 2 in Fig. 3.23 for the "near tongue" circumferential position. Fig. 3.23 shows that they are both low and they are almost the same(.31 at crossing 1 and .26 at crossing 2). Away from the tongue in Fig. 3.23, the crossing points are seen to be different(.47 at crossing 1 and .32 at crossing 2). The data is plotted vs the overall compressor ϕ and there is no direct measure of the local value of ϕ near the tongue. However the observed head behavior implies strongly that ϕ near the tongue is reversed long before overall ϕ reverses i.e. the impeller stalls at the tongue first.

The difference in crossing points in the "far tongue" trajectory is mainly a result of inlet temperature effects as described before. The elevated inlet air temperature which exists when the overall flow transition to forward occurs in the compression system is not present when the compressor is transitioning to backflow. This is unlike the behavior at the tongue region of the impeller which is in backflow for both crossing 1 and 2.

The circumferential variation in instantaneous impeller behavior is seen by a comparison between the "near tongue" and "far tongue" impeller trajectories shown in Fig. 3.23. At high ϕ both circumferential positions record similar ψ's but at ϕ = .35 the trajectories appear to diverge. The "near tongue" impeller head peaks at .29 at ϕ = .25, while the "far tongue" impeller head peaks near ϕ = 0 at a much higher value of .47 at shutoff. The observed peak in head at the "near tongue" location at ϕ = .25 also corresponds closely to the deep surge point of ϕ = .225 which again highlights the important role the asymmetric stall has on the compression system overall surge behavior. Local impeller reverse flow at the tongue when overall ϕ is

forward is also suggested by comparing the "far tongue" head levels of the backflow and recovery leg to the "near tongue" forward and transition to backflow region over the interval $-.125 < \phi < .2$. They are roughly similar in level suggesting again early flow reversal in the impeller at the tongue. The peak value of .47 which occurs at shutoff in the "far tongue" Kulite is close to the ideal value of .5 computed by Eq. 3.20.

As is shown in Fig. 3.24, the asymmetric stalling behavior of the impeller for operation at 33K is qualitatively similar to that observed at 48K. The equality in level in crossing 1 and 2 at the impeller tongue location is seen clearly in this figure which again is indicative of an early flow reversal at the tongue while the overall average flow is still forward. The crossing magnitude is higher than at 48K due to smaller temperature ratio effects. When the instantaneous value of overall flow coefficient is approximately .2(in transition from forward to backflow), the impeller head at the tongue peaks at a value of .41. As the flow coefficient decreases below .2, the head declines until the flow is reversed. At high negative flows, the head increases to higher values. Away from the tongue as in the 48K results, the impeller head trajectory exhibits a peak at roughly the shutoff point of .49, which is quite close to the computed ideal value of .5. After the peak, the head at the "far tongue" declines and follows the 33K impeller backflow characteristic. Both the "near tongue" and "far tongue" Kulite trajectories follow approximately the same path in Fig. 3.24 in backflow.

3.12.2 Stall Cell Observations

Some single cell rotating stall disturbances of 230 Hz @ 33K(34% of rotor speed) and 270 Hz @ 48K(42% of rotor speed) were observed with the inducer inlet Kulites by Fink[19] but the static pressure amplitude seen in terms of head coefficient were less than .01. The stall cell frequency scaled roughly with speed. These disturbances were strongest in the inducer section and grew weaker as one progressed meridionally back in machine. They also appeared to reach peak amplitude at a throttle condition where the scroll distortion is minimum and the compressor curve peaks. This indicates that the stall cells are a local phenomena connected with the inducer and are inhibited when scroll induced circumferential pressure distortion is high. These disturbances are also superimposed on the much lower surge frequencies

of surge and hence occur only on a transient basis in bursts at the massflow minimum points during mild surge massflow oscillations. Some evidence of this behavior is seen in the pressure traces(trace 1) of Fig. 3.18 and 3.20 but the magnitude of the pressure fluctuations in terms of head coefficient is on the order of .01. This is small relative to the fluctuations of order .05 seen in the these traces due to mild surge massflow oscillations.

The fact that the stall cells did not appear strongly through the machine suggests that they are not as significant in surge performance as for axial compressors. In a multistage axial machine, the stall cell usually extends through the machine as discussed in Day [9] and Lavrich[43] and creates a discontinuous actuator characteristic as was shown in Fig. 1.4(b).

Discontinuous characteristics have been observed in the maps of centrifugal compressors but phenomena other than stall cell behavior can account for this behavior. The time averaged centrifugal compressor map data of Emmons[16] in their Fig. 4 is one example. Data on typical compressor performance maps are usually of the low response type and hence really are time averaged quantities. The observed discontinuous behavior can be a consequence of time averaging when the compressor operates in surge.

For example, if the compressor is operating in deep surge its instantaneous operating point follows the trajectory as shown in Fig. 3.14. It is not a single point defined by the time averaged value of flow coefficient, head coefficient, and Mach index. The locus of the time averaged points for various throttle conditions is however the low response apparent characteristic as seen in performance map data. This time averaged apparent characteristic can be much steeper than the real time resolved instantaneous one such as shown in Fig. 3.14. The actual difference between the instantaneous and the time averaged characteristic depends on the overall compression system behavior as controlled by the magnitude of the B-parameter. This will be discussed further when the system model is discussed in Chap. 5.

Another effect which can modify the shape of the apparent characteristic is a strong stationary circumferential flow distortion created by the volute. When the distortion is present, the flow in the rotor frame is unsteady, and in general the overall circumferentially averaged performance of the compressor will differ from that when the distortion is absent. A distortion of this type can steepen the

circumferentially averaged characteristic relative to its axisymmetric(distortion-free) one. This effect is most pronounced when a circumferential sector of the compressor flow is locally reversed like that shown in Fig. 1.1(a). Such a distortion will be discussed in more detail in the next chapter.

When the compressor geometry is entirely axisymmetric, it is certainly possible that a rotating stall would develop and strengthen in amplitude to a level comparable with the tongue type of non-rotating stall observed in the data for the volute equipped compressor. With axisymmetric geometry, there would of course be no tongue or preferred direction for a non-rotating asymmetric stall to "lock onto" so the stall would most likely then rotate. However in most practical turbocharger arrangements, an asymmetric volute is usually used.

3.12.3 Diffuser Behavior

Evidence of the destabilizing nature of the diffuser on the overall system is seen in Fig. 3.25 and 3.26 where the headrise of the vaneless diffuser is observed to decline as the overall flow coefficient declines. The vaneless diffuser static to static head coefficient data is plotted vs overall compressor flow coefficient as a trajectory for both "near tongue" and "far tongue" positions in Fig. 3.25 for 48K and in Fig. 3.26 for 33K. Both illustrate a generally downward trend from high ϕ to $\phi = 0$. At high flow coefficients of .4, the headrise trajectory is fairly steeply positively sloped. At lower flow coefficients around .2, the slope of the headrise trajectory flattens particularly at the tongue region of the diffuser. At positive values of flow coefficient near shutoff the slope steepens again. The shutoff points for the vaneless diffuser are not the same particularly at the "near tongue" location. This hysteresis clearly contributes to the hysteresis observed in the overall compressor trajectory shown in Fig. 3.14 and 3.16. In backflow, the diffuser characteristic is negatively sloped.

In Fig. 3.27 and 3.28, the overall diffuser headrise at the two circumferential positions is shown. The overall diffuser headrise includes the volute as well as the vaneless diffuser. In a region around the deep surge point for 48K of $\phi = .225$, there is very little change in slope either at the "near tongue" or "far tongue" location. A similar constant slope behavior is seen in a region around the 33K surge

point of ϕ = .190. There is also a substantial amount of hysteresis in the data contributing to the hysteresis in the overall characteristic transient data.

The constant slope of the diffuser characteristic data around the deep surge point is a significant effect because it shows the very weak role the vaneless diffuser has on initiating surge in the compression system. This can be seen by the following argument. The overall characteristic slope of the compressor(total to static) ψ_c' is the sum of the its component characteristic slopes written as

$$\psi_c' = \psi_I' + \psi_D' \tag{3.24}$$

where ψ_I' is the slope of the impeller characteristic(total to static) and ψ_D' is the slope of the overall diffuser characteristic(static to static). Then slope changes in both components are important in surge initiation since the overall stability of the system depends on the magnitude of ψ_c' and B as given by Eq. 1.8. In the data of Fig. 3.25 and 3.26, the diffuser characteristic ψ_D' is approximately constant in a region around the surge point(ϕ = .225 @ 48K and ϕ = .190 @ 33K). On the other hand, there is a large variation in ψ_I' in the same region for the impeller data. As seen in the trajectories of Fig. 3.23 and Fig. 3.24, the impeller is steeply negatively sloped at high flows($\phi \simeq .4$) and becomes more positively sloped as throttling continues. At high flows, the impeller is strongly stabilizing to the system while at lower flows, the impeller becomes destabilizing. Throttling the impeller to lower values of flow coefficient clearly is destabilizing to the overall system. The role of the impeller in surge initiation is a strong one due to the large slope change with throttling. The diffuser's part in surge initiation is much smaller since its slope change with flow coefficient is relatively small. The contrasting trends of the impeller and vaneless diffuser will be discussed further in Chap. 4

As discussed in Cumpsty[8], the vaneless diffuser characteristic is generally always destabilizing(i.e. positively sloped). As the data of Fig. 3.25 and 3.26 shows, the diffuser characteristic appears more destabilizing at high flows than at flows near the surge point because it is more steeply positively sloped there. Hence

as throttle down commences from high flow($\phi \simeq .4$) to the surge point($\phi \simeq .225$@48K), the diffuser becomes less rather than more destabilizing to the system. In general, there is not a large change in slope in the vaneless diffuser characteristic for positive flows. The data again emphasizes the relatively weak effect the vaneless diffuser has on surge initiation and highlights the strong effect of the impeller.

3.13 Summary

The main points roughly in order of importance brought out in the data of this chapter are the following:

- The stalling element that is most responsible for surge initiation is the impeller. This agrees with the conclusion reached by Flynn and Weber[20]. Several forms of impeller stall are seen in the data. Among them are axisymmetric inducer stall(dominant), asymmetric volute induced inducer stall(dominant), and rotating stall(weak). These are the physical stalling mechanisms which create the downward sloping characteristic necessary to initiate dynamic instability and instability growth towards deep surge.
- The vaneless diffuser is seen clearly as a destabilizing element since it's characteristic slope is generally positive but the nearly constant slope of its characteristic with flow highlights its lack of importance in initiating surge.
- The large B surge line occurs at the peak of the characteristic.
  Surge oscillations develop around the characteristic peak at the Helmholtz frequency and grow slowly culminating in deep surge.
- The position of the characteristic peaks are speed dependent due to compressibility and perhaps its effect on the volute matching condition.
- The forward flow compressor characteristic is fairly flat and continuous to shutoff. It exhibits no abrupt stalling behavior.
- When operating in a deep surge cycle, the main pressure drop in the compressor occurs after $\phi = 0$ not before.
- The compressor exhibits pressure ratio hysteresis behavior over a deep surge cycle which is due to inducer stalling, density and temperature ratio effects(compressibility), and partly an effect of headrise hysteresis of the vaneless diffuser.
- The vertical position of the backflow characteristic relative to its forward flow

characteristic depends on the stage Mach index (strong compressibility effect).

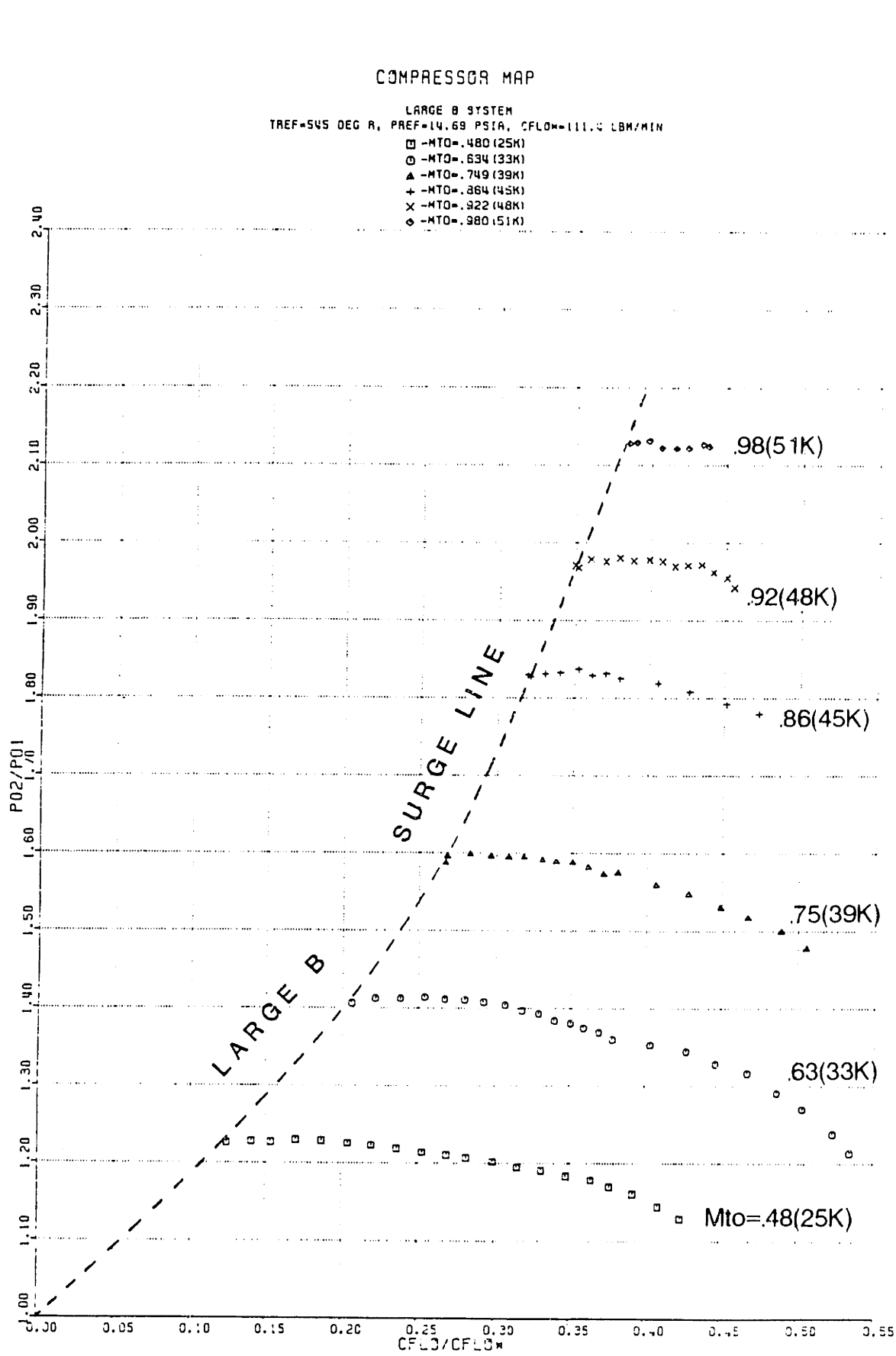

Fig. 3.1 Large B Compressor Map

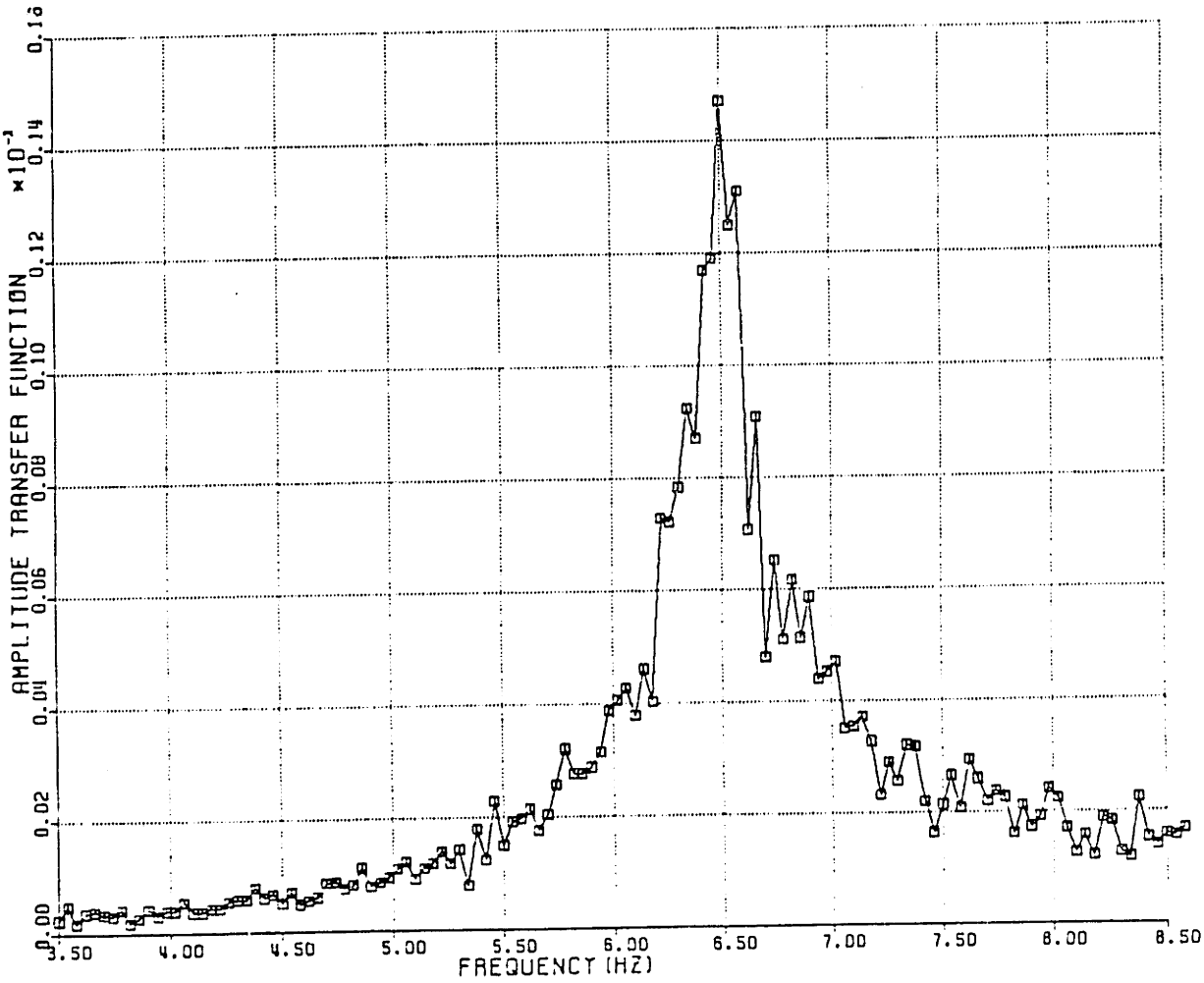

Fig. 3.2 Large B System Natural Frequency Measurement Results

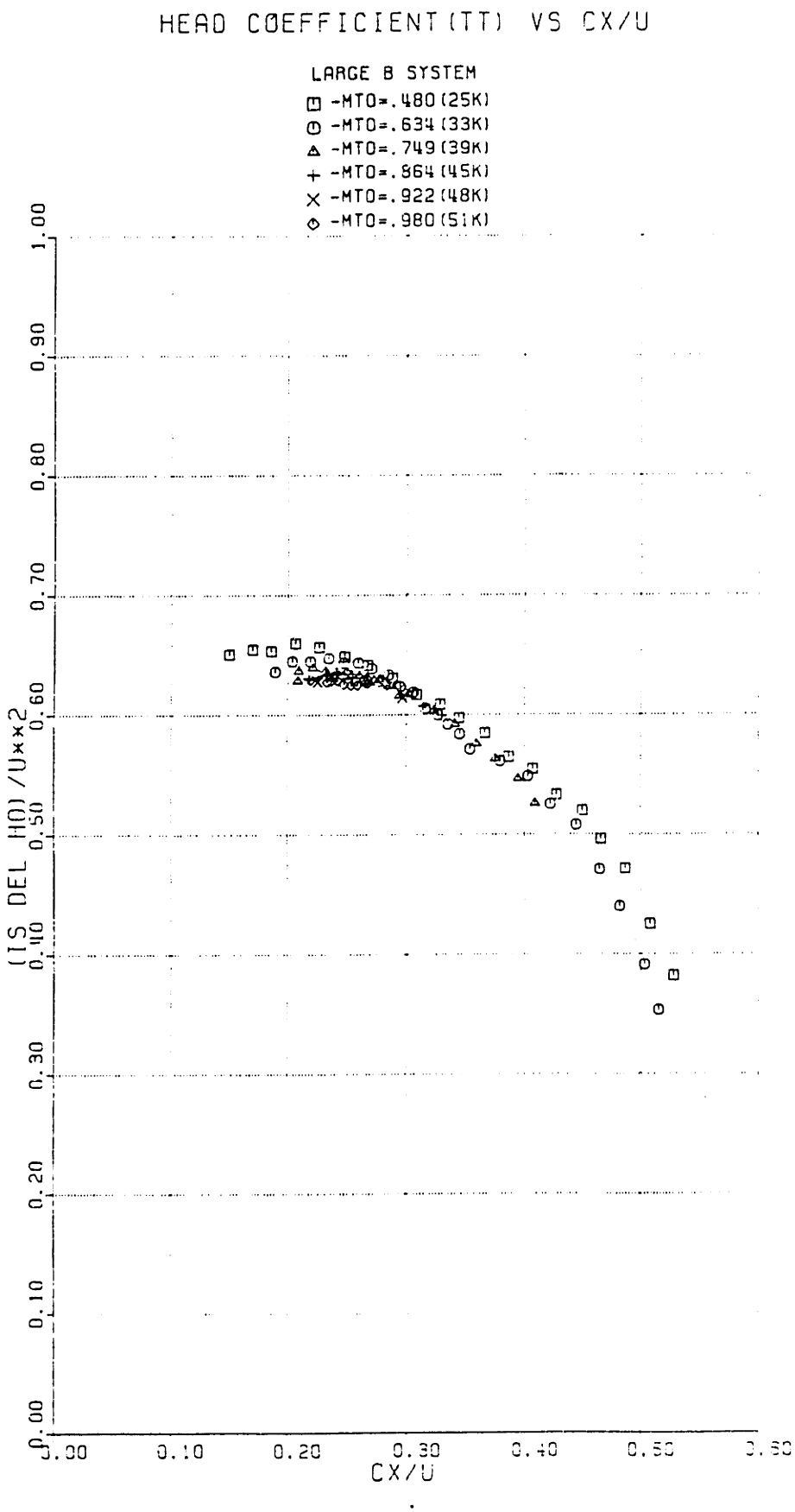

Fig. 3.3 Large B Compressor Head Coefficient vs Cx/U

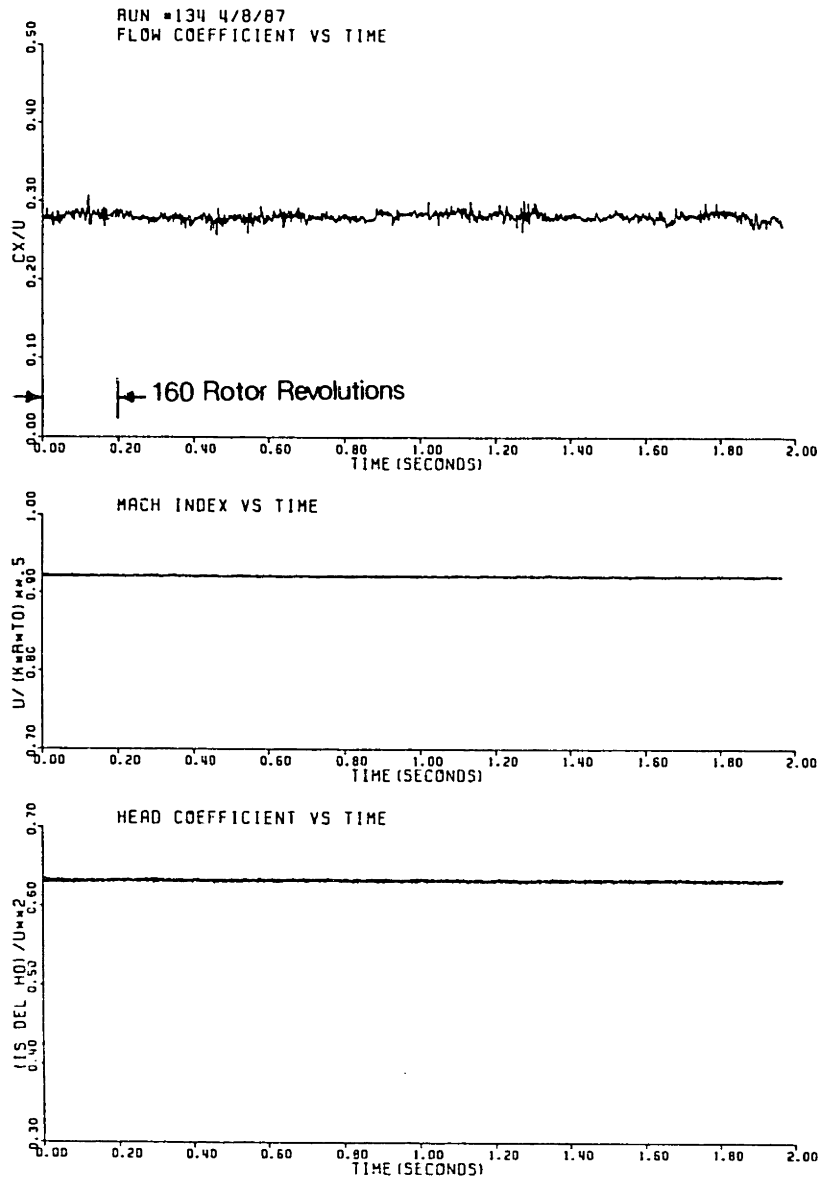

Fig. 3.4 Large B System Parameters in Non-Surge Operation($\phi_T \simeq .275$)

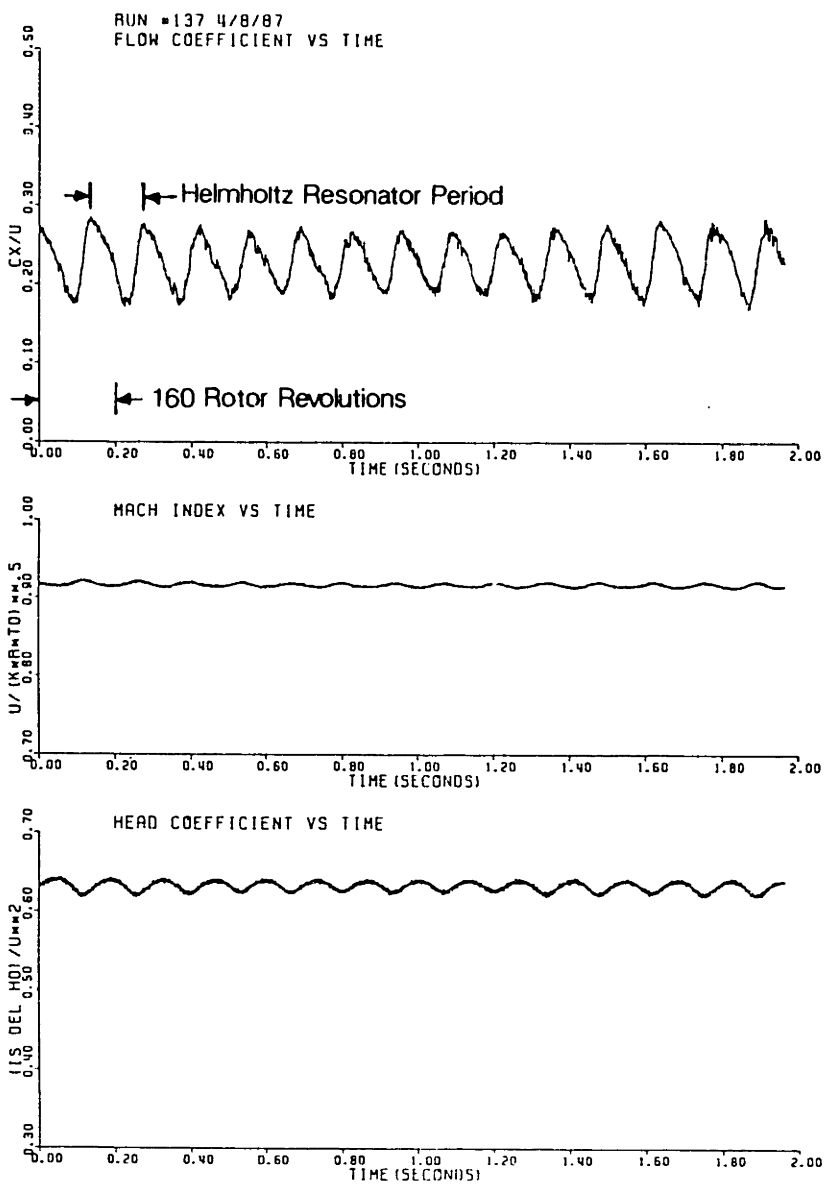

Fig. 3.5 Large B System Parameters in Mild Surge($\phi_T \simeq .23$)

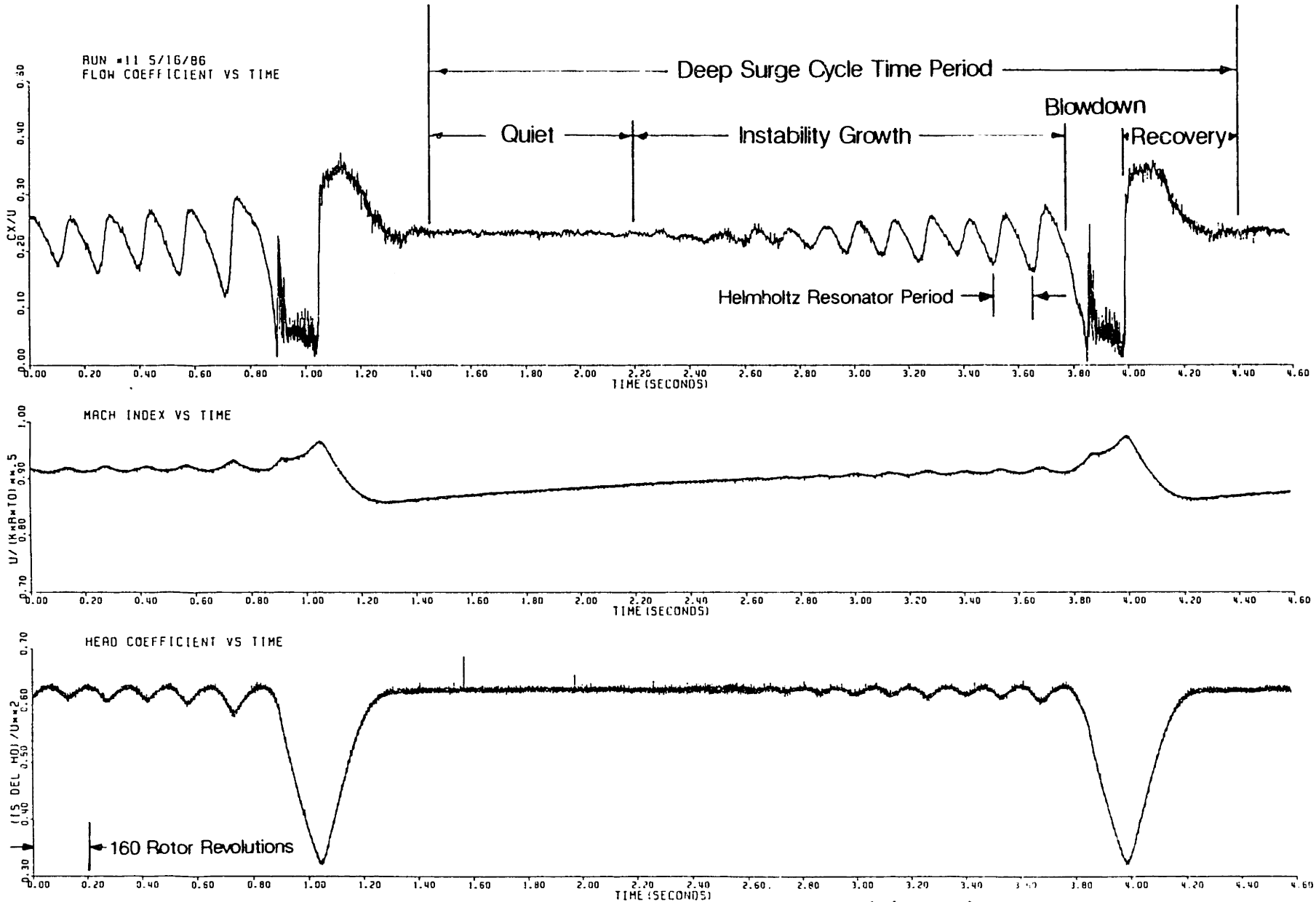

Fig. 3.6 Large B System Parameters in Deep Surge($\phi_r \simeq .225$)

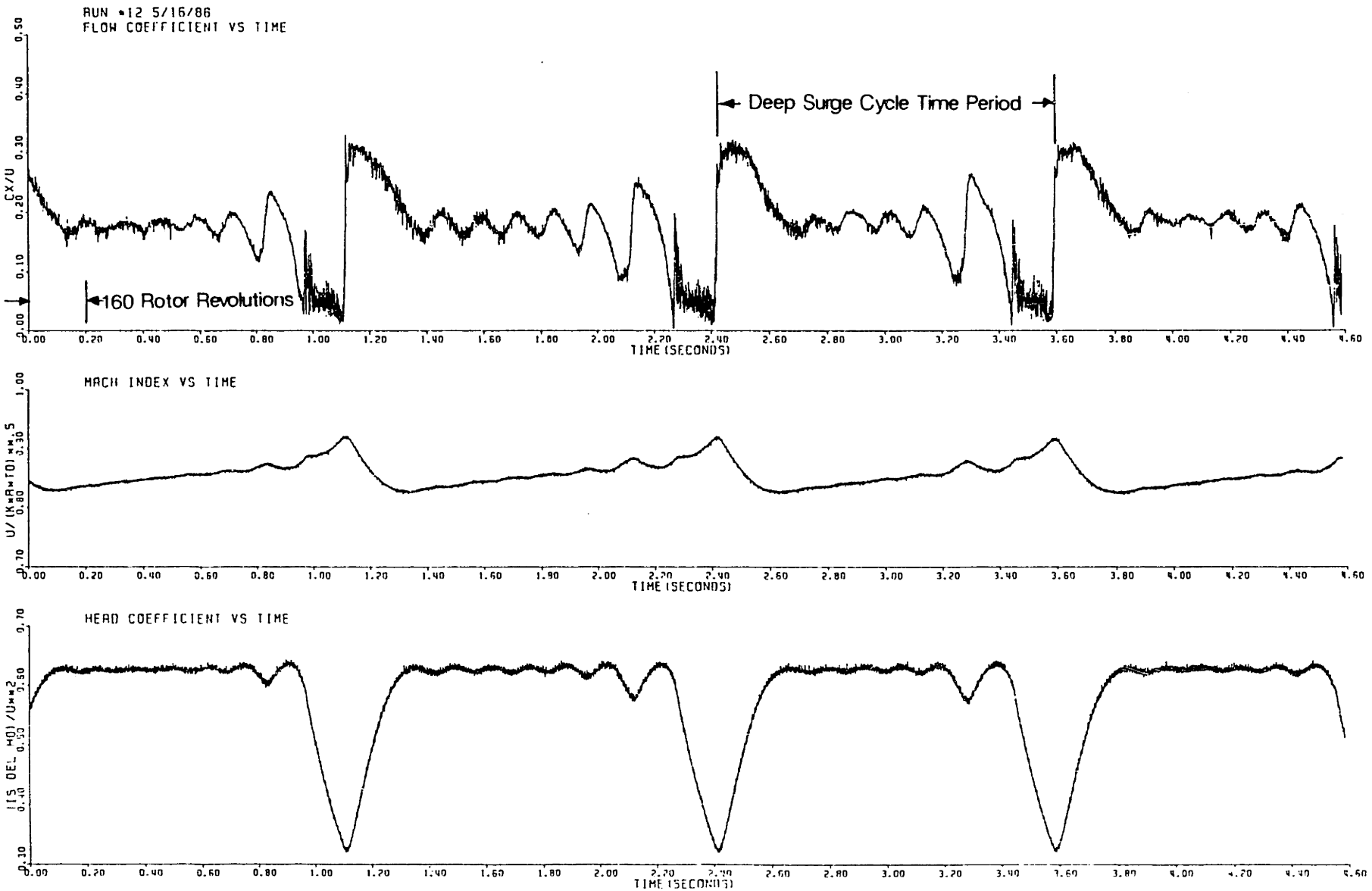

Fig. 3.7 Large B System Parameters in Deep Surge($\phi_T \simeq .19$)

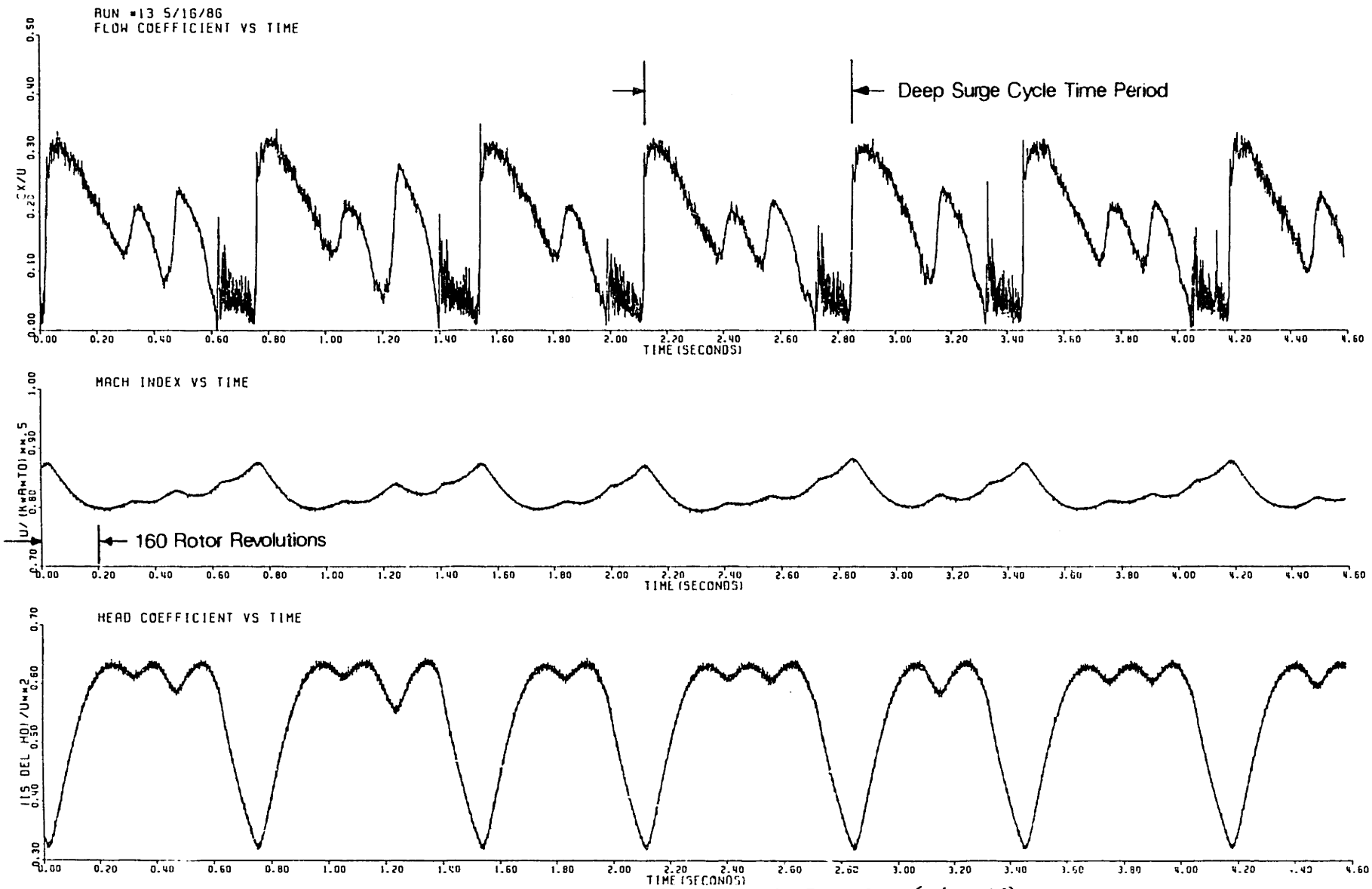

Fig. 3.8 Large B System Parameters in Deep Surge($\phi_T \simeq .16$)

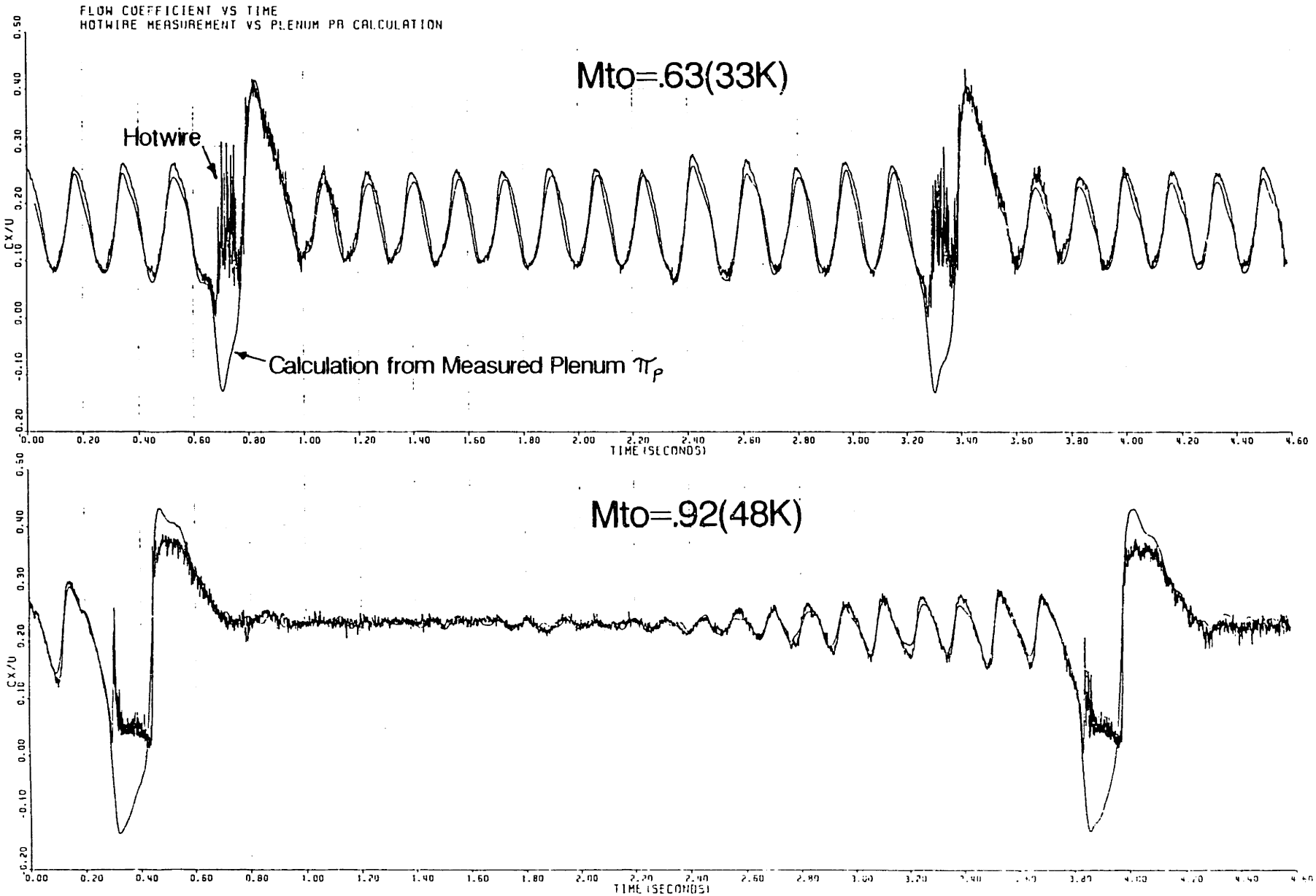

Fig. 3.9 Comparison of Hotwire Measured and Plenum π_p Derived Cx/U

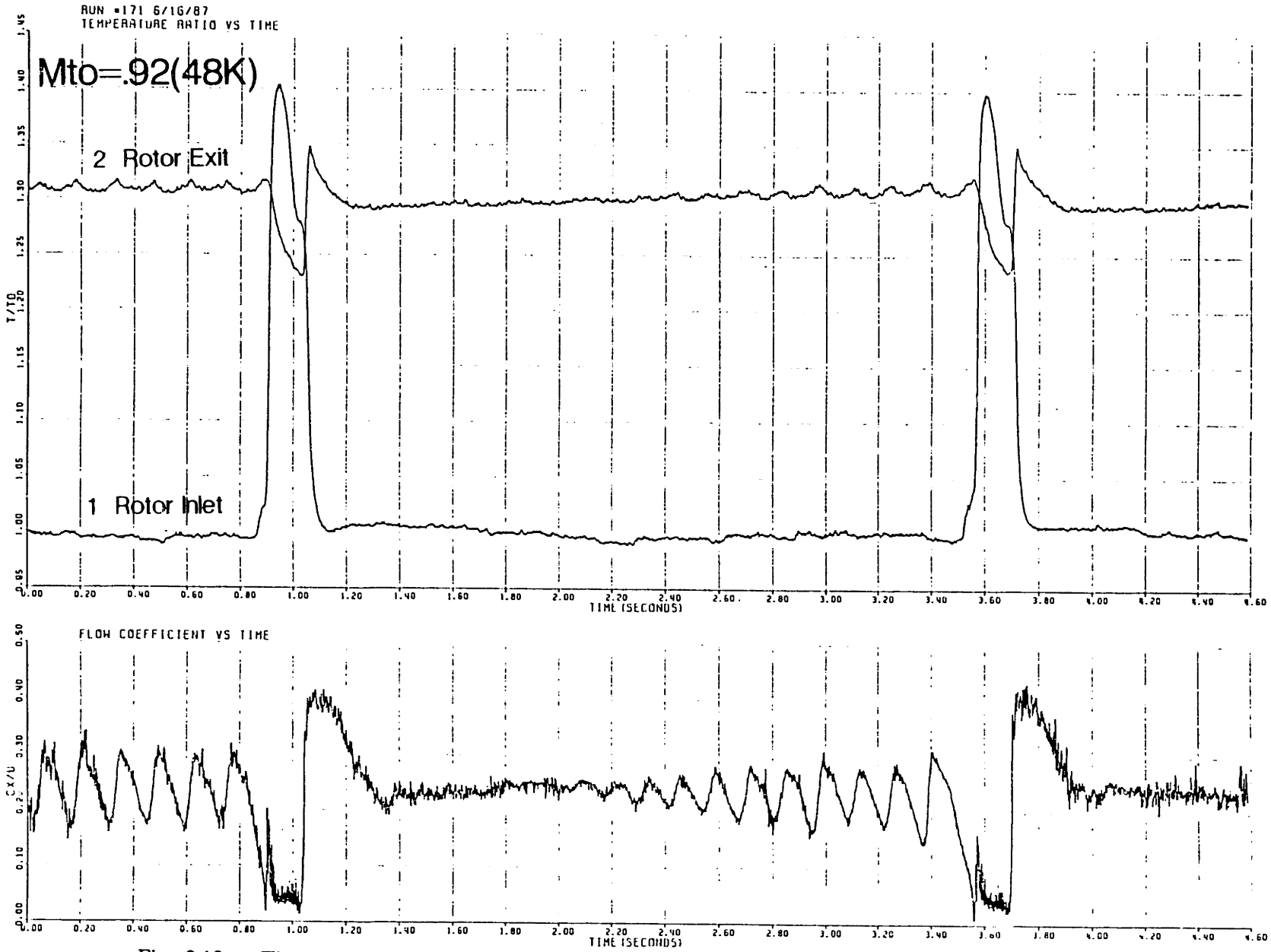

Fig. 3.10 Time Resolved Rotor Inlet and Exit Temperature in Deep Surge(Mto ≃ .92, ϕ_r ≃ .225)

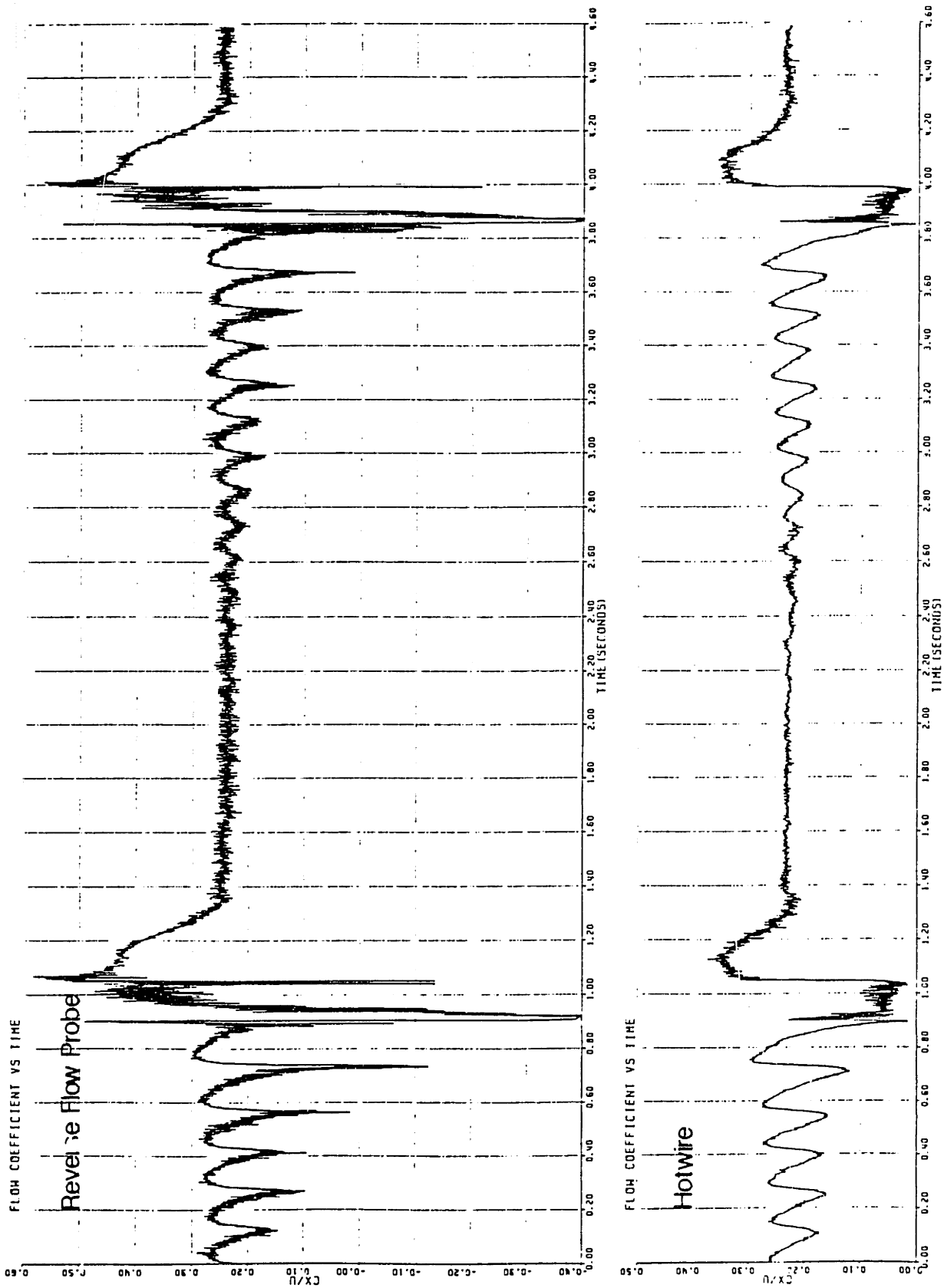

Fig. 3.11 Comparison of Reverse Flow Probe and Hotwire Measured Cx/U(Mto ≃ .92)

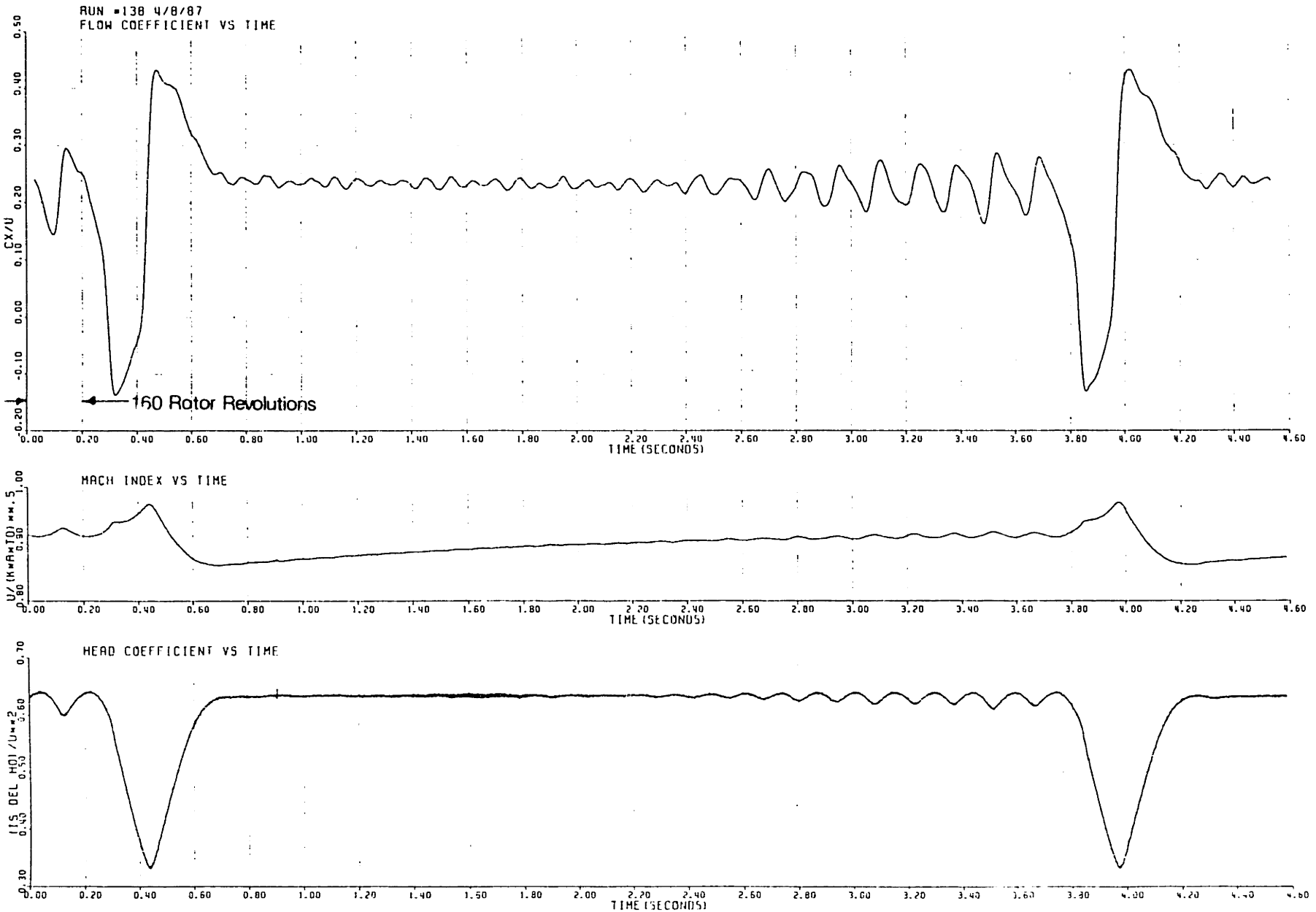

Fig. 3.12 System Parameters in Deep Surge(Mto ≃ .92, ϕ_T ≃ .225)

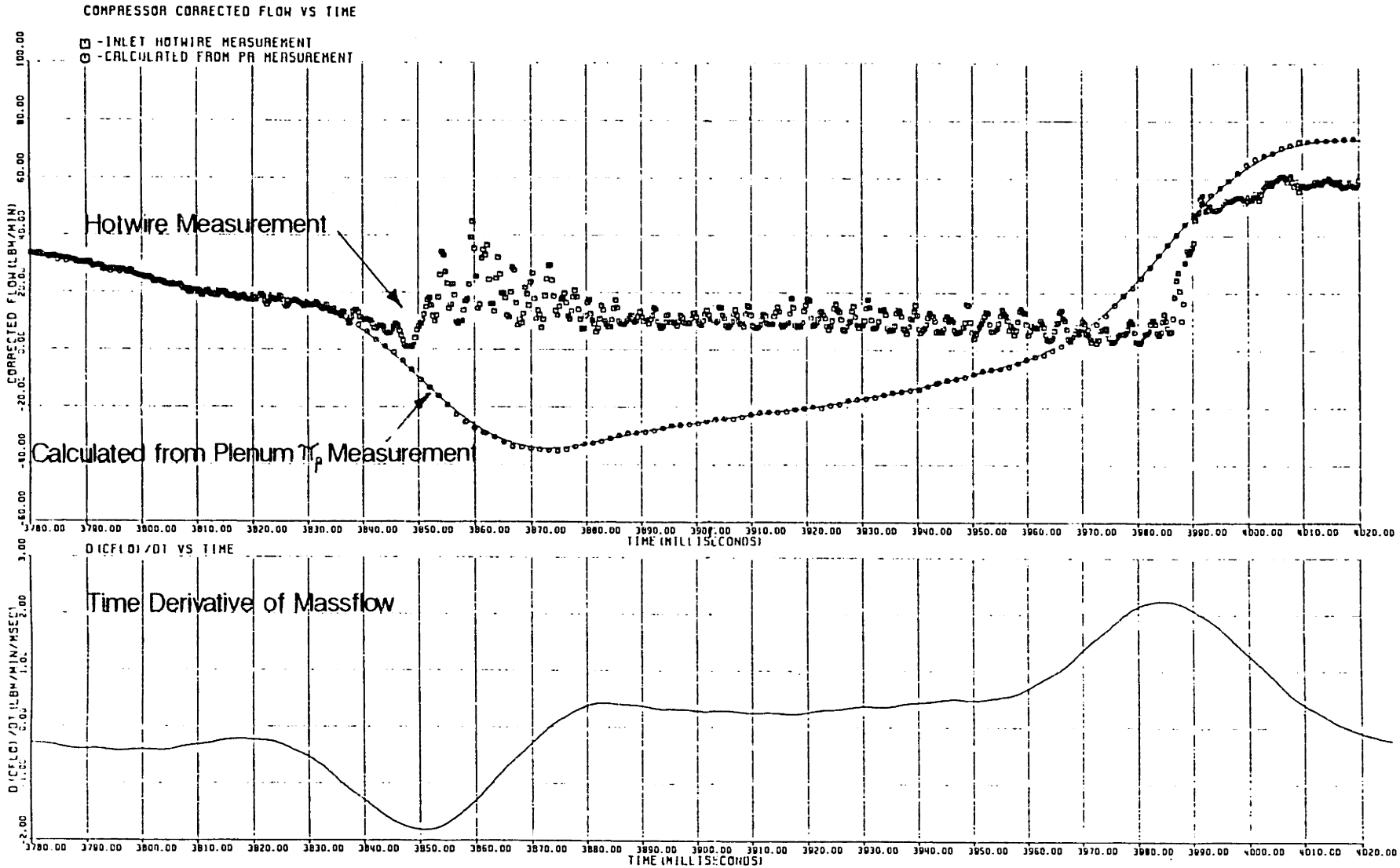

Fig. 3.13 Smoothing and Numerical Differentiation Results

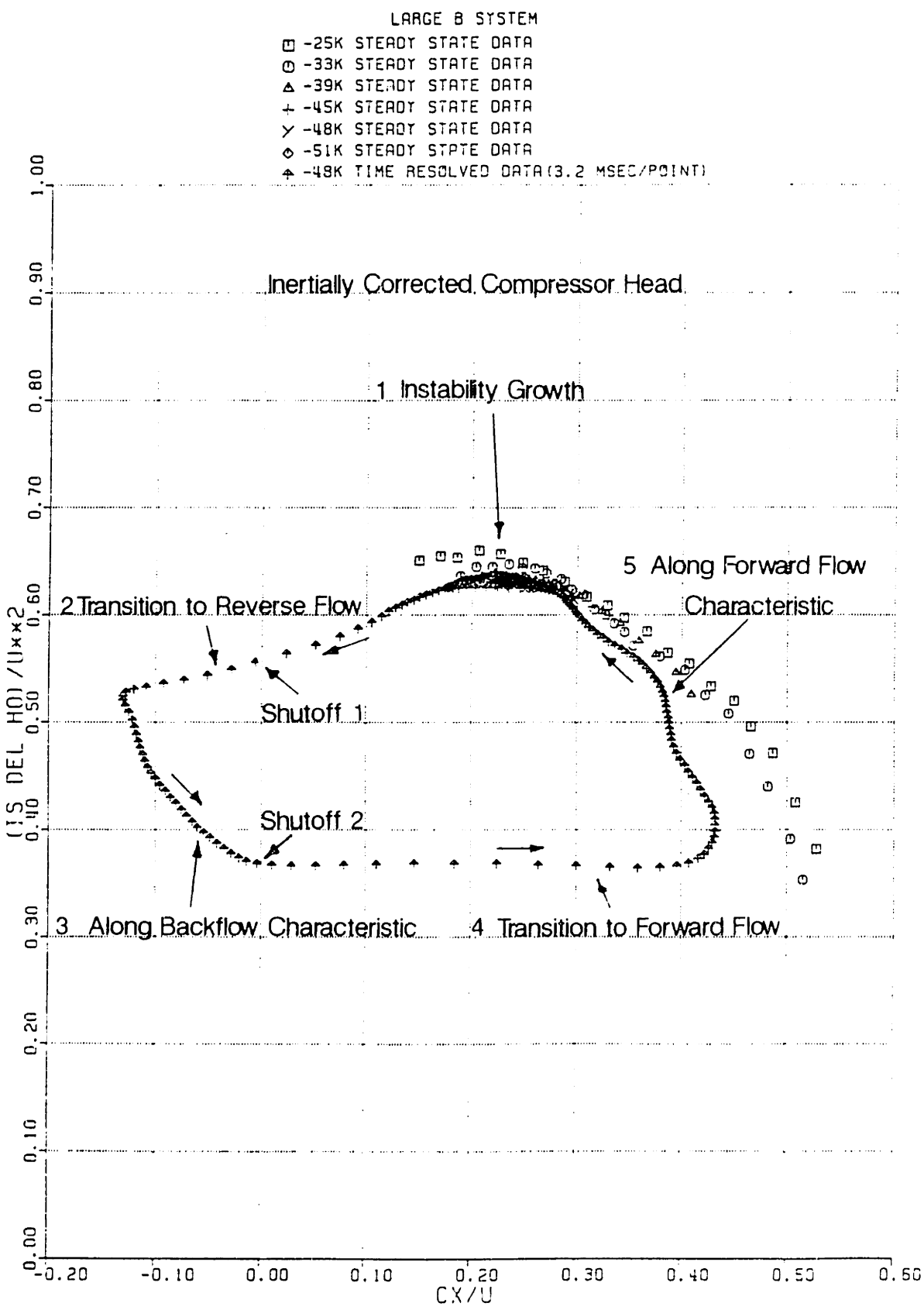

Fig. 3.14 Inertially Corrected Compressor Head Coefficient vs Cx/U in Deep Surge

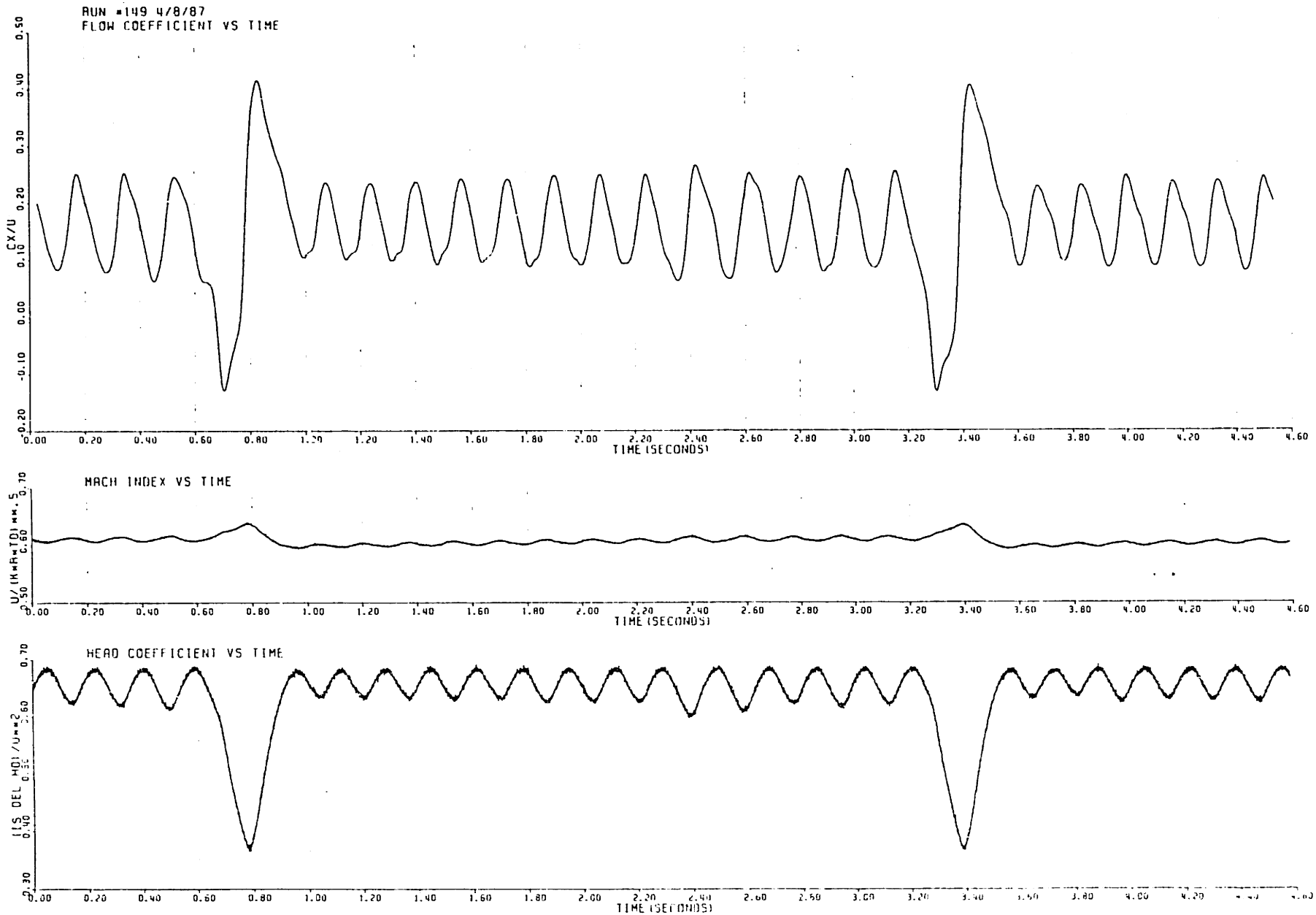

Fig. 3.15 System Parameters in Deep Surge(Mto ≃ .63, ϕ_r ≃ .16)

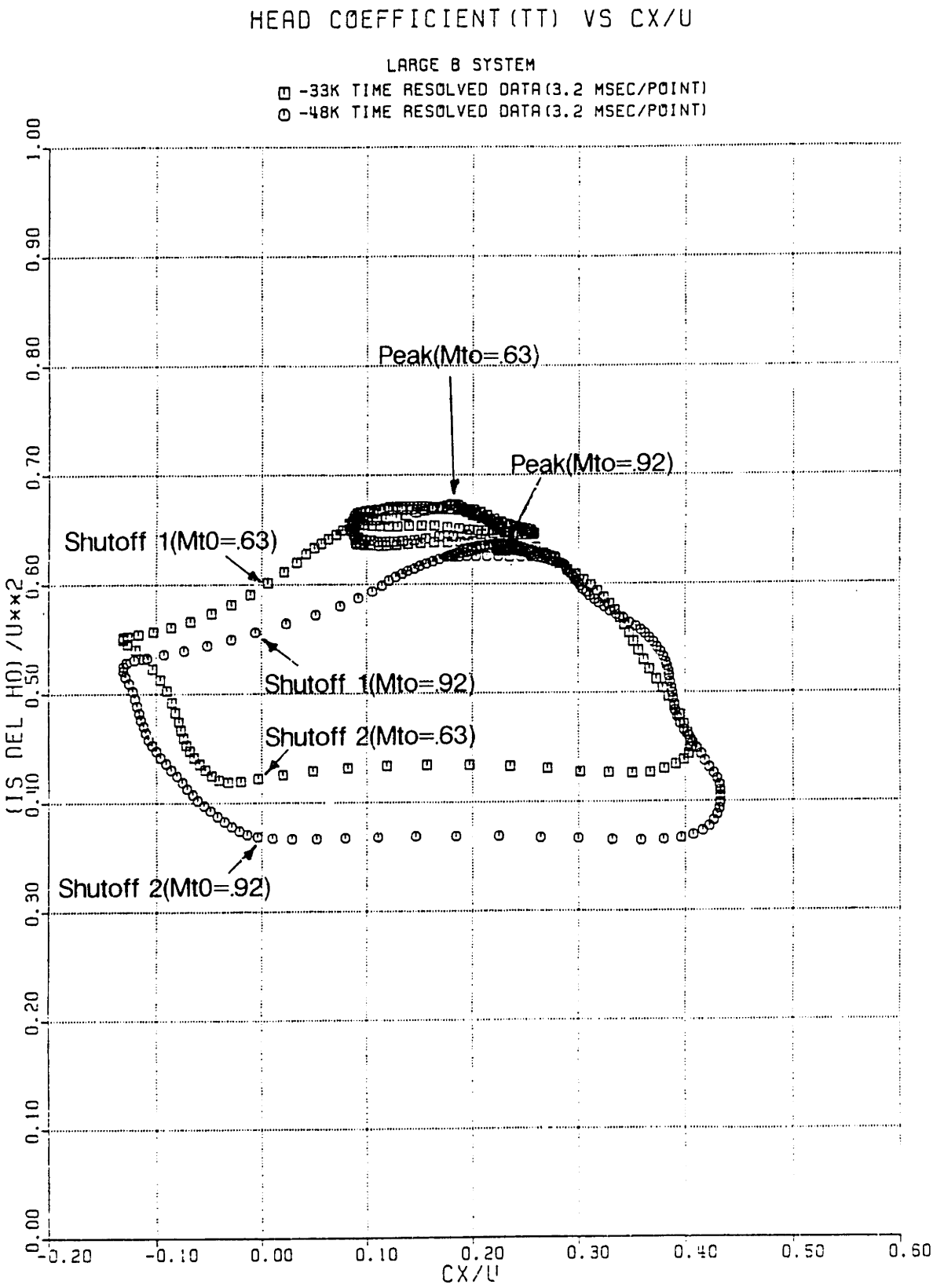

Fig. 3.16 Comparison of Inertially Corrected Compressor Head Coefficients vs Cx/U in Deep Surge

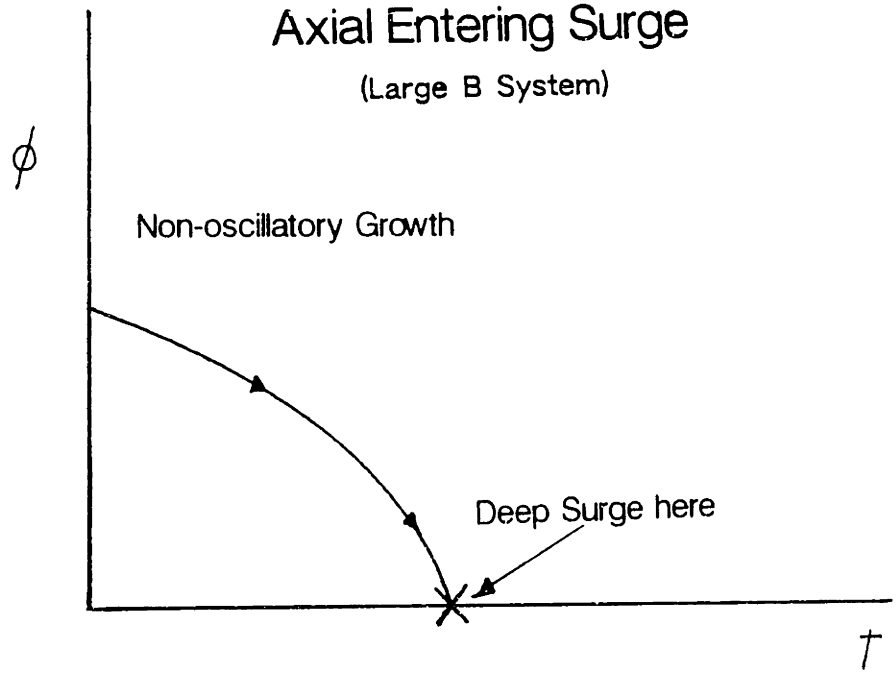

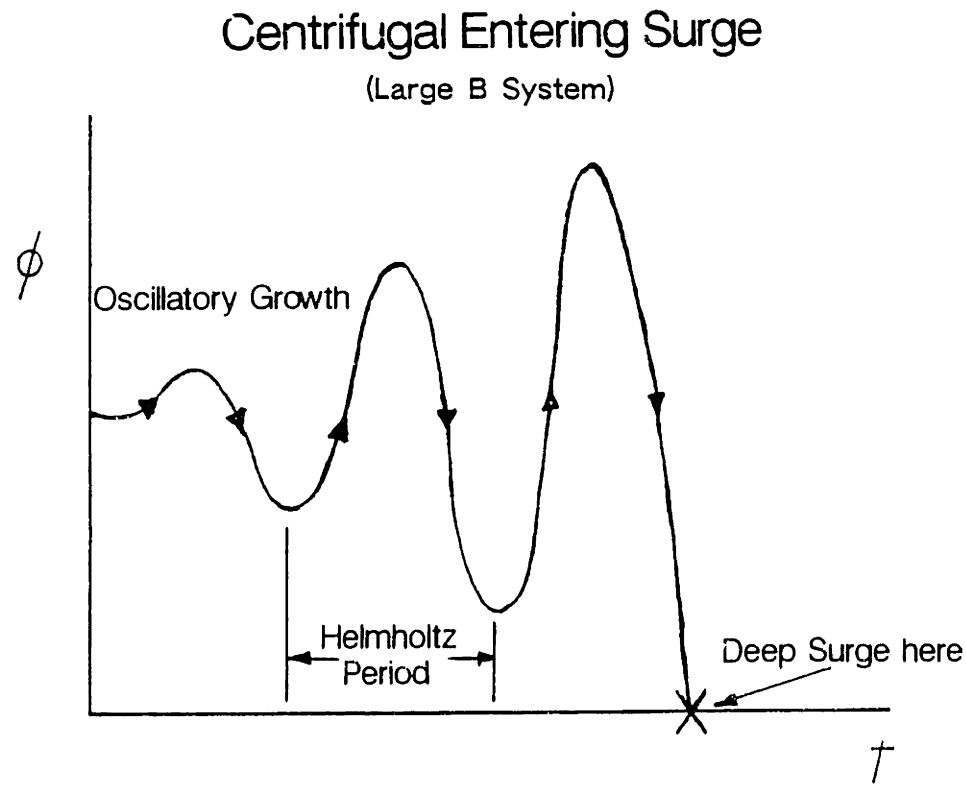

Fig. 3.17 Axial vs Centrifugal in Deep Surge Approach

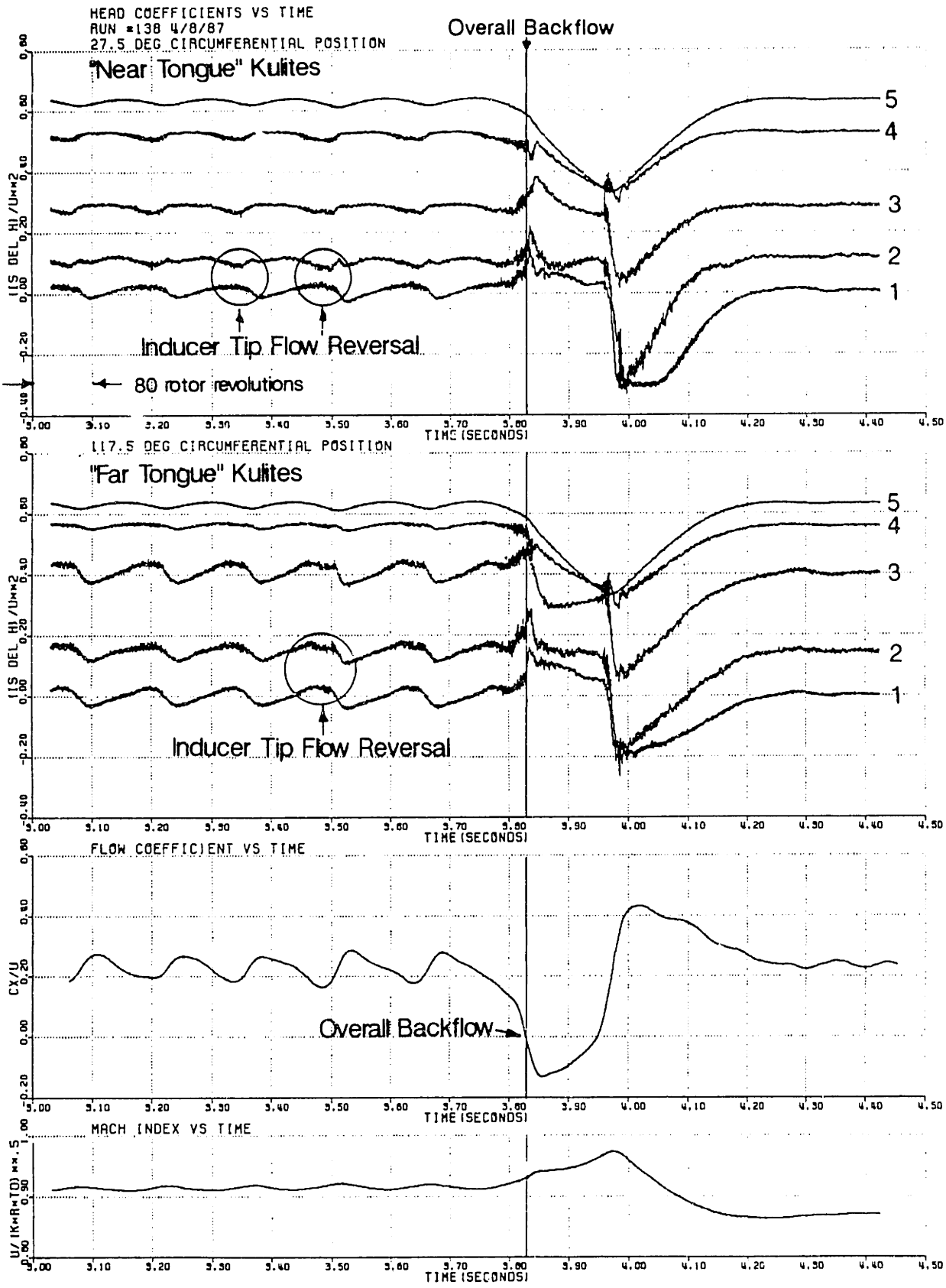

Fig. 3.18 Compressor Static Head Coefficients vs Time in Deep Surge(Mto ≃ .92)

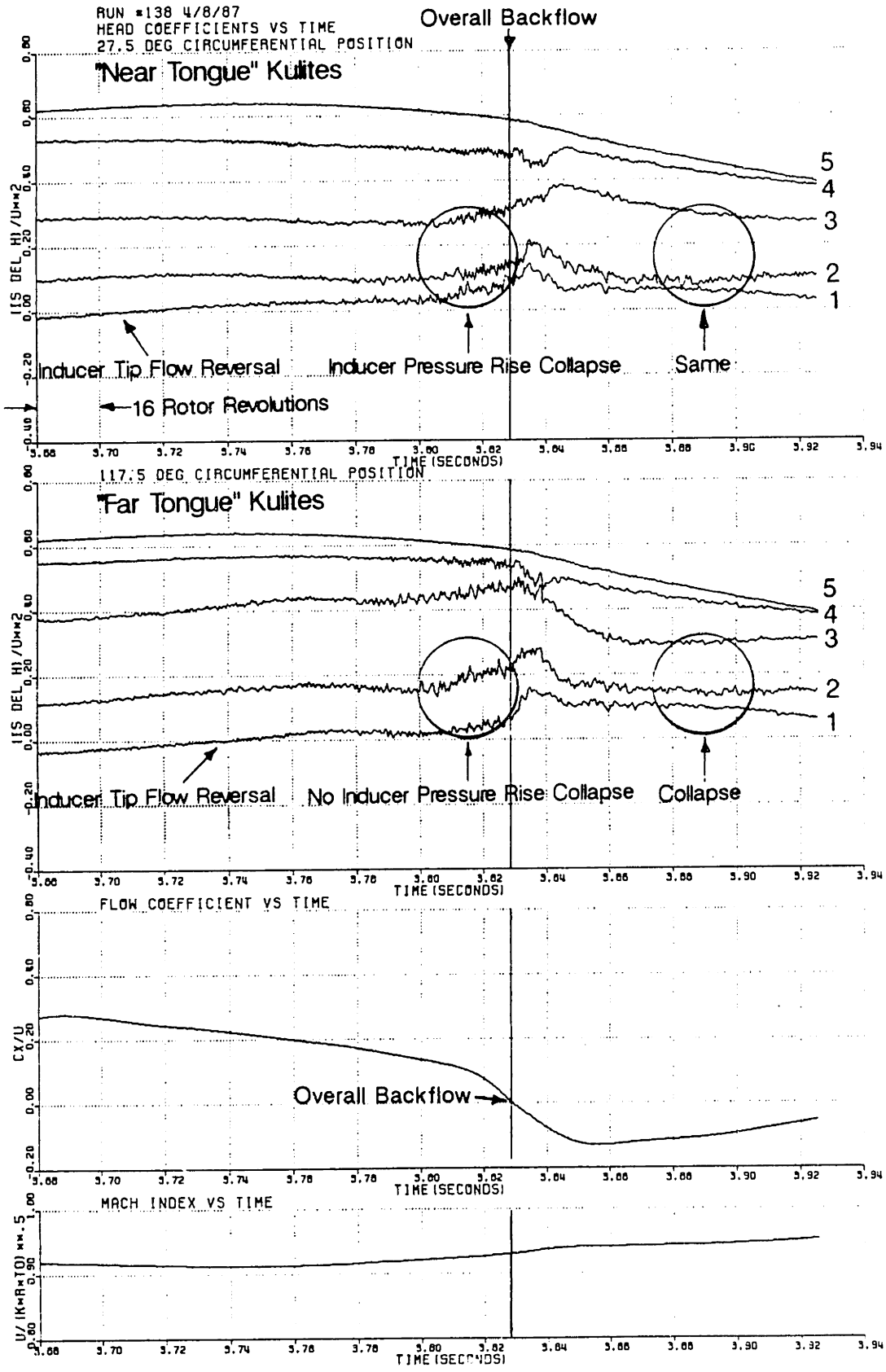

Fig. 3.19 Detail of Deep Surge Event(Mto ≃ .92)

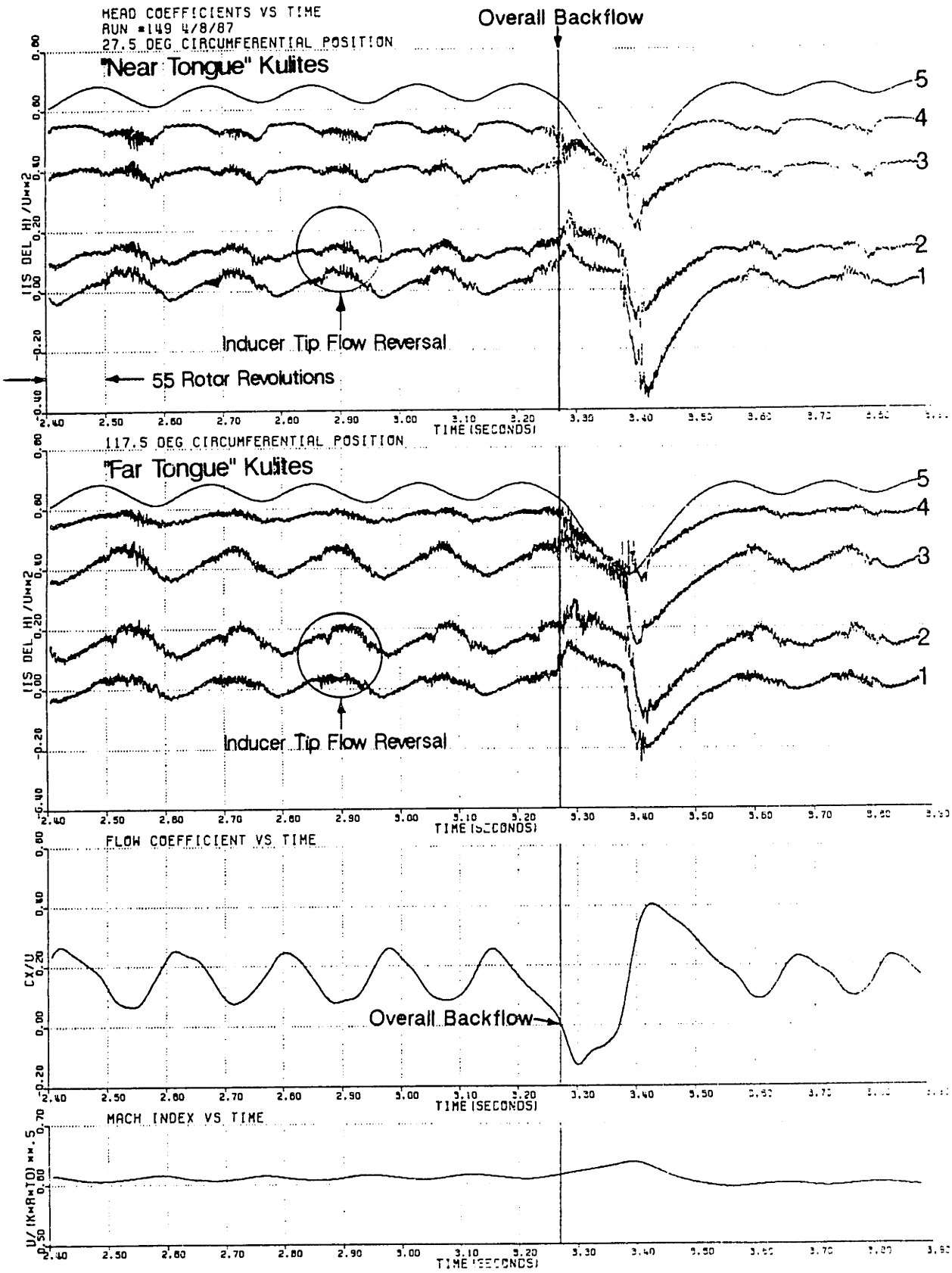

Fig. 3.20 Compressor Static Head Coefficients vs Time in Deep Surge(Mto ≃ .63)

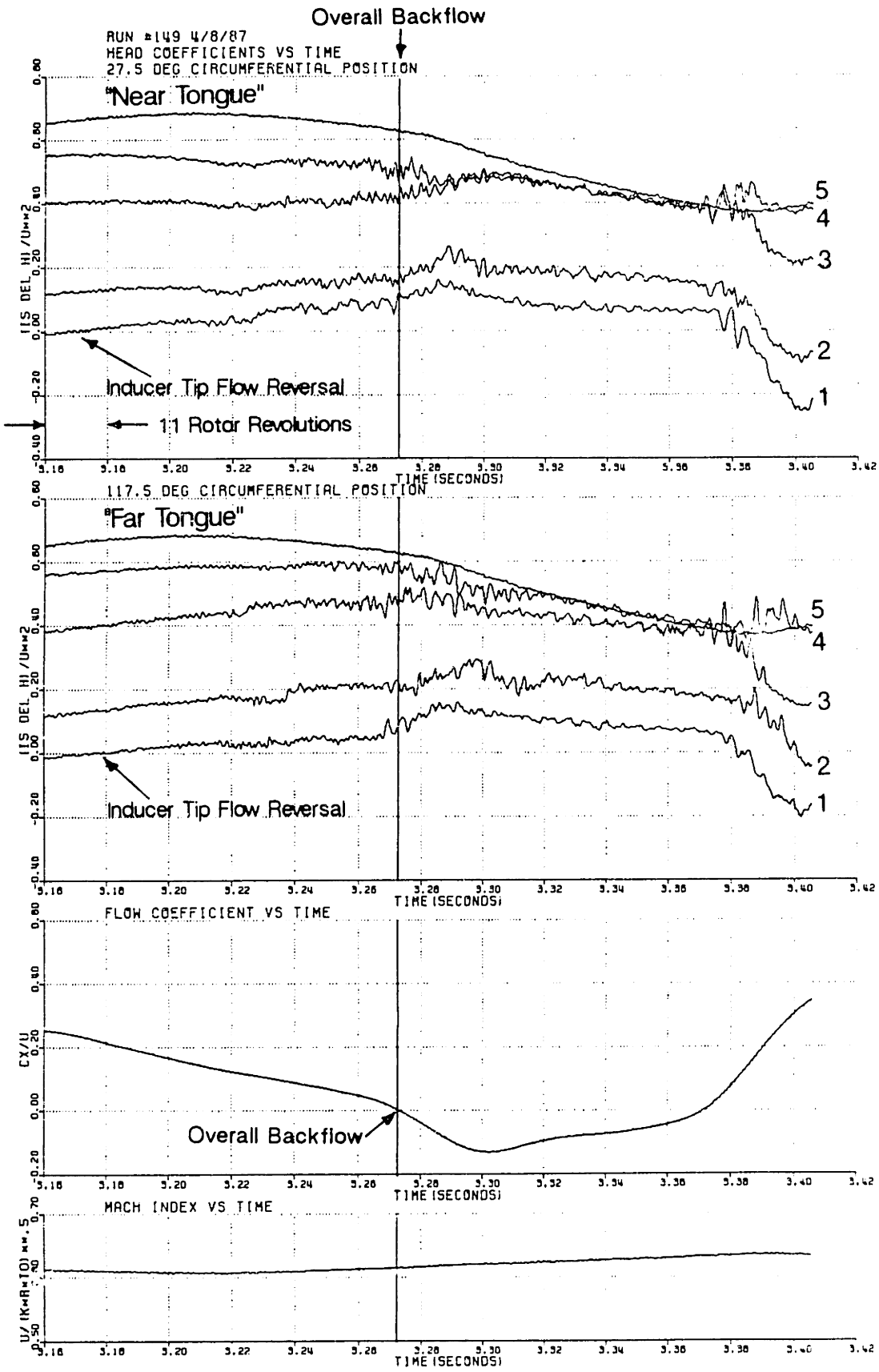

Fig. 3.21 Detail of Deep Surge Event(Mto ≃ .63)

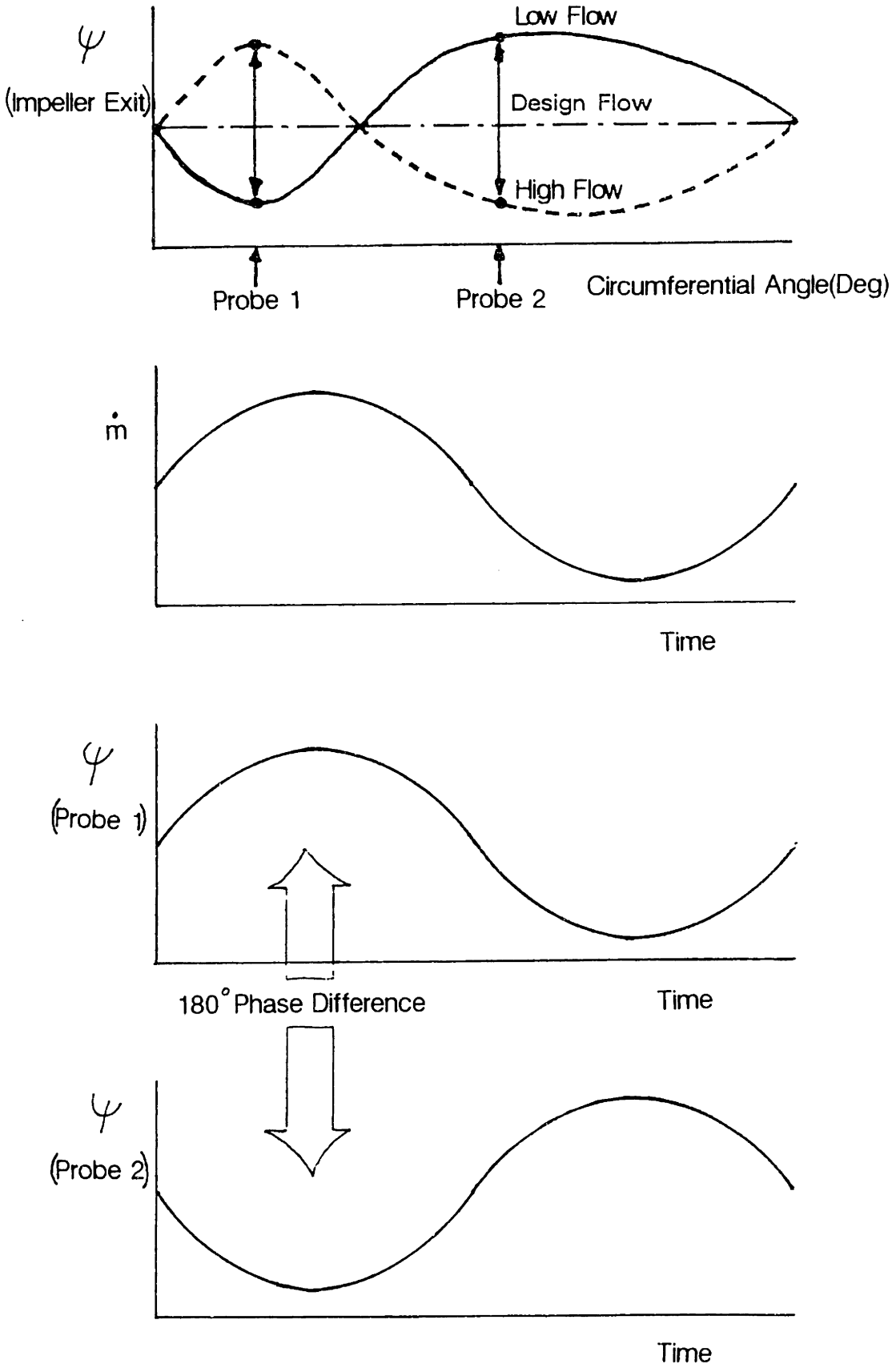

Fig. 3.22 Non-Rotating Circumferential Distortion Effect on Pressure Phase Measurements

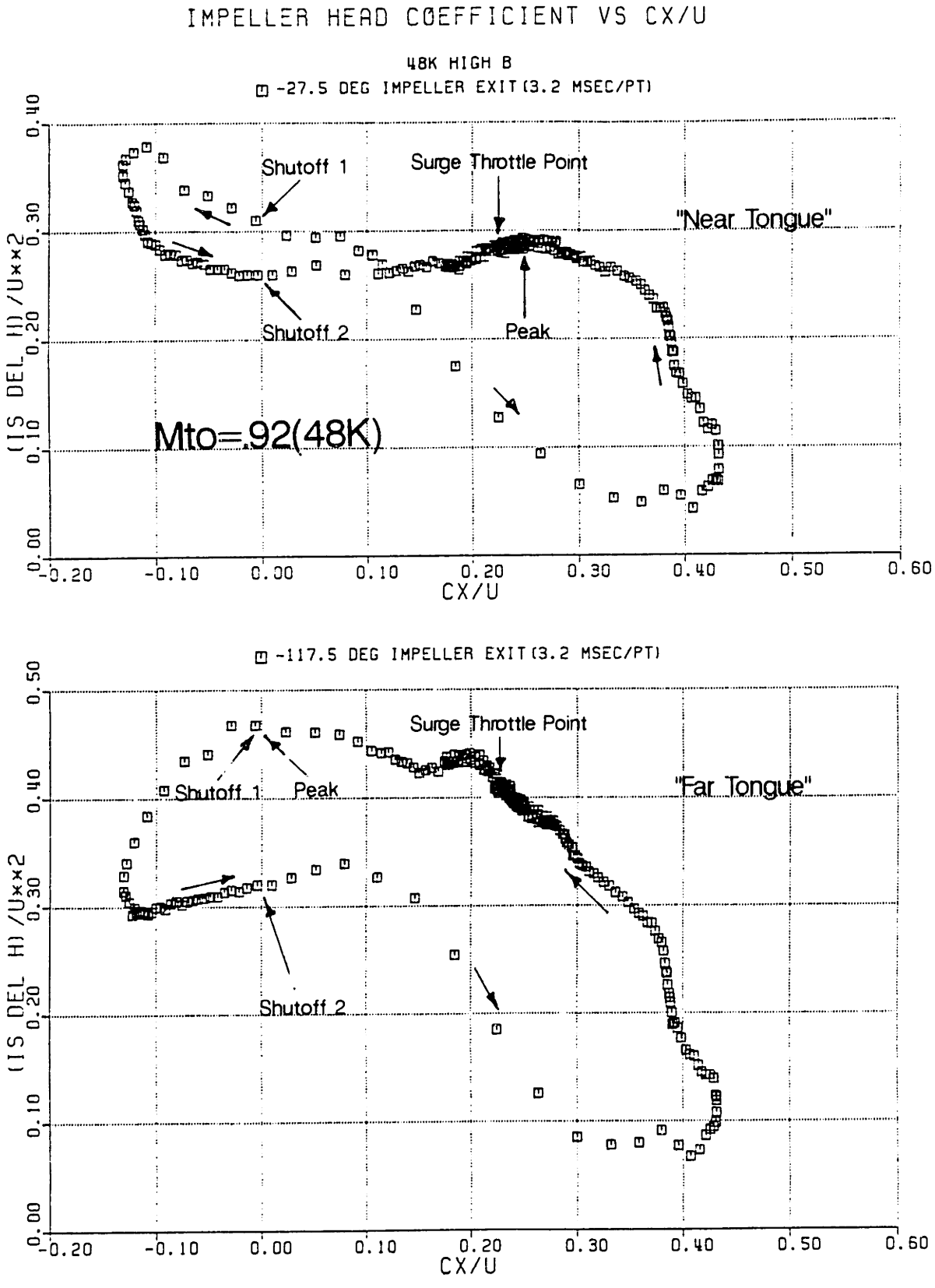

Fig. 3.23 Impeller Head Coefficient vs Cx/U(Mto ≃ .92)

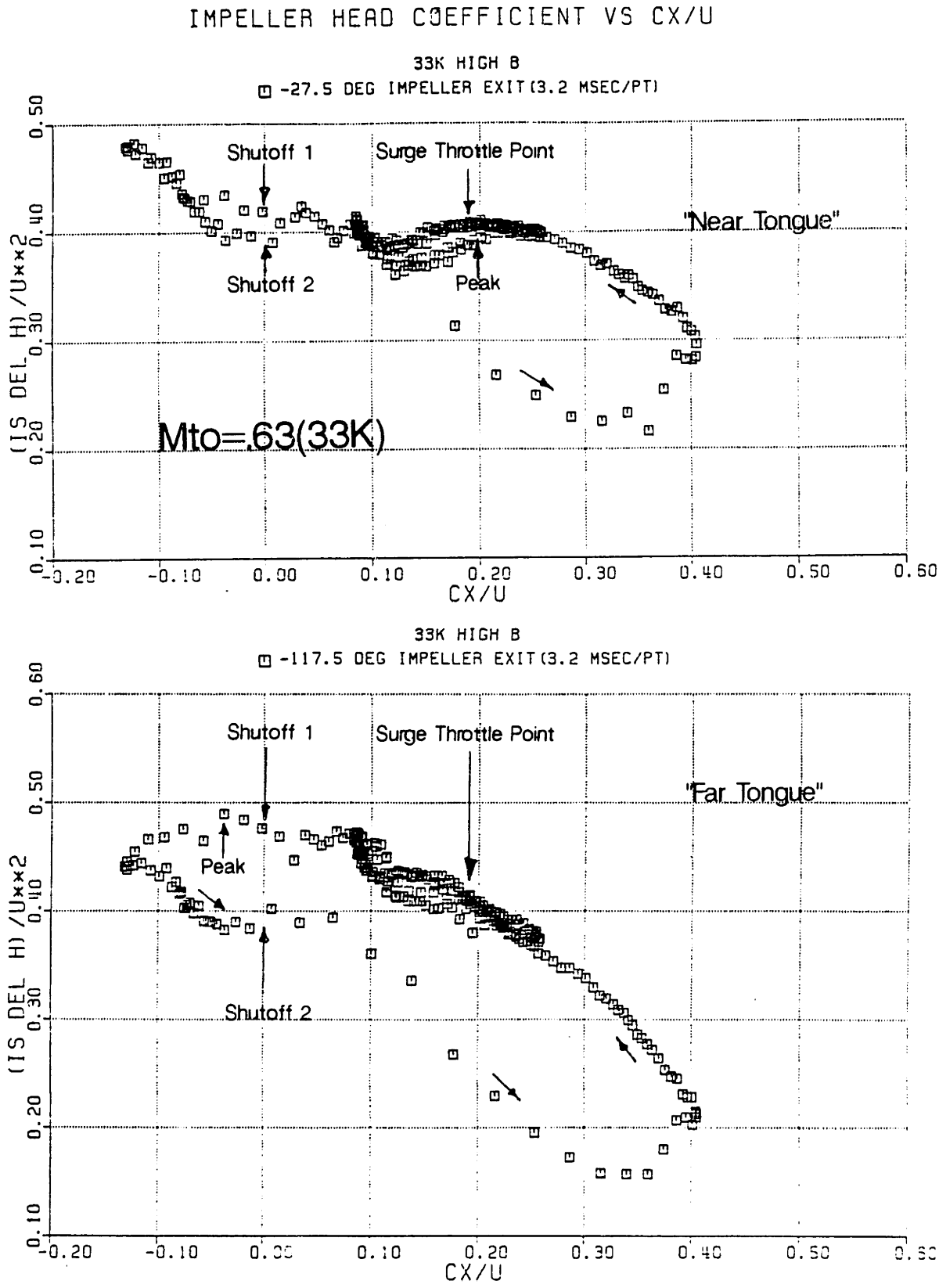

Fig. 3.24 Impeller Head Coefficient vs Cx/U(Mto ≃ .63)

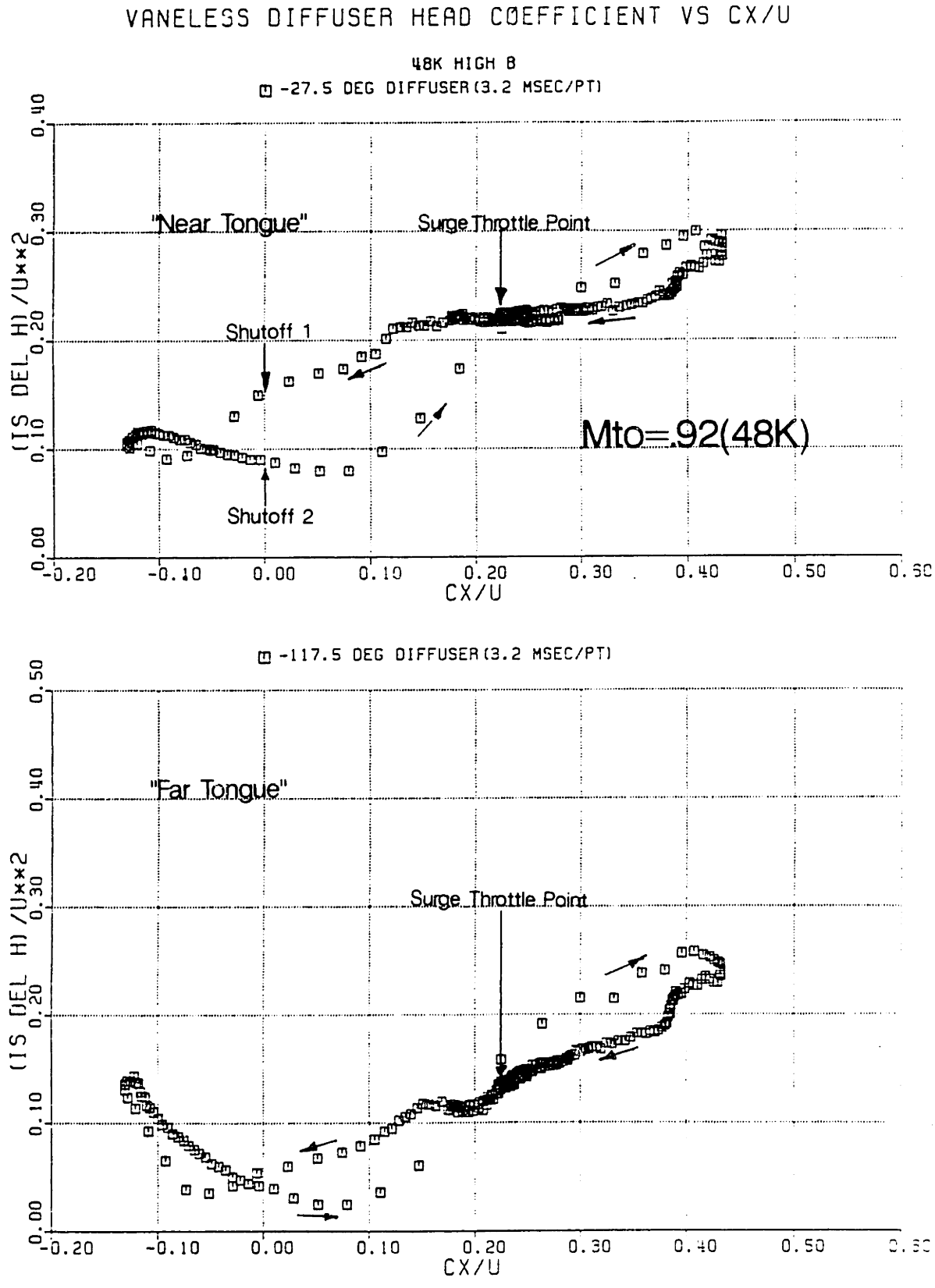

Fig. 3.25 Vaneless Diffuser Head Coefficient vs Cx/U(Mto ≃ .92)

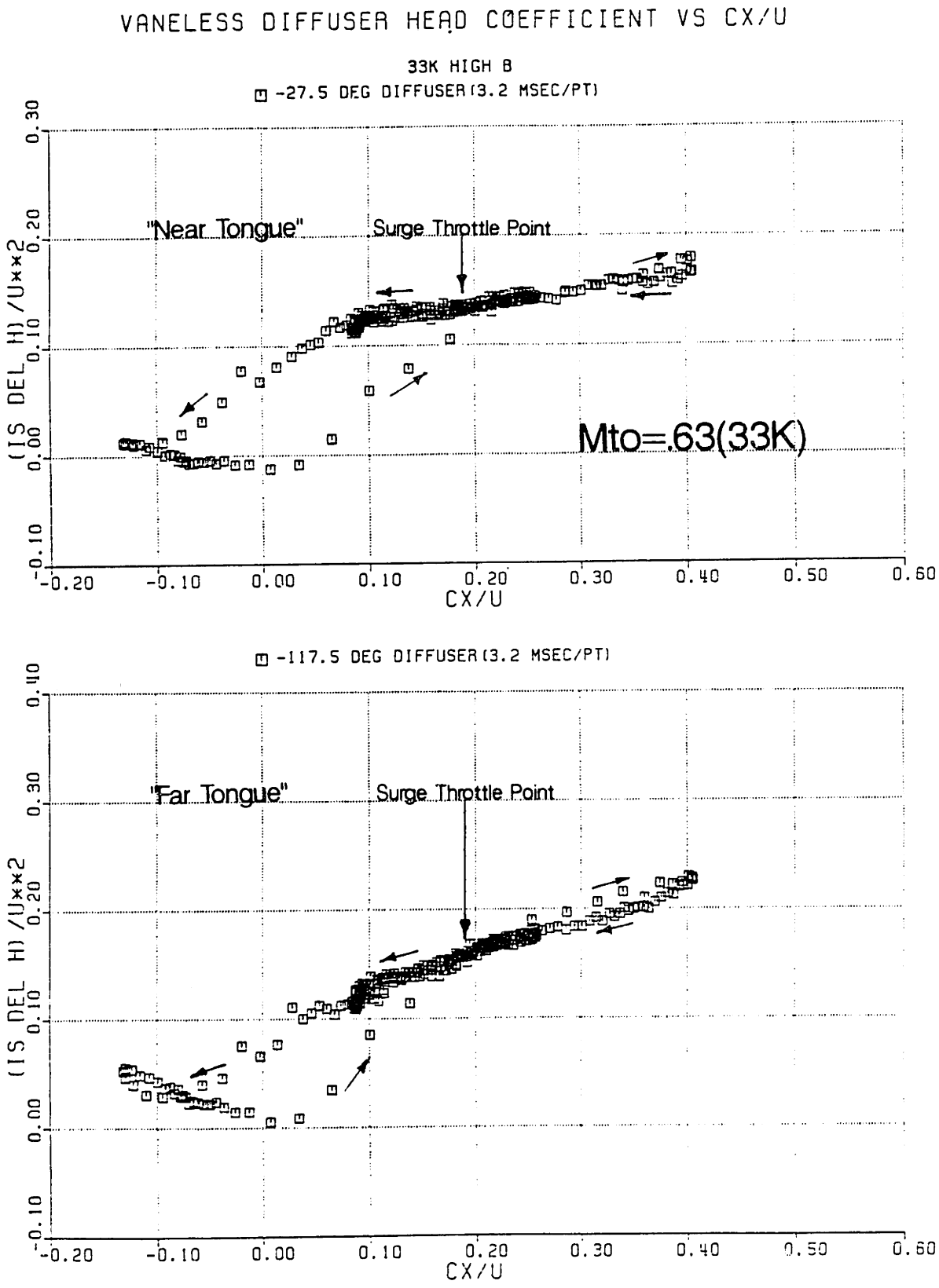

Fig. 3.26 Vaneless Diffuser Head Coefficient vs Cx/U(Mto $\simeq$ .63)

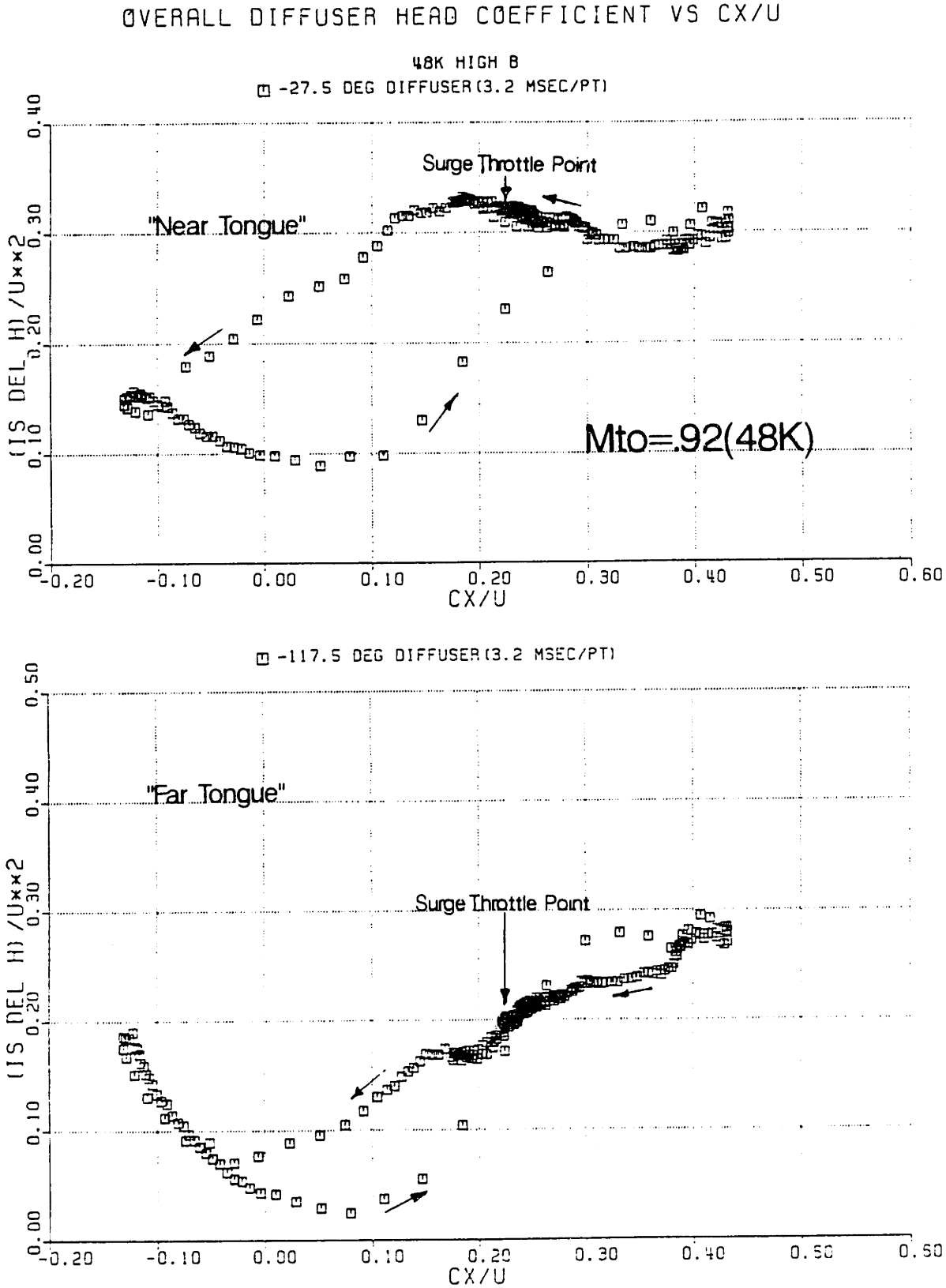

Fig. 3.27 Overall Diffuser Head Coefficient vs Cx/U(Mto ≃ .92)

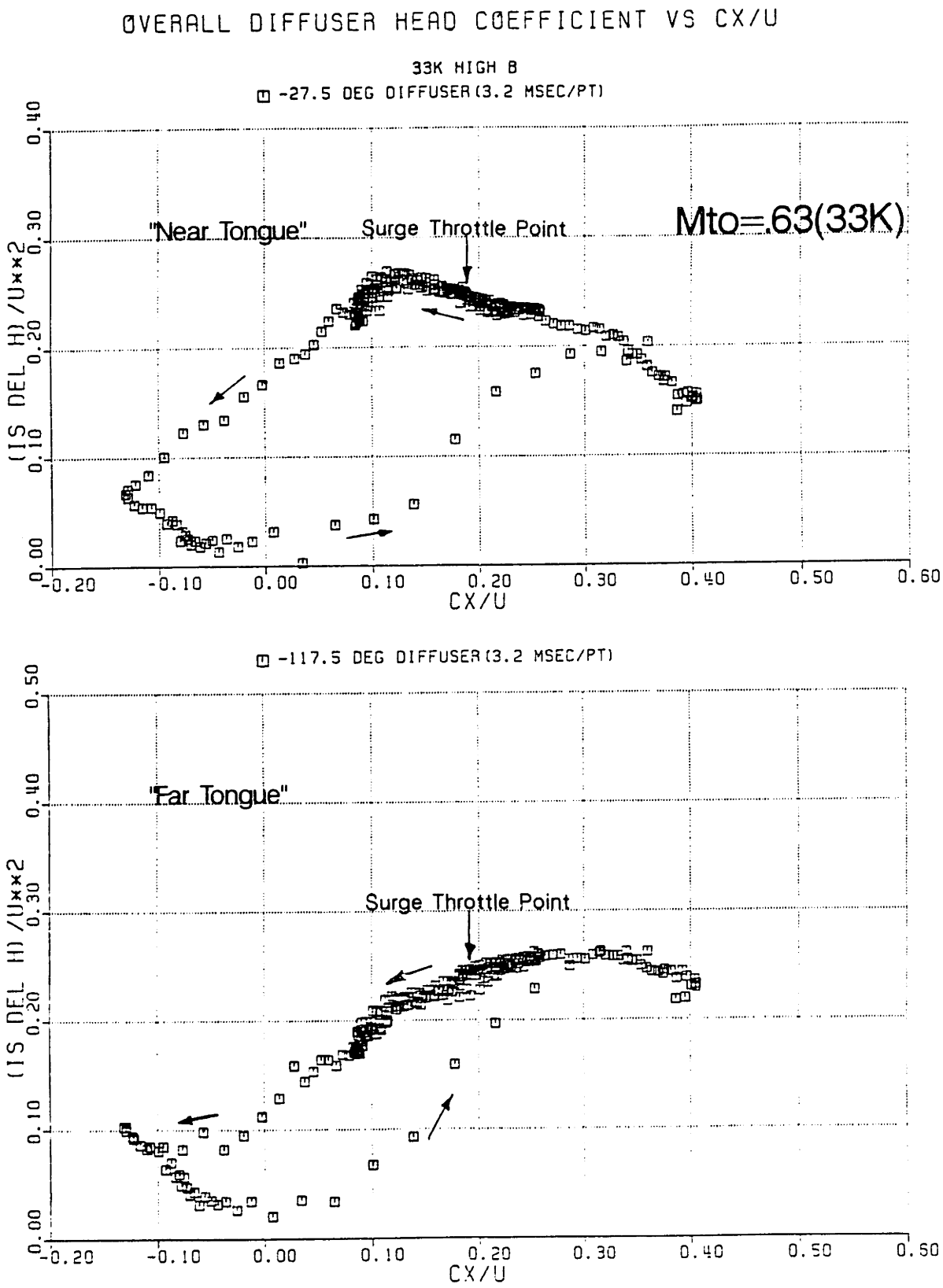

Fig. 3.28 Overall Diffuser Head Coefficient vs Cx/U(Mto $\simeq$ .63)

CHAPTER 4

SMALL B EXPERIMENTAL RESULTS AND DISCUSSION

4.1 Stability Argument for a Small B System and System Stabilization

In Chap. 3, several key points were brought out by the large B system transient data. First, deep surge results from a slowly growing dynamic instability when operating past the compressor characteristic peak. Several phenomena were seen as responsible to creating the compressor characteristic peaks. The main type of stall seen was impeller stall at the inducer tips which occured at both the "near tongue" and "far tongue" Kulite positions and was most severe at the "near tongue" location. The asymmetry in impeller stall appeared to be from a stationary circumferential flow distortion induced by the asymmetric down stream volute. Rotating stall in the impeller was seen but appeared unimportant relative to the stationary asymmetric inducer stall. The vaneless diffuser was destabilizing to the overall system since its overall characteristic was on average declining but in the region where surge is initiated, its characteristic slope did not change appreciably. Hence the initiation of surge was seen to be controlled by the impeller rather than diffuser. Evidence in the data showed that instability occured when inducer stall was present in the impeller. The deep surge throttle point was also seen to be close to the throttle point at which the impeller headrise at the "near tongue" circumferential position peaked and entered what appeared to be backflow.

All of these phenomena in Chap. 3 were viewed transiently during unstable system operation (i.e. in mild or deep surge). As seen in Fink[19], the surge line depends on the value of the B parameter. As B is reduced, the surge line position moves to the left. Eq. 1.8, as discussed in Sec. 1.4.2, showed that lowering B should stabilize the stage and move the surge line towards shutoff. As $B \rightarrow 0$, the critical value of C' at which instability occurs becomes a large positive number. The stability criterion of Eq. 1.8 then brings forth the following question: If B

is reduced to an extremely small value, would surge in the stage be eliminated? If this is true, then the compressor characteristic can then be viewed in steady state by reducing B. Lowering B, then provides a means of stabilizing the stage as Dean suggested, so that the stage stalling mechanisms that create a positive compressor characteristic can be studied in steady state. To do this, the large volume plenum was removed and a close coupled throttle valve placed downstream of the compressor volute exit.

4.2 Natural Frequency Measurement and B-Parameter Calculation

The B parameter for the new system was estimated by first measuring the natural frequency experimentally. The results are shown in Fig. 4.1. Two natural frequencies are seen, one at 87.2 Hz and another at 196 Hz(@ 83.3 deg F). The 87.2 Hz frequency seen appeared to be a quarter wave frequency of the ducting with one end closed which is given by

$$f_{\frac{1}{4}\,wave} = \frac{a}{4L} \tag{4.1}$$

where L is the duct length and a is the local speed of sound. For our compression system, L was assumed to be the shortest distance from inlet face to the throttle valve. This is found to be approximately 40 in(15.7 cm). Then for a speed of sound of 1140 ft/sec @ 83.3°F (348 m/sec @ 28.5°C), the calculated 1/4 wave frequency is 85.7 Hz which is within 1.7% of the measured value.

Using the measured natural frequency 87.3 Hz @ 545°R(29.6°C), the B-parameter is calculated from Eq. 1.1. For operation at the 48K corrected speed with a temperature ratio of 1.29, Rtip =2.518 in(6.39 cm), Utip = 1060 ft/sec(322 m/sec), and L = 3.33 ft(1.02 m), the B-parameter is found to be equal to .254. This compares with a large plenum system B of 2.74. Thus the small plenum system B-parameter is 9.3% of the large plenum system value.

4.3 Compressor Map and Overall Efficiency

Data points to define the compressor speedlines when operating in the small B system were taken in the same manner as was done in the large B system. The results are shown in Fig. 4.2. As can be seen, the previously unstable area of the compressor map is now visable. The speedlines are clearly extended to near shutoff. The speedlines are quite flat at lower speeds and gradually steepen at higher corrected speeds. There is some unsteadiness in massflow and pressure ratio near shutoff. The unsteady behavior during throttle down will be discussed in Sec. 4.5.

The compressor map data for both the small and large B systems as shown in Fig. 4.2 have been combined and replotted in terms of isentropic head coefficient vs flow coefficient shown in Fig. 4.3. One clear trend seen is a set of speed dependent peaks occuring in the data. At low corrected speeds (33K), the peak appears closer to shutoff than at higher corrected speeds(48K). In the large B system, system instabilities were seen to grow in a region around these peaks. Hence as corrected speed went up, mild(and deep) surge would occur at higher values of ϕ .

The positively sloped region to the left of each speed line peak is an area of greatly decreasing compressor efficiency. This is seen by looking at Fig. 4.4 which shows the overall adiabatic efficiency of the compressor. It is these inefficiencies which for a given B system produce the positively sloped head characteristic that is required to cause surge in the compression system. The stalling flow phenomena causing these inefficiencies will be discussed in Sec. 4.7.

4.4 Large B vs Small B Overall Compressor Performance

The steady state low B characteristic data is compared with the transient large B data(from Chap. 3) in Fig. 4.5. They are significantly different at low flows. The transient large B data is less steep than the steady state time averaged Scanivalve data. Both the 48K and 33K transient data joins their respective steady state data at the peak and diverge from it near shutoff. The instantaneous large B data appears flatter and lags the small B data in time. The lag appears to be associated with the time required for the inducer tips to stall. Evidence of this will be shown and examined in Sec. 4.7 when the small B high response Kulite pressure data is discussed.

4.5 Small B System Behavior during Throttling

Fig. 4.6 shows the behavior of the system(small B) parameters: compressor flow coefficient, Mach index, and system isentropic head coefficient for various throttle settings along the 48K speedline. The ϕ values given at the bottom of this figure are the calculated ones based on the measured flow through the calibrated inlet. Operation at a throttle setting of ϕ = .22, which is near the large B surge line(ϕ = .225), shows all 3 parameters to be quite flat. Where deep surge occured previously with large B, the system is now stable.

Reducing throttle to ϕ = .175 produces some system instability with a very small oscillation in flow coefficient appearing with frequency approximately equal to the measured 1/4 wave frequency of 87 Hz. Throttling the compressor to ϕ = .150 increases the amplitude of the flow instability to approximately 4% of mean flow coefficient of .15. At a throttle setting of ϕ = .125, other frequencies appear and the 1/4 wave frequency is no longer distinct. One lower frequency oscillation in head coefficient of amplitude approximately 3% of the mean is seen with frequency of approximately 23 Hz. The origin of this frequency is not known. At these throttle settings, the lowering of B was not sufficient to completely eliminate the instability, but the amplitudes were still quite small.

Further throttling to ϕ = .075 produces choppy behavior in the hotwire measured flow coefficient and isentropic head coefficient and also a significant drop in the system head. Sharp upward and downward spikes appear in both traces. More throttling to ϕ = .025 produces a large increase in the DC level of the hotwire output and a high degree of unsteadiness in measured flow and system pressure. In this throttling condition, the region in front of the impeller was found to be swirling in the rotor direction. This will be discussed more fully in Sec. 4.7. The extent of the swirling flow was such that the hotwire was inside the swirling region, so for this and lower throttling settings the hotwire is no longer reliable.

In the righthand plot of Fig. 4.6, the system parameters are shown with the throttle valve downstream of the compressor completely shutoff(ϕavg = 0). Again the hotwire output DC level is shifted up with a high degree of unsteadiness present in both the hotwire and Kulite outputs. A large amplitude oscillation in the head coefficient of approximately 185 Hz frequency is seen which corresponds to one of the natural frequencies excited by the random noise source shown in Fig. 4.1. The

approximate head levels during this oscillation varyed between an upper limit of ψ = .51 to a lower limit of ψ = .30.

As has been shown, the main effect of lowering system B by downsteam volume reduction has been one of stabilization. The amplitude of mild surge occuring in the compression system has been attenuated. A determination of the deep surge line for the small B system is imprecise due to the hotwire unreliability at low flows. However, the behavior of the system head suggests that it is very close to shutoff. When in deep surge for large B, the system head coefficient reaches a minimum value of .37 at shutoff 2. In the small B time resolved results of Fig. 4.6, such behavior is not seen until the valve is completely shutoff. Without high response instrumentation, one would be unaware that any surge was occuring at all in the system because of the small amplitude, high frequency, and a general lack of external signs such as blowdown noise, speed changes etc. which were unmistakable in the large B system deep surge of Fig. 3.6.

4.6 Small B System Compressor Component Measurement Description

The sources of the inefficiencies seen in Fig. 4.4 in the tested compressor which cause surge are seen by looking in turn at the diffuser and impeller components separately in the partially small B system and comparing these results with the large B results. Stall behavior in each component will be discussed from the results of four separate measurements performed while the compressor was operating in the small B system. The four measurements included:

- Impeller total exit pressure measurement with a single Kiel probe.
- Circumferential casing static pressure measurement.
- Kulite time resolved casing static pressure measurement.
- Flow visualization of inducer stall.

4.7 Discussion of Small B Stalling Phenomena in the Compressor Components

4.7.1 Impeller Stalling Phenomena

Evidence of impeller stall is seen in the results of the impeller exit total pressure measurement done with the single Kiel probe inserted downstream of the

impeller. As discussed in Chap. 2, the probe was circumferentially located 152.5 deg in the rotor direction away from the tongue and approximately angled in the flow direction. The measurement was done for both the large and small B system. The results in terms of the isentropic head coefficient vs ϕ are shown in Fig. 4.7 along with, for comparison, the overall compressor isentropic head coefficient and the compressor work coefficient. As seen in Fig. 4.7, the impeller head peaks at $\phi = .1$ for 33K and $\phi = .175$ at 48K. At flows below the peaks, impeller stalling occurs at this circumferential location and the curves turn down sharply.

The impeller efficiency(total to total) from the Kiel probe measurement is shown in Fig. 4.8. This is calculated using the overall work coefficient shown in Fig. 4.7. The efficiency peaks at approximately $\phi = .225$ and drops rapidly at $\phi = .1$. The sharp downturn in efficiency at $\phi = .1$ corresponds to an impeller inducer stall.

To verify and visualize this stalled flow associated with the inducer, a wire mesh with short yarn tufts was installed 3.5 in(8.9 cm) or roughly 1.2 inducer tip diameters upstream of the inducer leading edge. Photographs of the tufts were taken as the compressor was throttled down. This is seen by the photographic sequence 5(a)-5(c) on page 225 of the inducer inlet screen tufts while running at a corrected speed of 33K. In Photo 5(a), which corresponds to $\phi = .125$, the tufts are completely axial. In Photo 5(b) where $\phi \simeq .11$, the tip tufts are observed to turn towards the tangential rotor direction. In Photo. 5(c) at $\phi = .1$, the inner radius tufts are also observed to shift dramatically from axial to the tangential rotor rotation direction. The inducer tip stall results in a swirling flow ahead of the inducer. At lower throttling conditions of $\phi < .1$, this swirling flow was seen to be several diameters upstream engulfing the inlet hotwire used to measure the transient 1-D unsteady massflow.

The Kiel head measurement of impeller exit total pressure was taken at one impeller circumferential location. For axisymmetric flow conditions, a measurement at one circumferential position is sufficient to characterize the impeller pressure ratio. When the pressure field is asymmetric, measurements are required over the entire impeller circumference. To assess the degree of asymmetry in the impeller, diffuser, and volute flow field, circumferential static pressure measurements were made at 3 meridional locations around the compressor. As discussed in Chap. 2, 16 equally spaced taps were located at the leading edge of the impeller, a second set at

the impeller exit, and a third set were located at the outer radius of the vaneless diffuser. These are shown in Fig. 2.10 and 2.11 in Chap. 2.

An asymmetry in flow and pressure at the tongue circumferential position of the impeller is seen by examining the circumferential pressure distortion results for the impeller. The 33K and 48K total to static head coefficients vs circumferential angle for the impeller are shown in Fig. 4.9 and 4.10. Fig 4.9 shows the circumferential pressure variation for high flow coefficients at 33K and Fig. 4.10 shows the pressure distortions for low flow coefficients at both 33K and 48K corrected speed. The tongue location is at 0° in these figures with circumferential position being positive in the rotor direction. A severe pressure distortion is seen in Fig 4.9. As the compressor is throttled down to ϕ = .275, the distortion disappears. With further throttling shown in Fig. 4.10, the distortion reappears and is most depressed at 45° from the tongue location. At a higher corrected speed of 48K, the depressed region near the tongue is more severe than at 33K.

The static pressure distortion shown in Fig. 4.9 and 4.10 is similar to the distortion shown in Fig. 4.11 from Lorett and Gopalakrishnan[44]. The stationary circumferential pressure distortion is induced by the downstream asymmetric volute. The design point or match point of the volute is the operating point of minimum circumferential flow distortion. When operating off design, a non-rotating steady distortion "locked" to the tongue of the volute develops.

In Fig. 4.9 - 4.10, the distortions are plotted for various circumferentially averaged flow coefficients. The average flow coefficient given is calculated from the calibrated inlet duct using the manometer measurement. At very low flow coefficients below a ϕ of .05, an error develops in this measurement. Some of the error is due to inlet flow unsteadiness and some is due to the large amount of swirl present in the inlet tube at these low throttle positions. In the trace which is labeled "Cx/U = 0", the manometer read zero but the throttle valve was not yet closed. In the trace which is labeled "shutoff", the throttle valve was physically closed. In Fig. 4.9 - 4.10 and other low flow data of this chapter, "shutoff" refers to operation with the throttle valve physically closed. "Cx/U = 0" refers to a throttle valve setting where the flowrate manometer reads zero. This convention has been retained for all the circumferential distortion data.

The circumferentially averaged value of impeller head coefficient(both total to

static and total to total) from Fig. 4.9 and 4.10 are shown in Fig. 4.12. The total to total value is obtained from the total to static value using a calculated axisymmetric average impeller exit Mach number. The average impeller exit Mach number $M_{\bar{2}}$ can be determined for an axisymmetric flow of an ideal gas if the flowrate $\dot{m}$, circumferential normal area Ar, static pressure P, total temperature To, absolute tangential velocity C_θ , ratio of specific heats K, and gas constant R are known. To find C_θ requires requires an estimate of the impeller slip factor. The slip factor was estimated by correcting the work coefficient for shroud friction. The correction proceedure and its results are described in App. F. The analysis to determine the absolute impeller exit Mach number is described in App. G.

A main point of interest in the impeller total to static head characteristic curve is its slope behavior around the large B system surge initiation points(ϕ = .190@33K and ϕ = .225 @48K). Clearly the slope changes from a stabilizing negative value to a more destabilizing value near zero at the respective surge initiation points. If the compressor is operating without a vaneless diffuser, the overall system is stable with the characteristic shown in Fig. 4.12. However with a vaneless diffuser characteristic of positive slope present, the impeller characteristic slope change causes instability in the large B system. The instability occurs when(Eq. 3.24) the sum of vaneless diffuser and impeller slopes becomes positive. High response data of the vaneless diffuser in Chap. 3 showed positively sloped behavior of its characteristic. Additional data of the destabilizing positively sloped diffuser characteristic will be shown in Sec 4.7.2 in the discussion of the vaneless diffuser.

The circumferentially averaged total to total impeller head shown in Fig. 4.12 levels off at higher values of flow coefficient than the value obtained by the Kiel head measurement shown in Fig. 4.8. This is because the Kiel probe was located away from the tongue in a circumferential impeller region where the compressor total pressure is higher. When the total pressure is averaged over the whole circumference which includes the depressed regions near the volute tongue, it is lower.

The total to total head in Fig. 4.12 turns down strongly at about ϕ = .05 towards the total to static head. This is an effect of shroud friction which reduces the slip parameter and absolute value of velocity C_θ at the wheel exit at low flow coefficients. The total to total curves meet the total to static curves at shutoff

because C_θ is zero there. The slip parameter derived in App. F explains this observed behavior.

Another point of interest shown by Fig. 4.12 is the value of total to static head at shutoff. From Eq. 3.20 it was found that for $R_1/R_2 << 1$ the ideal head coefficient(total to static) for an impeller at shutoff is .5. However data at the shutoff point for 48K is seen to be approximately .29. The much lower headrise than ideal is a result of a total loss in head recovery at the inducer tip. This is seen by estimating the ideal head recovery of the inducer tip with a simple analysis. The details of this analysis are shown in App. H. If the flow in the absolute frame is assumed to be axial and compressible, the relative inlet Mach number at the inlet tip region of the inducer is given by

$$M_{1rel} = \left\{ \frac{(1+\phi_1^2) M_{T0}^2 \left(\frac{R_1}{R_2}\right)^2}{\left(1 - \frac{(\kappa-1)}{2}\left(\frac{R_1}{R_2}\right)^2 M_{T0}^2 \phi_1^2\right)} \right\}^{1/2} \tag{4.2}$$

where ϕ_1 is the inducer inlet tip flow coefficient and R_1/R_2 is the ratio of inducer tip radius to impeller exit radius. The total to static pressure ratio in the relative frame at the inducer inlet is simply

$$\left(\frac{P_{01}}{P_1}\right)_{rel} = \left(1 + \frac{\kappa-1}{2} M_{1rel}^2\right)^{\frac{\kappa}{\kappa-1}} \tag{4.3}$$

If a total loss of velocity head occurs at the inducer tip, the pressure ratio given by Eq. 4.3 roughly represents the loss in pressure ratio in the impeller tip stall. Written in terms of isentropic heads(total to static) as defined in 3.10, this pressure ratio loss is

$$\psi_{loss} = \frac{\frac{1}{2}\left(\frac{R_1}{R_2}\right)^2 \left(1+\phi_1^2\right)}{\left(1 - \frac{(\kappa-1)}{2}\left(\frac{R_1}{R_2}\right)^2 M_{T0}^2 \phi_1^2\right)} \tag{4.4}$$

For the tested impeller, Rinducer tip = 1.467 in(3.725 cm), Rimpeller tip = 2.518 in(6.394 cm) and R_1/R_2 = .583. For ϕ = 0, and Mach index of .922(@48K), the expected loss in impeller head from Eq. 4.4 is equal to .17. Then the estimated impeller shutoff head is the ideal value of .5 minus .17 or .33. This is within 14% of the measured value of .29.

The circumferentially averaged overall efficiency(total to total) of the impeller using the data of Fig. 4.12 is shown in Fig. 4.13 along with the measured overall compressor efficiency(total to total). The impeller efficiency curves exhibit similar trends as the overall compressor efficiency. The dominance of the impeller stalling processes on the overall compressor efficiency is seen clearly by this comparison. Also the efficiency peaks occur at higher values of flow coefficient than the points where surge was initiated in the large B system. The inducer stall occuring in the impeller is the flow mechanism responsible for the declining efficiency past the peak.

Evidence of inducer stall and asymmetry from the downstream volute is also seen by examining the inducer leading edge wall static pressures. The 16 circumferential taps over the inducer leading edge were used to estimate the variation in tip flow coefficient. Assuming axial flow from ambient pressure to the tip measured static pressure, the axial velocity was calculated using 1-D isentropic flow relations. This is a rough calculation since the circumferential velocity component that exists at the inducer inlet due to the circumferential pressure gradient is ignored. When the pressure exceeded or equaled ambient pressure, the axial velocity was set equal to zero since it was then reversed and emanating from the rotor tips. Fig 4.14 and 4.15 show the results of this calculation for 33K and 48K. Results for operation above the volute match point are shown in Fig. 4.14 and below in Fig. 4.15. The equivalent inducer tip incidence angle is shown on the right scale of these figures for the test impeller's measured blade tip angle of 54.4°(relative to axial direction).

In Fig. 4.14, for a corrected speed of 33K, the tip flow coefficient is highest in a region located at the tongue. In Fig. 4.15, as the compressor is throttled down below the match point, the tip ϕ drops rapidly to zero at the tongue at a mean flow coefficient of ϕ = .150 and at ϕ = .125 is completely stalled. The flow distribution at ϕ = .150 is a non-rotating stall of the inducer blades. At a higher

corrected speed of 48K, also shown in Fig. 4.15 for below match point operation, this non-rotating stall of the blades is again most severe at ϕ = .15. At a throttle setting of ϕ = .1, the tip region over the entire circumference stalls.

The error associated with this estimate of axial flow coefficient depends on the amplitude of the flow coefficient distortion relative to its mean value. The error was estimated by assuming a pure cosine 1st harmonic distortion in axial flow coefficient at the inducer face($Cx(\Theta)$) and then finding the corresponding 1st harmonic in circumferential velocity that must exist there($C_\Theta(\Theta)$) such that both 1st harmonics satisfy Laplace's equation. The difference between the purely cosine axial velocity distribution $Cx(\Theta)$ and an axial velocity distribution with magnitude equal to $(Cx(\Theta)^2 + C_\Theta(\Theta)^2)^{.5}$ then provides an estimate of the error associated with the axial flow coefficient estimate. The flow was assumed to be essentially 2-D with axis along the inlet axial flow direction(X) and along an unwrapped circumferential direction(Θ). The boundary conditions are constant flow far upstream($X = -\infty$), a periodic solution along the sides($Y = 0, 2\pi$), and a prescribed axial flow coefficient distortion at the inducer face($X = 0$).

The solution to this problem is described in Koff[41]. The circumferential velocity 1st harmonic is found to lead the axial flow coefficient 1st harmonic by 90° and be of equal magnitude. The maximum error as defined above depends on the circumferential angle and the ratio of distortion ϕ amplitude to mean ϕ. As an example, if the mean flow coefficient is .3 and the distortion amplitude is .025(approximately the measured distortion level for ϕ = .25 @ 48K in Fig. 4.15), the maximum error in the estimated axial flow coefficient is small being approximately .001 @ Θ = 120° or .3% of the mean flow. More importantly, the error becomes zero in the circumferential position region of interest where the 1st order harmonic in axial flow coefficient is minimum(tongue). At a lower mean flow coefficient of .075 with a distortion amplitude of .075(approximately the measured distortion level for ϕ = .150 @ 48K in Fig. 4.15), the maximum error in the axial flow coefficient estimate increases to .0375 @ Θ = 120° or 50% of mean flow. However error is still zero at Θ = 0° (the tongue) and Θ = 180° via this analysis.

The circumferentially averaged incidence angle at the inducer tip from the data of Fig. 4.14 and 4.15 is shown in Fig. 4.16 along with the large and small B surge points found in Chap. 3. The inducer incidence angle is found to be positive below

a mean flow coefficient of .325. At the 48K large B surge point, the incidence angle is a positive 13° and at 33K it is approximately 15°. Since the inducer blades are thin, positive flow incidence angles of this magnitude cause separation to occur on the suction side of the blading which then leads to tip flow reversal.

Results of the low B transient Kulite pressure data also shows severely stalled tip flow at the inducer. With the Kulites in identical positions in the impeller and vaneless diffuser as for the large B system, the unsteady static pressures at the wall were recorded again for various throttling conditions up to shutoff. This includes both the "near tongue" Kulites and "far tongue" Kulites. Fig 4.17 through 4.20 show the unsteady pressure data at four throttle conditions ϕ = .2, .1, .05, and shutoff.

There are several main effects seen in small B Kulite data. The first is an overall inducer tip stall as ϕ goes down as shown by the above atmosphere values (trace 1). The tip stall worsens as ϕ is reduced below ϕ = .1. A second effect is the large overall unsteadiness in the time traces when ϕ drops below .1. At ϕ = .05 shown in Fig. 4.19, throttling condition we see unsteadiness at both near tongue and far tongue locations which is roughly in phase. This is surge, i.e. an overall oscillation in the overall annulus averaged massflow. At shutoff, shown in Fig 4.20, the effect is more pronounced. FFT results for the inducer Kulites(trace 1) show the two system natural frequencies as measured by the random noise source to predominate the inducer Kulite signal(trace 1). These are shown in Fig. 4.21 for ϕ = .05 and shutoff ϕ = 0.

The asymmetry in stall behavior of the inducer is also visable in Fig. 4.17 thru 4.20. The inducer headrise shown by the difference between trace 2 and 1 is much larger away from the tongue than at the near tongue position. The asymmetry is a result of the volute induced flow distortion discussed earlier.

The impeller traces in Fig. 4.20, which shows the compressor heads at shutoff conditions, is of interest when they are compared with the large B time resolved data at shutoff shown in Fig. 3.19. The main feature is a much lower impeller exit head(trace 3) in the far tongue position for low B than for large B. In the large B results, the impeller has a head of approximately .47. at shutoff, while the small B results averages approximately .35. A small time lag in the impeller response could explain this behavior. Near shutoff for large B, the flow is no longer quasisteady

since the reduced frequency becomes large. A finite time is required for the inducer tips to stall, during which a vortex is shed and convected downstream. Near the tongue, the impeller is stalled already because of the volute induced flow asymmetry. Further evidence of the lagging behavior will be discussed in Chap. 5, when a time lag is introduced into the dynamic model.

The weakness of rotating stall is seen in the FFT results of the inducer Kulites at a flow coefficient of approximately .225 for a corrected speed of 33K. This corresponded to the throttle point where the rotating stall frequency observed in Fink[19] reached maximum amplitude. The vertical axis represents the magnitude of the pressure fluctuations in terms of head coefficient. One block represents .0005 in head coefficient. The magnitude of the rotating stall seen at a frequency of 220Hz is .0015 which is very small. The quarter wave frequency at 87 Hz is also seen in Fig. 4.22 along with a 1/rev rotor frequency of 550 Hz. The magnitude of both these frequencies are larger than the rotating stall amplitude observed.

4.7.2 Diffuser Stalling Phenomena

To examine the vaneless diffuser and the effects of the distortion on Cp in the vaneless space, a circumferential diffuser value of Cp was calculated from the measured distortion static pressure data at various throttle conditions. The vaneless diffuser Cp is defined as

$$C_p(\theta) = \frac{\frac{P_3(\theta)}{P_2(\theta)} - 1}{\left\{1 + \frac{(\kappa-1)}{2}\overline{M}_2^2\right\}^{\frac{\kappa}{\kappa-1}} - 1} \qquad (4.5)$$

where P_2 and P_3 are the circumferentially measured static pressures respectively at the vaneless diffuser inlet and exit and $\overline{M}_2$ represents the average axisymmetric value of inlet Mach number. $\overline{M}_2$ is calculated by the method discussed in App. G.

The vaneless diffuser $C_p(\theta)$ using Eq. 4.5 are shown in Fig. 4.23 and Fig. 4.24. Data for high flow operation at 33K above the match point of the volute is shown in Fig. 4.23. Operation at low flow throttling conditions for both 33K and 48K are shown in Fig. 4.24. In Fig 4.23 at $\phi = .5$, a low depressed region is seen near the tongue at 45°and a high region at 292°. As throttling decreases towards

minimum distortion value at ϕ = .275, the variation in Cp disappears. At lower throttle conditions in Fig. 4.24, a depressed region of Cp develops at the tongue. As throttling continues, the gradient of Cp between 0° and 45° reaches a peak value of roughly .15/45° and then the overall DC level of Cp drops rapidly.

At 48K seen in Fig 4.24, the same effects are evident, but the depressed region of Cp is more severe. The cause of the depressed Cp region at the tongue is due to the reduced flow coefficient there which is induced by the downstream scroll when operated off the match point. As was seen in the estimate of circumferential variation in axial flow in the inducer in Sec. 4.7.1, the volute affects the circumferential distribution of massflow through the compressor. At the tongue where the flow coefficient is lower, the swirl angle is higher and the vaneless diffuser Cp is lower.

Evidence of diffuser stall as compressor ϕ is reduced is shown in Fig. 4.25, which shows the circumferentially averaged value of Cp vs Θ. The trend is downward, showing degrading diffuser performance as the compressor is throttled. Both 33K and 48K show the same effect. The same data in Fig. 4.26 plotted vs inverse swirl parameter defined as C_r/C_θ shows identical behavior. Plotted in this fashion, the 33K and 48K data almost coincide showing the relative insensitivity of Cp to Mach number.

The circumferentially averaged pressure rise of the vaneless diffuser plotted in terms of head coefficient(static to static) is shown in Fig. 4.27 along with, for comparison, the circumferentially averaged impeller head coefficient(total to static) and the vaneless diffuser exit head coefficient(total to static). The vaneless diffuser exit head coefficient shown in Fig. 4.27 is approximately equal to the sum of the impeller and vaneless diffuser characteristic shown there.

To ascertain the most critical component in surge initiation, it is important to observe the slope behavior of both the impeller and vaneless diffuser characteristic in Fig. 4.27 since system stability depends on the sum of the component characteristic slopes(given by Eq. 3.24). For operation at 33K, the vaneless diffuser head shows a downward trend for high flows, a flattening at ϕ = .2, and a downward trend again for ϕ = .1. At higher corrected speed of 48K, the diffuser characteristic flattening occurs at ϕ = .2 and then turns downward at ϕ = .175 to shutoff. Over most of the flow range the characteristic is positively sloped and is

therefore destabilizing to the system. On the average, the slope of the vaneless diffuser characteristic does not change radically with flow coefficient. Hence the vaneless diffuser is seen to be in general destabilizing. At high flows, where the overall system is stable, the vaneless diffuser is strongly destabilizing. Stability of the overall compression system occurs in spite of the destabilizing nature of the diffuser because the overall characteristic(roughly equivalent to the sum of the impeller and vaneless diffuser characteristic shown in Fig. 4.27 if the volute contribution is small) is negatively sloped.

The impeller is responsible for stabilizing the overall system at high flow coefficients via Eq. 3.24 since its characteristic in Fig. 4.27 is steeply negatively sloped. At roughly ϕ = .2, the impeller characteristic flattens out along with the vaneless diffuser characteristic. The flattening of the impeller characteristic occurs at approximately ϕ = .225 at 48K and ϕ = .175 at 33K which correspond closely with the large B measured deep surge points on the compressor map. At these points, the sum of the vaneless diffuser and impeller characteristic slope becomes zero which for the large B system results in a system instability. As has been shown, inducer tip stall is the phenomena responsible for the flattening impeller characteristic which via Eq. 3.24 destabilizes the overall system.

The data of Fig. 4.25 through 4.27 shows the main effect on diffuser performance as ϕ is reduced since the circumferential variation has been averaged out. How much of this downward trend is due to the distortion and how much would be expected under axisymmetric conditions is not clear. It is difficult to assess the separate effects of the axisymmetric and asymmetric stall in these results. It is clear that the downstream volute adds an additional asymmetric stall to the diffuser when the compressor operates away from the volute's matching condition. The volute's role on the overall stage stalling and surge point is discussed in the next section.

4.8 Influence of the Volute Match Point on Compressor Stalling Behavior

The matching condition or design point of the volute is defined as the point where axisymmetric flow occurs in the impeller and diffuser. At the match point operating condition, the geometric expansion area of the volute with circumferential angle is such that flow and pressure circumferential distortions in the impeller and vaneless diffuser are minimized. When the flow coefficient is reduced from the match

point, the volute geometric expansion rate($dA_\theta/d\theta$) will be too rapid for both axisymmetric flow in the impeller and for full volute channel flow. Similarly, when the flow coefficient exceeds the match point value, the volute expansion rate will be insufficiently rapid for axisymmetric flow. When operating in either of these two conditions, circumferentially non-uniform flow and pressure distortion will be present.

The volute matching condition for an incompressible pump is discussed in Lorett and Gopalakrishnan[44]. Following their analysis, which assumes incompressible flow in the volute, but recognizing the stagnation density jump across the impeller and vaneless diffuser from compressibility, the volute matching Φ becomes corrected speed dependent due to the higher density in the volute. Basically Eq. 1 of their analysis, which specifies the volume flowrate in the volute at any circumferential angle θ at the match condition, is modified and becomes

$$Q_\theta = \frac{\theta}{2\pi} \frac{\Phi A_c U}{\left(\frac{\rho_3}{\rho_0}\right)} \tag{4.6}$$

with θ being the angle in the volute relative to the tongue, and ρ_3/ρ_0, the compressor density ratio(tt). Continuity of flow at each circumferential section of the volute of cross sectional area A_θ requires

$$Q_\theta = C_\theta A_\theta \tag{4.7}$$

Conservation of angular momentum from the impeller exit radius(R_0) to the volute centerline radius (R) is given by

$$C_\theta R = C_{\theta_0} R_0 \tag{4.8}$$

Combining Eq. 4.6 through 4.8 and employing the definition of the slip parameter $\sigma = C_{\theta_o}/U$, results in the following equation for the volute matching condition. This is

$$\sigma = \left\{ \frac{\left(\frac{\Theta}{2\pi}\right)\left(\frac{A_c}{R_o}\right)}{\left(\frac{A_\theta}{R}\right)} \right\} \frac{\bar{\phi}}{\left(\frac{\rho_3}{\rho_o}\right)} \tag{4.9}$$

The term in brackets { } is a constant since it is a function of geometry alone which is fixed to give axisymmetric flow at the design point or matching condition. Graphically then the volute match point is determined by the intersection of Eq. 4.9 with the slip factor curve derived in App. F.

Assuming $\eta = .72$ = constant(from the average peak of Fig. 4.4) and calculating the match lines described by Eq. 4.9 and assuming that the match point corresponds to $\bar{\phi} = .25$, $\sigma = .86$ at 33K(approximate measured minimum distortion point), the approximate match lines are drawn in Fig. 4.28. The intersection points correspond to the points of minimum circumferential distortion from the volute. The main trend is a pushing out of the match point from $\bar{\phi} = .25$ @ 33K to $\bar{\phi} = .44$ @ 69K. Reducing $\bar{\phi}$ below the match point as calculated by Eq. 4.9 causes the circumferential distortion to grow with a depressed region of diffuser Cp near tongue. The compressor isentropic head can be expected to peak somewhere below the match point $\bar{\Phi}$ and thus create a positive characteristic necessary for surge to begin.

The overall compressor efficiency shown in Fig. 4.4 has peaks which also roughly correspond to the match points calculated. The data presented earlier showed the volute's adverse effect on the impeller and diffuser performance at the tongue circumferential position. The volute sets up an asymmetric flow in the vaneless diffuser and in the rotor frame, an asymmetric unsteady channel flow in the impeller. A low flow occurs at the tongue circumferential position. The additional losses generated here in the impeller and vaneless diffuser over the axisymmetric values cause the overall compressor characteristic to peak roughly where the distortion is minimum. The peaks in compressor head coefficient vs flow coefficient move progressively further to the right as wheel tip speed and overall compressor density ratio increase. Hence for a large B system, the surge line will also move to the right in the same fashion as the Mach index is increased.

There are also some additional losses generated in the scroll itself which adversely effect stage performance. The losses are seen in Fig. 4.29, which compares the circumferentially averaged vaneless diffuser exit head(total to static) with the volute exit head(total to total) as measured by a Kiel probe in the volute discharge pipe. The upper plot compares these two heads for 33K operation while the lower curve compares them at 48K corrected speed. At high flow coefficients(ϕ > .35) above the match point(ϕ = .225 @ 33K), all of the velocity head entering the volute appears to be lost. At low flow coefficients(ϕ < .075) below the match point for both 33K and 48K operation, similar behavior is seen. The amount of head recovery in the volute at the compressor peak while small is not insignificant and is roughly 5% of the overall compressor head(total to total).

It is not possible to ascertain from the present experimental results what the true compressor axisymmetric characteristic is. If this were known, then the amount of additional losses from flow asymmetry in the impeller, vaneless diffuser, and volute could be assessed. The present results suggest that volute is a strong determinant in the position of the compressor characteristic peaks. Consequently a successful surge prediction requires that one model the circumferential flow distortion induced by the volute and its effect on the impeller and vaneless diffuser performance. It is necessary to predict how a centrifugal compressor stage characteristic deviates from its axisymmetric one when a downstream volute is present in the stage. If one is able to calculate the deviation in shape from the axisymmetric curve, then one can then predict where surge will occur when the volute is present.

From the volute discussion, deviations from the axisymmetric behavior should correlate with the deviation from the match point. Hence a volute mismatch parameter for use in correlating the additional losses might be defined as

$$V = \left| \frac{\{G\}\Phi}{\sigma\left(\frac{P_3}{P_0}\right)} - 1 \right| \qquad (4.10)$$

Increasing V would incur increasing efficiency penalties from axisymmetric conditions.

4.9 Calculation of Circumferential Variation of Flow Coefficient

As we have seen in the data, the volute introduces a circumferential variation in flow. In the rotor frame, this is an unsteady flow. We saw this variation in flow clearly in the inducer tip flow coefficient data. To estimate the amount of variation in mean flow around the circumference, one can integrate the equation

$$\left(\frac{2L}{R}\right)\frac{d\Phi}{d\Theta} = \widetilde{\Delta P}_{ss}(\Phi) - \widetilde{\Delta P}(\Theta) \qquad (4.11)$$

which is the momentum equation for 1-D unsteady flow in the impeller channels. L is the effective impeller channel length, R is the impeller tip radius, $\widetilde{\Delta P}_{ss}(\Phi)$ is the steady state impeller axisymmetric curve, and $\widetilde{\Delta P}(\Theta)$ is the measured circumferential value of total to static impeller Cp. The integration was done by Chue[7] using a Fourier collocation technique. A slightly modified version of the Chue code was provided for the present analysis by Chen[6]. The analysis assumes the flow is incompressible and that the compressor's instantaneous Cp deviates from its steady state value by an inertial lag term. The lag term represents the pressure forces needed to accelerate or decelerate the flow in the impeller channel when a flow distortion in the absolute frame is present.

To estimate the circumferential variation in Φ, the Chue code was used to integrate Eq. 4.11. The technique requires one to supply an axisymmetric curve of the rotor. Such a curve will uniquely determine an impeller channel Cp as a function of flow coefficient. The axisymmetric curve for the impeller was estimated using the circumferentially averaged static pressure data for forward flow and the Kulite transient data in backflow. The curve for 33K is shown in Fig. 4.30 and 48K in Fig. 4.31. The 33K and 48K Cp distortion profiles used are obtained from the measured head coefficient data shown in Fig. 4.9 and 4.10.

The results of the integration of Eq. 4.11 using Chue's code with a channel inductance of (2L/R) = 2.014 are shown in Fig 4.32 and 4.33. In Fig. 4.32, which shows 33K high flow throttle points, we see a high flow regime near the tongue at the throttle value of Φ = .5. This was also seen in the independent inducer tip data shown in Fig. 4.14. As Φ is lowered past the minimum distortion point, a depression

in $\bar{\Phi}$ is seen at the tongue in Fig. 4.33 as was seen in Fig 4.15. At a higher corrected flow of 48K, the depression in $\bar{\Phi}$ is seen to be more severe. This was also seen independently in the inducer data of Fig. 4.15.

The integration results show that the mean flow at the tongue while depressed is not reversed until the mean circumferentially averaged flow is very low to $\bar{\Phi} = .025$. The compressibility effects occuring in the compressor which are ignored in this model are most important when the compressor is in backflow. This was seen in the data of Chap. 3. It is not clear how the compressibility effects would alter the results of Fig. 4.32 and 4.33. It is also not clear how the non-quasisteady impeller behavior effects this result. The actual tongue flow coefficient may be reversed in the impeller at much higher throttle settings than predicted by the incompressible analysis.

4.10 Flow Distortion Corrected Vaneless Diffuser Cp Results

Using the circumferential flow distortion profiles calculated in Fig. 4.32 and 4.33, the circumferential diffuser $Cp(\Theta)$ was recalculated using a local value of impeller exit absolute Mach number. This circumferentially varying Mach number depends on the local values of flow coefficient and slip parameter. The slip parameter as a function of flow coefficient is obtained by the proceedure described in App. F. Then the definition of vaneless diffuser Cp is

$$C_p(\Theta) = \frac{\frac{P_3(\Theta)}{P_2(\Theta)} - 1}{\left\{1 + \frac{(K-1)}{2} M_2^2(\Theta)\right\}^{\frac{K}{K-1}} - 1} \qquad (4.12)$$

The distortion corrected values of Cp at 33K are compared with the uncorrected results in Fig. 4.34 for high flows and in Fig. 4.35 for low flows. At high flows, the correction is most significant in the last quadrant of the circumference from 270° to 360°. This is so because the flow coefficient as seen in Fig. 4.32 is much larger than the mean and hence the calculated impeller exit Mach number will also be larger than the mean value. In the other quadrants, the correction is much smaller. In the data at the lower flows shown in Fig. 4.35, the corrected and uncorrected data are not significantly different except at flow coefficients below $\phi = .1$. At

these low flow coefficients, the slip factor as a function of ϕ starts dropping to zero due to shroud friction. This effect then reduces the value of impeller exit Mach number from the mean value and results in an upward correction in the Cp calculated.

The circumferential average of distortion corrected vaneless diffuser Cp values is compared with the uncorrected values in Fig. 4.36. There is some qualitative difference between the two sets of data. In the corrected data in the flow coefficient region $.125 < \phi < .5$, the vaneless diffuser Cp is seen to be quite flat with a drop of only 12% from Cp = .8 @ ϕ = .5 to Cp =.7 @ ϕ = .125. There is very little stalling of the diffuser in the large B surge initiation area around ϕ = .2. Below ϕ = .125, the Cp drops rapidly to lower values of Cp = .45 which is indicative of diffuser stalling. This stalling occurs in the flow regime where the tips of the impeller inducer blades are already severely stalled. The stalling behavior could be a result of an adverse upstream effect the severely stalled inducer blades have on the vaneless diffuser Cp. Or it is simply due to the very high swirl angle in the diffuser which leads to higher diffuser losses.

4.11 Summary

The main points brought out in the data of this chapter are the following:

- Small B surge line occurs near shutoff far to the left of the large B surge line. Small B enhances overall system stability.
- Time averaged characteristics in the unstable range are steeper than the instantaneous ones. This is possibly due to a characteristic time lag associated with inducer stall formation.
- Impeller stall occurs at the inducer tips and is most severe at the circumferential position nearest the volute tongue.
- The vaneless diffuser overall circumferentially averaged Cp drops as flow coefficient and inverse swirl parameter are reduced and is destabilizing to the overall stage.
- Volute match points are speed dependent due to compressibility effects
- Overall stage isentropic head peaks correlate roughly with volute match points.
- Operation below minimum distortion point accompanied by large inefficiencies.
- Depressed flow velocity region exists in the impeller and diffuser at the tongue

circumferential location when throttled past volute match point.

- Impeller and vaneless diffuser performance are also most depressed near the tongue circumferential position.
- The circumferential asymmetry in flow induced by the volute grows more severe with increasing speed and with increasing deviation from the volute match point. The deviation from the match condition is encompassed in the parameter V.
- A good surge prediction model requires predicting how the axisymmetric compressor characteristic(impeller and diffuser) is modified by the presence of a downstream volute.
- Incompressible flow integration predicts depressed flow at tongue but not reversed flow.
- Rotating stall in the compressor tested was much weaker than the 1/rev non-rotating volute induced stall.
- The susceptability of a centrifugal compressor to volute induced flow distortion is dependent on the parameter (2L/R). Higher values produce a more distortion resistant device.

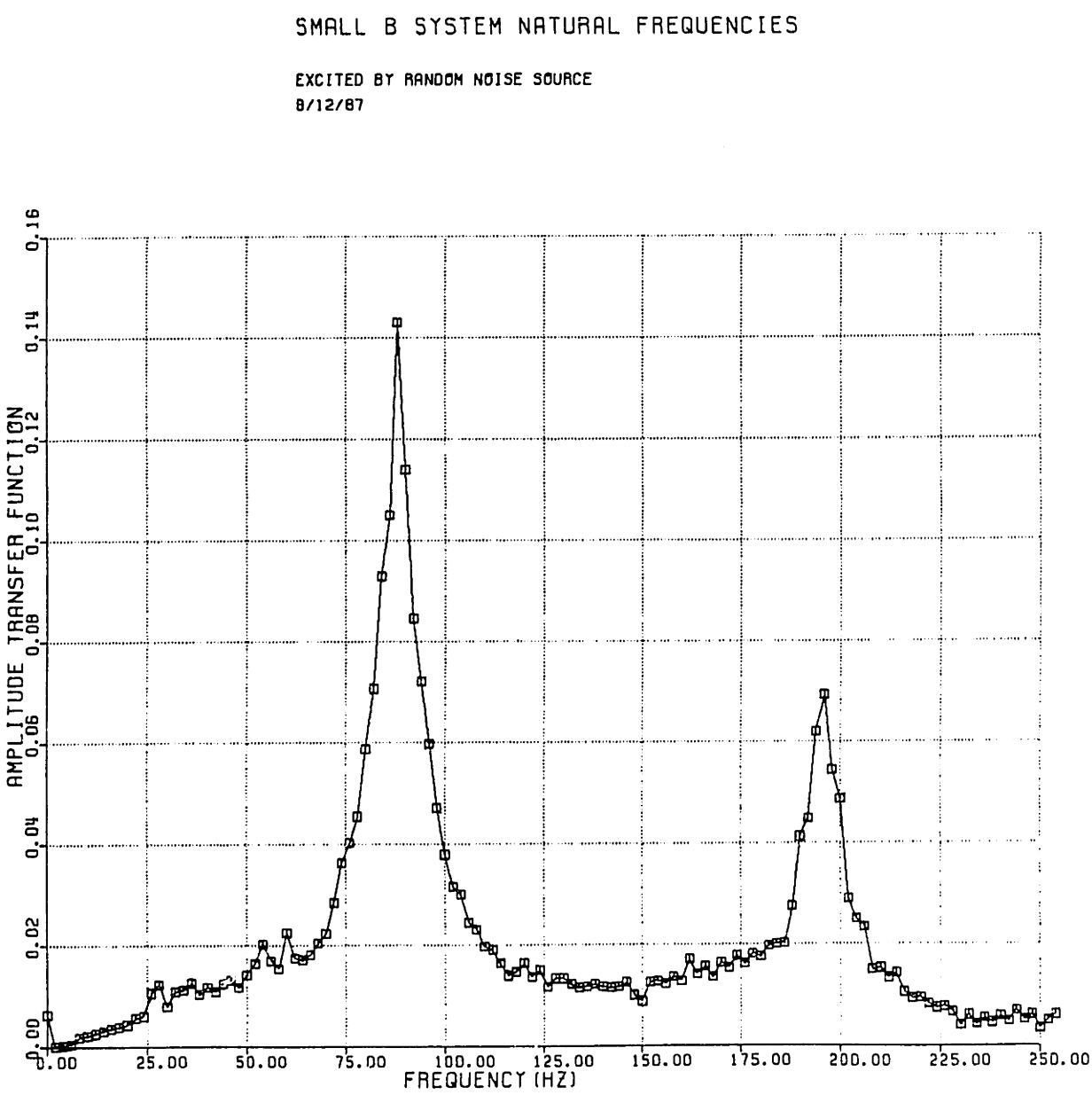

Fig. 4.1 Small B System Natural Frequency Measurement Results

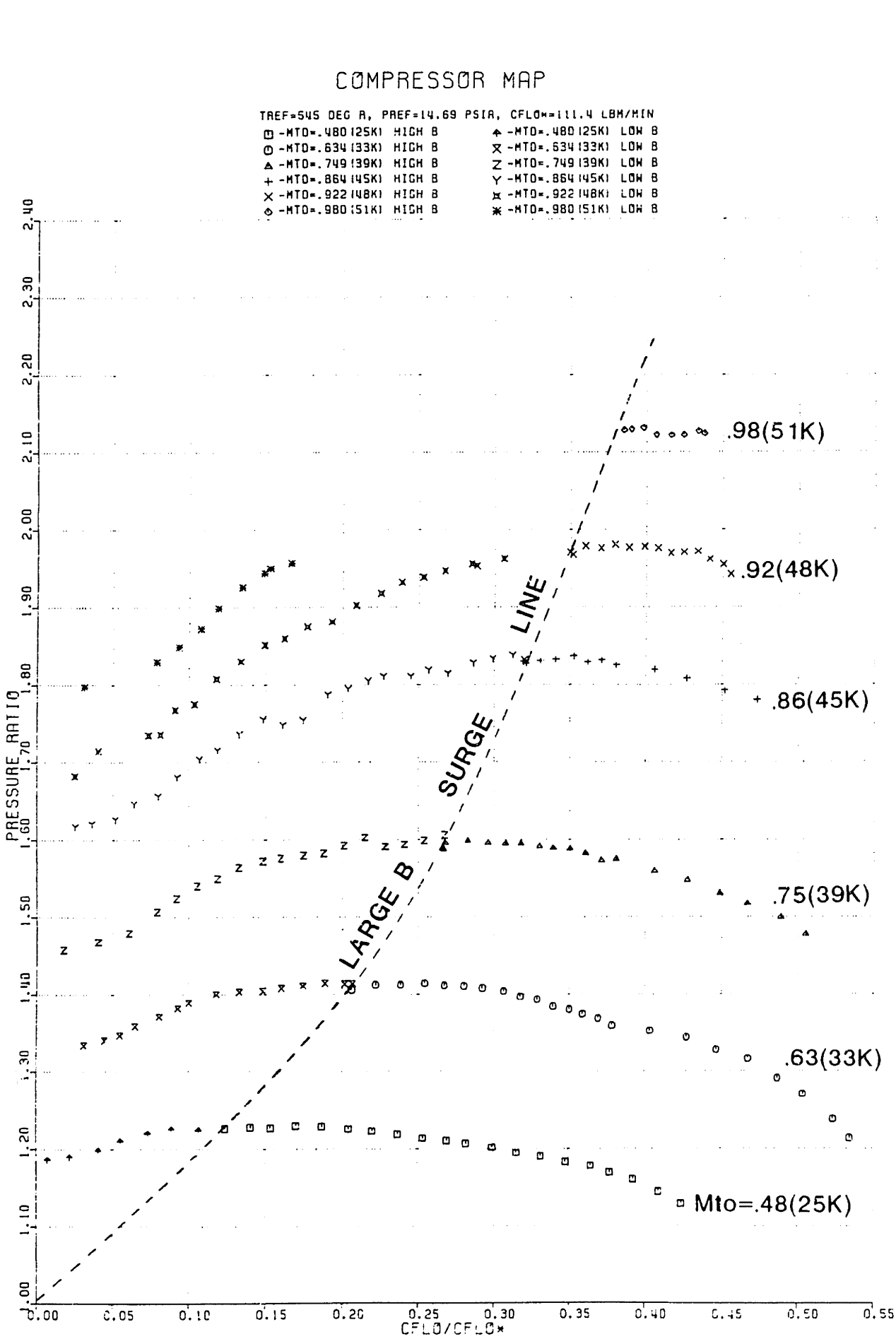

Fig. 4.2 Compressor Map

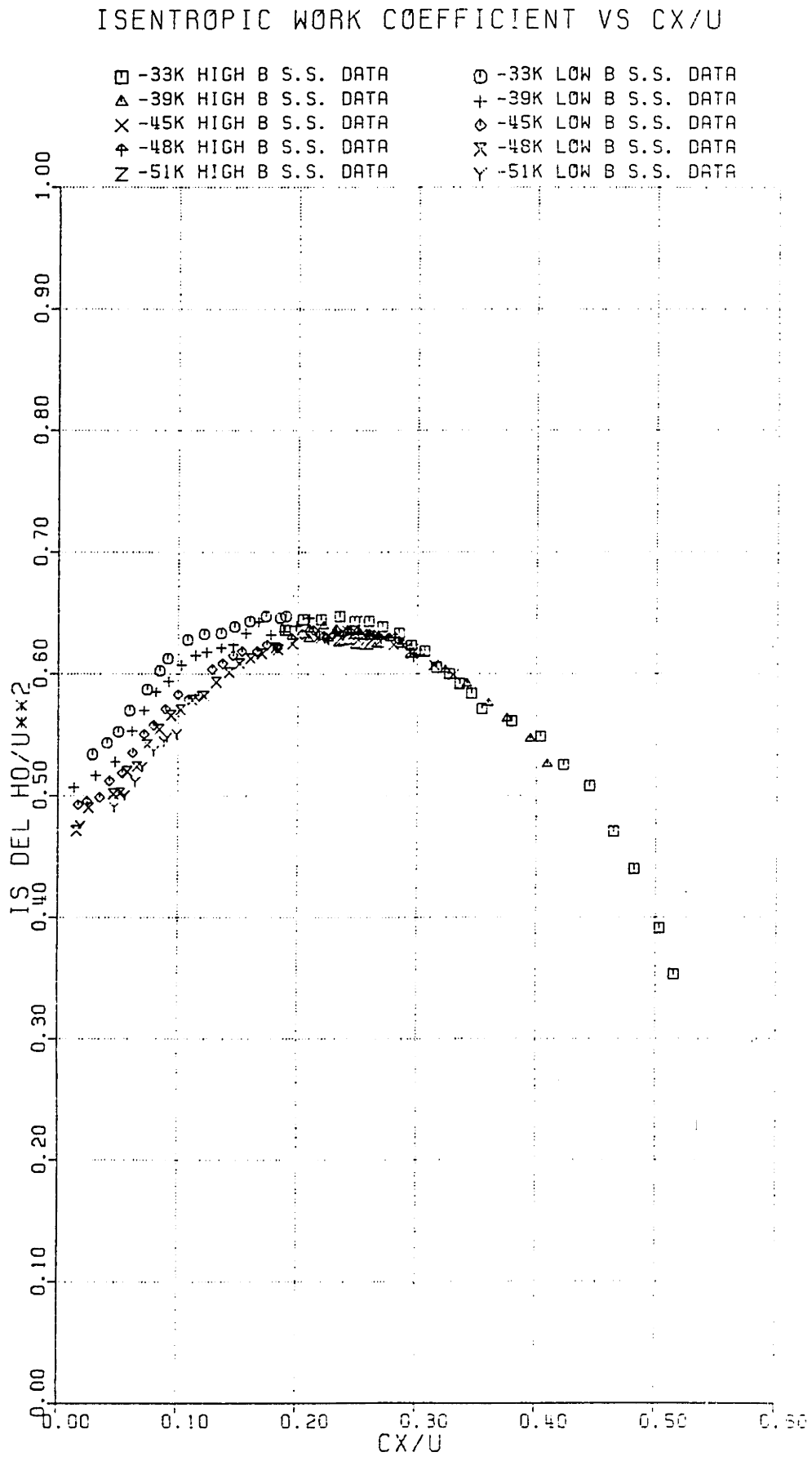

Fig. 4.3 Compressor Head Coefficient vs Cx/U

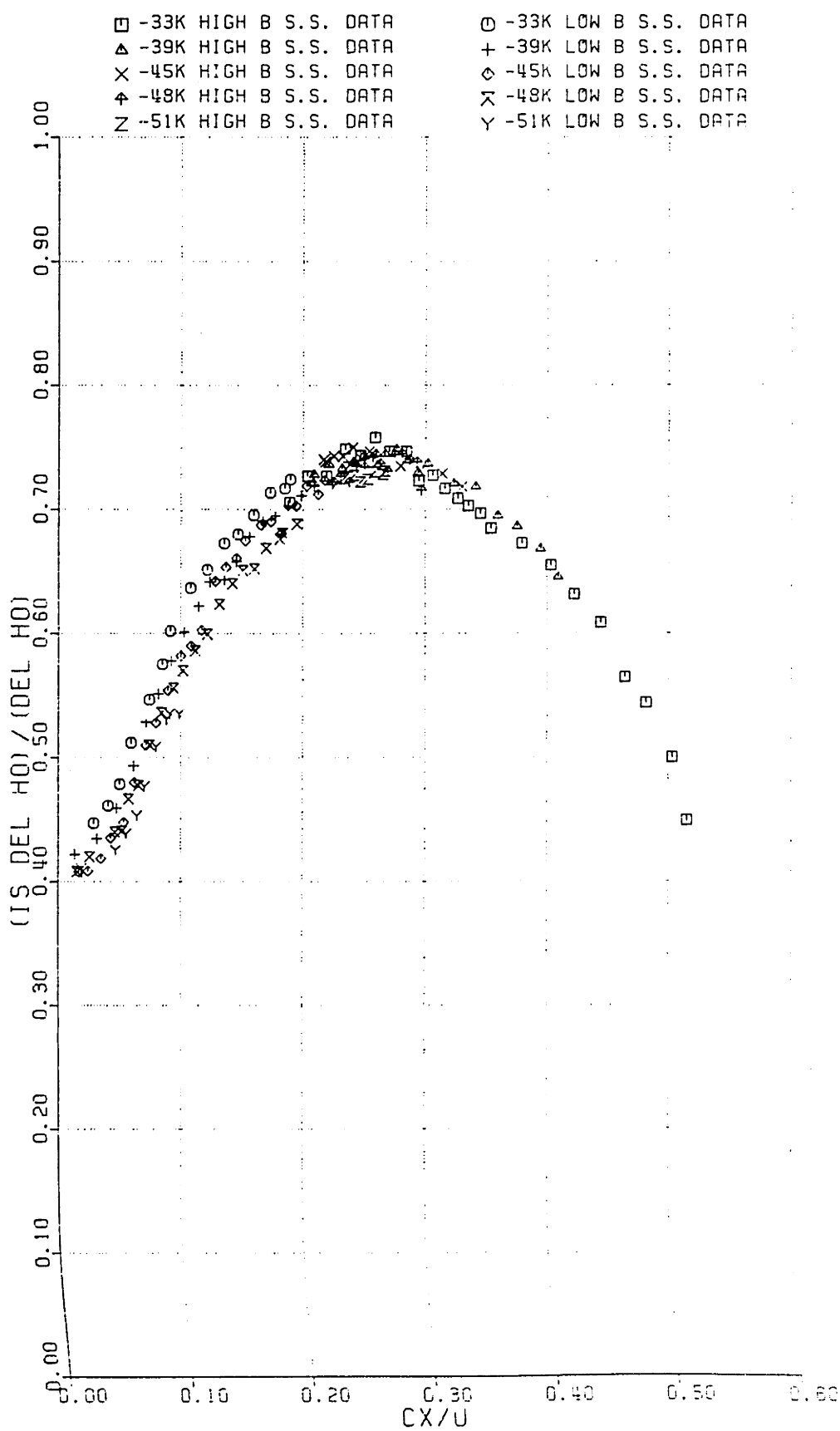

Fig. 4.4 Compressor Efficiency vs Cx/U

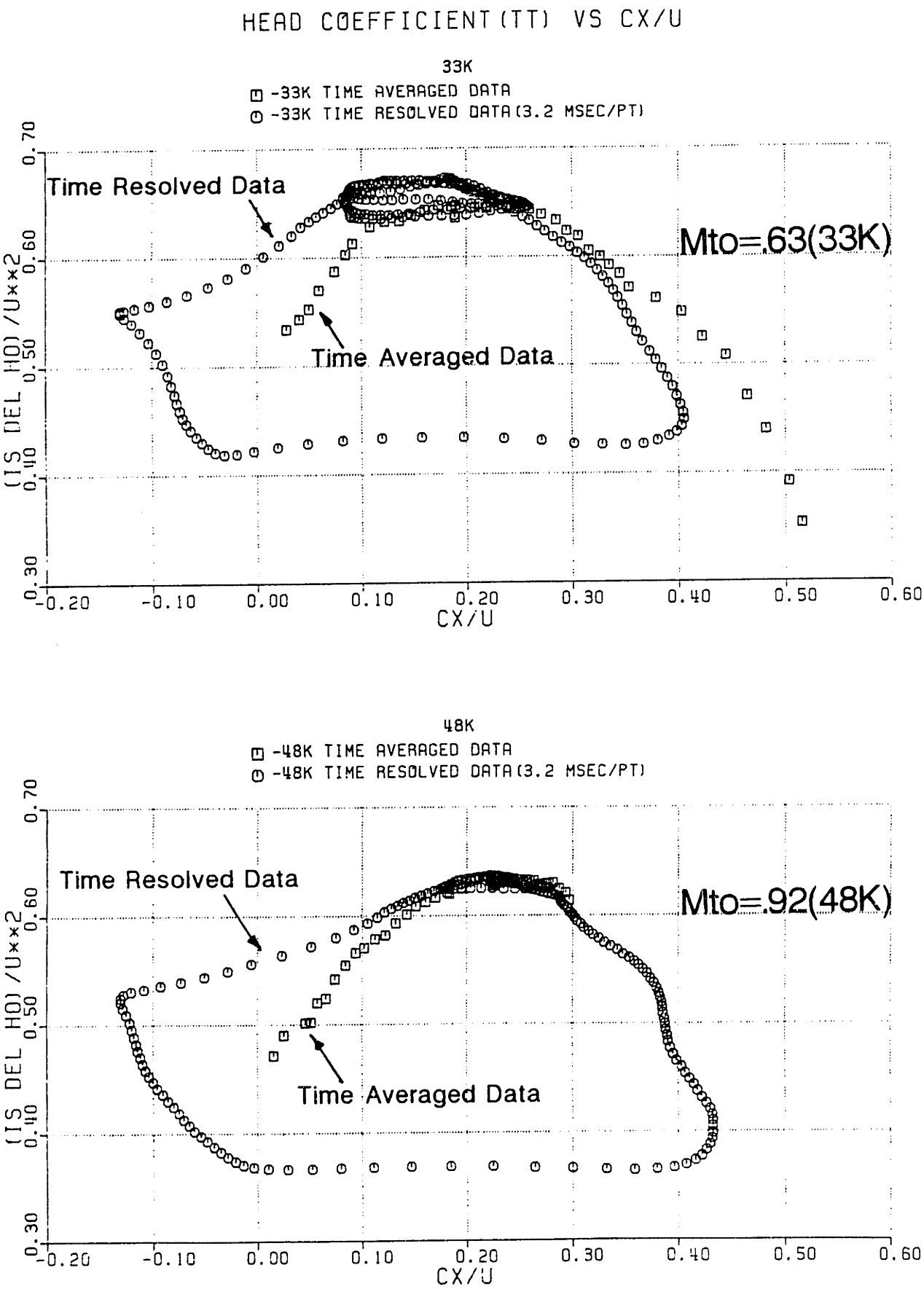

Fig. 4.5 Small B Time Averaged vs Large B Time Resolved Characteristic Data

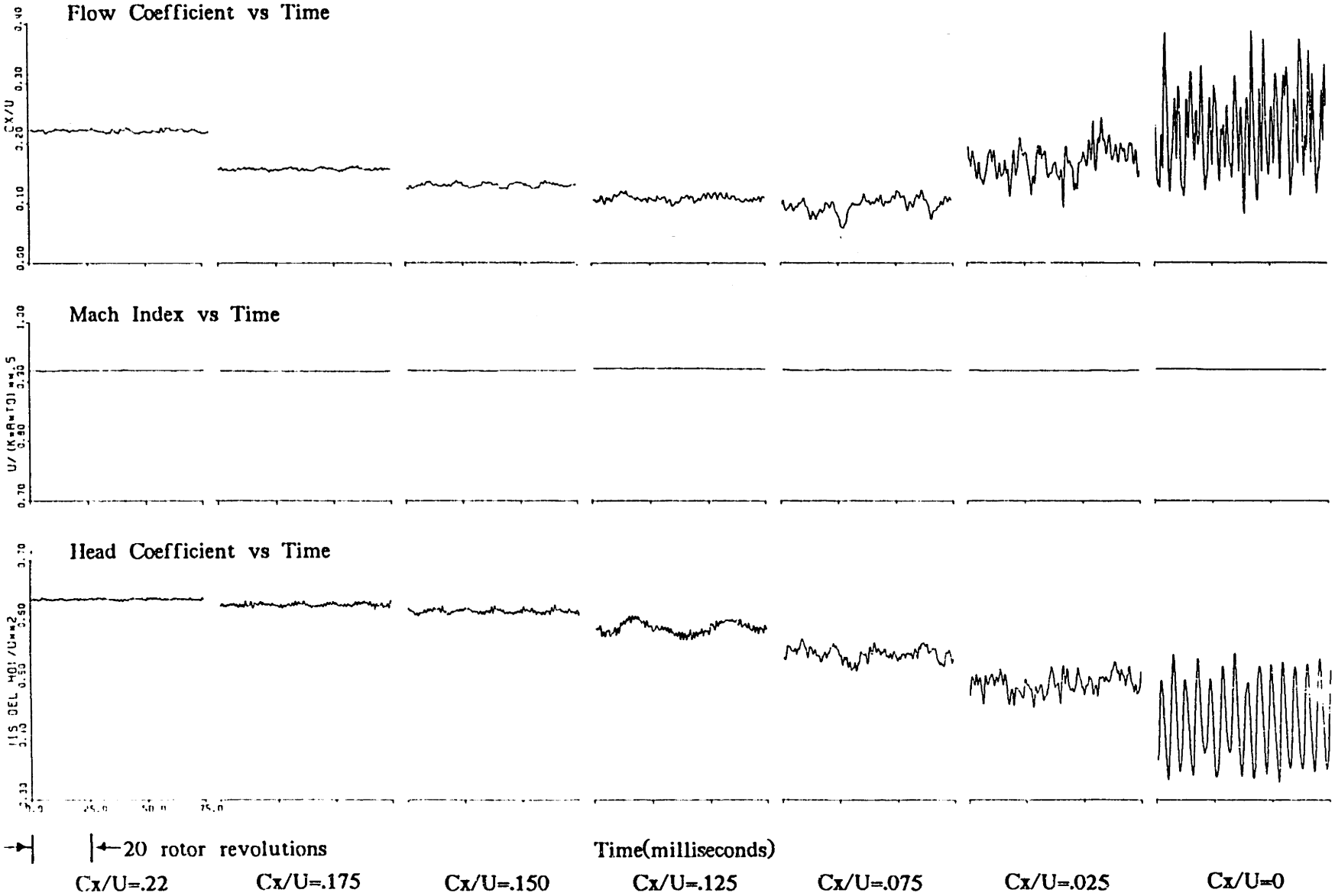

Fig. 4.6 Small B System Parameters vs Time at Various Throttle Settings(Mto ≃ .92)

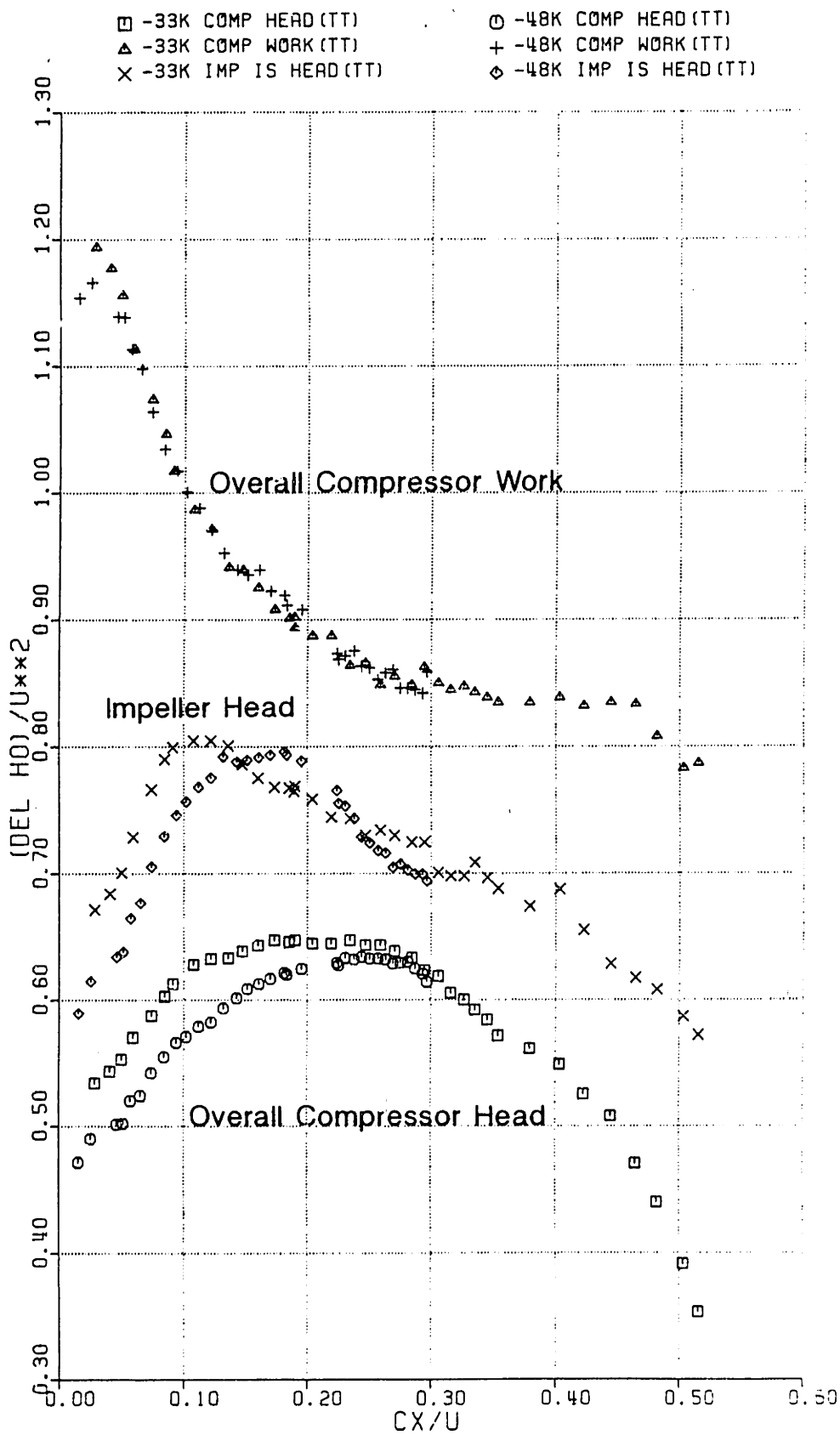

Fig. 4.7 Small B Head Coefficients vs Cx/U

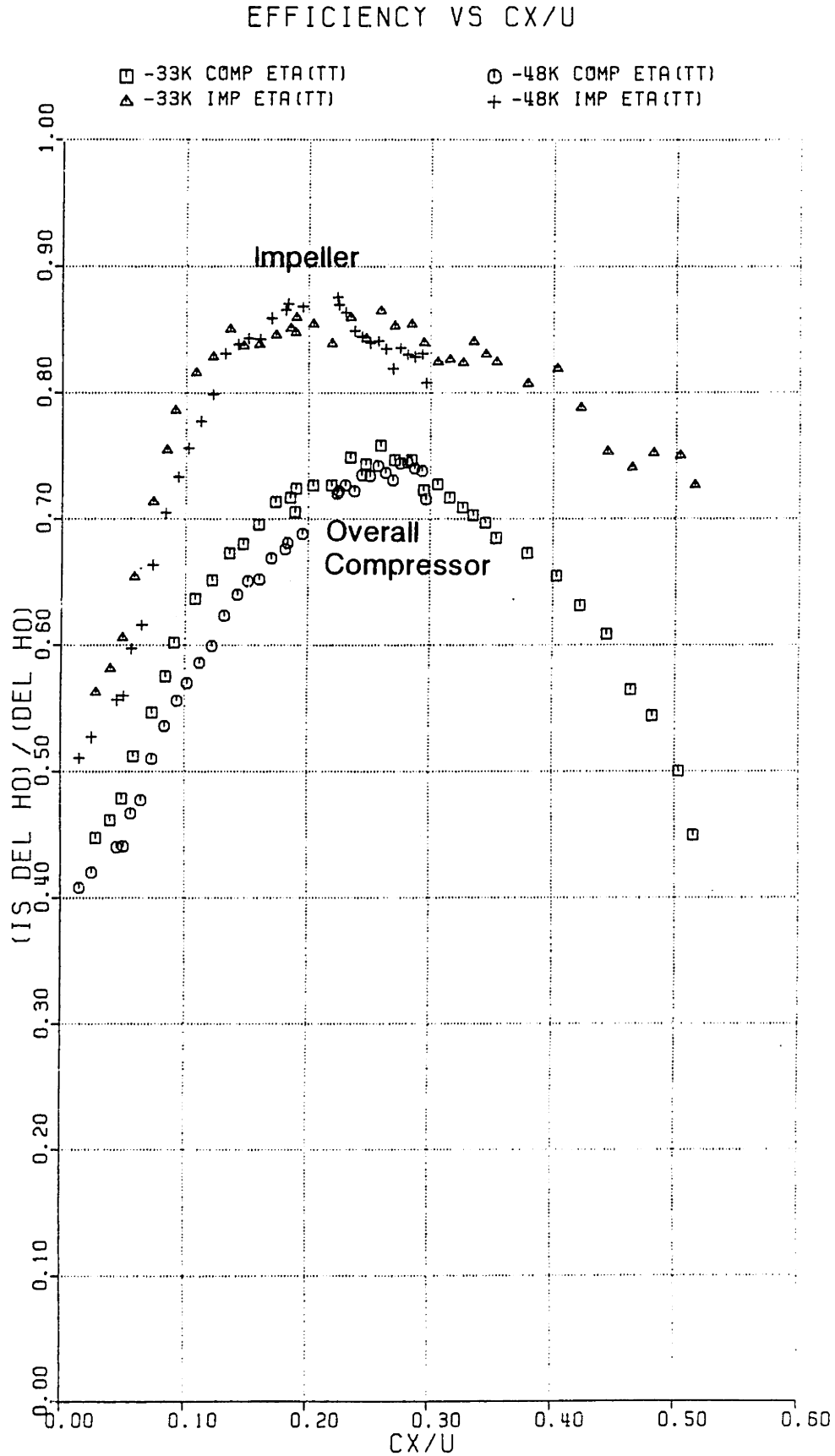

Fig. 4.8 Impeller and Overall Compressor Efficiency vs Cx/U

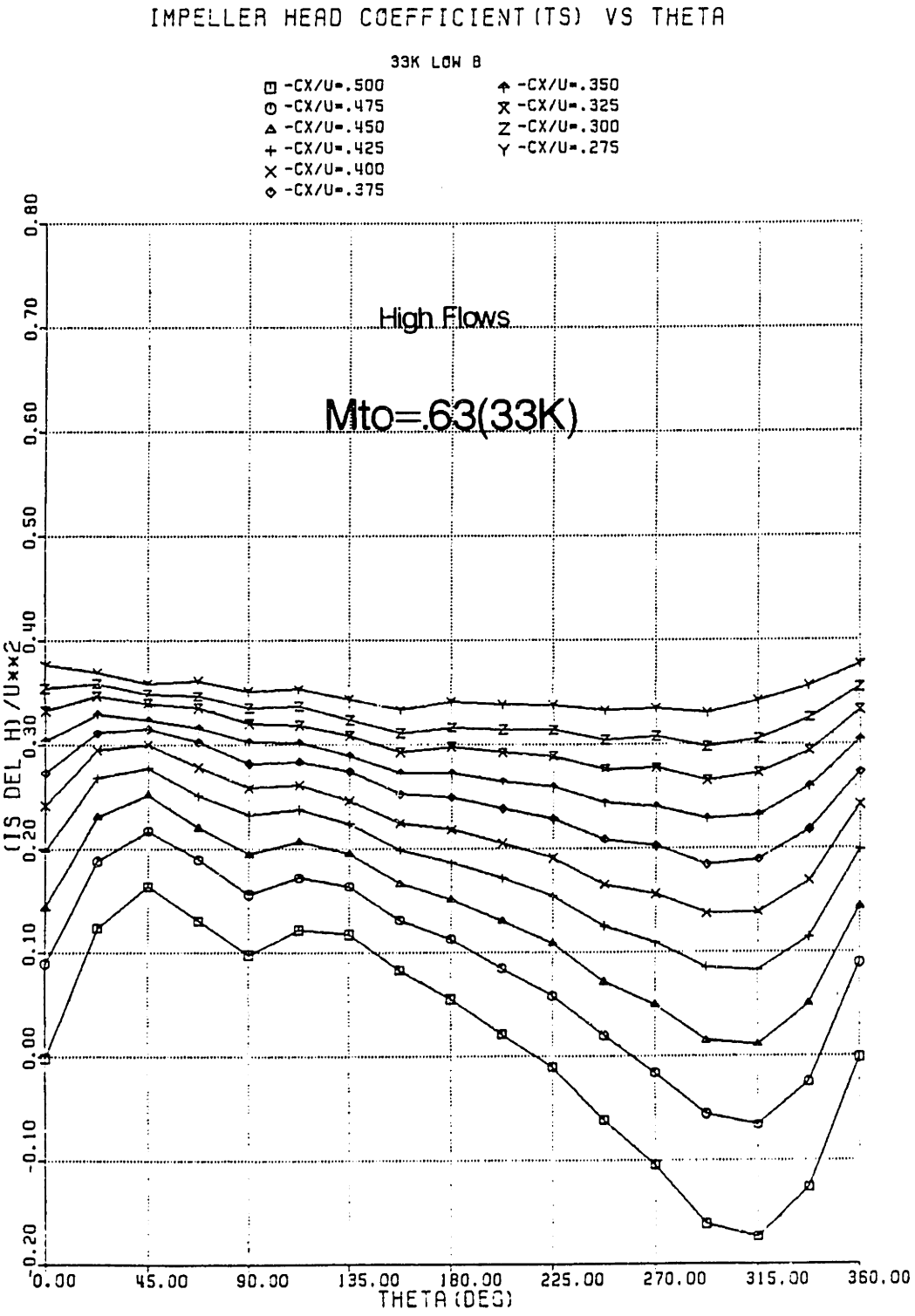

Fig. 4.9 Impeller Head Coefficient vs Theta at High Mean Cx/U(Mto ≃ .63)

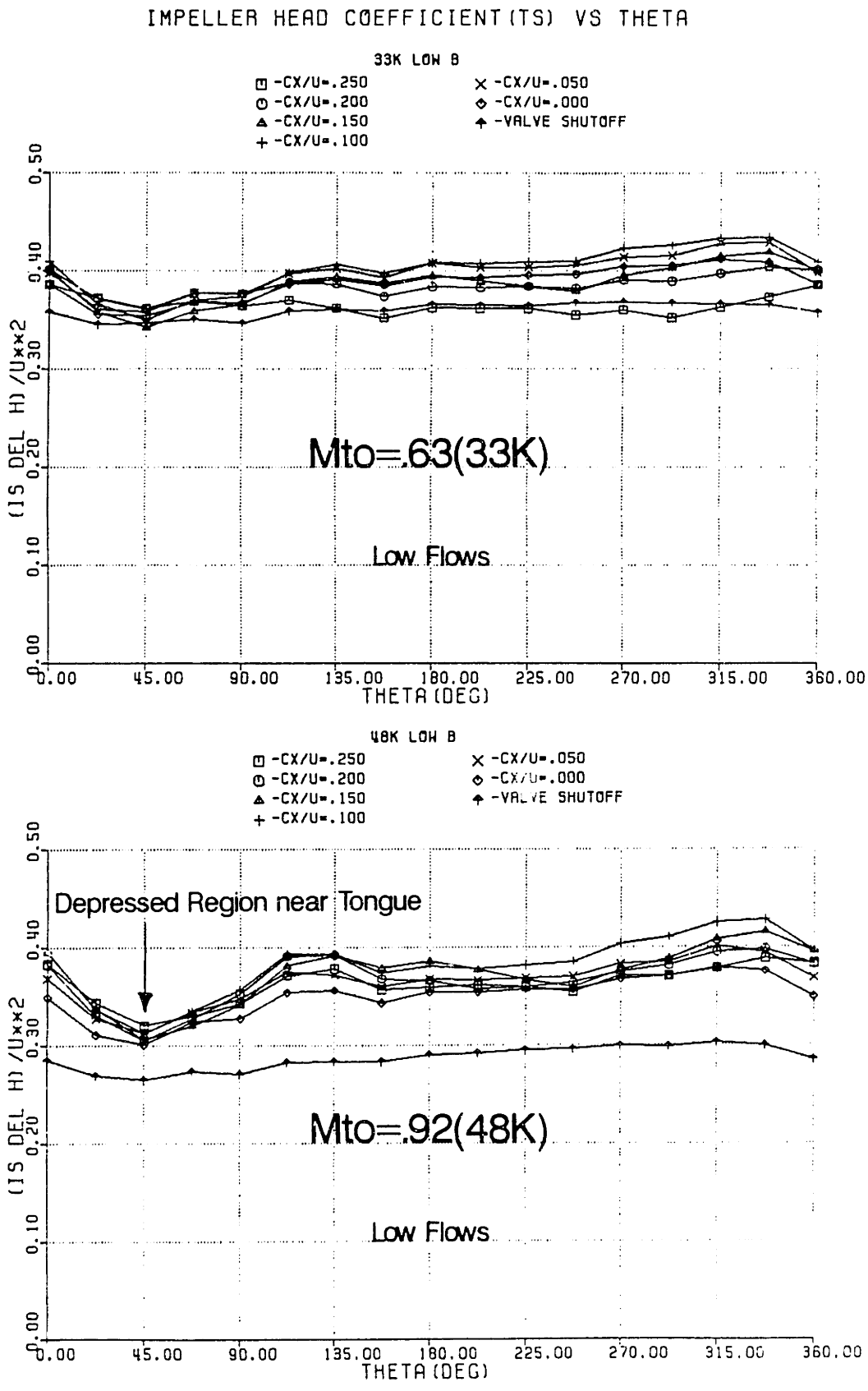

Fig. 4.10 Impeller Head Coefficient vs Theta at Low Mean Cx/U

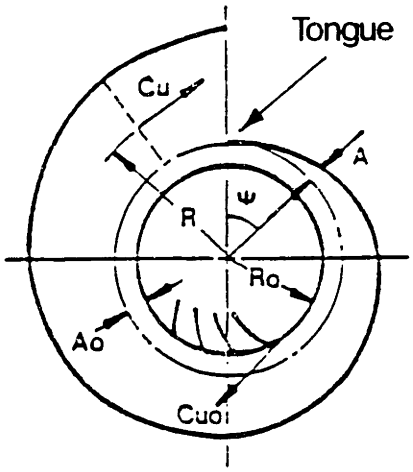

Volute geometry and velocity notation

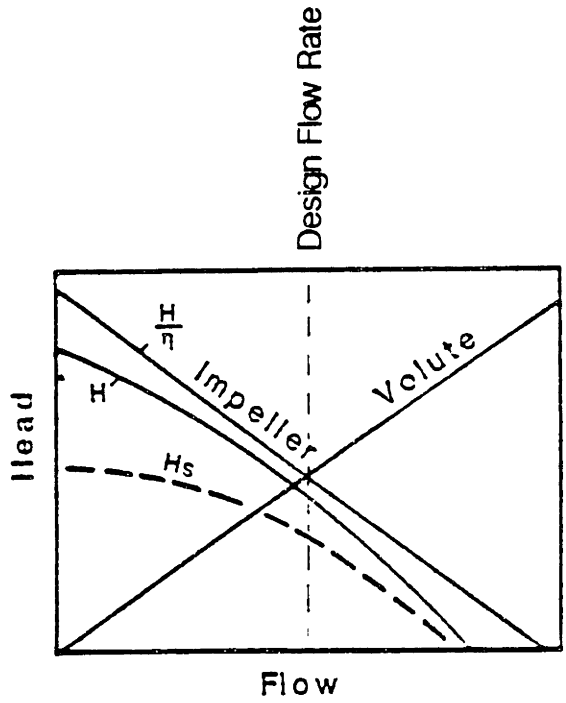

Volute - Impeller Matching

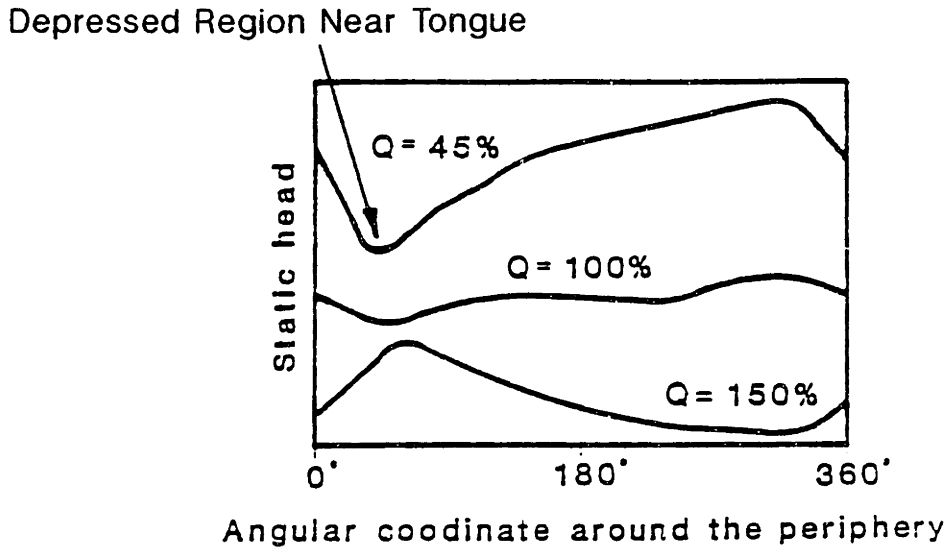

Typical experimental observation of static head variations around impeller periphery

Fig. 4.11 Volute Induced Head Distortion, from [44]

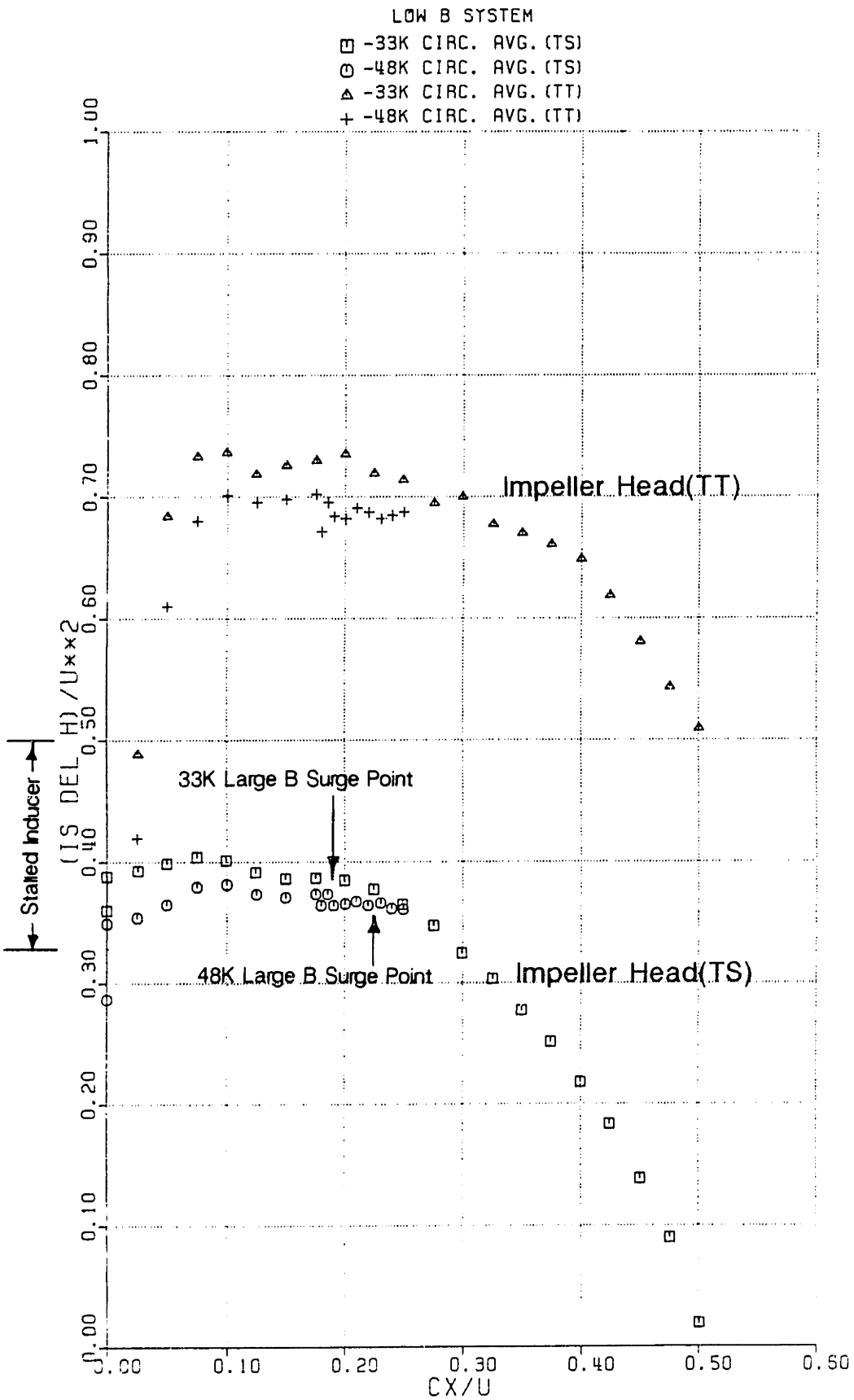

Fig. 4.12 Impeller Head Coefficients vs Cx/U

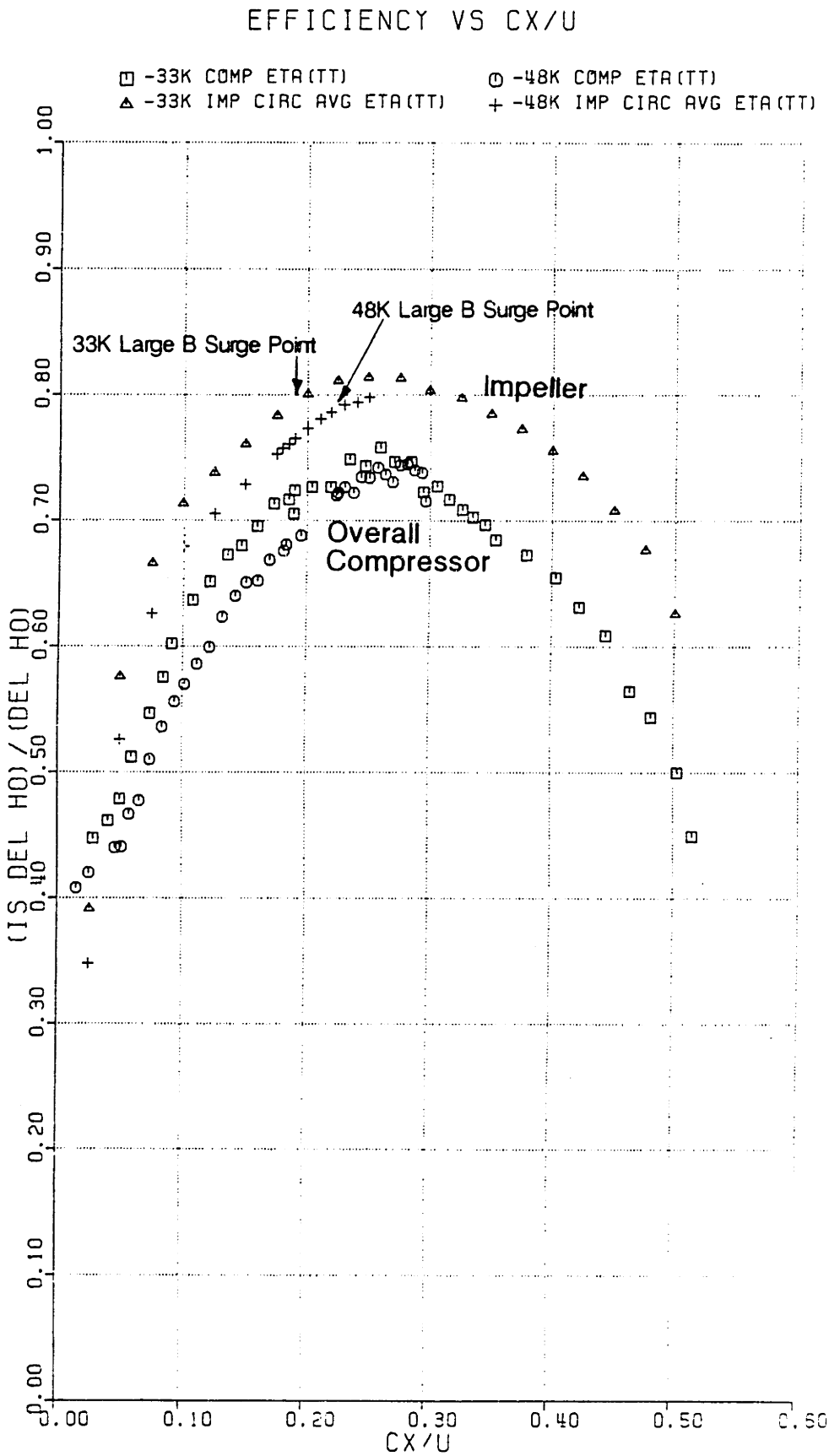

Fig. 4.13 Circumferentially Averaged Impeller and Overall Compressor Efficiency vs Cx/U

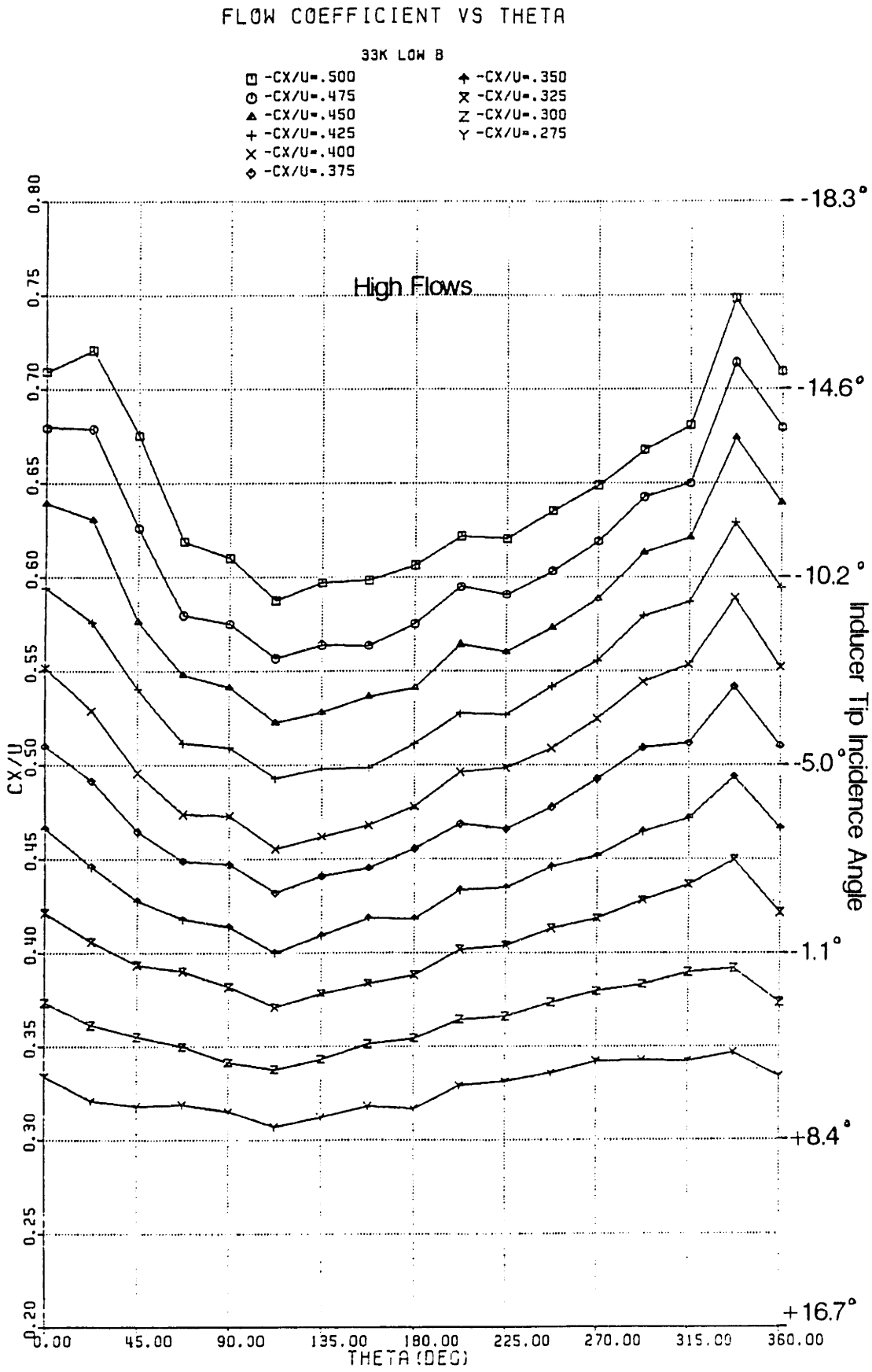

Fig. 4.14 Estimated Circumferential Variation in Inducer Flow Coefficient at High Mean Flow Coefficients(Mto ≃ .63)

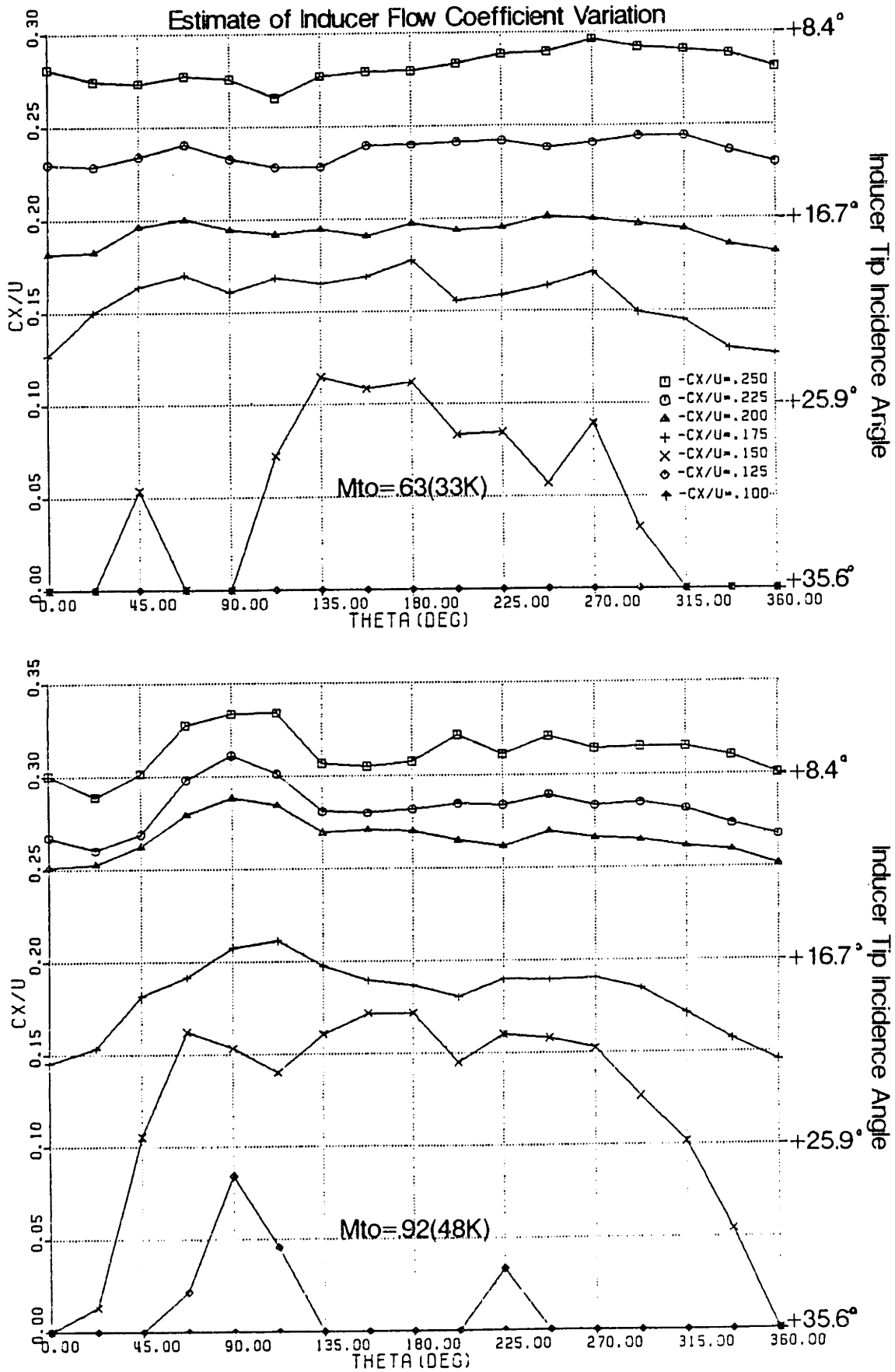

Fig. 4.15 Estimated Circumferential Variation in Inducer Flow Coefficient at Low Mean Flow Coefficients

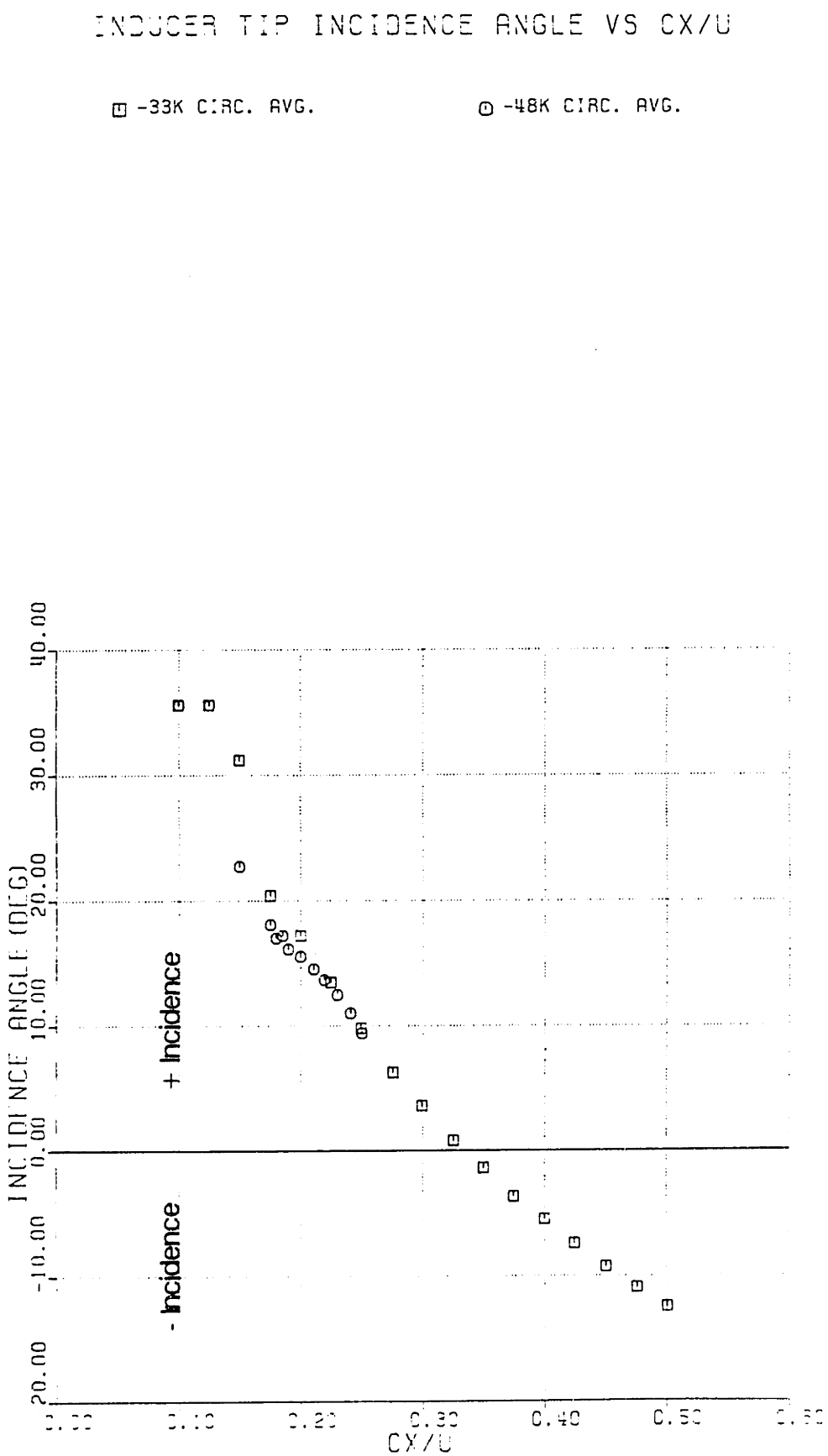

Fig. 4.16 Estimated Inducer Tip Incidence Angle vs Cx/U

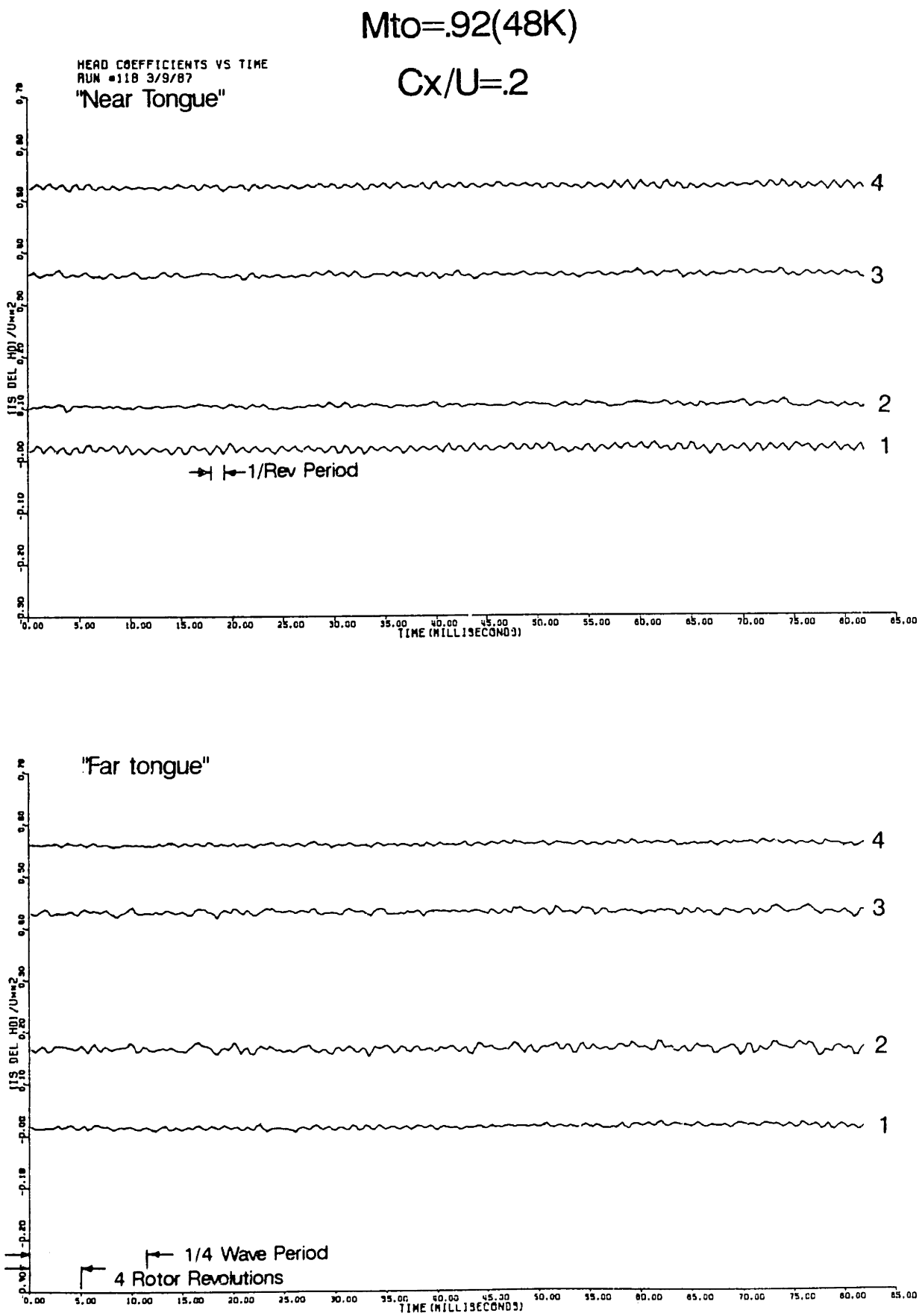

Fig. 4.17 Compressor Head Coefficients vs Time(Mto $\simeq$ .92, $\phi_T \simeq$ .20)

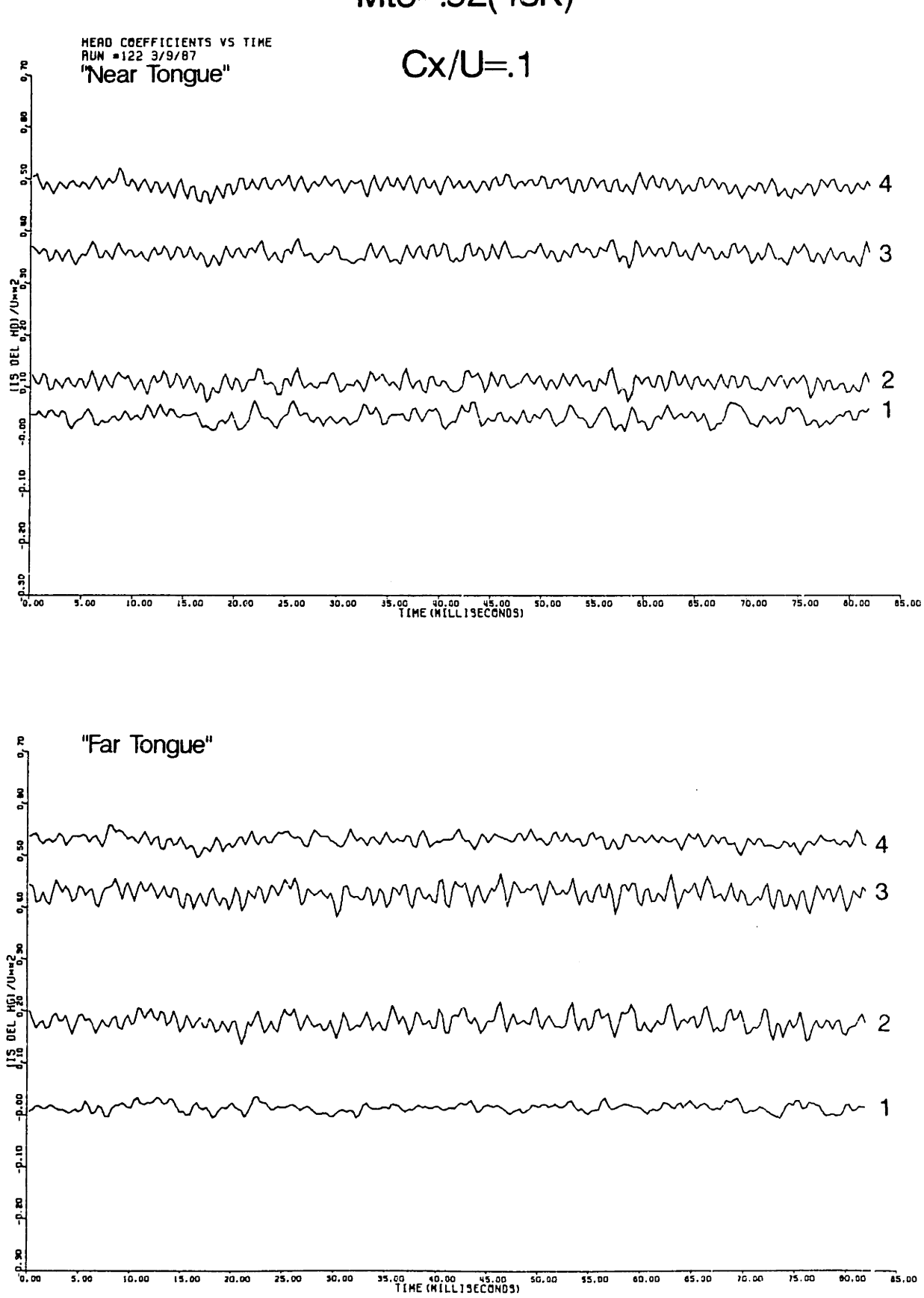

Fig. 4.18 Compressor Head Coefficients vs Time(Mto $\simeq$ .92, $\phi_T \simeq$ .10)

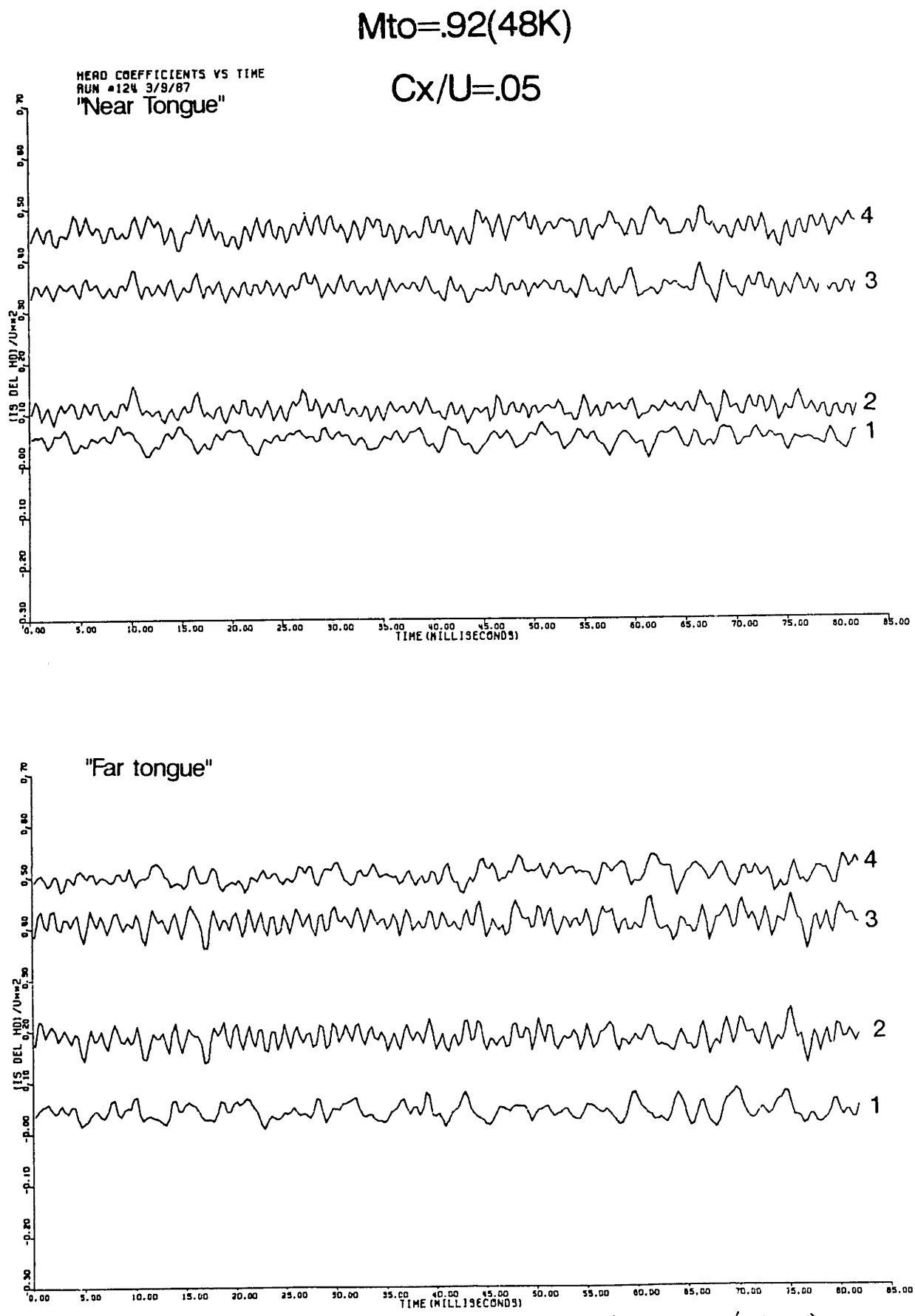

Fig. 4.19 Compressor Head Coefficients vs Time(Mto ≃ .92, ϕ_T ≃ .05)

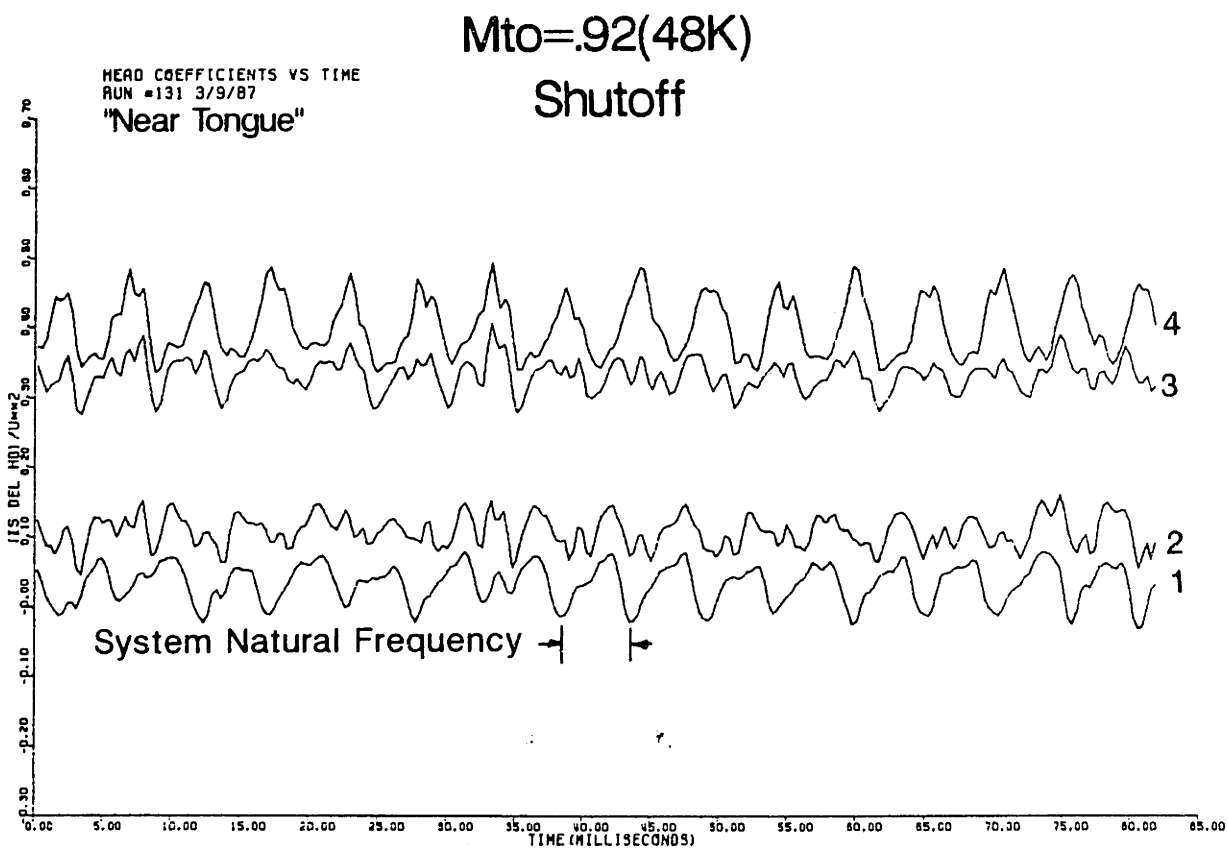

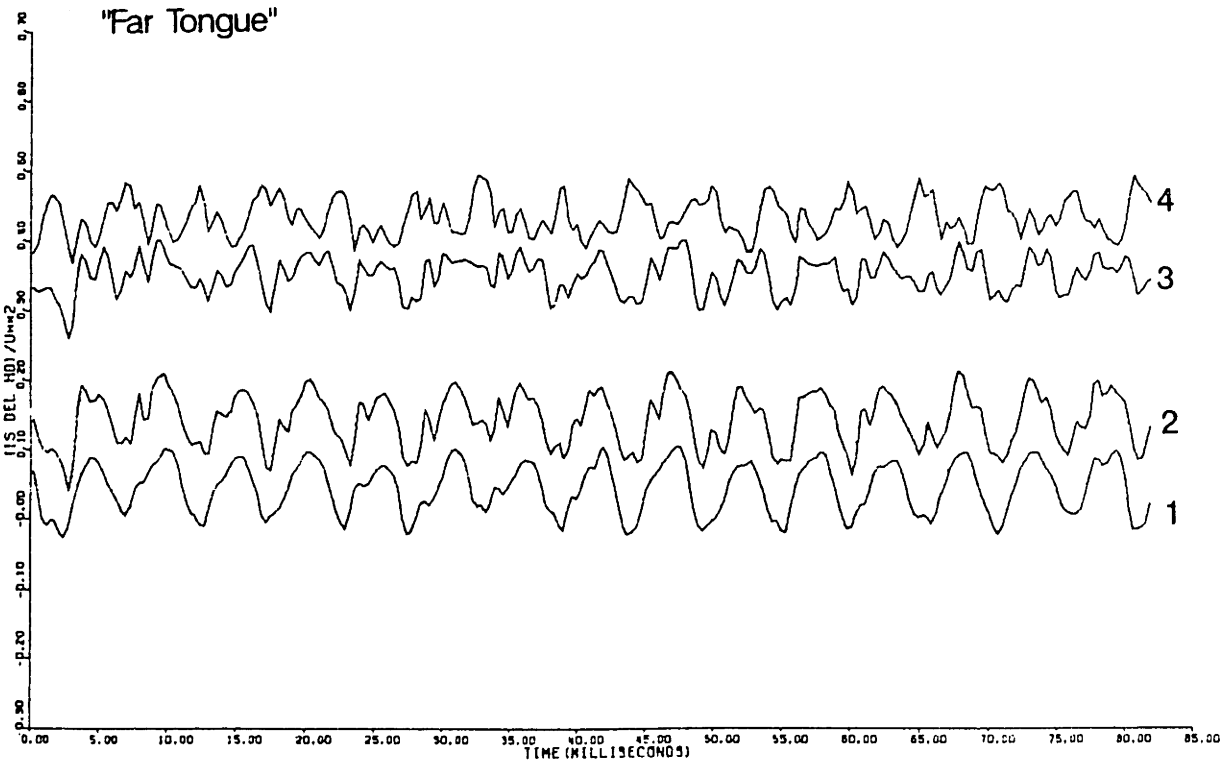

Fig. 4.20 Compressor Head Coefficients vs Time(Mto ≃ .92, Shutoff)

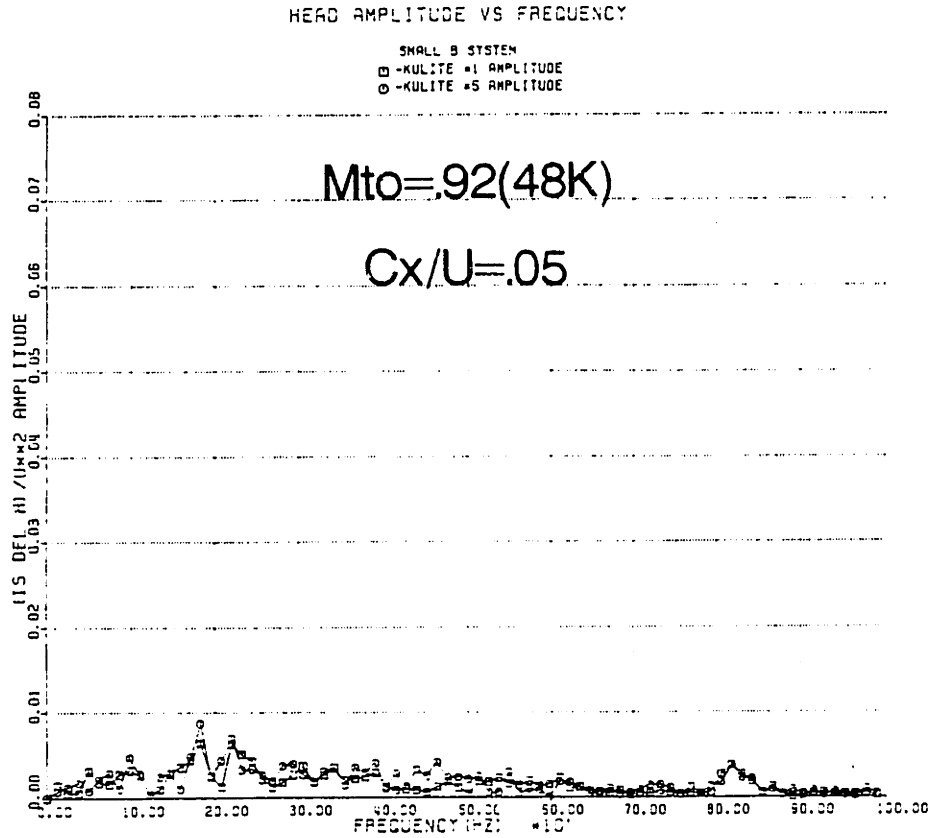

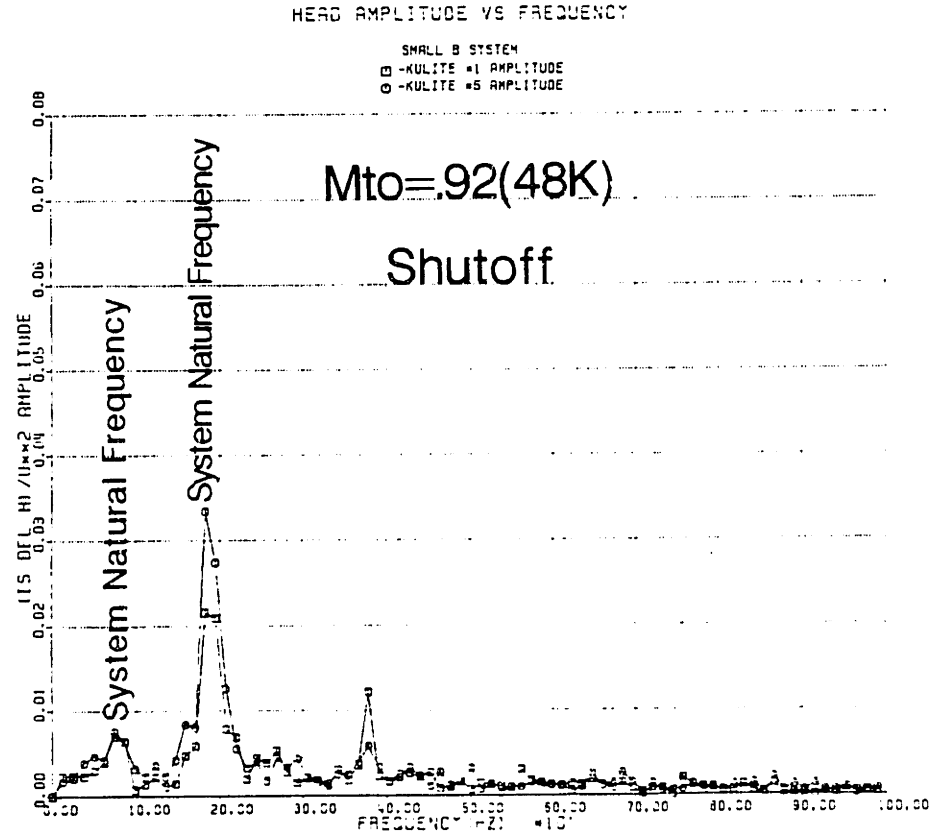

Fig. 4.21 Inducer Kulite FFT Results at Low Mean Flow Coefficients(Mto ≃ .92)

INDUCER STATIC PRESSURE DATA FFT

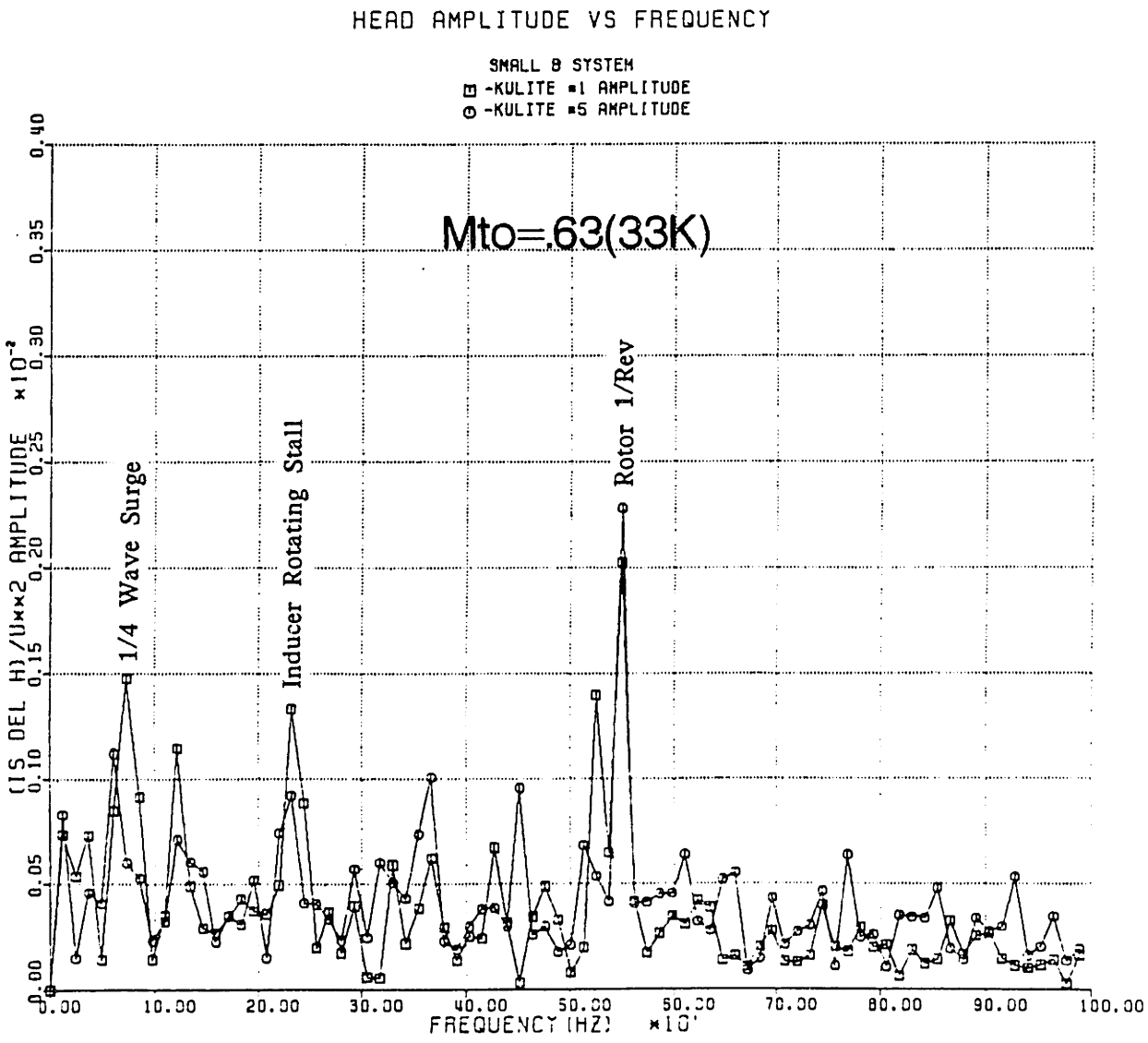

Fig. 4.22 Inducer Kulite FFT Results at Throttle Point of Maximum Stall Cell Pressure Amplitude(Mto ≃ .63)

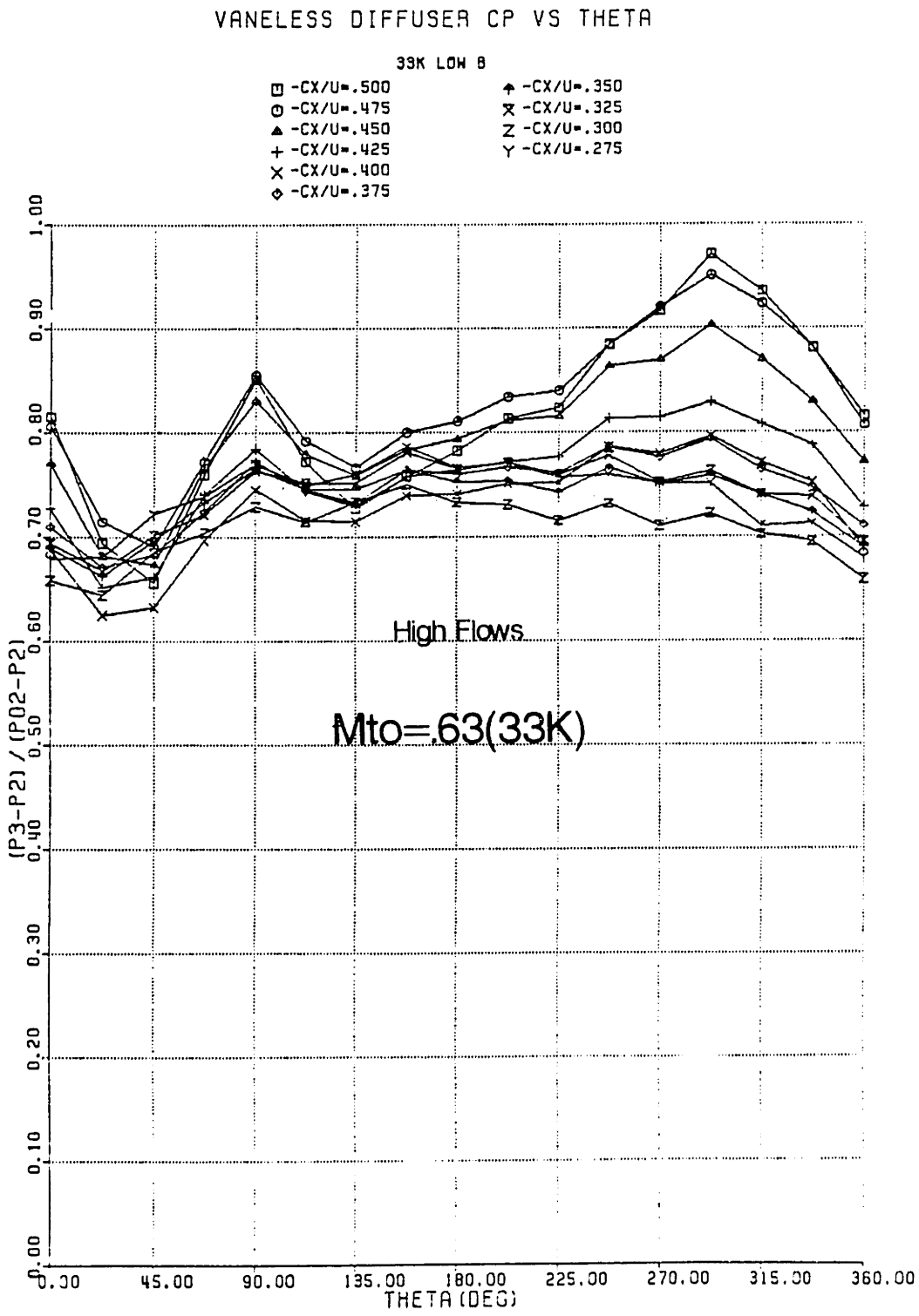

Fig. 4.23 Circumferential Variation in Vaneless Diffuser Cp(Mto $\simeq$ .63)

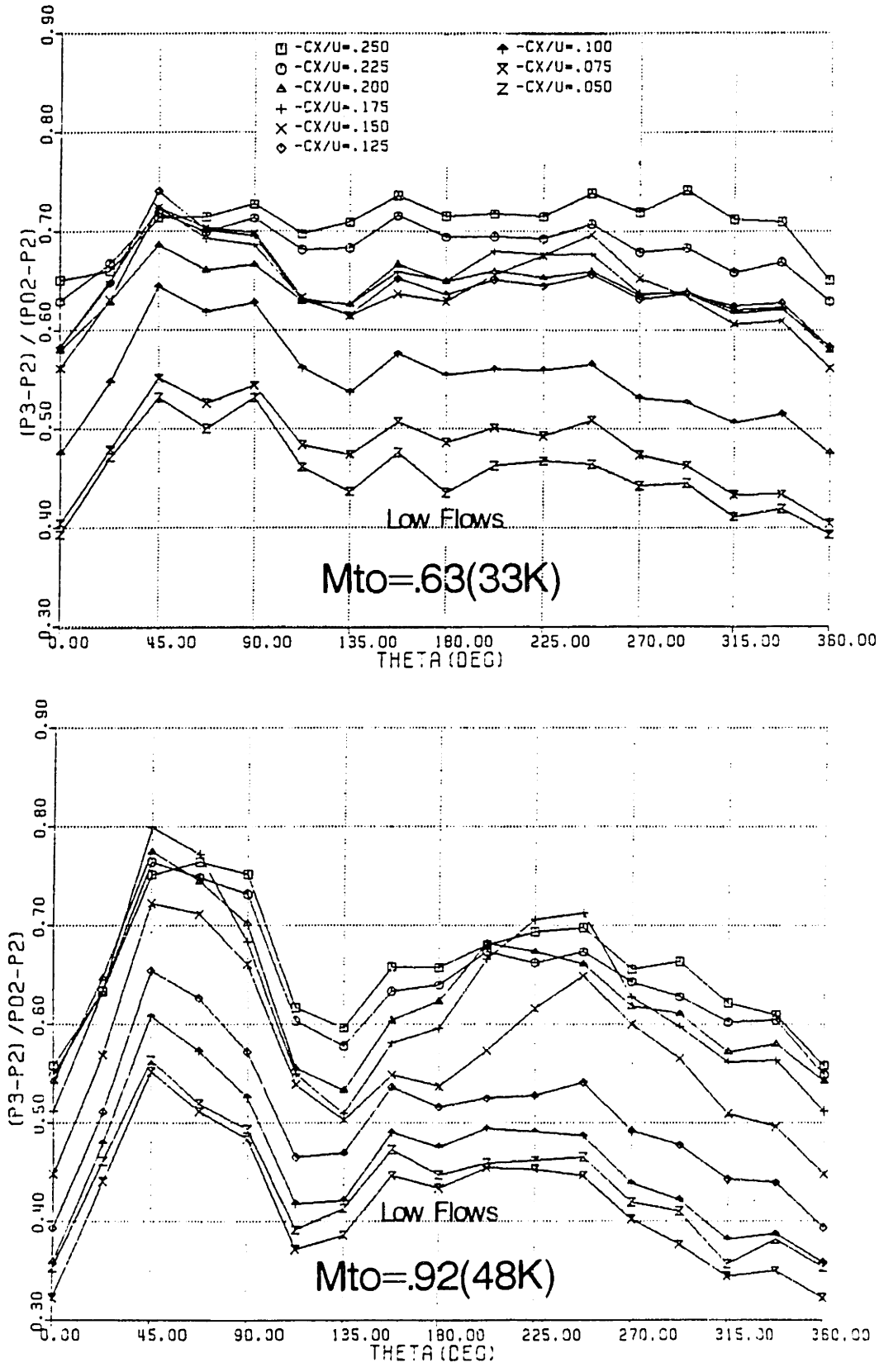

Fig. 4.24 Circumferential Variations in Vaneless Diffuser Cp

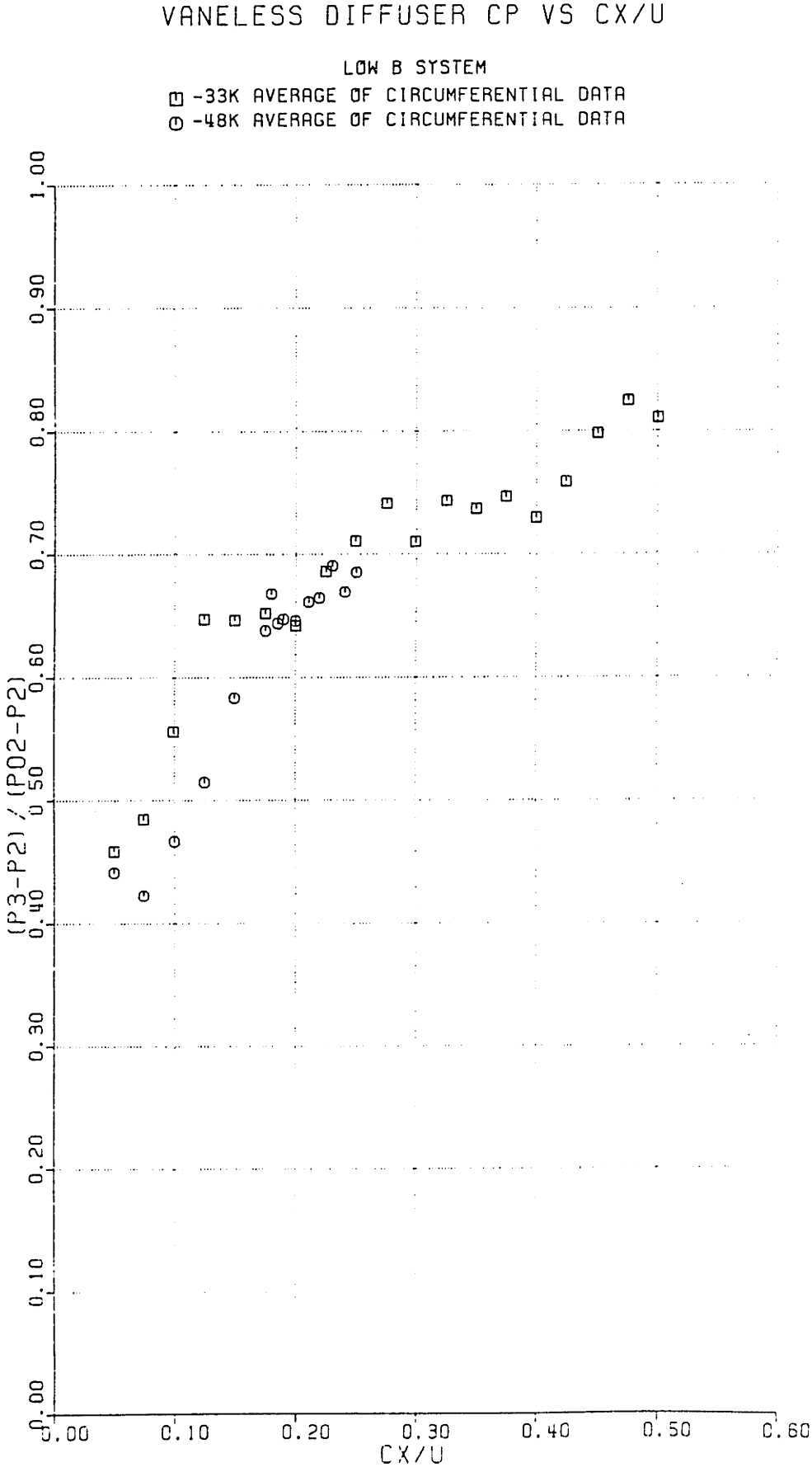

Fig. 4.25 Circumferentially Averaged Vaneless Diffuser Cp vs Cx/U

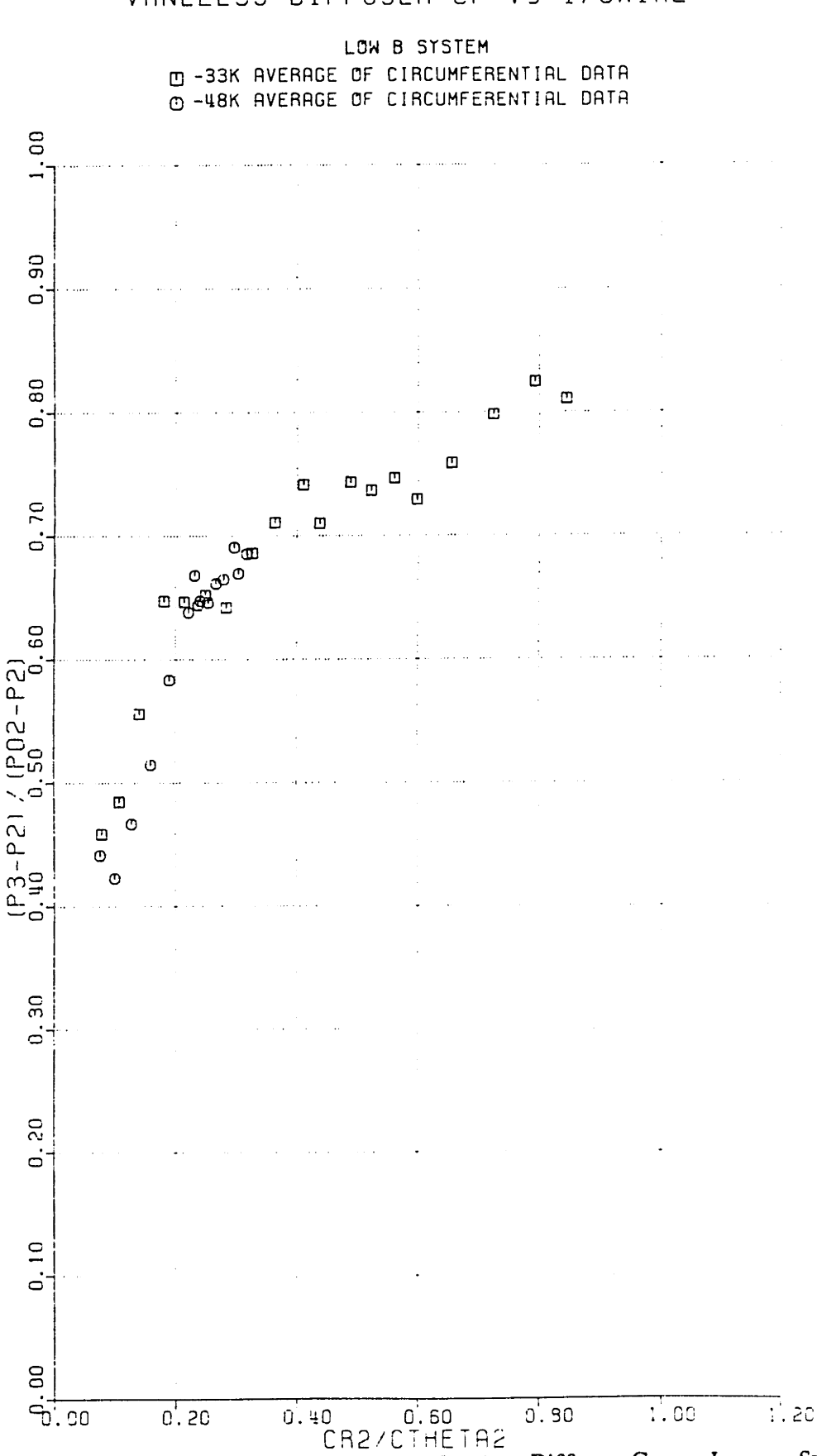

Fig. 4.26 Circumferentially Averaged Vaneless Diffuser Cp vs Inverse Swirl Parameter

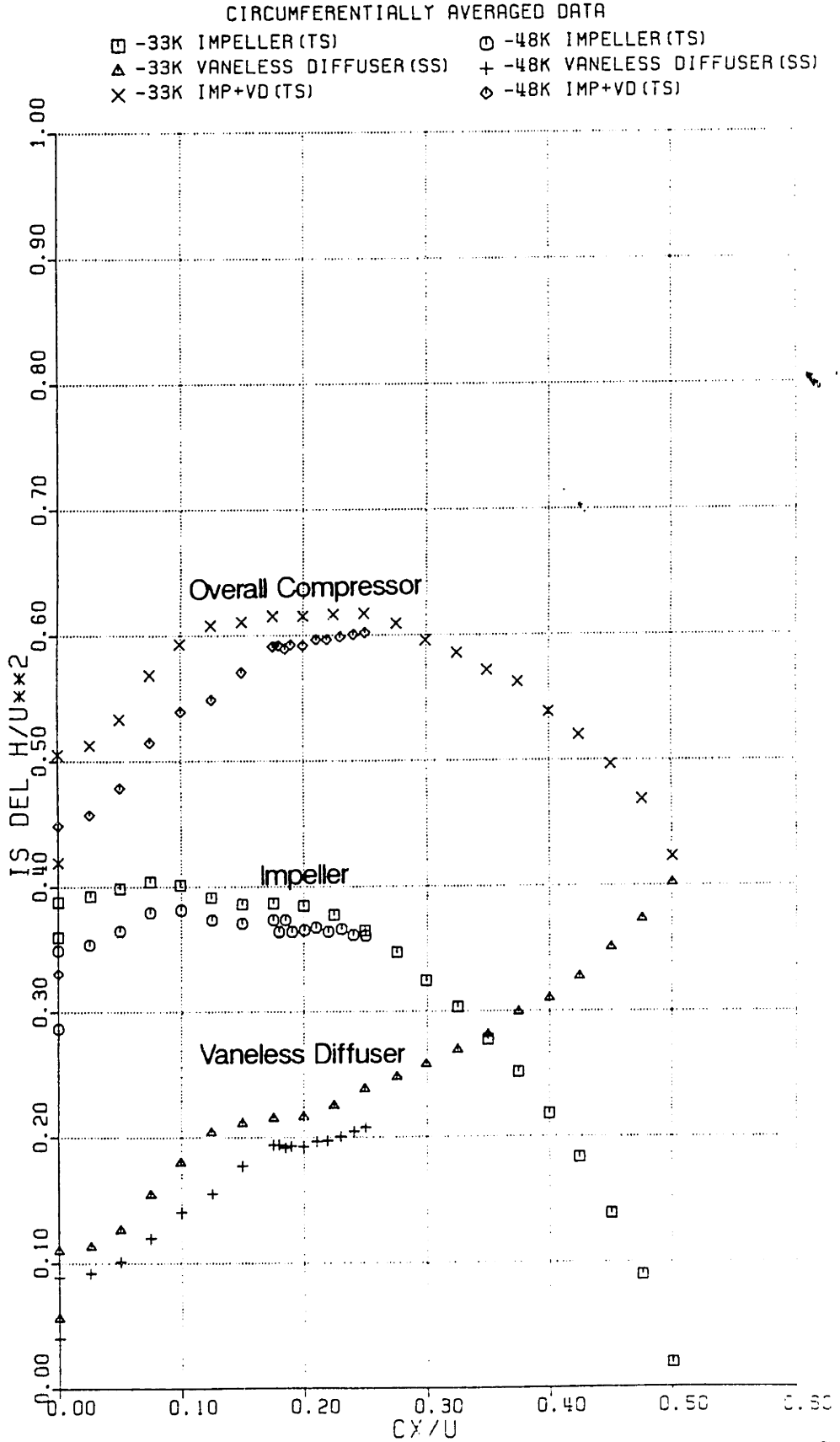

Fig. 4.27 Component Circumferentially Averaged Head Coefficients vs Cx/U

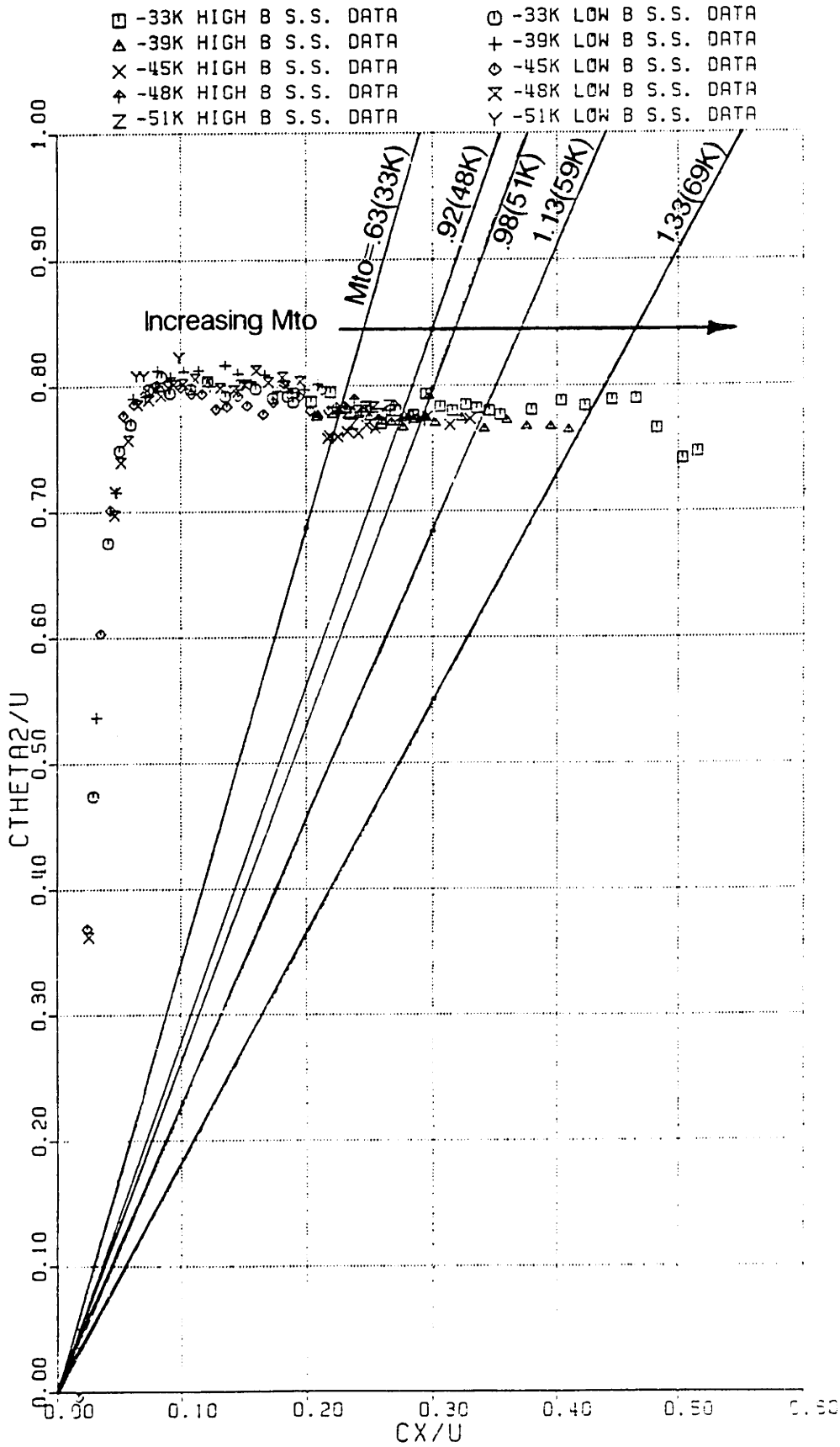

Fig. 4.28 Volute Matching Conditions

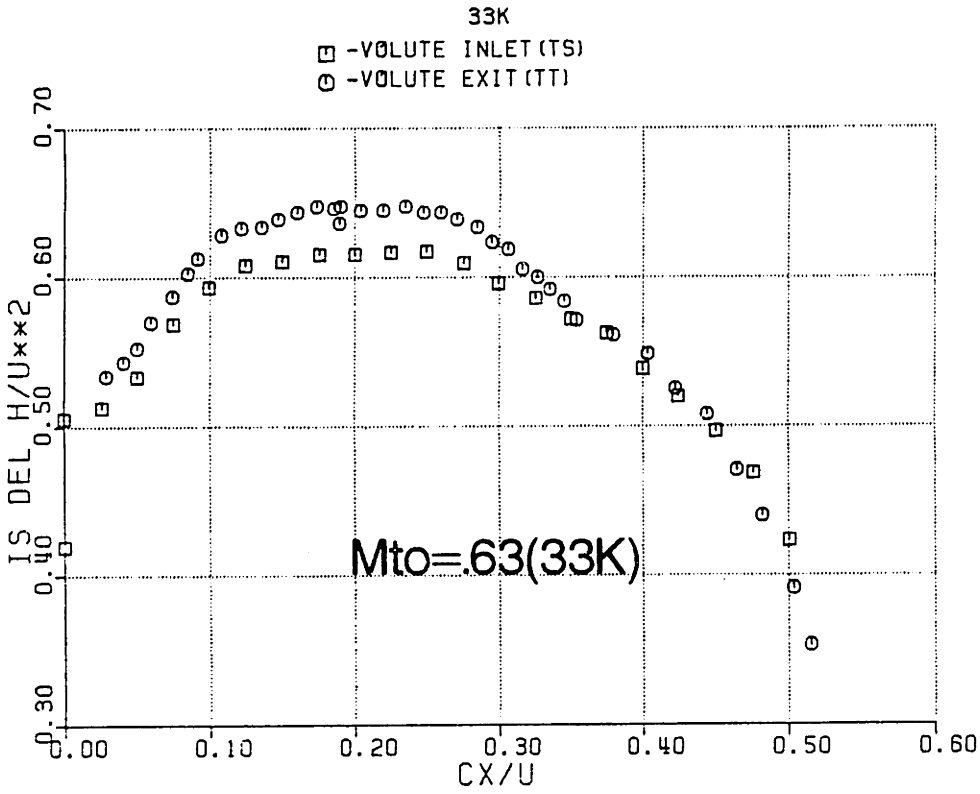

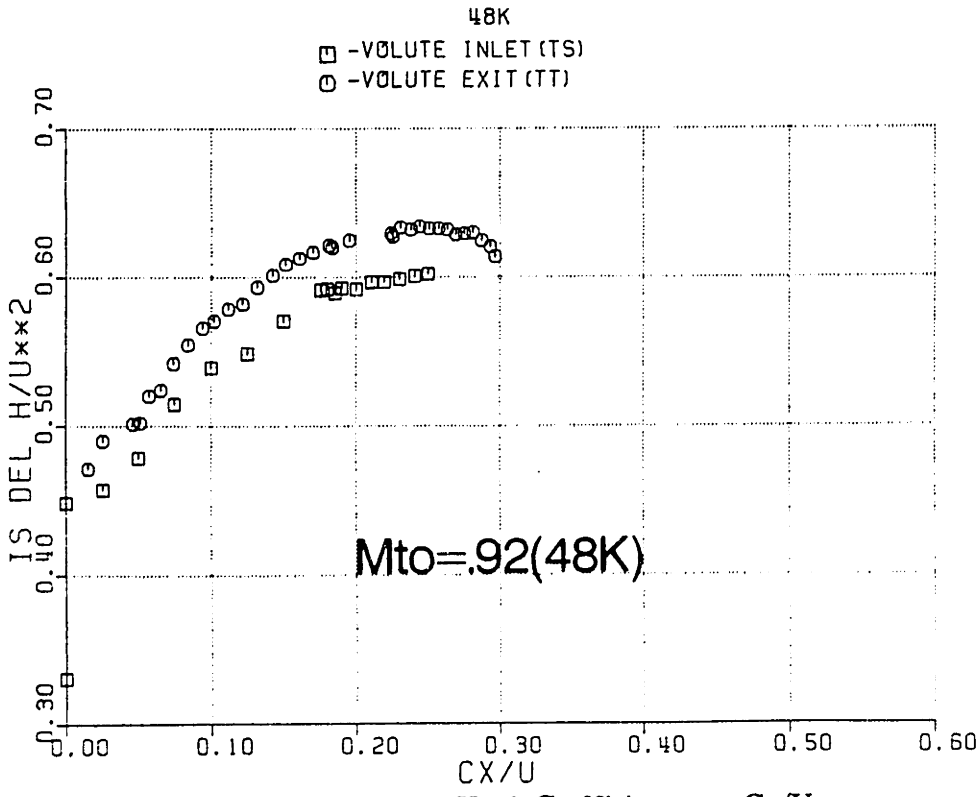

Fig. 4.29 Volute Head Coefficients vs Cx/U

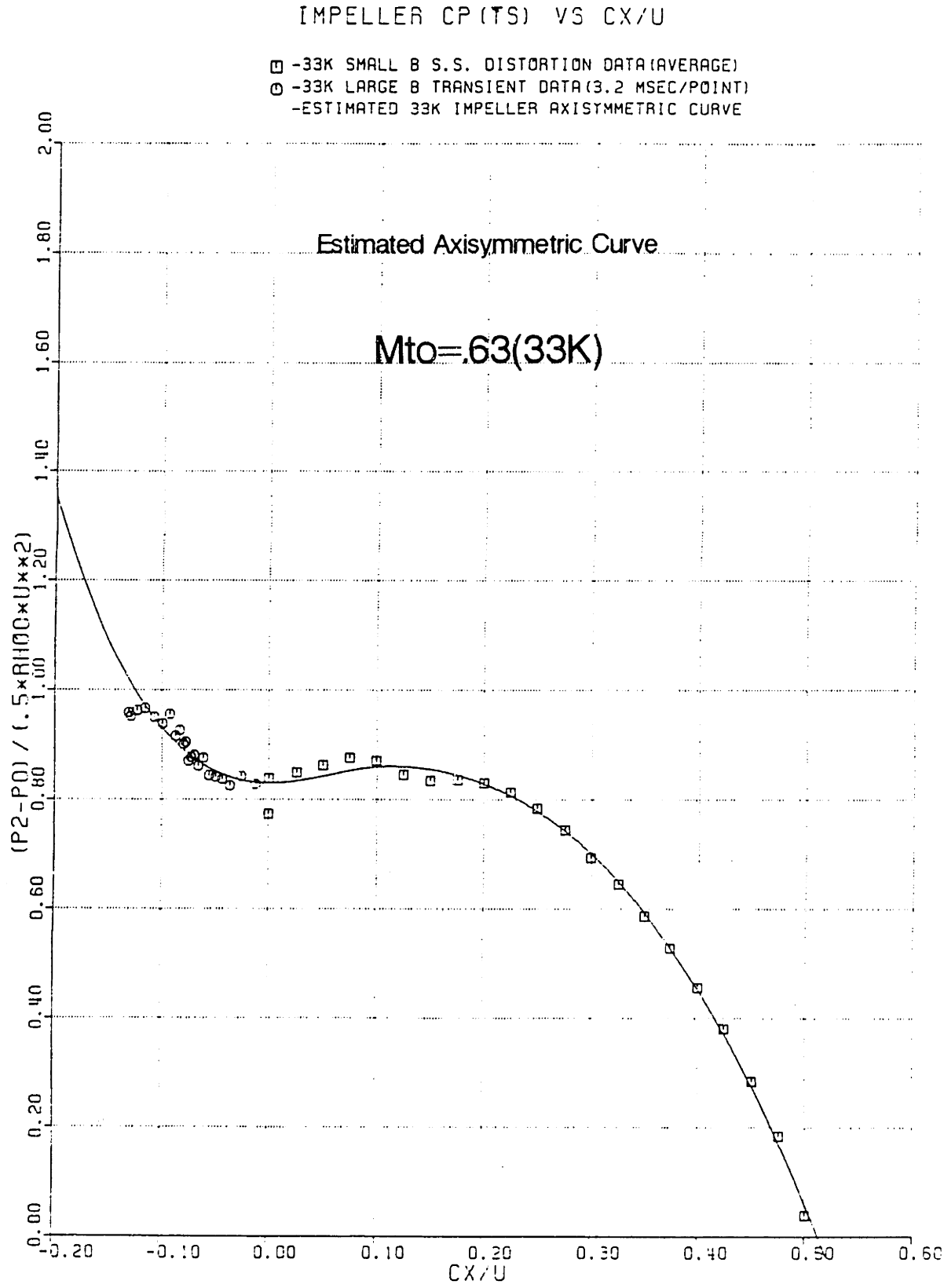

Fig. 4.30 Estimated Axisymmetric Curve of Impeller Cp vs Cx/U(Mto ≃ .63)

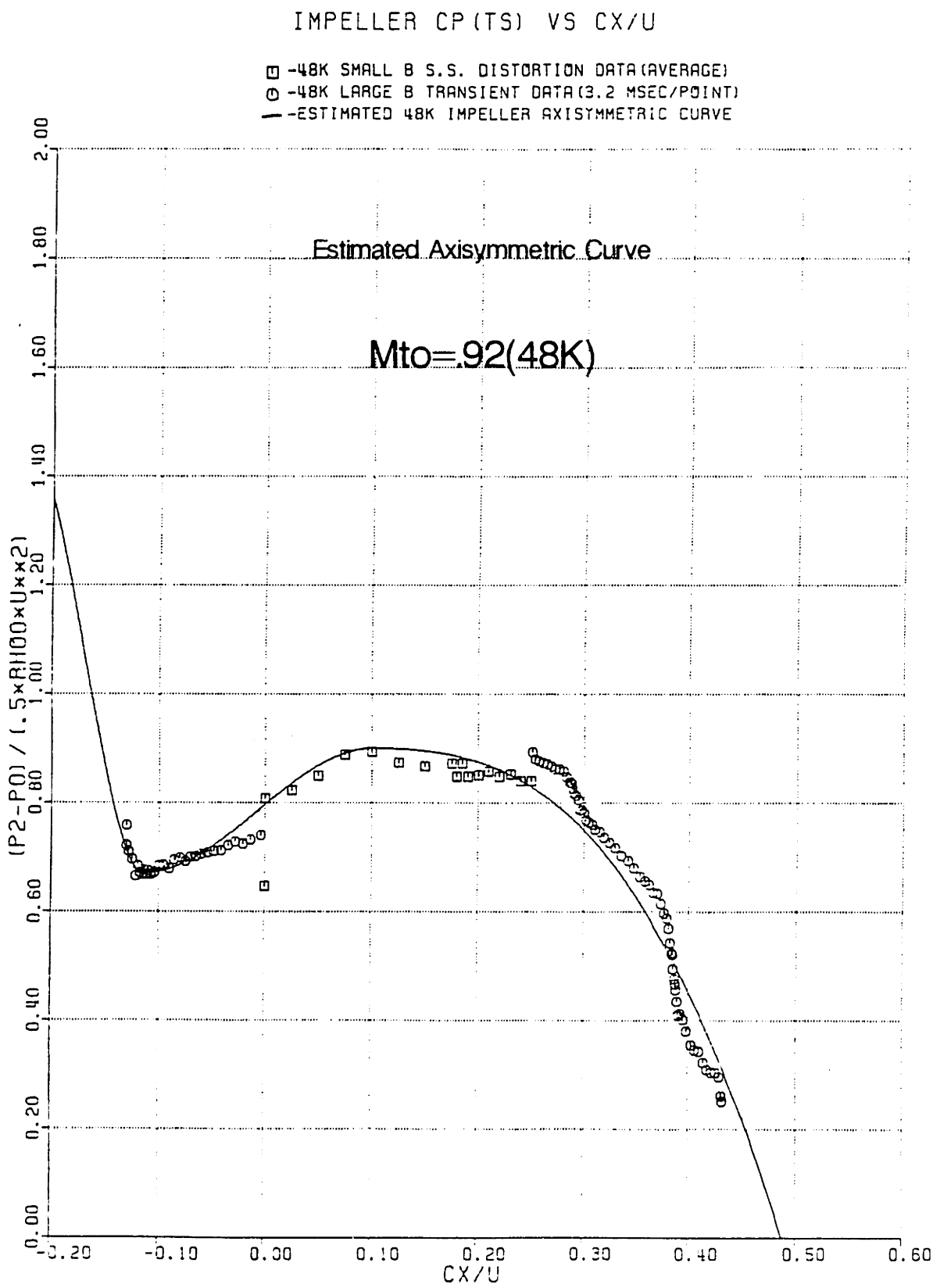

Fig. 4.31 Estimated Axisymmetric Curve of Impeller Cp vs Cx/U(Mto $\simeq$ .92)

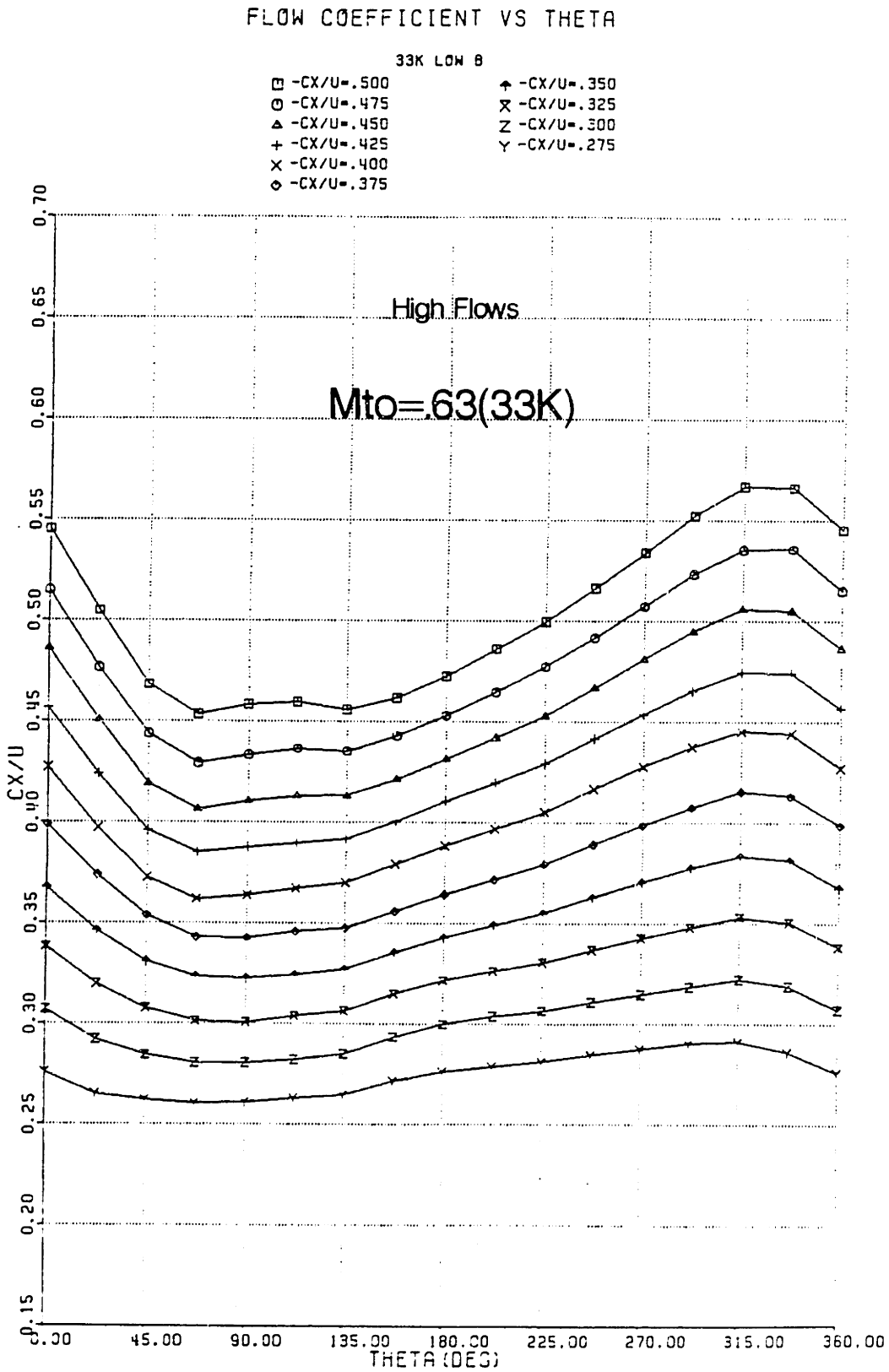

Fig. 4.32 Circumferential Variation in Impeller Flow Coefficient at High Mean Flow Coefficients(Mto ≃ .63)

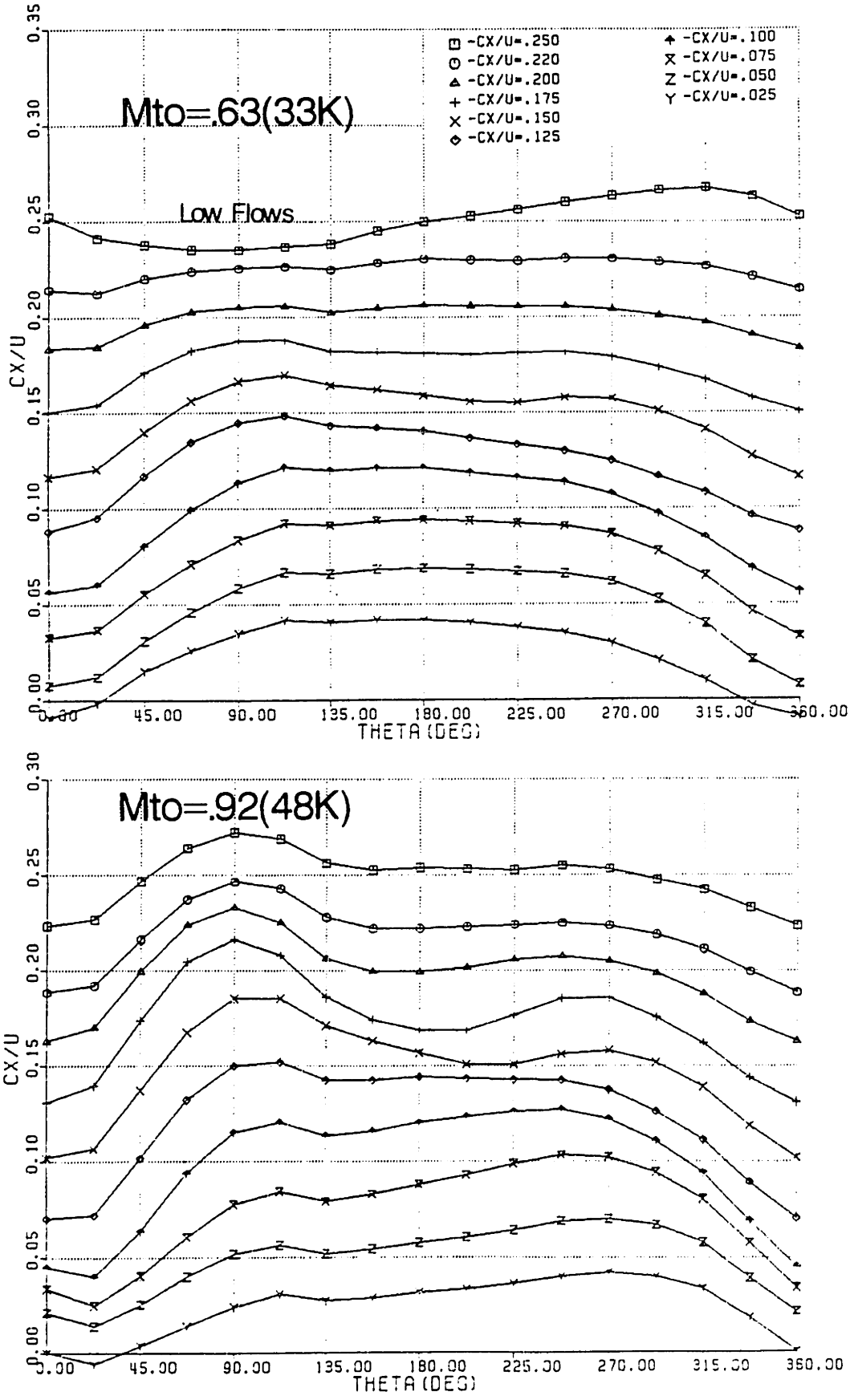

Fig. 4.33 Circumferential Variation in Impeller Flow Coefficient at Low Mean Flow Coefficients

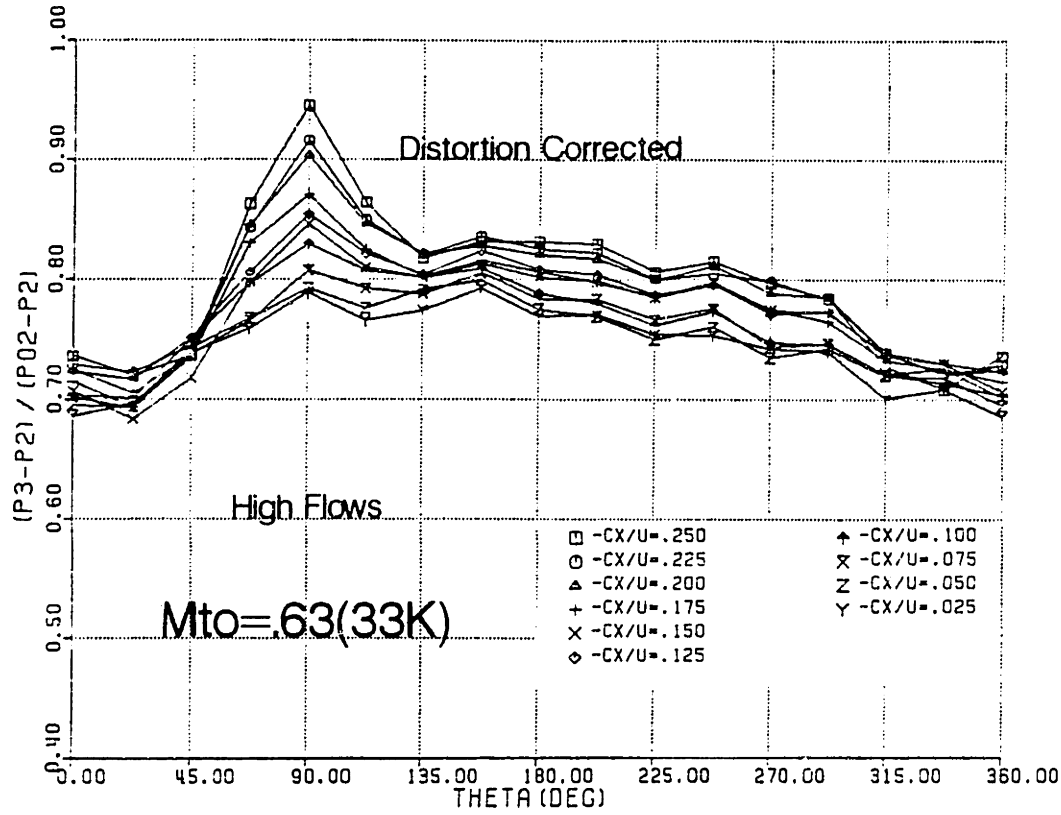

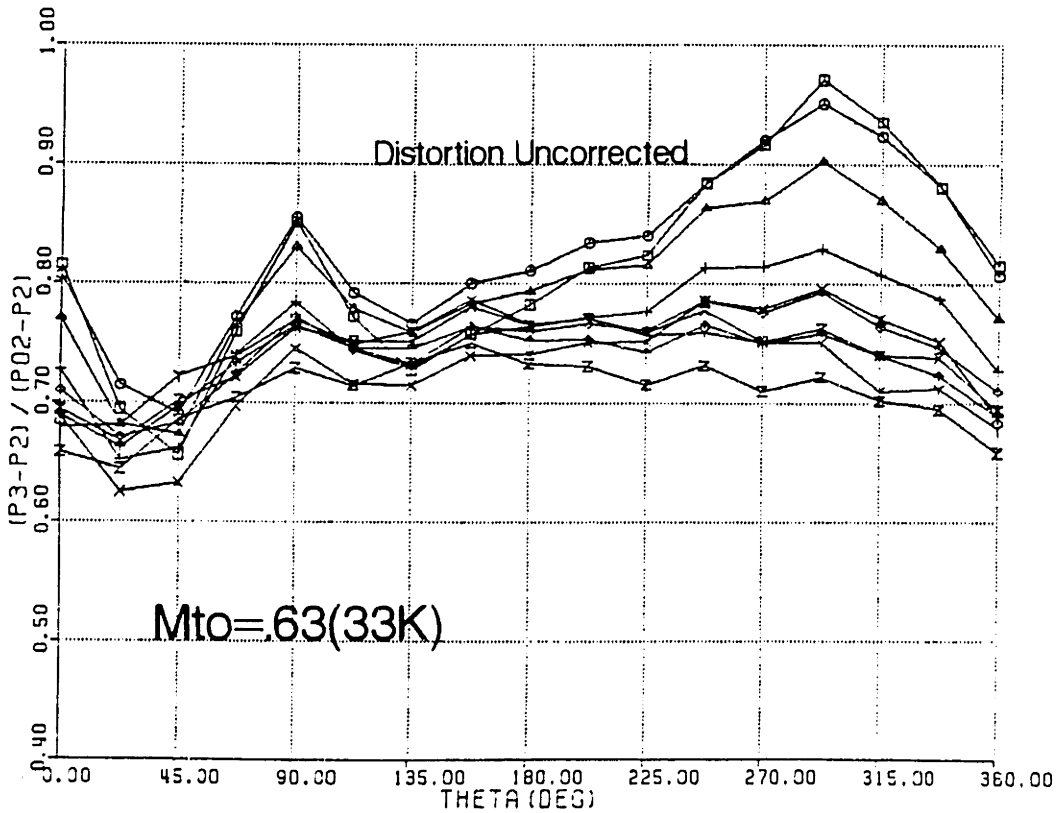

Fig. 4.34 Distortion Corrected vs Non Corrected Variation in Circumferential Vaneless Diffuser Cp at High Mean Flow Coefficients(Mto ≃ .63)

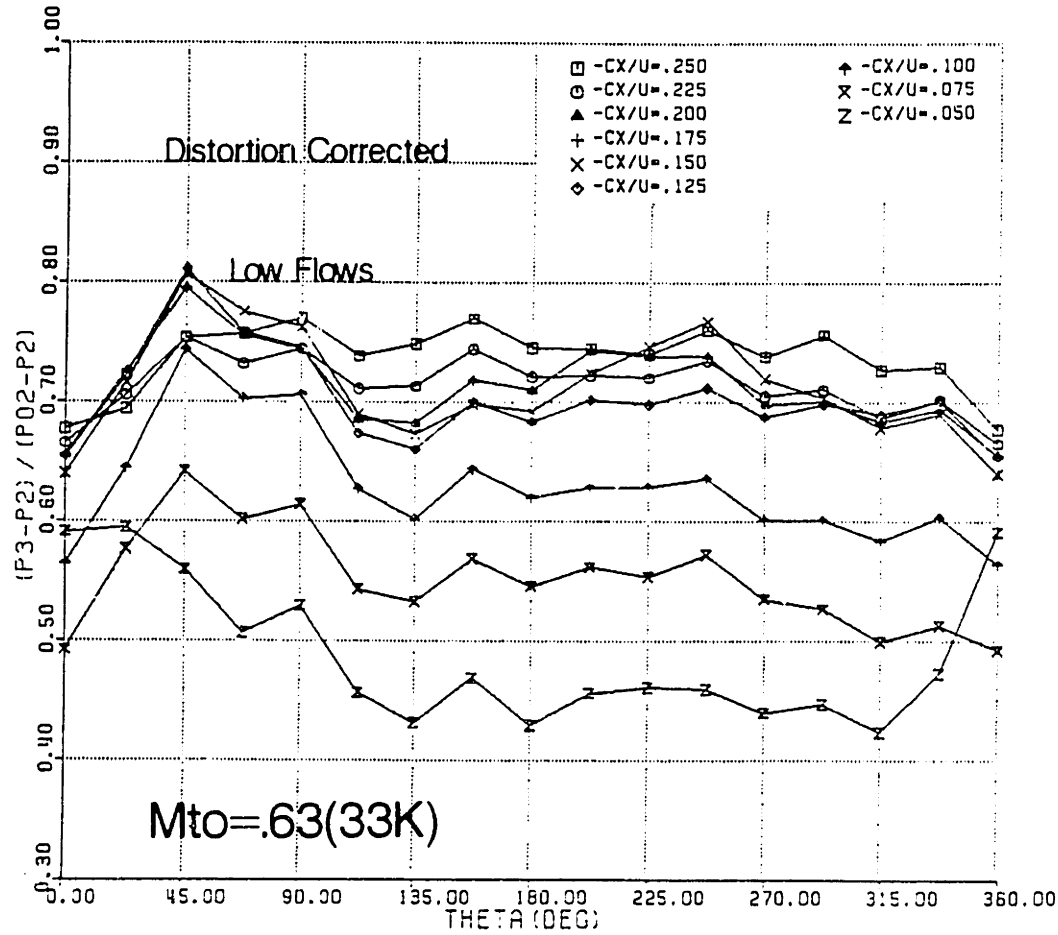

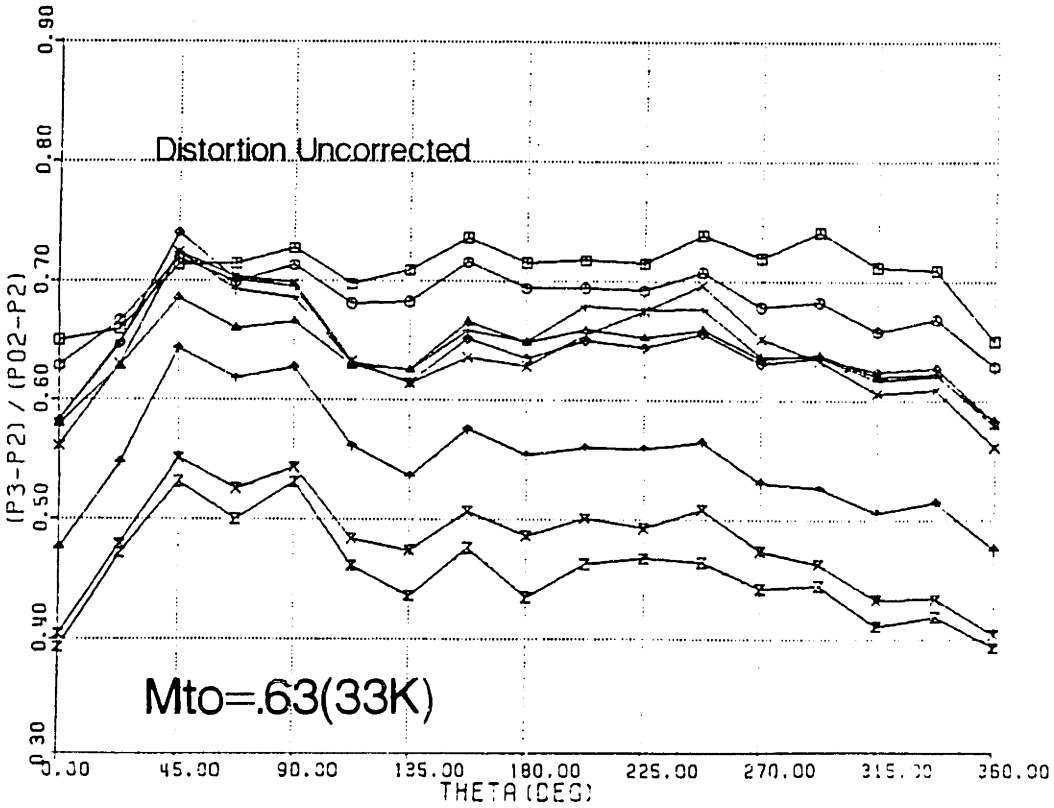

Fig. 4.35 Distortion Corrected vs Non Corrected Variation in Circumferential Vaneless Diffuser Cp at Low Mean Flow Coefficients(Mto ~ .63)

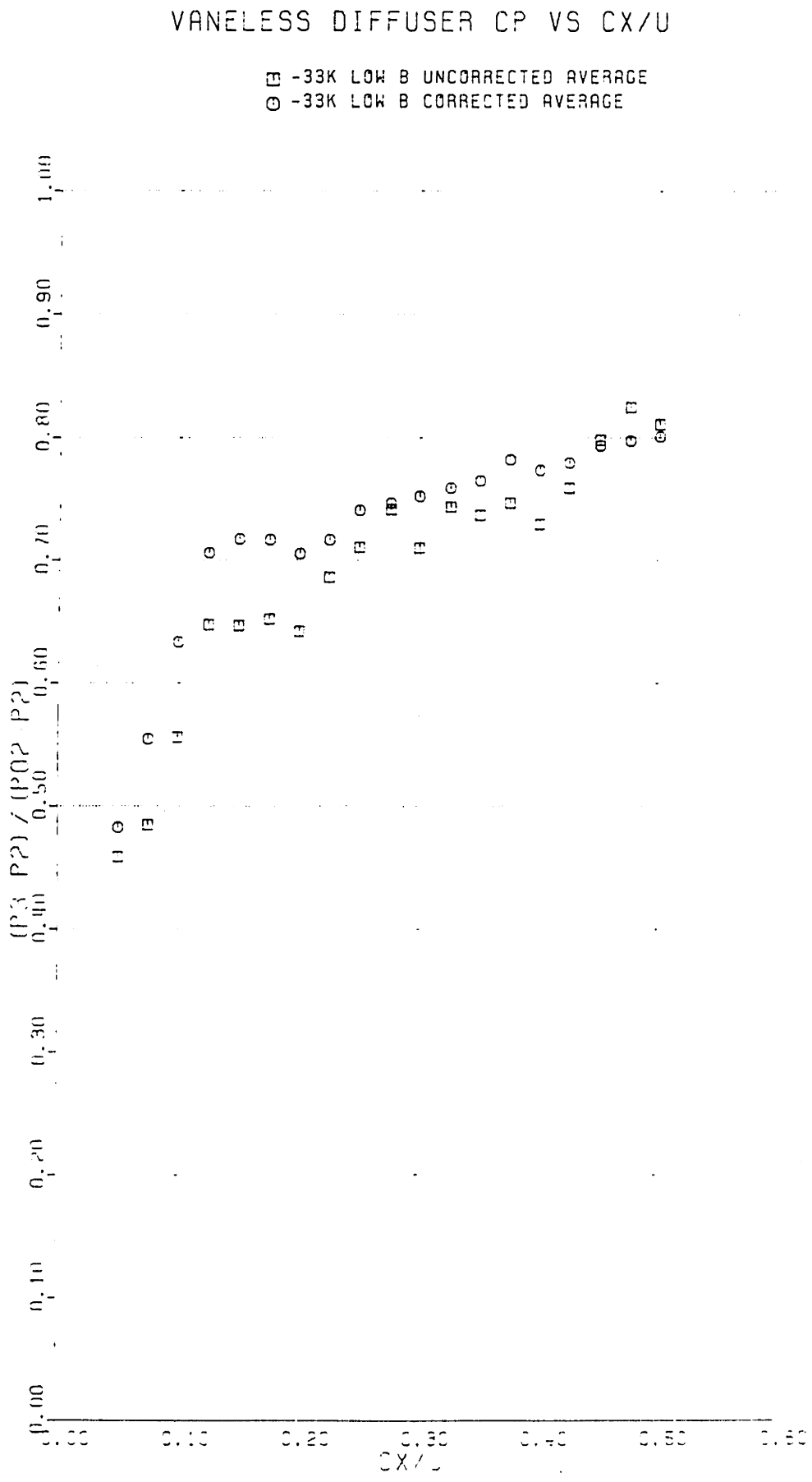

Fig. 4.36 Distortion Corrected and Non Corrected Circumferentially Averaged Vaneless Diffuser Cp vs Cx/U(Mto ≃ .63)

CHAPTER 5

SYSTEM DYNAMIC MODEL

5.1 Introduction and Assumptions

In Sec. 3.7, we showed how an instability in massflow was initiated when the compressor slope was positive and greater than the quantity $1/B^2 T'$. For very small instabilities within the confines of the linearized region around the equilibrium point, Eq. 1.6 described the growth in the perturbation quantity $\delta\bar{\Phi}_c$. However, once the perturbations magnitudes are of sufficient size, the linearized analysis is no longer valid. To find the system time response requires integration of a set of coupled non-linear system equations.

The basic elements of the compression system model considered in this chapter are identical to that considered by Taylor[51], Greitzer[25], and others. As shown in Fig. 5.1, the model is composed of a compressor operating in a pipe and emptying into a plenum. As discussed in App. A, the duct acts as an inductance in the system from the fluid inertia. The plenum acts as capacitance since it adds "springiness" to the system from compressibility. The model developed in this chapter deviates from previous treatments in that the assumption of constant rotor speed is relaxed and the rotor speed is allowed to vary. The B-parameter becomes a time dependent variable to be calculated along with compressor flow coefficient and plenum pressure ratio.

There were significant speed fluctuations in the large B data of Chap. 3 and it was thought that the behavior of the compressor in the time domain might be influenced by these fluctuations. Similar fluctuations are seen in turbochargers driven by the exhaust pulses from reciprocating internal combustion engines. In such installations, highly unsteady drive torques on the compressor are present. Because it was not clear how such speed oscillations would impact the instability point and post instability surge dynamics, they were included in the model.

The major assumptions in the dynamic model are:

- 1-D unsteady incompressible flow in the duct connecting the compressor to the plenum.
- Isentropic plenum expansion or compression assuming ideal gas.
- Variable compressor rotor speed.
- Density discontinuity across the compressor which is modeled as an actuator disc.
- Choked throttle nozzle where flow is assumed quasisteady and compressible.
- Inlet duct and throttle duct lengths are short and inductance free.
- Negligable velocity in the plenum chamber.
- Constant area duct with area taken to be the inducer eye reference area.
- Negligable gas angular momentum in the compressor passages compared to the wheel angular momentum.

Two types of compressor characteristic behavior are modeled in this chapter. In the initial dynamic modeling, the compressor operation is assumed to be quasisteady and its operating point is always found to be on its steady state characteristic of pressure and torque(i.e. $\tilde{f} << 1$). A second type of compressor characteristic considered exhibited a small 1st order time lag from steady state on the order of the through flow time of the compressor. This was done to model the instantaneous response of the impeller blading and vaneless diffuser when operating in surge.

Two different turbine drive torque characteristics were used in the model. For the first characteristic, the turbine torque was assumed to be constant and equal to the compressor torque at the equilibrium starting point. In a second type of characteristic, the turbine torque characteristic was that of a choked turbine. This second case corresponded more closely with the large B configuration since the turbine drive was being supplied by flow from the compression system plenum and acted as a throttle.

5.2 Governing Equations

The governing equations in the model are conservation of momentum in the duct L, conservation of mass in the plenum, and conservation of angular momentum in the turbo-spool. Conservation of momentum in the duct is written as

$$L \frac{d}{dt}\left(\rho_a C_{xa}\right) = \Delta P_c - \Delta P_p \tag{5.1}$$

Mass conservation in the plenum is given by

$$\frac{d}{dt}\left(\rho_p V_p\right) = \dot{m}_{in} - \dot{m}_{out} \tag{5.2}$$

Conservation of angular momentum in the turbocharger spool is given by

$$I \frac{d\omega}{dt} = \Gamma_D - \Gamma_c \tag{5.3}$$

where Γ_c and Γ_D are the compressor torque and drive torque respectively.

In Eq. 5.3, the angular momentum of gas in the compressor passages in the control volume is much lower than that of the rotor metal so has been neglected. Also Γ_c, the compressor torque, is the total drive torque needed to drive the compressor so it includes the torque needed to overcome the shroud wall friction.

These three equations are nondimensionalized in a fashion similar to that in Greitzer's model. Mass flows are nondimensionalized by $\rho_0 AcU$, the pressure differences by $1/2\,\rho_0 U^2$, and time by $1/\omega_H$. Torques are nondimensionalized by $\rho_0 AcRtU^2$ to form the torque coefficients. ω_H is the Helmholtz resonator frequency which is given by

$$\omega_H = a_{p0}\left(\frac{A_c}{V_p\ L_c}\right)^{1/2} \tag{5.4}$$

where ap0 is the speed of sound in the plenum. Employing this nondimensionalization and remembering that B is now considered a variable, the three nondimensional equations can be written. Conservation of momentum in the duct is given by

$$\frac{1}{B^2}\frac{d}{d\tilde{t}}\left(\Phi_c B\right) = \widetilde{\Delta P}_{co} - \widetilde{\Delta P}_{po} \tag{5.5}$$

Mass continuity in the plenum becomes

$$\frac{1}{B}\frac{d}{d\tilde{t}}\left(\widetilde{\Delta P}_{po} B^2\right) = \frac{\tau_p}{\tau_{po}}\left(\Phi_c - \Phi_t\right) \tag{5.6}$$

If we define A, the inertia parameter, as

$$A = \frac{2\rho_a L_c A_c r_T^2}{I} \tag{5.7}$$

then conservation of turbospool angular momentum is expressed as

$$\frac{dB}{d\tilde{t}} = A B^2\left(\tilde{\Gamma}_{DO} - \tilde{\Gamma}_{CO}\right) \tag{5.8}$$

As can be seen by the definition, as $I \rightarrow \infty$, $A \rightarrow 0$ and the derivative term dB/dt will then go to zero in Eq. 5.8 for a finite torque difference. This is the condition of constant speed. When A is zero, then the system of three coupled equations degenerates into two equations Eq. 5.5 and Eq. 5.6.

If we substitute Eq. 5.8, the expression for dB/dt, into Eq. 5.5 then it can be rewritten as

$$\frac{d\Phi_c}{d\tilde{t}} = B\left(\widetilde{\Delta P}_{co} - \widetilde{\Delta P}_{po}\right) + A B \Phi_c\left(\tilde{\Gamma}_{CO} - \tilde{\Gamma}_{DO}\right) \tag{5.9}$$

A similar substitution into Eq. 5.6 yields

$$\frac{d\widetilde{\Delta P}_{po}}{d\tilde{t}} = \frac{1}{B}\frac{\tau_p}{\tau_{po}}\left(\Phi_c - \Phi_t\right) + 2AB\,\widetilde{\Delta P}_{po}\left(\widetilde{\Gamma}_{co} - \widetilde{\Gamma}_{DO}\right) \qquad (5.10)$$

Eq 5.8, 5.9, and 5.10 are a coupled set of nonlinear equations to be solved for B, Φ_c, and $\widetilde{\Delta P}_{po}$ to predict the behavior of the compression system. $\widetilde{\Delta P}_{co}(\Phi_c)$, $\widetilde{\Gamma}_{co}(\Phi_c)$ in Eq. 5.9 and Eq. 5.10 are the compressor pressure and torque characteristics respectively.

In Eq. 5.10, the expression for temperature ratio in the plenum is given by the isentropic relation

$$\tau_p = \tau_{po}\left(\frac{\pi_p}{\pi_{po}}\right)^{\frac{\kappa-1}{\kappa}} \qquad (5.11)$$

where τ_{po} and π_{po} represent the initial state of the plenum which is determined by the equilibrium starting state of the compression system. The initial plenum equilibrium state is obtained from the pressure and torque steady state characteristics of the compressor. π_p in Eq. 5.11 represents the current pressure ratio of the plenum and is calculated by using

$$\pi_p = 1 + \frac{\kappa}{2}\,\widetilde{\Delta P}_{po}\,M_{TO}^2 \qquad (5.12)$$

The Mach index Mto in Eq. 5.12 is directly related to B by

$$M_{TO} = \left(\frac{2\omega_H L_c}{a_o}\right) B \qquad (5.13)$$

The throttle nondimensionalized flowrate Φ_t is given by

$$\Phi_T = f(M_t)\left(\frac{A_T}{A_c}\right)\frac{\pi_p}{\sqrt{\tau_p}\ M_{TO}} \tag{5.14}$$

where Mt is the throttle throat Mach number. The function f(Mt) is given by

$$f(M_t) = \frac{M_t}{\left(1 + \frac{\kappa-1}{2} M_t^2\right)^{\frac{\kappa+1}{2(\kappa-1)}}} \tag{5.15}$$

When the flow is choked, Mt = 1 and the throttle throat area At/Ac is fixed to its equilibrium value given by

$$\left(\frac{A_T}{A_c}\right) = \frac{\Phi_c \sqrt{\tau_{co}}\ M_{TO}}{f(M_t=1)\,\pi_{co}} \tag{5.16}$$

5.3 Compressor Characteristics

The simultaneous solution of Eq. 5.8 - 5.10 using additional relations specified in Eq. 5.11 - 5.16 requires two sets of compressor characteristics, a pressure rise and a torque characteristic which specify $\widetilde{\Delta P_{co}}(\Phi_c)$ and $\widetilde{\Gamma_{co}}(\Phi_c)$ in Eq. 5.8 - 5.10. The pumping characteristic is shown in Fig. 5.2 and the torque characteristic is shown in Fig. 5.3. These characteristics are obtained from the steady state and transient data discussed in Chap. 3 and 4. These characteristics are defined differently depending on the direction of flow. For forward flow, the flow coefficient is defined by

$$\phi_f = \frac{\dot{m}}{\rho_1 A_c U} \tag{5.17}$$

where ρ_1 is the static density for compressible flow through the reference area. When the flow Mach number is low $\rho_1 = \rho_0$, and $\phi_f = \Phi$. The pressure

characteristic is given in terms of the normally defined head coefficient, which is given as

$$\psi_f = \frac{\pi^{\frac{K-1}{K}} - 1}{(K-1)\, M_{TO}^2} \tag{5.18}$$

for forward flow.

In backflow, the flow coefficient is defined as

$$\phi_b = \frac{\dot{m}}{\rho_a A_c U} \tag{5.19}$$

where ρ_a refers to the static density in the upstream pipe of length L. When the Mach number is low in the pipe, $\rho_a = \rho_p$. The backflow headrise coefficient is defined as

$$\psi_b = \frac{1 - (1/\pi)^{\frac{K-1}{K}}}{(K-1)\, M_{TP}^2} \tag{5.20}$$

where Mtp is the Mach index calculated with the plenum temperature as reference(=U/(KRTp)$^{.5}$).

The torque coefficients are defined as

$$\tilde{\Gamma}_f = \frac{\Gamma_c}{\rho_1 A_c r_T U^2} \tag{5.21}$$

in forward flow and

$$\tilde{\Gamma}_b = \frac{\Gamma_c}{\rho_a A_c r_T U^2} \tag{5.22}$$

in backflow.

5.4 Constant Drive Torque Stability Analysis

Before solving Eq. 5.8 - 5.10 numerically, a linearized stability analysis was performed assuming constant drive torque. The compressor torque slope is defined as

$$\Gamma_c' = \frac{\delta \tilde{\Gamma}_{co}}{\delta \Phi_c} \tag{5.23}$$

and the turbine drive torque slope is defined as

$$\Gamma_D' = \frac{\delta \tilde{\Gamma}_{DO}}{\delta B} \tag{5.24}$$

The turbine torque in this stability analysis is by definition only dependent on the spool speed. Other effects such as fluctuations in the drive turbine massflow will not be considered in this analysis.

The compressor and throttle slopes are defined as

$$C' = \frac{\delta \tilde{\Delta P}_{co}}{\delta \Phi_c} \tag{5.25}$$

and

$$T' = \frac{\delta \tilde{\Delta P}_{po}}{\delta \Phi_T} \tag{5.26}$$

respectively.

Introducing perturbation quantities into Eq. 5.8 - 5.10 and using the slope relations defined by Eq. 5.23 and 5.24, then the linearized form of Eq. 5.8 is given by

$$\frac{d\delta B}{d\tilde{t}} = -\bar{A}\bar{B}^{a}\Gamma_c'\delta\Phi_c + \bar{A}\bar{B}^{a}\Gamma_D'\delta B \tag{5.27}$$

In this and subsequent equations, overbarred quantities refer to the values at the equilibrium operating point. The linearized form of Eq. 5.9 is

$$\frac{d\delta\Phi_c}{d\tilde{t}} = \left(\bar{B}C' + \bar{A}\bar{B}\Gamma_c'\bar{\Phi}_c\right)\delta\Phi_c - \bar{B}\delta\widetilde{\Delta P}_{po} - \bar{A}\bar{B}\bar{\Phi}_c\Gamma_D'\delta B \tag{5.28}$$

Eq. 5.10 is linearized to yield

$$\frac{d\delta\widetilde{\Delta P}_{po}}{d\tilde{t}} = \left(\frac{1}{\bar{B}} + 2\bar{A}\bar{B}\overline{\Delta P}_{po}\Gamma_c'\right)\delta\Phi_c - \frac{1}{\bar{B}\bar{T}'}\delta\widetilde{\Delta P}_{po} - 2\bar{A}\bar{B}\overline{\Delta P}_{po}\Gamma_D'\delta B \tag{5.29}$$

In matrix form, Eq. 5.27 - 5.29 comprise a set of coupled first order linear differential equations. This is

$$\frac{d}{d\tilde{t}}\begin{bmatrix}\delta\Phi_c\\ \delta\widetilde{\Delta P}_{po}\\ \delta B\end{bmatrix} = \begin{bmatrix}\left(\bar{B}C' + \bar{A}\bar{B}\Gamma_c'\bar{\Phi}_c\right) & \left(-\bar{B}\right) & \left(-\bar{A}\bar{B}\bar{\Phi}_c\Gamma_D'\right)\\ \left(\frac{1}{\bar{B}} + 2\bar{A}\bar{B}\overline{\Delta P}_{po}\Gamma_c'\right) & \left(-\frac{1}{\bar{B}\bar{T}'}\right) & \left(-2\bar{A}\bar{B}\overline{\Delta P}_{po}\Gamma_D'\right)\\ \left(-\bar{A}\bar{B}^{a}\Gamma_c'\right) & (0) & \left(\bar{A}\bar{B}^{a}\Gamma_D'\right)\end{bmatrix}\begin{bmatrix}\delta\Phi_c\\ \delta\widetilde{\Delta P}_{po}\\ \delta B\end{bmatrix}$$

For non-trivial solutions of the form $e^{r\tilde{t}}$ to exist, then det[A - rI] = 0. A is the coefficient matrix defined above in the matrix equation dX/dt = [A] X. If we substitute the variables a - h for the elements of [A] so that A is given as

$$\bar{A} = \begin{bmatrix} a & b & c \\ d & e & f \\ g & o & h \end{bmatrix} \tag{5.30}$$

then r must satisfy the characteristic equation given by

$$r^3 - (a+e+h)r^2 + (ae+ah+eh-bd-cg)r + (bdh+ceg-aeh-bfg) = 0 \tag{5.31}$$

For solutions to be stable, from Routh stability criterion [14], the coefficients of $r^3 + A2r^2 + A1r + A0 = 0$ must satisfy the conditions A2 > 0, A1 > 0, A0 > 0 and A1 x A2 - A0 > 0. Then stability condition 1 is given by

$$(a + e + h) < 0 \tag{5.32}$$

Condition 2 is

$$(ae + ah + eh - bd - cg) > 0 \tag{5.33}$$

Condition 3 is given by

$$(bdh+ceg-aeh-bfg)>0 \tag{5.34}$$

Condition 4 is specified as

$$(ae+ah+eh-bd-cg)(a+e+h)+(bdh+ceg-aeh-bfg)<0 \tag{5.35}$$

The assumption of constant drive torque which is speed independent is found by differentiating the definition of drive torque coefficient which is

$$\Gamma_D' = \frac{1}{\rho_0 U^2 A_c r_T}\frac{d\Gamma_D}{dB} - \frac{2\tilde{\Gamma}_D}{B} \tag{5.36}$$

For speed independence,

$$\frac{d\Gamma_D}{dB} = 0 \tag{5.37}$$

Hence for the present stability analysis, the drive torque slope was set to

$$\Gamma_D' = -\frac{2\bar{\Gamma}_c}{\bar{B}} \tag{5.38}$$

Stability of the system was checked by calculation of each of the four stability criterion specified in Eq. 5.32 - 5.35 at each value of flow coefficient. The wheel

inertia for the turbospool was obtained from measurements done at Cummins and was equal to 7.38E-04 ft-lbf-sec (1.00E-03 N-m-sec^2). The inertia parameter for the large B system is calculated using Eq. 5.7 and typical values of ρ_o = 2.26E-03 slug/ft^3 (1.17 Kg/m^3), Lc = 4.16 ft(1.27 m), Ac = 3.85E-02 ft^2 (3.58E-03 m^2), and rt = .210 ft(6.39 cm) to give a value of A of .043.

Two parameter variations were investigated in calculating the stability of the system. In the first, the nominal equilibrium value of B was varied from the large B system value of 2.74(=Bo) while A was held fixed. The results are shown in Fig. 5.4 which shows the instability value of ϕ vs log(B/Bo). As shown in Fig. 5.4, the large B system becomes unstable at ϕ = .24 which corresponds with the peak of the pressure characteristic defined in Fig. 5.2. As the value of B is reduced, the instability value of ϕ is also reduced. In each of these cases, stability condition #4 was violated. For a B value of .25, which is the value of B for the small B system of Chap. 4, the system instability is predicted to occur at ϕ = .19 in Fig. 5.4. The main trend is one of stabilization as B is reduced.

The effect of A, the inertia parameter on stability was also calculated and the results are shown in Fig. 5.5. Here B was held fixed at 2.74 and A was varied from its current value of .043(=Ao). As was the case for the variation in nominal B, in each case stability condition # 4 is violated at the instability point. As A is increased, which corresponds to a reduction in wheel inertia, a stabilizing trend is seen in which the instability value of ϕ is reduced. Hence lower inertia wheels are stabilizing. However the stabilizing effect appears small and is only seen when A is increased by a factor of ten. Significant stabilization is seen when A is increased by a factor of one hundred, but it is difficult to imagine a practical compression system where A would be so large. For practical values of A, the weakness of the instability variation with A shows that the instability point could be predicted quite closely by ignoring the speed fluctuations in the stability analysis(A = 0 case).

The small stabilizing effect of lower inertia wheels from speed variations is seen by considering operation of the compressor around an equilibrium point on a section of the compressor characteristic. When the compressor operation is at a lower flow coefficient than equilibrium, the compresor torque is lower than the equilibrium value. Since the drive torque is constant, then the compressor must

necessarily speed up as a result of the torque mismatch. Higher speed naturally results in a higher compressor pressure rise for a given pressure rise coefficient. This then drives the massflow in the duct back toward equilibrium. Similarly, when the compressor operates at flow coefficients above the equilibrium value, the compressor torque increases above equilibrium and the compressor slows down. The speed reduction reduces the pressure rise in the compressor and this reduction in pressure drives the duct massflow back towards the equilibrium. The effect is equivalent to a less positive compressor characteristic in a constant speed case, which is also stabilizing.

5.5 Constant Drive Torque System Response Numerical Results

To find the system response to a perturbation in massflow, Eq. 5.8 -5.10 were solved numerically by a fourth order Runge Kutta integration proceedure. The equilibrium B value was set to a value of 2.74 and the inertia parameter A was set to .043. Drive torque is assumed to remain constant for these calculations. The equilibrium throttle point was set at a specified equilibrium flow coefficient and a perturbation in compressor massflow is introduced. For an equilibrium value of ϕ = .24, which corresponds to operation just to the right of the compressor peak, the system response is shown in Fig. 5.6. The upper trace shows instantaneous flow coefficient, the middle trace shows instantaneous speed, and the lower trace shows plenum head coefficient. Time on the horizontal axis is given in terms of Helmholtz resonator periods. The initial perturbation in flow coefficient of .01 is seen to decay with time.

Reducing the flow coefficient slightly to ϕ = .2398, as shown in Fig. 5.7, produces a small oscillation in flow coefficient which neither grows nor decays with time. This is the onset of mild surge.

When the equilibrium throttle is reduced to ϕ = .2397, the system enters deep surge as is shown clearly in Fig. 5.8. The main features of this deep surge behavior are Helmholtz type growing oscillations in massflow followed by a blowdown phase during which the plenum empties a significant percentage of its compressed air volume back through the compressor. The speed is seen to first peak during the blowdown phase and then drop to a speed below the equilibrium value. The speed drops rapidly during the forward flow recovery phase because the compressor flow

coefficient and torque coefficient are for a short period of time much higher than the equilibrium throttle point values. After the blowdown, there is a long quiet period in which the compressor speed is seen to slowly recover to its equilibrium value.

It is important to remember that the compressor characteristic used for these calculations is time independent. Both the torque and pressure characteristic are assumed quasisteady and continuous in the two flow regimes of positive and negative flow. There are no time lags of any kind assumed in the compressor's operation in unsteady flow. Fig. 5.8 shows a slowly growing oscillation develop and after a short period of time, the deep surge event occurs. Abrupt stalling of the compressor actuator characteristic is not necessary to produce the trigger-like stalling behavior shown. All that is necessary is a positively sloped compressor characteristic and a B value of sufficient size.

A slightly further reduction in flow to $\phi = .235$ as shown in Fig. 5.9, shows similar surge triggering behavior as in Fig 5.8. However the throttle reduction has significantly reduced the time between blowdowns. Fig. 5.9 shows two distinctly different time scales. The Helmholtz order frequency is seen shortly before the blowdown occurs. The time between blowdowns is seen to be roughly 25 Helmholtz resonator periods which is much longer. It is here that the significance of the speed fluctuations are seen in the time dependent behavior of the system. The allowance of small speed variations adds a new energy storage element in the compression system which changes the time behavior. A new time scale is added solely as a result of the speed variations. Deep surge in Fig. 5.9 is "triggered" when the speed reaches a critical value.

To see that the long period between blowdowns is a result of speed variations only, the system response was calculated with a very large wheel inertia($A = 0$). This is the condition of constant rotor speed. The infinite inertia results are compared with the test wheel inertia results for a throttle setting of $\phi = .235$ in Fig. 5.10. As seen in the comparison, the long quiet period between deep surges is eliminated in the infinite inertia results. When relatively small speed variations of $\pm 5\%$ are present in the compressor turbospool, the system response in time is substantially different from that if the speed is constant.

The system response with further reductions in compressor throttling are shown

in Fig. 5.11 through 5.13. At a throttle setting of ϕ = .23, Fig. 5.11 shows the quiet period between blowdowns to be roughly 13 Helmholtz cycles. In Fig. 5.12, which shows the results for a throttle setting of ϕ = .2, the quiet period is gone, the forward flow leg is greatly compressed, and the flow coefficient response resembles the infinite inertia results shown in Fig. 5.10. Additional throttling to ϕ = .1, as shown in Fig. 5.13, shows similar behavior as at ϕ = .2. The forward flow leg is seen to be compressed with increased throttling.

5.6 Quasisteady Model Comparison of Theory with Experimental Results

The surge simulation results and the large B experimental data of Chap. 3 for a throttling setting of ϕ = .235 are compared in Fig. 5.14. The main qualitative features of the time behavior observed in the experimental data are simulated in the dynamic model results shown. As was discussed in the large B results, the four regimes of flow are clearly seen in the simulation results. First a quiet period where the flow coefficient is seen to decrease slightly with time. Secondly mild surge Helmholtz oscillations in massflow develop. In the third regime, the deep surge blowdown process occurs. In the last regime, the flow recovers to forward flow again to repeat the deep surge cycle.

In the precursor period to deep surge, increasing speed affects the system stability in two ways. First as speed is increased for constant flow, the flow coefficient decreases, which is destabilizing because the compressor characteristic slope increases with decreasing ϕ. Second as speed increases, B increases proportionally which as we have seen is also a destabilizing effect. Since the speed behavior is periodic, the critical combination of B and compressor slope necessary for the compression system to enter deep surge also occurs in a periodic manner. Speed fluctuations are thus important in the dynamics when the compression system enters deep surge.

5.7 Effects of Drive Characteristic on Deep Surge Results

In the previous results, the turbine torque was assumed to be constant and the throttle was assumed to be choked. In the large B rig discussed in Chap. 3, most of the throttling in the compression system occurs in the turbine which operates choked.

The turbine is also the drive for the compressor and hence the drive torque output varies with the flowrate and plenum pressure. To examine the sensitivity of the earlier model results to the drive assumptions, the surge simulation was run with the turbine drive torque output varying directly with plenum pressure. A comparison of the results for constant drive torque and drive torque which varies directly with plenum pressure are shown in Fig. 5.15. Qualitatively, the differences between these two results are seen to be quite small. The main effect is a slight lengthening of the quiet precursor period to deep surge. This is due to the lower available drive torque when the plenum pressure is minimum which lengthens the time for reacceleration of the rotor back to its equilibrium value.

5.8 Effect of Time Lags on System Response

In Fig. 4.5 of Chap. 4, the instantaneous compressor operation for the large B system was seen to be flatter at low flow coefficients below $\phi \simeq .1$ than when operating in the low B system. From a system view, the large B instantaneous compressor behavior appears to lag the small B behavior in time. A physical mechanism presented in Chap. 4 showed the divergence a result of the differing circumferential extent of impeller stalling seen in small vs large B. Hence a time lag observed in the data might roughly correspond to the time required for the inducer tip blade to stall, shed a vortex, and then convect downstream through the impeller and vaneless diffuser.

To simulate the finite time response of the compressor blading, the compressor's instantaneous characteristic was modeled as a first order system. The time constant was assumed to be equal to the throughflow time of the impeller and vaneless diffuser. The instantaneous and steady state compressor pressure rise coefficients are related by

$$\frac{d\widetilde{\Delta P_{co}}}{d\tilde{t}} = \frac{1}{\tilde{\tau}_c}\left(\widetilde{\Delta P_{coss}} - \widetilde{\Delta P_{co}}\right) \tag{5.39}$$

where $\widetilde{\Delta P_{co}}$ is the instantaneous compressor pressure rise coefficient and $\widetilde{\Delta P_{coss}}$ is the steady state value. $\tilde{\tau}_c$ is related to the throughflow time of the compressor

nondimensionalized by the Helmholtz resonator period. Eq. 5.8, 5.9, 5.10 along with Eq. 5.39 form a set of coupled nonlinear 1st order equations which can be integrated to find the system response.

The compressor throughflow time in Eq. 5.39 is given approximately by

$$\tau_T = \frac{L_T}{C_x} \tag{5.40}$$

where Lt is the meridional length of the impeller and vaneless diffuser and Cx is the axial flow velocity. When nondimensionalized by the Helmholtz resonator period, the throughflow time constant is given by

$$\tilde{\tau}_T = \left\{\frac{1}{2}\frac{L_T}{L_c}\right\}\frac{1}{B\,|\bar{\Phi}_c|} \tag{5.41}$$

The value of the nondimensional time lag for the experimental large B system for operation at $\bar{\Phi} = .1$ is calculated from Eq. 5.41 using values of B = 2.74, Lc = 4.16 ft(1.27 m), Lt = .28 ft(.085 m), and found to be equal to .12. For a Helmholtz frequency of 7.35 Hz, the throughflow time τ_t is approximately 2.7 ms.

5.9 Time Lag Stability Analysis

Before numerically integrating Eq. 5.8, 5.9, 5.10 and 5.39, a stability analysis was performed to examine the effect of a time lag on the overall stability point. Since it was found in Sec. 5.3 that speed fluctuations(for practical values of A) had a very small effect on the system stability point, a stability analysis was performed assuming constant speed(A=0). Eq. 5.28 becomes

$$\frac{d\,\delta\bar{\Phi}_c}{d\,\tilde{t}} = \bar{B}\,\delta\widetilde{\Delta P}_{c_0} - \bar{B}\,\delta\widetilde{\Delta P}_{\rho_0} \tag{5.42}$$

Eq. 5.29 is

$$\frac{d\,\delta\widetilde{\Delta P}_{po}}{d\,\tilde{t}} = \frac{1}{\bar{B}}\,\delta\Phi_c - \frac{1}{\bar{B}T'}\,\delta\widetilde{\Delta P}_{po} \tag{5.43}$$

Introducing perturbation quantities into Eq. 5.39, it can be written as

$$\frac{d\,\delta\widetilde{\Delta P}_{co}}{d\,\tilde{t}} = \frac{1}{\bar{\bar{\tau}}}\left(C'\delta\Phi_c - \delta\widetilde{\Delta P}_{co}\right) \tag{5.44}$$

Eq. 5.42, 5.43, and 5.44 are a set of coupled first order linear equations which can be written in matrix form as

$$\frac{d}{d\tilde{t}}\begin{bmatrix}\delta\Phi_c\\ \delta\widetilde{\Delta P}_{po}\\ \delta\widetilde{\Delta P}_{co}\end{bmatrix} = \begin{bmatrix}0 & -\bar{B} & \bar{B}\\ 1/\bar{B} & -1/(\bar{B}T') & 0\\ C'/\bar{\bar{\tau}} & 0 & -1/\bar{\bar{\tau}}\end{bmatrix}\begin{bmatrix}\delta\Phi_c\\ \delta\widetilde{\Delta P}_{po}\\ \delta\widetilde{\Delta P}_{co}\end{bmatrix}$$

As was shown in Sec. 5.3, the stability of this system is given by Eq. 5.32-5.35 where the coefficients of the matrix A given in Eq. 5.30 are those given above.

The stability conditions from the Eq. 5.32-5.35 were calculated using the characteristic shown in Fig. 5.2 at various throttle point values of ϕ and at various levels of time lag. When one or more of the stability conditions were violated, the throttle point and B-parameter at the point of instability defined a point on a stability boundary curve. The results of the time lag stability analysis is shown in Fig. 5.16. Instability boundaries, which define combinations of flow coefficient and B-parameter separating stable from unstable operation, are shown for varying amounts of compressor time lag. Quasisteady refers to operation with no time lag. A throughflow time of 1 shown in Fig. 5.16 is the reference throughflow time

and refers to the time taken for a fluid particle to traverse the impeller and vaneless diffuser of the tested compressor. At a flow coefficient of .1, as was shown above, this time is equivalent to 2.7 ms or .12 when nondimensionalized by the resonator period. The effect on stability of compressors with longer or shorter throughflow lengths are also plotted to examine the sensitivity of time lag magnitude on the instability point.

The main effect shown by Fig. 5.16 is one of stabilization for low B as the time lag is increased from quasisteady. For large B values, the instability point is not affected significantly by compressor time lags. However at smaller values of B, the instability point is shifted favorably towards shutoff. The stabilizing effect for a time lag of 1 relative to the non time lag quasisteady is rather weak. However when the time lag is increased to 5 times the reference value, there is a significant shift in the instability point towards shutoff. Below a B value of approximately .5 for this large time lag, the system appears to always be stable from this analysis.

5.10 Time Lag System Response Numerical Results

For the large B system, initial equilibrium operating point of ϕ = .235, constant drive torque, and time lag of 2.3 times the reference time lag, the results of the numerical integration of the coupled Eq. 5.8, 5.9, 5.10 and 5.39 are shown in Fig. 5.17 along with the earlier quasisteady results. Smaller values of time lag did not alter the numerically results significantly from the quasisteady no time lag case. The main difference between the time lag vs no lag results case shown is in the mild surge precursor period to deep surge. With a small time lag, the mild surge period is substantially longer and the Helmholtz oscillation amplitude larger than in the simulation quasisteady results. The time lag has the effect of flattening the instantaneous compressor characteristic relative to its quasisteady one which leads to a slower growing instability as was discussed in Sec. 3.10.

5.11 Time Lag Model Comparison of Theory with Experiment Results

The results of the time lag simulation are shown in Fig. 5.18 through Fig. 5.20 along with the corresponding large B experimental results of Chap. 3. Operation to the right of the mild surge line at ϕ = .275 in Fig. 5.18 shows the

compression system to be stable in both the simulation and the experimental results. When the throttle setting is reduced to ϕ = .236, as shown in Fig. 5.19, the compression system is seen in both the simulation and experiment to enter continuous mild surge. The amplitude of the sustainable mild surge oscillations calculated in the simulation are much larger than the quasisteady results shown earlier in Fig. 5.7. The time lag introduced has the effect of stabilizing the mild surge oscillations and this effect considerably improves agreement with the experimental results shown.

Reducing the throttle to ϕ = .235 causes the compression system to enter the deep surge mode shown in Fig. 5.20. Good agreement is seen between the theory and experimental data over all four distinct regions of operation of the overall deep surge cycle. The deep surge precursor period of large amplitude mild surge is clearly seen which was attenuated in the earlier quasisteady results. The long period between deep surges of the compressor due to speed variations is again clearly visable.

5.12 External System Effects

In the stability analysis and in most of the integration results discussed in this chapter we have assumed that the throttle area remains constant and the external drive torque is constant. The dynamic behavior seen are of self excitated oscillations. We have not considered external forms of excitation such as unsteady driveline torque fluctuations or variable throttling which are usually present in typical turbocharger installation. These effects may be destabilizing under certain amplitude and frequency conditions and thereby influence the position of the surge line. The dynamic effects of both of these forms of excitation can be calculated by minor modifications of the basic model presented in this chapter.

5.13 Summary

The main points brought out in this chapter are the following:

- The system behavior in surge is dominated by the variable B.
- A quasisteady variable B compressor model predicts qualitatively most of the observed system dynamic features of surge behavior.

- Speed fluctuations have little effect on the instability point for practical values of the A-parameter but they are critical in the type of deep surge "triggering" behavior commonly observed in compression systems. The surge dynamics are affected by the addition of another energy storing element, the compressor rotor. The main effect is to increase the time interval between blowdowns over the constant speed case. They also have a role in the stabilization of mild surge massflow oscillations.
- Introducing a small time lag associated with the compressor throughflow time in the variable speed model improves the quantitative agreement with experiment in mild surge operation and has a stabilizing effect on large mild surge oscillations.

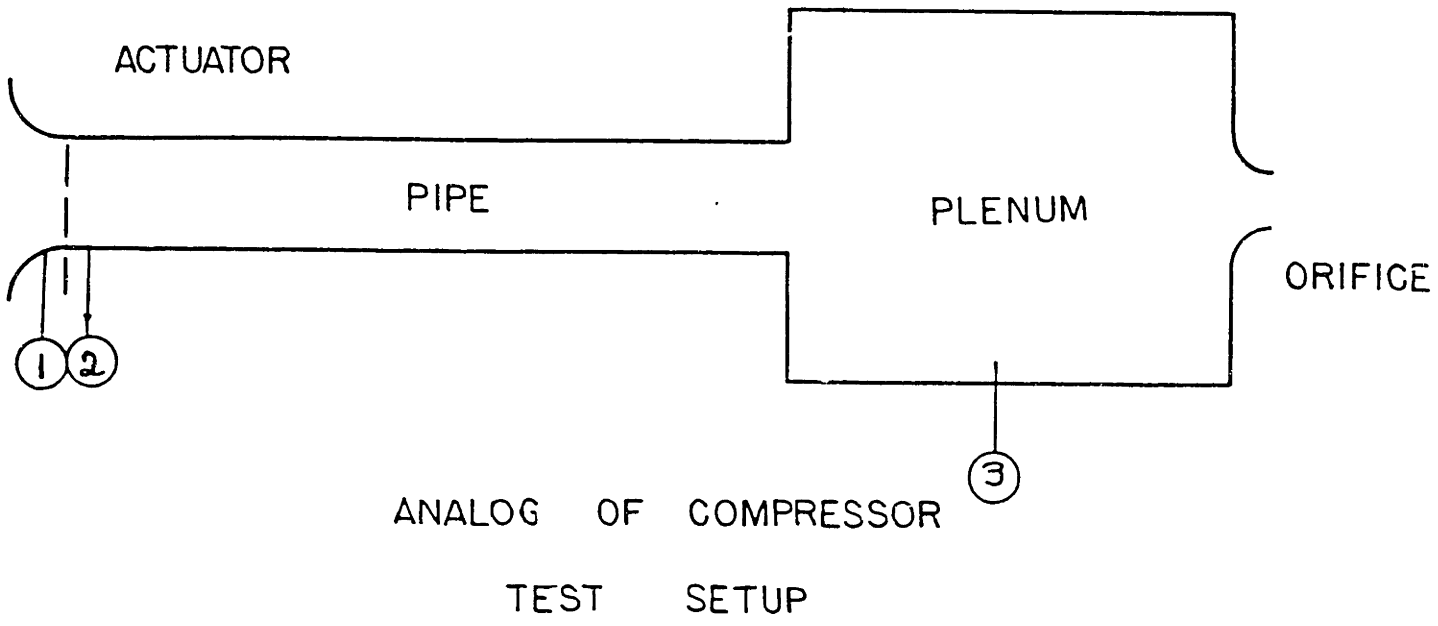

Fig. 5.1 Compression System Model, from [51]

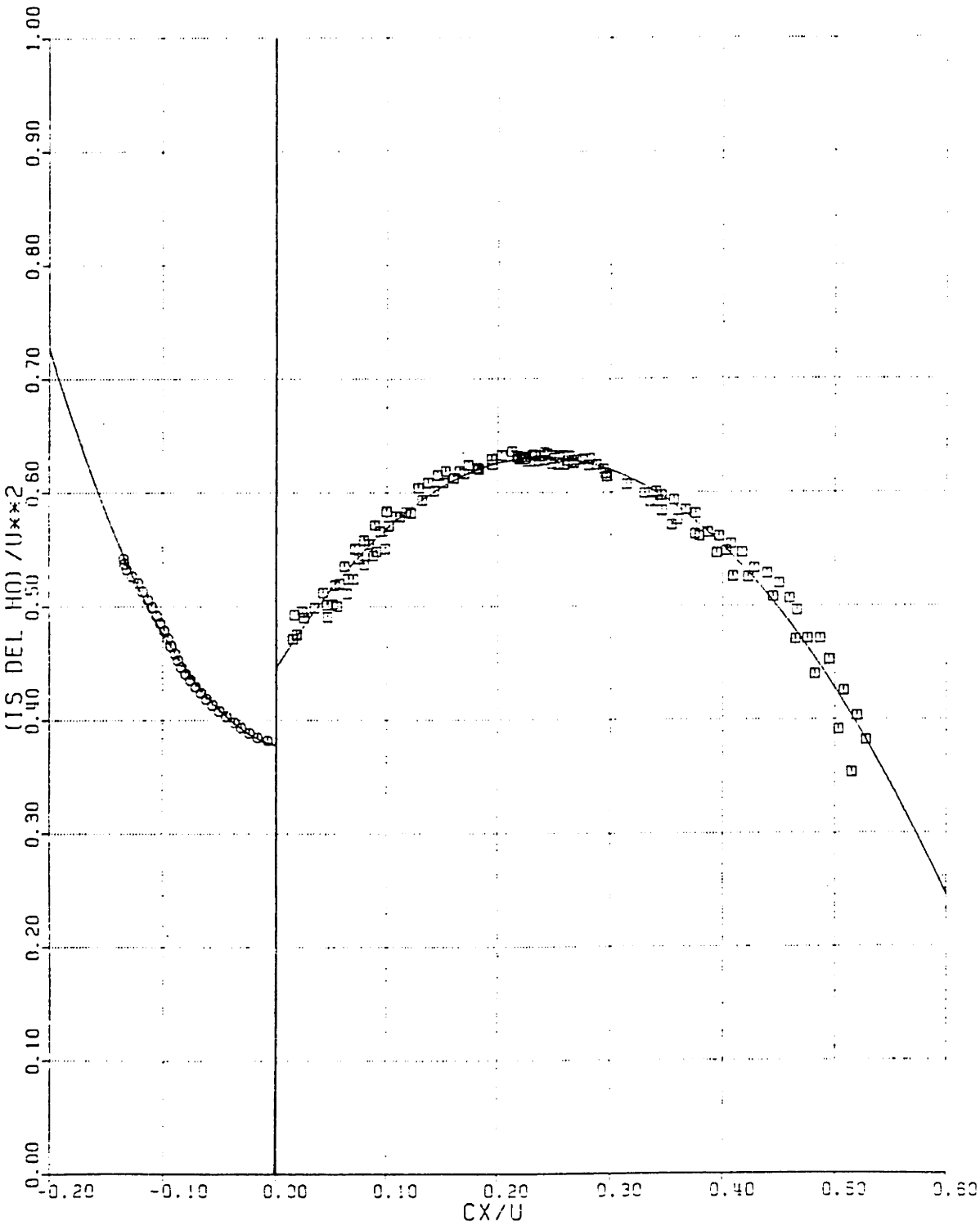

Fig. 5.2 Compressor Pumping Characteristic

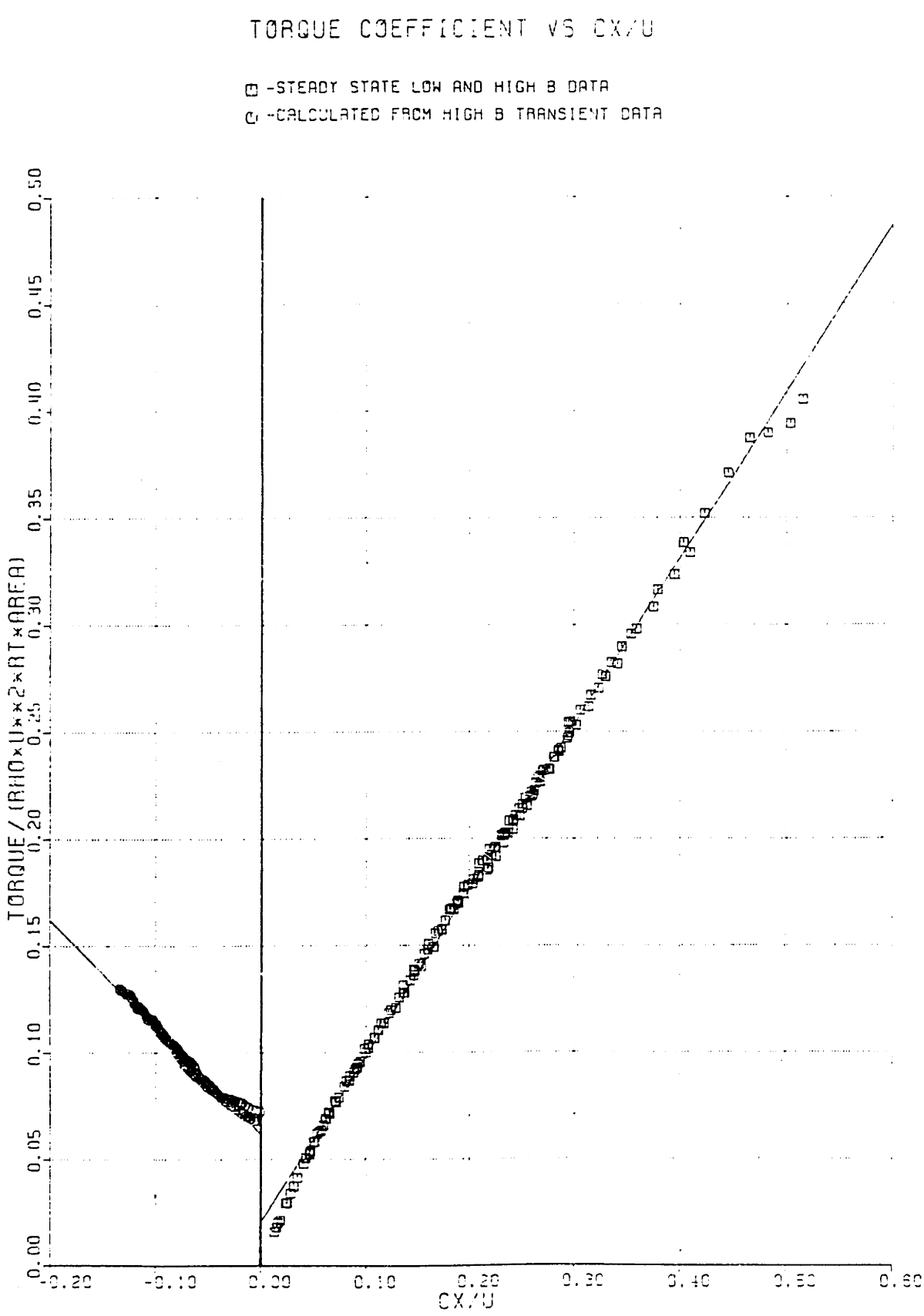

Fig. 5.3 Compressor Torque Characteristic

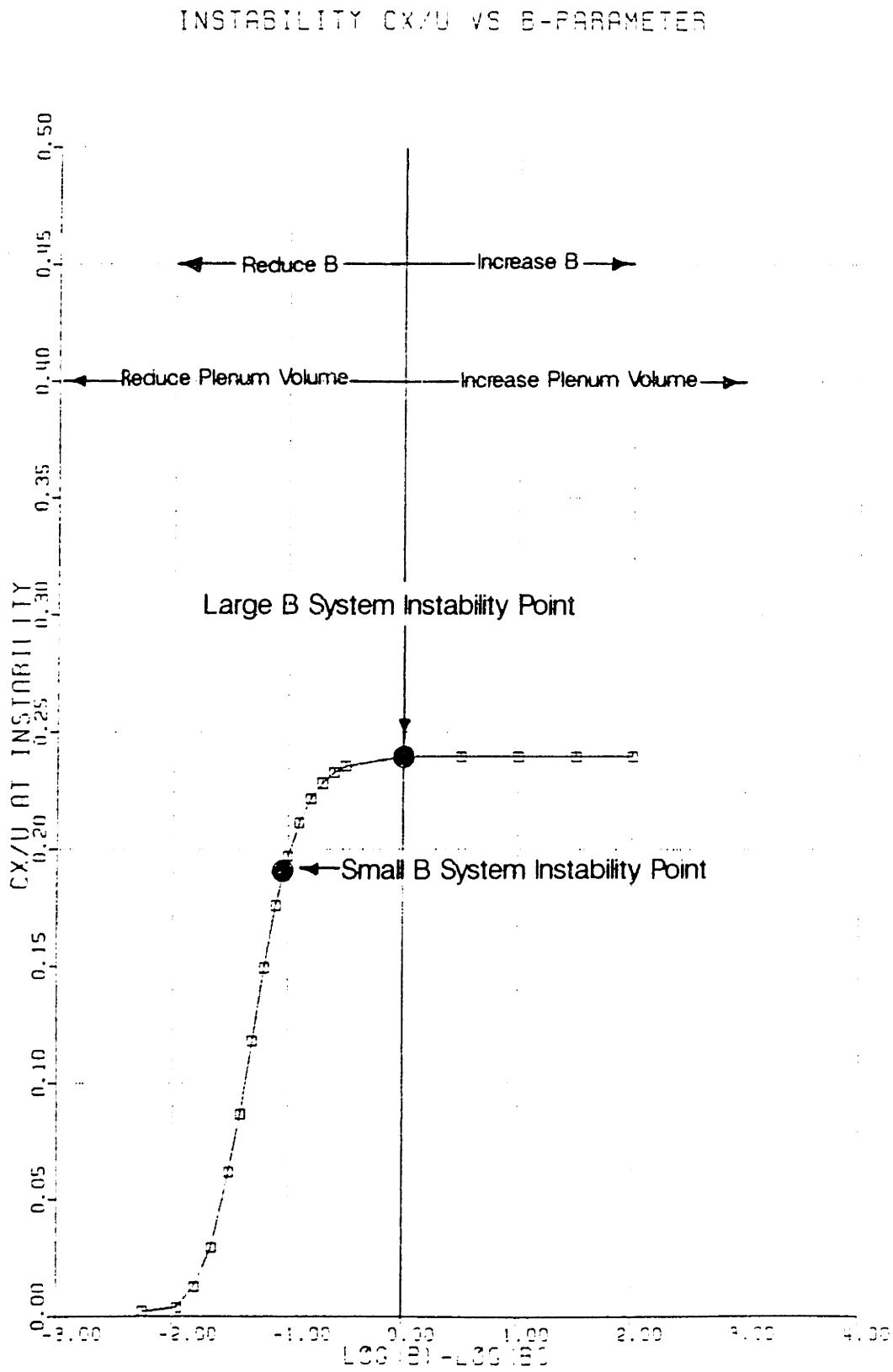

Fig. 5.4 Instability Cx/U vs B-Parameter for Quasisteady Model(A=constant)

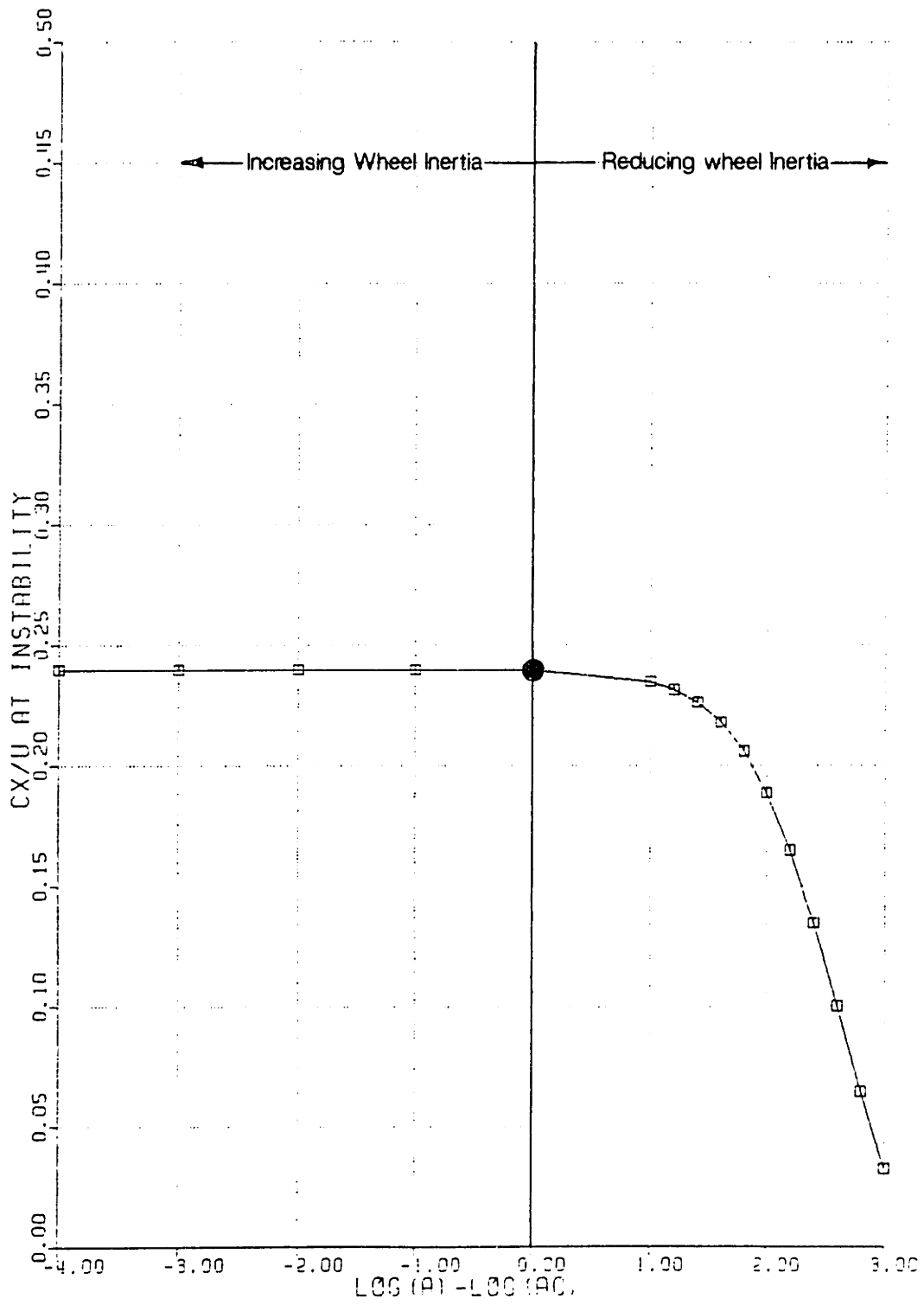

Fig. 5.5 Instability Cx/U vs A-Parameter for Quasisteady Model(B=constant)

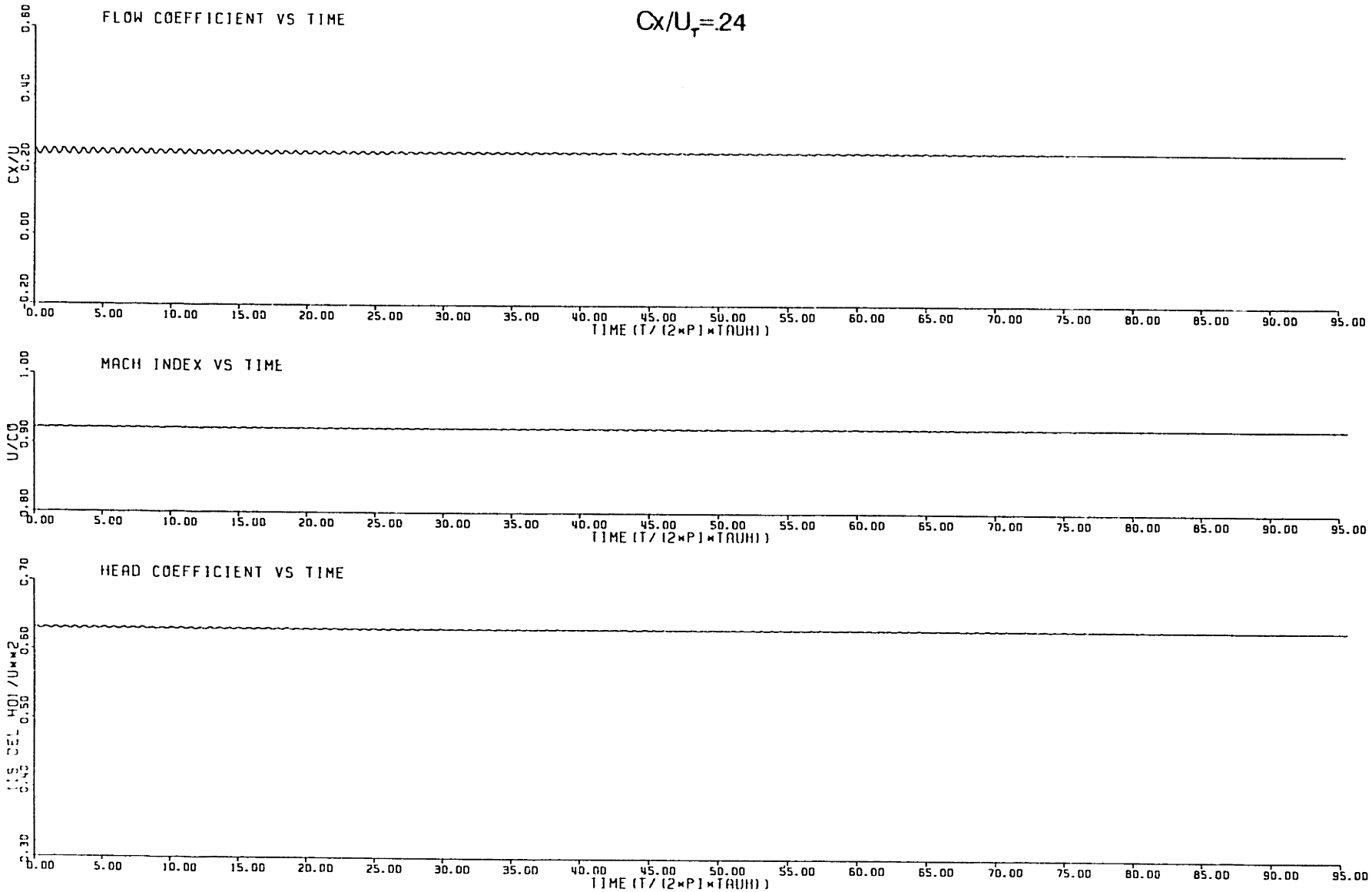

Fig. 5.6 Quasisteady Model Large B System Parameters vs Time($\phi_\tau = .24$)

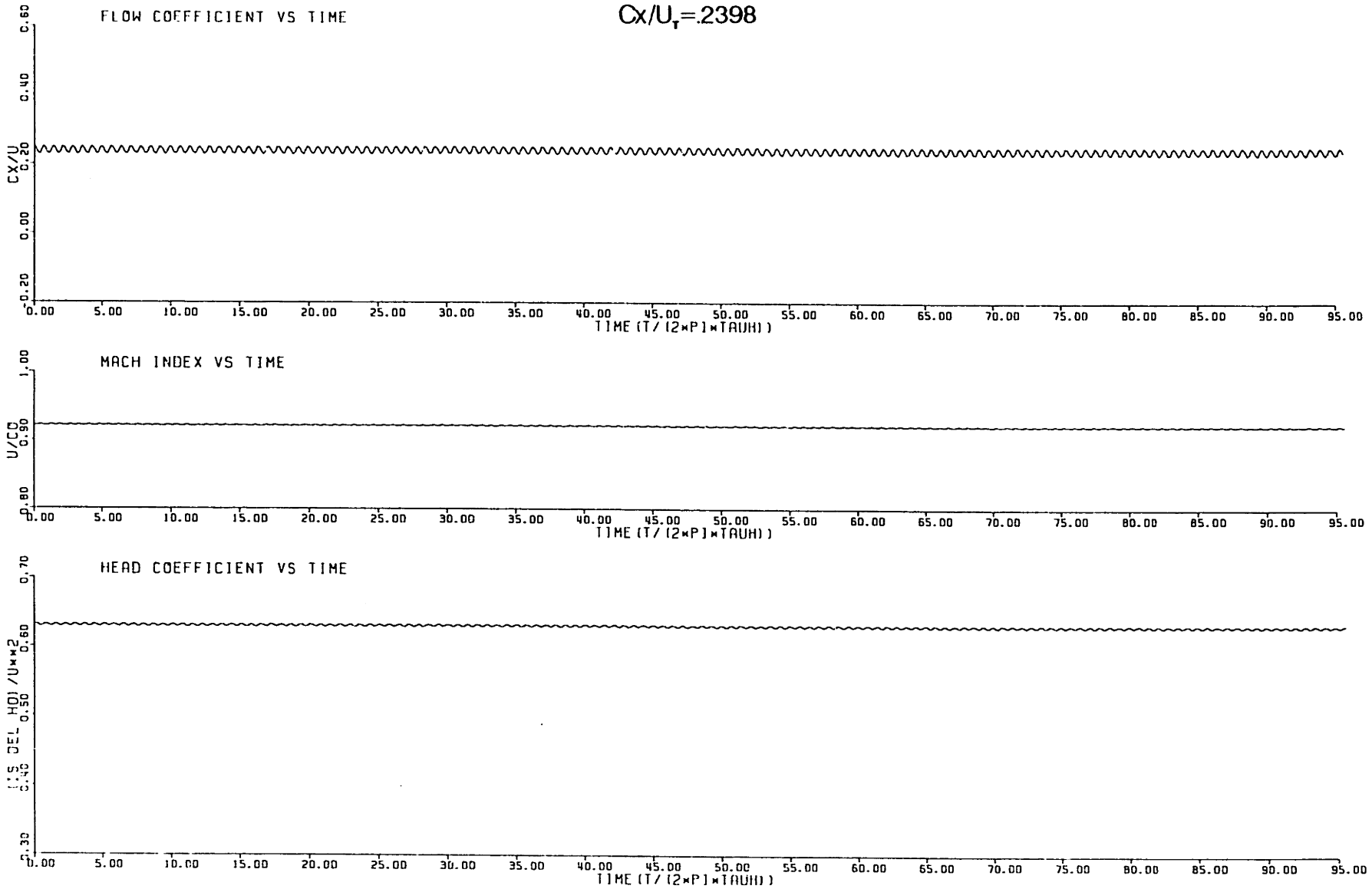

Fig. 5.7 Quasisteady Model Large B System Parameters vs Time(ϕ_T = .2398)

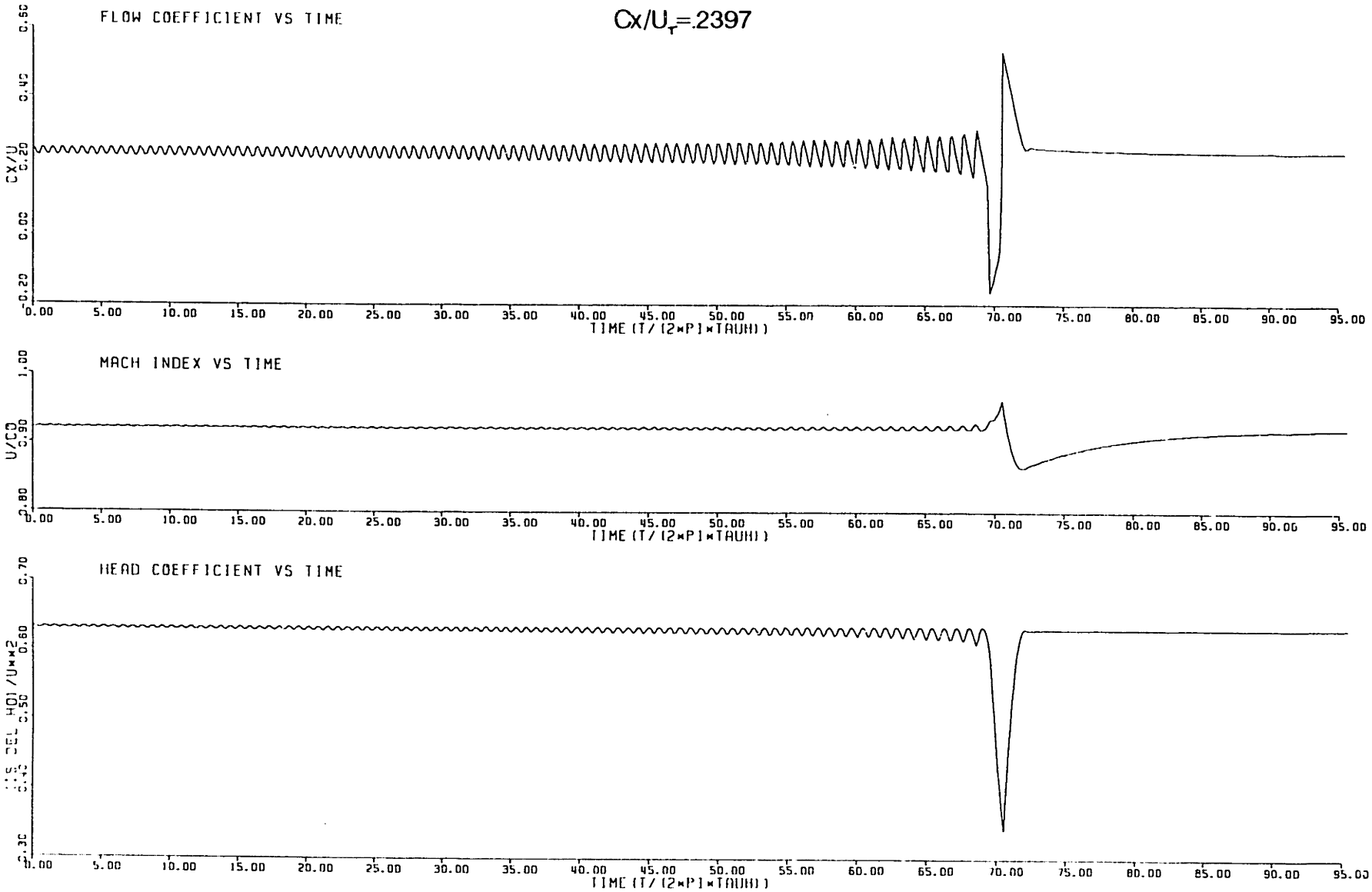

Fig. 5.8 Quasisteady Model Large B System Parameters vs Time(ϕ_T = .2397)

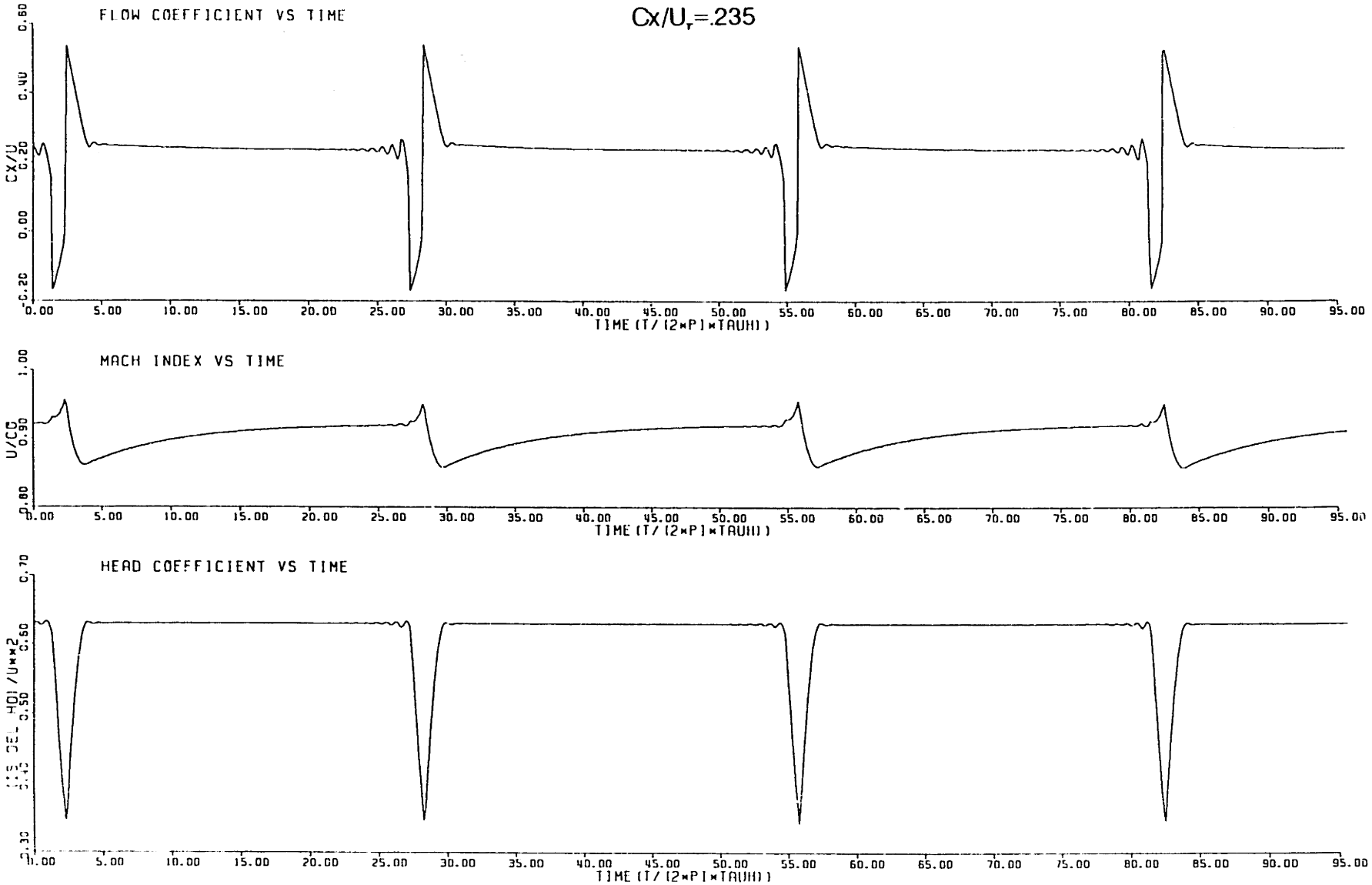

Fig. 5.9 Quasisteady Model Large B System Parameters vs Time(ϕ_r = .235)

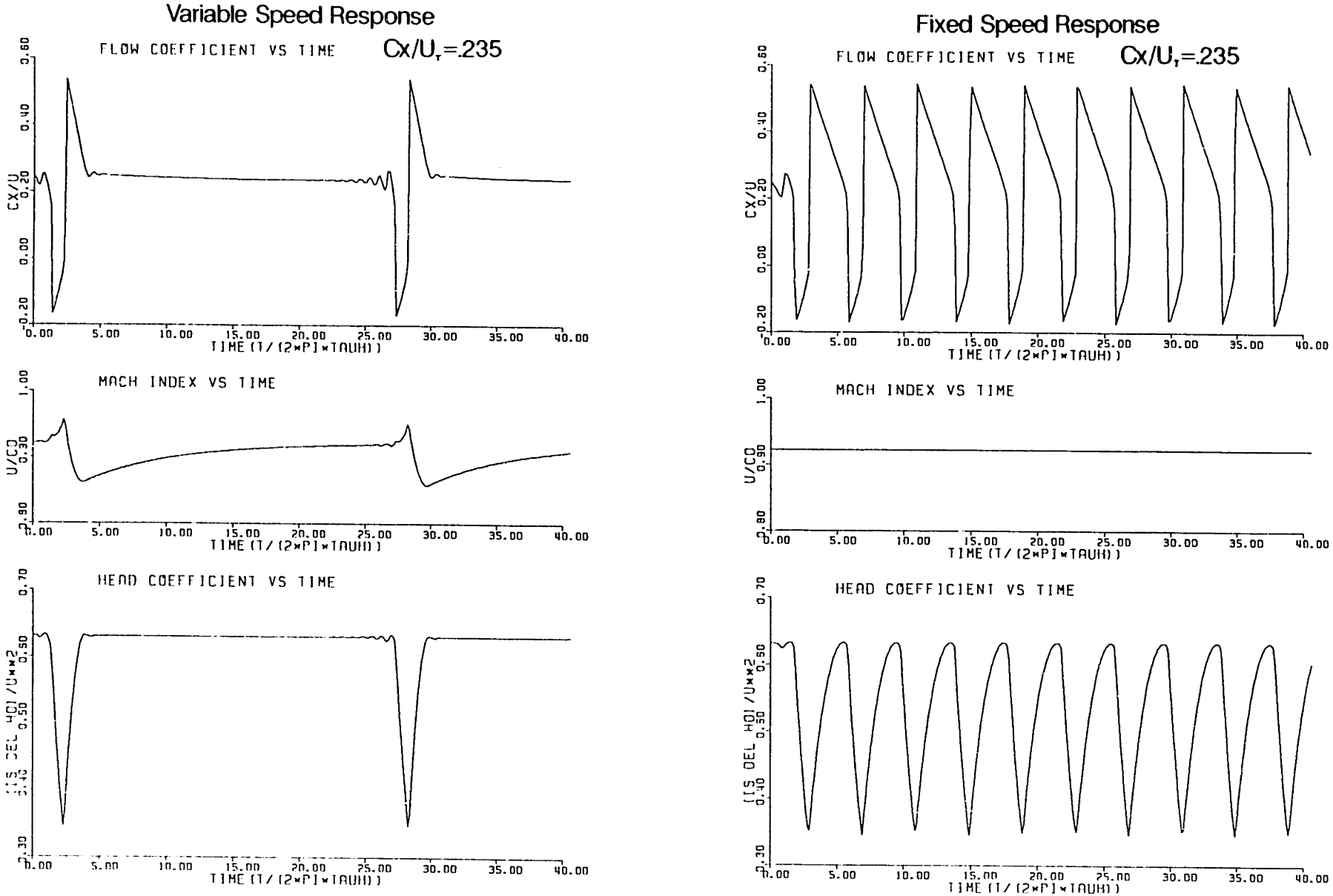

Fig. 5.10 System Response with and without Speed Fluctuations(ϕ_τ = .235)

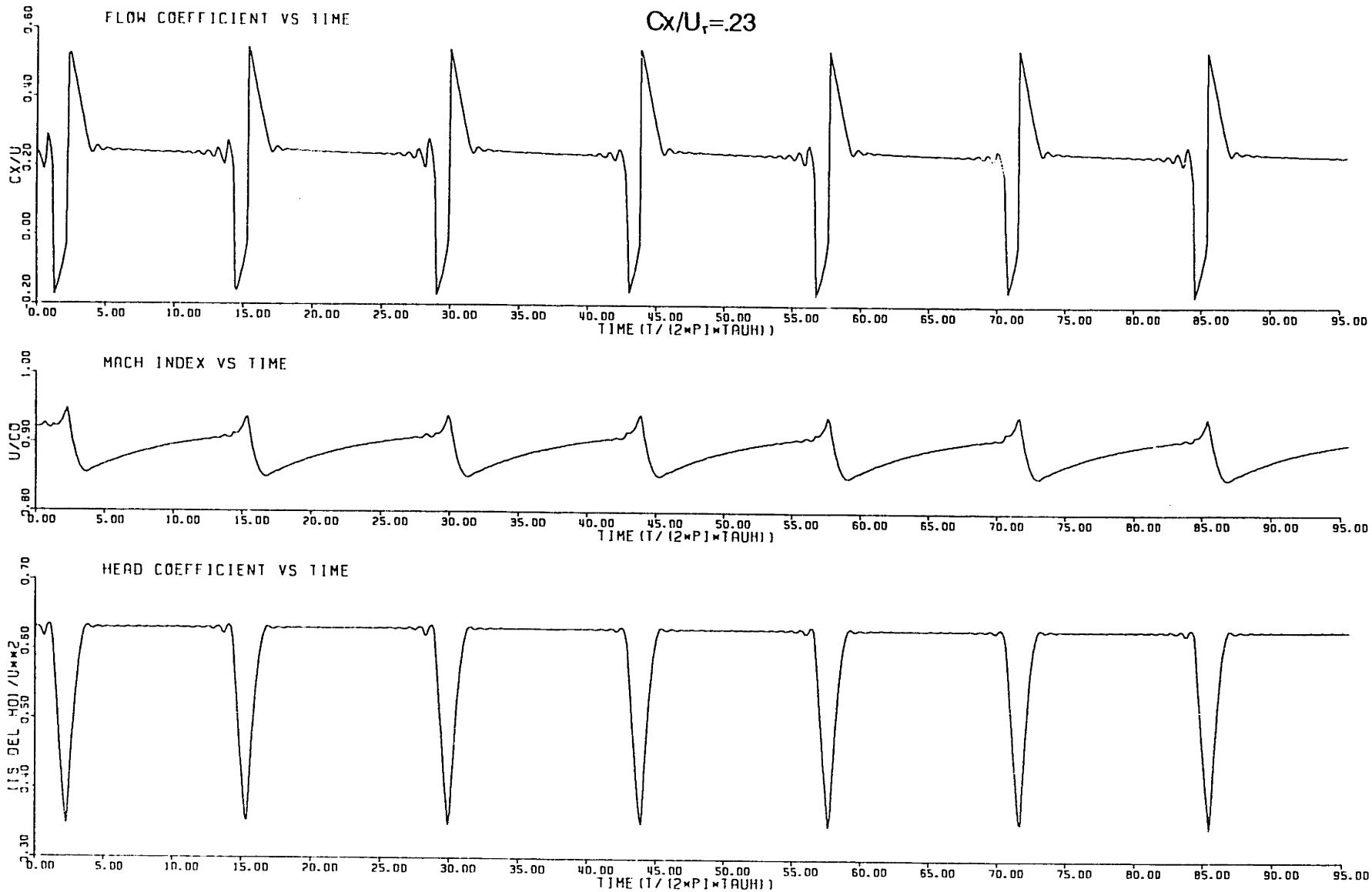

Fig. 5.11 Quasisteady Model Large B System Parameters vs Time(ϕ_r = .23)

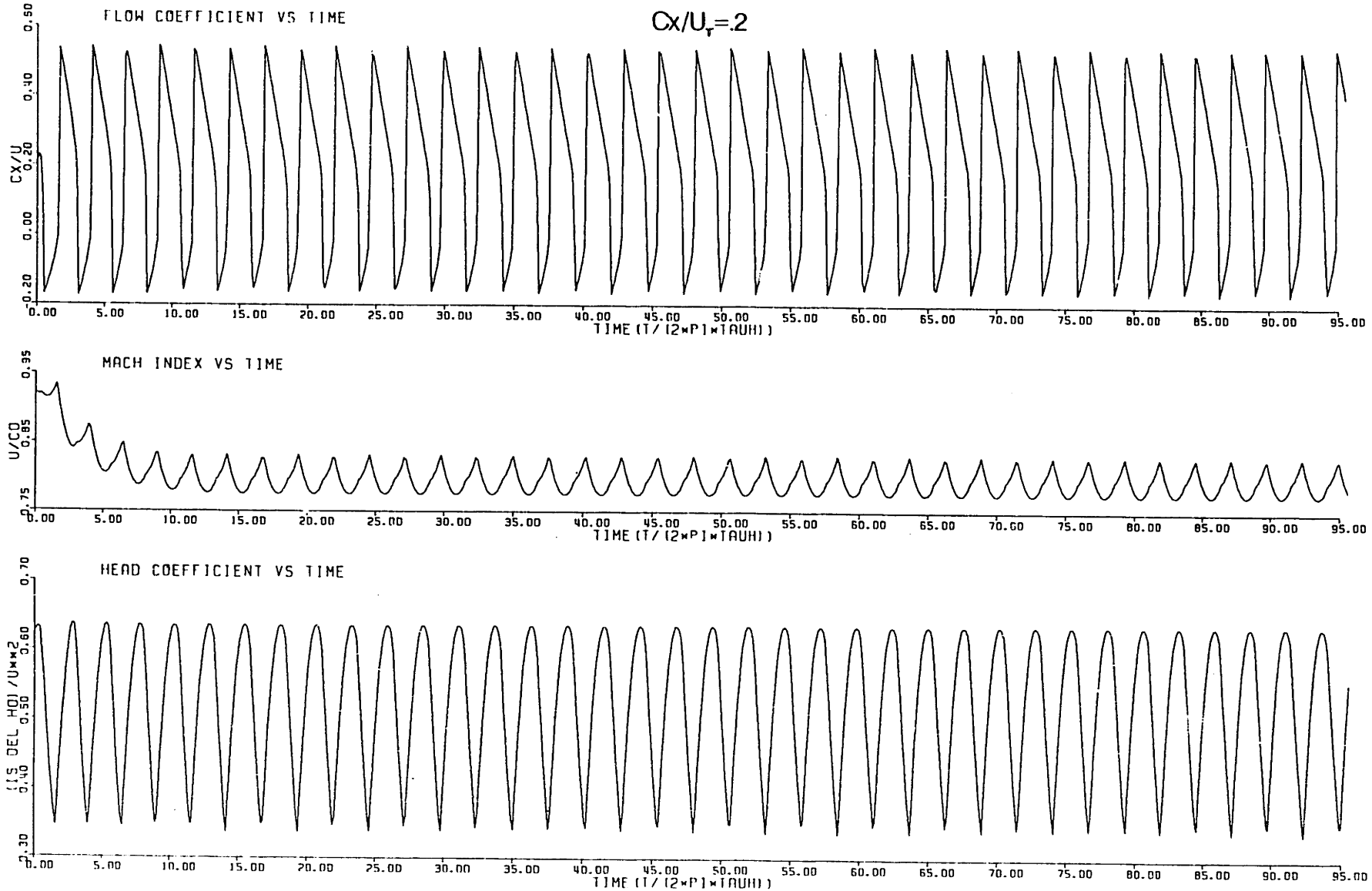

Fig. 5.12 Quasisteady Model Large B System Parameters vs Time(ϕ_r = .20)

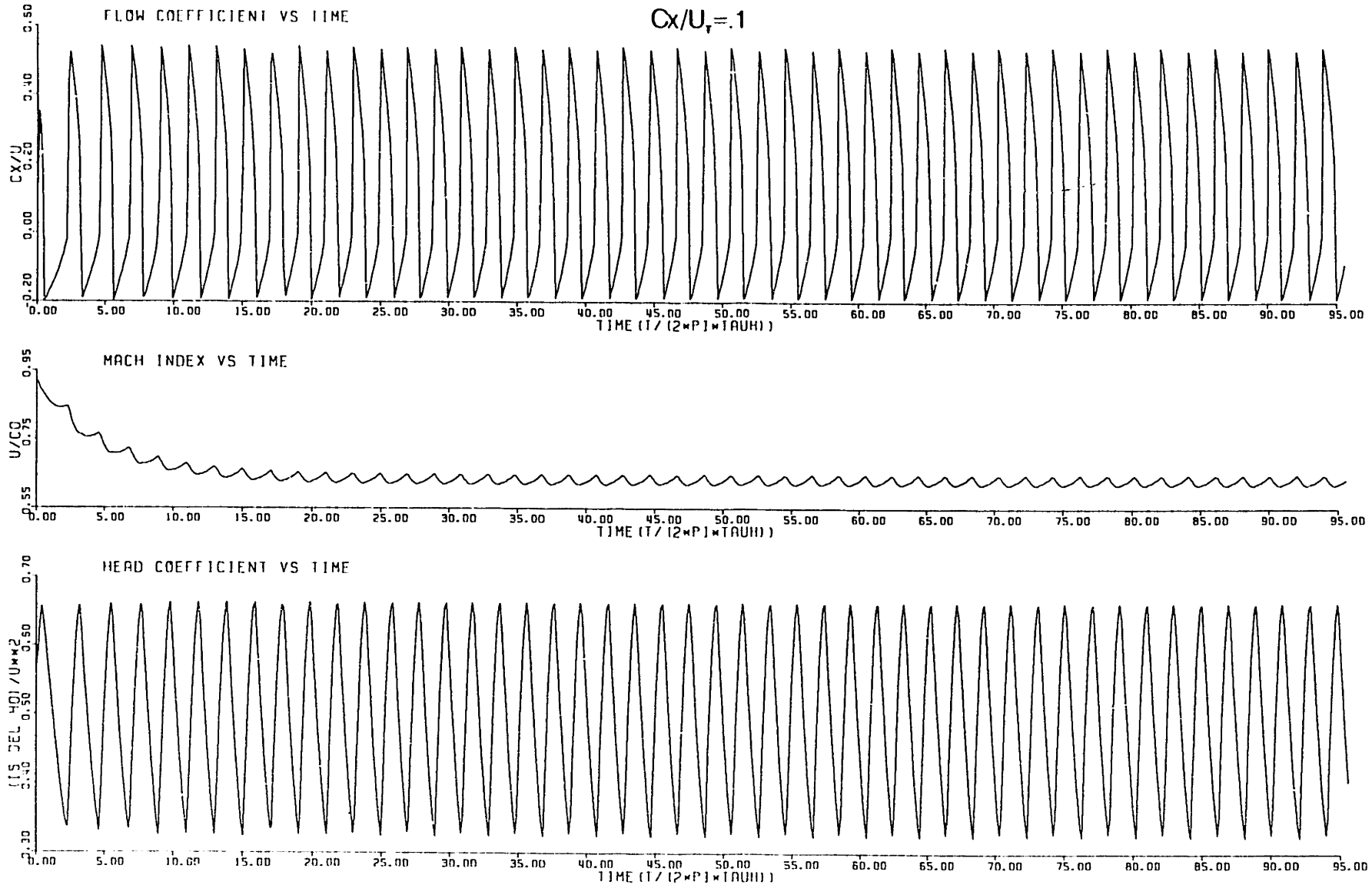

Fig. 5.13 Quasisteady Model Large B System Parameters vs Time(ϕ_r = .1)

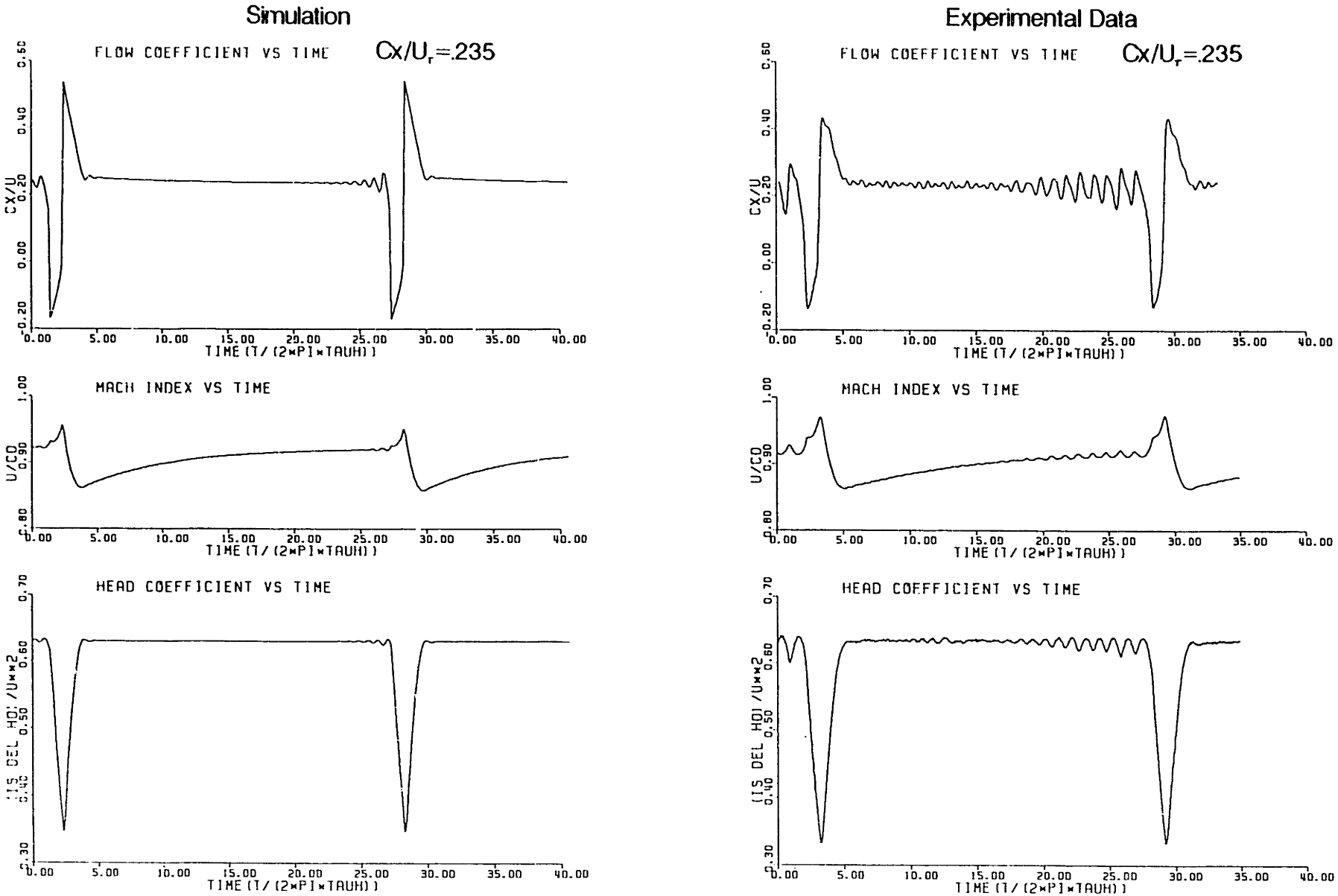

Fig. 5.14 Quasisteady Model Simulation Results vs Experimental Results(ϕ_r = .235)

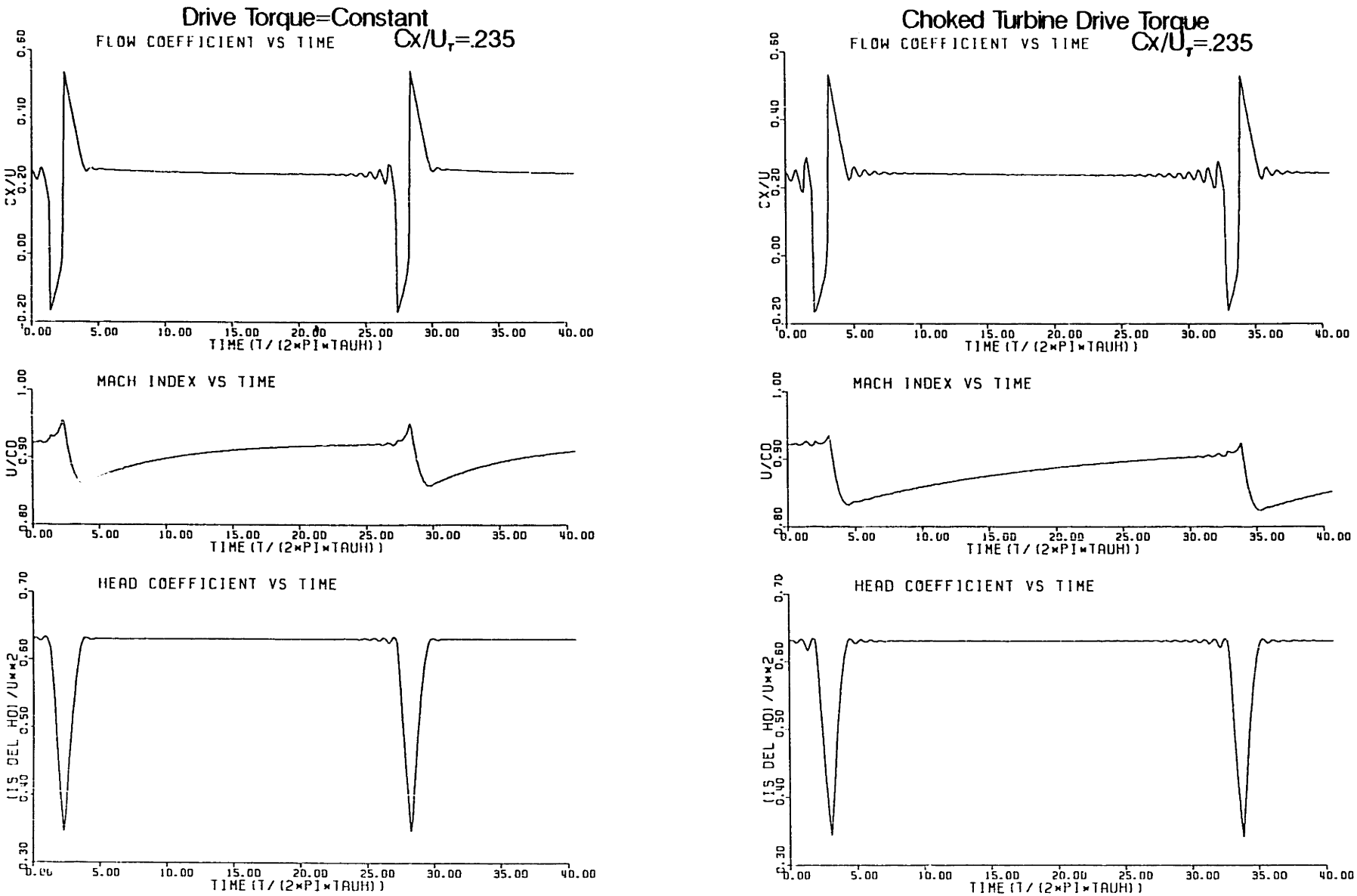

Fig. 5.15 Constant Drive Torque vs Choked Turbine System Response(ϕ_T = .235)

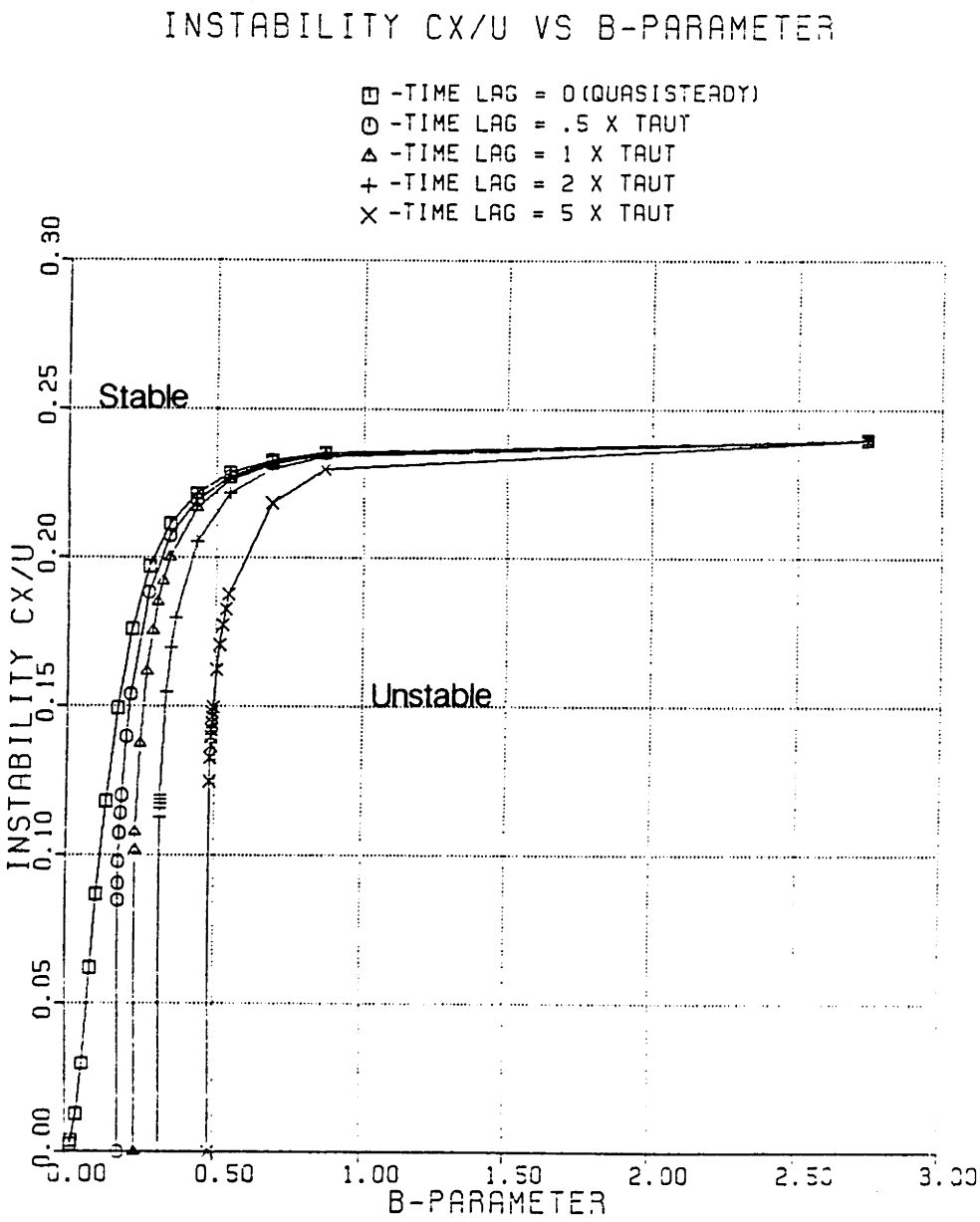

Fig. 5.16 Instability Cx/U vs B-Parameter with Compressor Time Lags

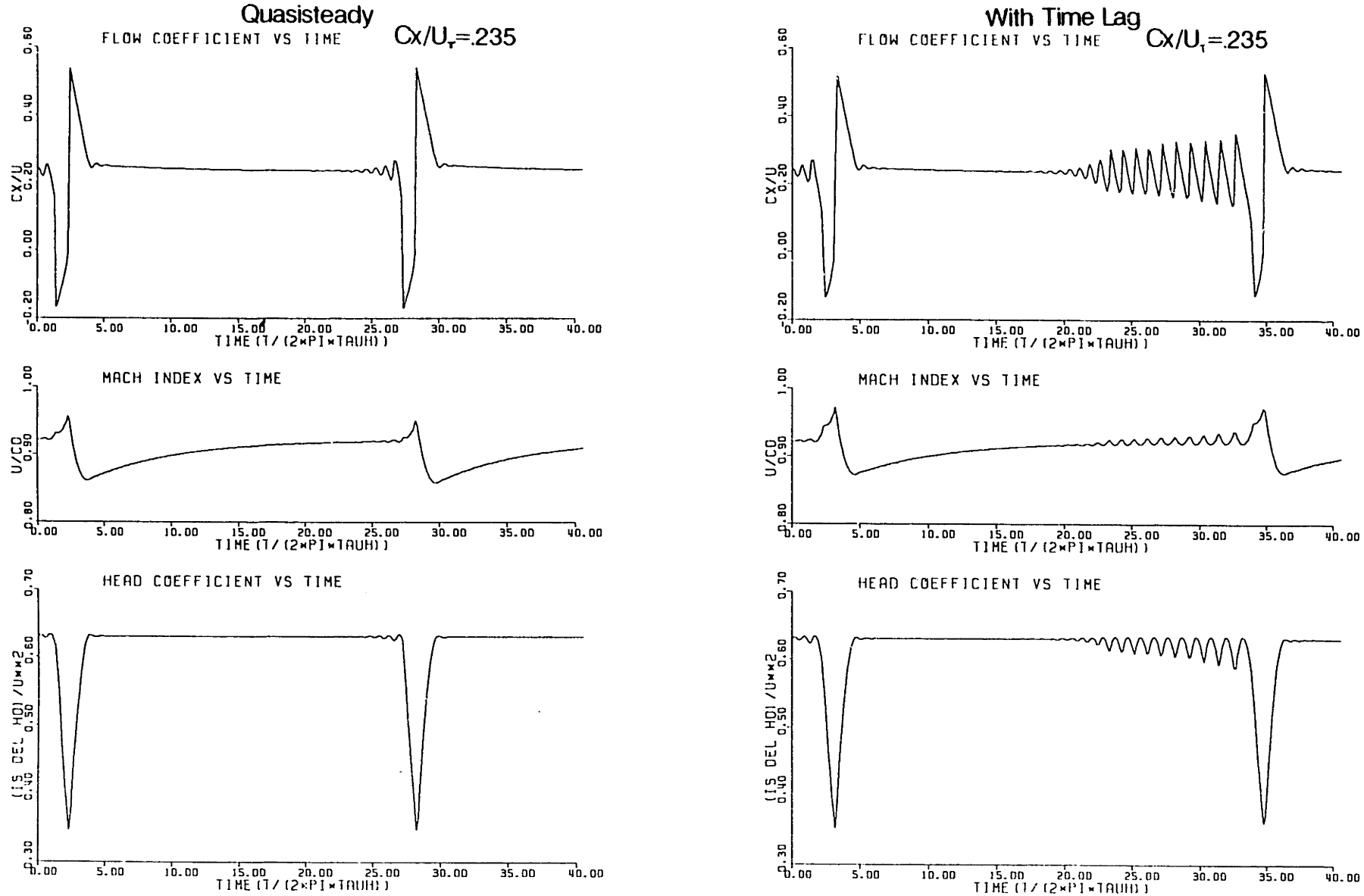

Fig. 5.17 Quasisteady Model Results vs Time Lag Model Results

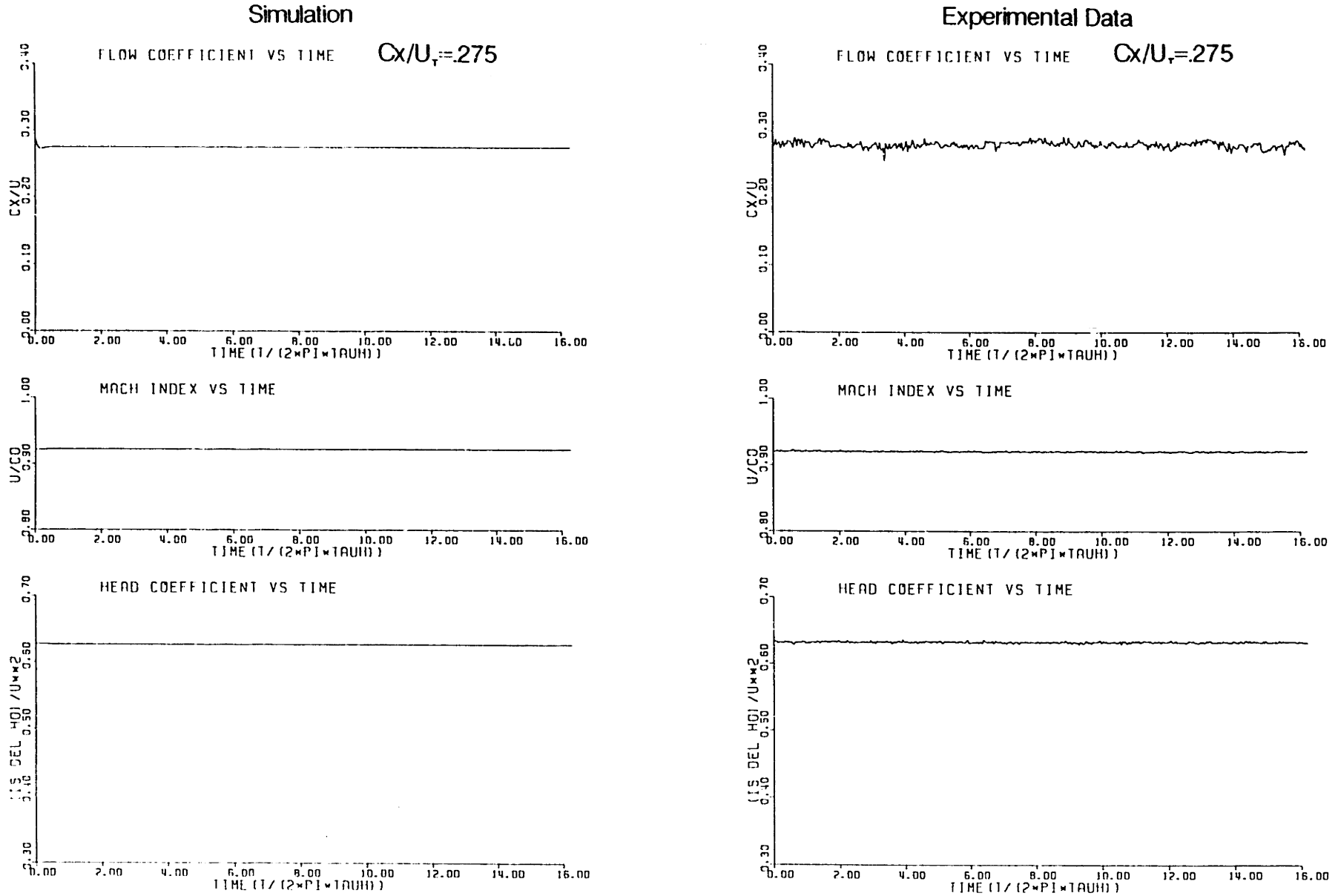

Fig. 5.18 Time Lag Model Results vs Experimental Results in Non-Surge(ϕ_T = .275)

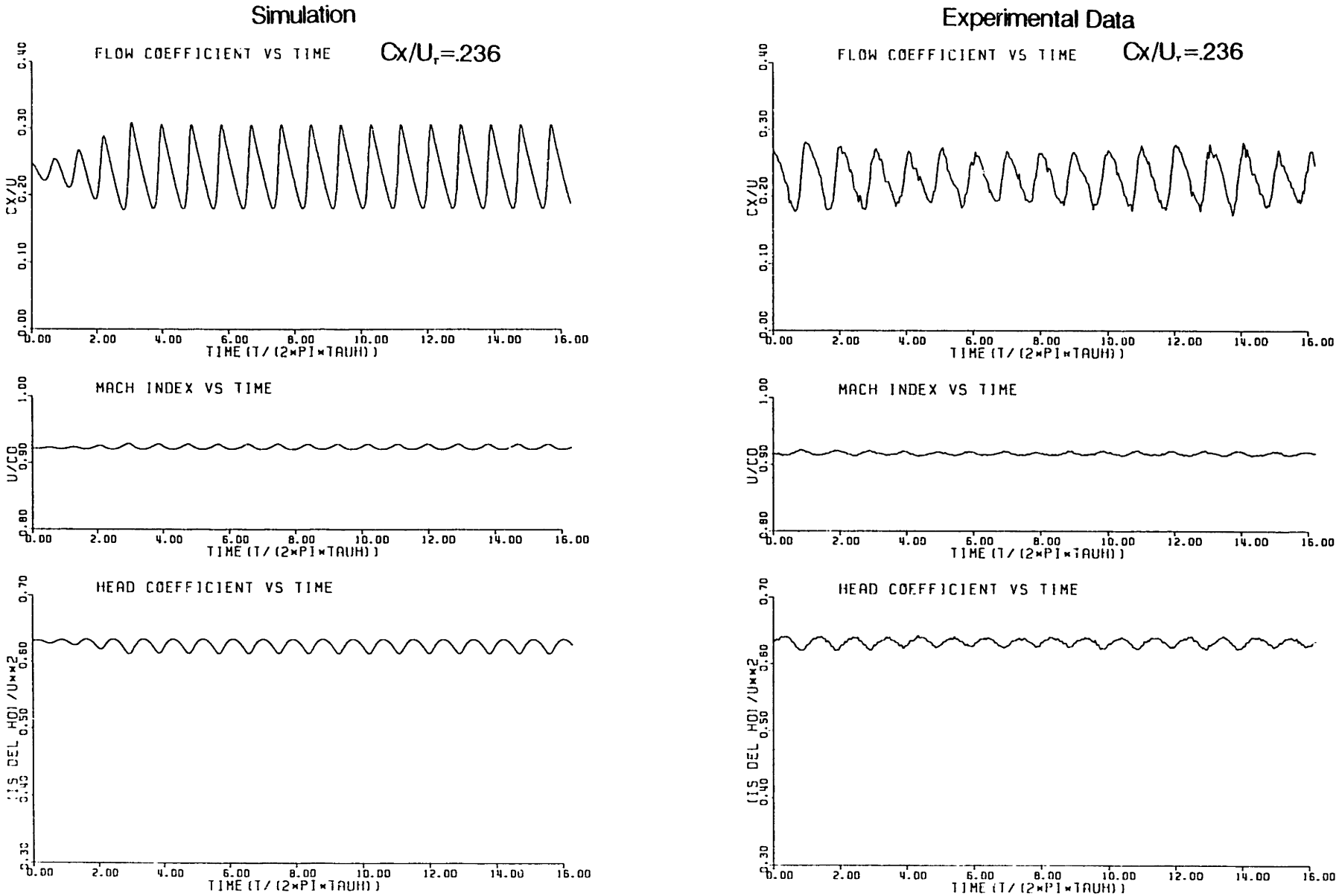

Fig. 5.19 Time Lag Model Results vs Experimental Results in Mild Surge(ϕ_r = .236)

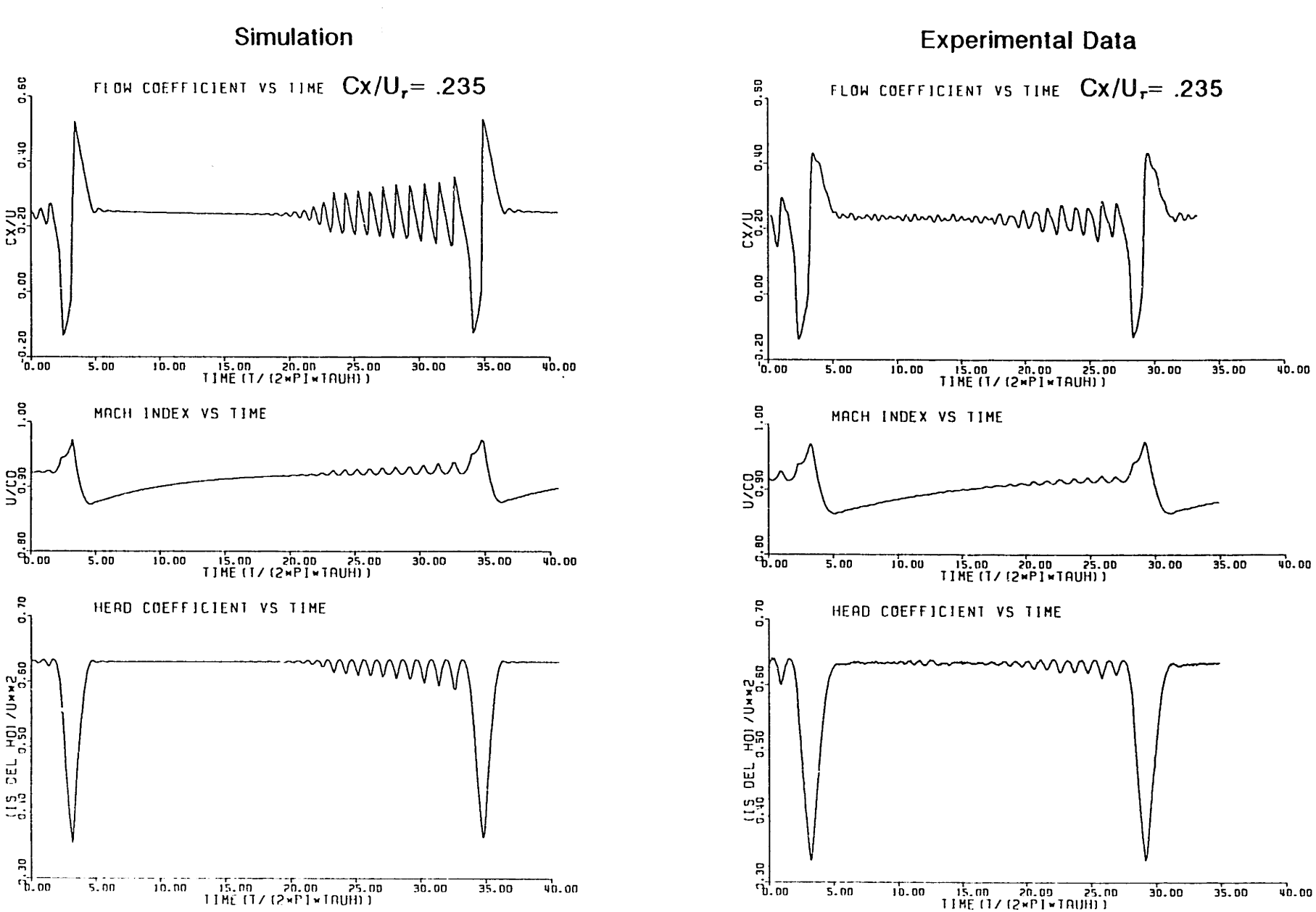

Fig. 5.20 Time Lag Model Results vs Experimental Results in Deep Surge(ϕ_T = .235)

CHAPTER 6

SUMMARY AND CONCLUSIONS

6.1 Centrifugal Compressor Surge Initiation Flow Phenomena Summary

Surge initiation flow phenomena and the dynamics of centrifugal compressors operating in surge have been examined in this thesis. These topics were investigated experimentally by means of time resolved and low response data taken in two compression systems of large and small B-parameter and theoretically via a system model.

One topic concerned identifying the flow mechanism and component which "triggers" the overall flow reversal of deep surge. A number of questions were posed in Chap. 1 related to surge initiation and fluid mechanic details of component stall in the centrifugal compressor prior to and during surge. To review, these included the following:

- Which component, impeller, diffuser, volute, etc. is most significant in the stage stalling that initiates deep surge?
- What are the time resolved details of flow breakdown in the stalling component?(axisymmetric?, rotating stall?, progressive?, abrupt? etc.)
- How does an asymmetric scroll influence surge behavior?
- What nondimensional parameters govern the impeller and/or diffuser stall behavior?
- What do the "hidden" low flow and backflow characteristics of the compressor look like?
- How does compressibility influence the stall process?

For a compressor with a continuous time independent characteristic, the results of a simple stability analysis in Chap. 1 showed the instability point to depend on three quantities, the compressor characteristic slope C', the throttle characteristic slope T', and the magnitude of the B-parameter. Instability and surge initiation occurs when the overall compressor characteristic slope $C' > 1/(B^2 T')$. The overall

compressor characteristic slope C' is the sum of the impeller characteristic slope(total to static) and the vaneless diffuser slope(static to static). Hence the surge initiation point is controlled by both the impeller and vaneless diffuser characteristic slope behavior. Time resolved and low response data showed the impeller characteristic to be highly stabilizing at high flows(steep negatively sloped characteristic) and destabilizing (neutral or positively sloped) in the flow region where surge initiation began in the compressor. Conversely the vaneless diffuser was found to be very destabilizing(steep positively sloped characteristic) at high flows and less destabilizing(less positively or neutrally sloped characteristic) near the surge point. The impeller, by its more rapidly changing characteristic slope(minus to plus) at the large B surge point, was seen to be the more significant component in surge initiation.

Several types of impeller stall were seen in the data of both Chap. 3 and 4. Among the types seen in the data are axisymmetric inducer stall(dominant), asymmetric volute induced inducer stall(dominant), and rotating stall(weak). All of the types of impeller stall observed were progressive rather than abrupt in their effect on the impeller actuator characteristic. The impeller stall occuring was concentrated mainly at the inducer tips, generally non-rotating, and circumferentially asymmetric due to the presence of an asymmetric downstream volute. In the time domain for the large B system, inducer tip stall and flow reversal at the tongue occured well in advance of the overall flow reversal of deep surge. In the mild surge precursor period to deep surge, the inducer tip stall appeared transiently at the surge massflow minima. Time resolved and time averaged data also showed the most severe stalling of the inducer tips to occur at the volute tongue circumferential position. This was a result of a circumferential flow distortion established by the volute when operated off its design point. The tongue stall in the impeller increased in severity at higher values of compressor Mach index when the compressor was operated away from the volute design point.

Some rotating stall was seen in the impeller time resolved static pressure data but was very weak relative to the overall inducer tip stall and volute induced stationary stall observed at the tongue. The rotating stall also appeared to be attenuated when the compressor was operated off the volute match point. Because of its overall weakness relative to the other types of stall seen, rotating stall was

not seen as a major factor in initiating surge.

Data of the vaneless diffuser showed it clearly as a destabilizing element since its characteristic slope is generally positive but the small slope change of its characteristic with flow at the surge onset point highlighted its less important role in initiating surge. The diffuser Cp was seen to decline at low flows but not until inducer tip stall was well established. The data showed that the diffuser was actually more destabilizing at high flows than at low flows where surge was initiated. At the high flows, the impeller's highly negatively sloped characteristic stabilizes the overall stage.

The volute influences surge behavior by creating a circumferential flow distortion in the compressor when operation occurs away from the volute design point. The asymmetry induced by the volute interacts with both the upstream vaneless diffuser space and the impeller. The most significant effect of the volute is to set up a low flow circumferential region near the volute tongue when operated below the volute match point. At the tongue, both the inducer tips and vaneless diffuser are more severely stalled and their efficiency more depressed, and the effect is more extreme as compressor Mach index increases.

Several parameters govern impeller and diffuser stall behavior. Among the most important for impeller behavior are the reduced frequency $\tilde{f}$, the incidence flow angle at the impeller tips, the channel inductance given by (2L/R), and the Mach index, which governs the level of compressibility effects present. Relatively small incidence angles of flow are seen to stall the thin inducer blade tips of the impeller. The reduced frequency is important for operation in surge because the response of the impeller blading and vaneless diffuser depends on it. When the reduced frequency is much less than one, the compressor behaves quasisteadily. High channel inductance attenuates circumferential flow distortions in impeller channels induced from upstream and downstream pressure disturbances and suppresses rotating stall. As the Mach index increases, the flow coefficient of minimum circumferential pressure distortion(volute match point) increases. The volute induced local stalling of the inducer tips at the tongue also worsens the overall stage performance as Mach index rises.

The vaneless diffuser behavior is governed chiefly by the swirl parameter. The overall pressure rise coefficient Cp of the vaneless diffuser was seen to decline as

the swirl parameter was increased. Cp was not very sensitive to inlet Mach number for the range of conditions tested.

Circumferential distortions induced by the volute penalize the diffuser and impeller performance relative to their performance with axisymmetric flow. The volute mismatch parameter V may be important in correlating the additional losses induced by the volute when the compressor deviates from axisymmetric flow conditions.

The hidden low flow characteristics, which were exposed in the small B stabilized system, is smooth and continuous for forward flow to shutoff. The backflow characteristic is negatively sloped. There is a pressure rise hysteresis or discontinuity at shutoff depending on whether approached from forward or reverse direction which is a significant effect in modeling deep surge behavior. Some of this discontinuity is an inlet gas temperature effect. In the transition from back to forward flow, the compressor reingests the hot gases from the deep surge plenum blowdown process and therefore operates temporarily at lower corrected speed. When the proper inlet temperature is used to calculate the headrise coefficient, some of this observed hysteresis in the characteristic disappears. Some of the hysteresis is due to a time lag effect associated with inducer stalling.

6.2 Summary of Centrifugal Compressor Surge Dynamics

The second topic in this thesis was the overall dynamics of centrifugal compressors operating in surge. These are important when modeling the compression system dynamic behavior in surge. Many of these questions arose from the results of Toyama[51] and modeling efforts carried out in Dean and Young[12]. From their modeling efforts, several types of behavior were postulated to be occuring in the compressor during surge. These included:

- The time mean actuator characteristic is steeper than the instantaneous characteristic.
- The rotor wheel inertia was important.
- The compressor is time dependent and does not remain instantaneously on a unique "actuator" characteristic.

From these postulated behaviors, a second set of research questions regarding surge dynamics evolved to be addressed in the thesis. These included the following:

- What are the critical system parameters associated with surge in centrifugal

compressors?

- How does the variation of system parameters effect the position of the surge line?
- Does the actuator characteristic exhibit appreciable hysteresis?
- How is the compressor's instantaneous operation in surge described on a compressor map?
- How significant are real time lags associated with such unsteady fluid mechanic phenomena such as stall cell growth, and vortex shedding?
- How significant are apparent time lags associated with speed fluctuations?
- What degree of complication is required in a system model to properly predict the system surge behavior?

In this thesis, we have emphasized the effect of the B-parameter on surge performance. For dynamics, it is clearly the most important parameter. The main requirement for surge is a positively sloped characteristic. When this is met, then B governs where the instability will occur. Lowering B stabilizes a system and moves the surge line towards shutoff. This was seen in the small and large compressor maps.

The characteristic behavior of the compressor at low flows was examined in systems with large and small B. The compressor instantaneous characteristic trajectory at low flows for a large B-parameter system was found to be much flatter than the time averaged value in a low B-parameter stabilized system. In essence, the instantaneous characteristic lagged the time averaged characteristic. One mechanism that accounts for the difference between these two measured characteristics was the differing circumferential extent of the non-rotating inducer tip stall present in the two measurements. In the large B results at shutoff, the inducer tips were stalled fully only at the tongue. In the small B results however at shutoff, the inducer tips were fully stalled over the entire circumference. The flatness of the large B instantaneous characteristic at low flows contrasts with the more abrupt type of characteristic typical of multistage axial compressors operating in surge and leads to slow growth of the surge massflow instability.

To analyze the compression system dynamic behavior, a model was formulated which allowed the speed of the compressor to fluctuate. In this system model, the compressor was assumed to always operate quasisteadily on a unique time independent actuator characteristic. Results of the quasisteady model simulation compared

closely with experimental data and showed that small speed fluctuations are responsible for the time dependent surge "triggering" behavior commonly observed in many practical centrifugal compression systems. This behavior consists of periodic deep surge blowdowns separated by a throttle dependent, variable length, quiet and mild surge precursor period. The periodic deep surge behavior of the system is due only to the speed variations since the compressor is assumed to be quasisteady with a continuous, smooth characteristic in forward flow. The triggering effect is not a result of transitions from primary to secondary legs of an abrupt type actuator compressor characteristic. When the speed is held constant, the long precursor period between blowdowns seen in the variable speed model results disappears.

The importance of speed fluctuations in surge behavior is governed by the inertia parameter A. As A is increased, speed effects become more important. Lowering the turbospool rotor inertia(which increases A) adds a stabilizing effect to mild surge oscillations. For practical values of A, the effect on the initial instability point is small relative to constant speed, and the principle effect of speed variations is seen in the time domain dynamics of the nonlinear case where the excursions from an equilibrium point are large.

To model the effect of unsteadiness in the inducer stall process, a small first order lag in the compressor characteristic was introduced into the variable B model. The time lag was on the order of the throughflow time of the compressor, since the lag was to simulate a vortex being shed off the stalling inducer and convected downstream through the impeller and diffuser. When this small lag was introduced into the variable B model, it helped to stabilizing the mild surge oscillations and yielded good agreement with the experimental results. The stabilizing effect of the time lag was stronger than that due to speed oscillations. A stability analysis also showed the stabilizing trend of a first order time lag.

The good agreement with experiment obtained with the dynamic model is encouraging for surge prediction. As a predictive tool of surge behavior, the model should be useful in situations where various forms of external excitation are present. Unsteady throttling and unsteady drive effects which are present in practical turbocharger installations should be amenable to analysis by the model.

6.3 Summary of Contributions

The contributions of this thesis may be listed as follows:

1) A set of detailed time resolved measurements of a centrifugal compressor has been obtained that show inducer stall to be a key items in initiating surge.
2) Instantaneous compressor characteristics are much flatter than the time averaged ones.
3) In surge initiation, the compressor pressure ratio does not drop significantly until after the overall massflow is reversed not prior as is the case in axials.
4) The vaneless diffuser is always destabilizing but does not initiate surge by abrupt stalling.
5) Rotating stall is not found to be of importance for surge initiation.
6) A dynamic model has been developed which includes some of the effects compressibility, speed variations, and time lags.
7) The inclusion of speed effects changes the time behavior of the system substantially from previous models.
8) The results of this model agree qualitatively and quantitatively with the measured experimental system dynamic behavior.
9) Both time lags and speed oscillations are shown to introduce stabilizing effects on compressor behavior in mild surge.
10) The results of this work have laid some of the groundwork necessary in the new field of active control of surge instabilities. The results of this thesis have illuminated some of the details of stall in centrifugal compressors and also provided verification for compressor models used in developing surge control algorithms.

6.4 Implications for Active Control of Surge

Some of the results in this work have some implications for active control of surge in centrifugal compressors. For developing wide range compressors, there are clearly three paths that can be taken to eliminate surge in the desired operating range. One method is to eliminate the positively sloped characteristic which is necessary for the surge to begin in the desired operating range. Of course, this is the most difficult, since the underlying fluid mechanic stalling processes in the machine must be understood and then closely controlled in each component. A second method is to lower B sufficiently so that even when operating on the positively

sloped characteristic, the compression system is stable. Many times, this is impossible to achieve in practice due to the ducting requirements in the application.

If neither of these two methods are possible, a third option has emerged. This is active control of surge instability. In an active control strategy, the object is to generate a counter disturbance in the blading or plenum which will cancel the self excited initial instability of the uncontrolled system. Such control has been demonstrated at low tip Mach numbers on a centrifugal compressor by Haldemann, Pinsley, Greitzer, and Epstein[29] here at G.T.L. The strategy is to prevent the instability from growing to a large size by the introduction of a counter phased disturbance. If done correctly, the power required to do this can be insignificant compared to the shaft power absorbed by the compressor.

The type of control stategy required to control compressor surge depends mainly on the type of compressor characteristic envolved. If the compressor characteristic is of the abrupt hysteresis type such as for a multistage axial compressor, then the controller must control the onset of rotating stall which is the fluid mechanic mechanism causing the "abruptness". This is discussed by Chen[6]. If the compressor is smooth and continuous up to shutoff, then the control strategy requires generating a disturbance near the Helmholtz frequency. This may be a fairly simple control problem compared to the job of trying to inhibit the onset of rotating stall.

The dynamic behavior observed and analyzed in this thesis is significant to the effort to actively control surge instabilities in centrifugal compressors. The flatness and abrupt-free nature of the instantaneous actuator compressor characteristic and slow growth of the surge instability observed should allow a relatively simple active control strategy to be successfully implemented to stabilize the system. The mild surge precursor period observed due to speed fluctuations also increases the chances that an implementation of active control will be successful in the stabilization process.

The dynamic model developed may also be of use for work in active control strategies on practical compression systems since it includes some compressibility, speed, and time lag effects, which are not accounted for in the simpler surge models. These effects may have some impact on the controller algorithms to be explored in the years ahead in the active control effort.

6.5 Recommendations for Future Research

Several areas of investigation will prove fruitful to realizing the goal of wide range surge-free centrifugal compressors. Some experimental work should focus on the inducer tip stall flow field particularly in the circumferential region of the compressor nearest the tongue. It can not be overemphasized that this should be done in a system of very small B so that the overall compression system remains stable when the tip stall occurs. One particularly useful instrument for such 3-D flow field measurements is the laser velocimeter. The results of this work may provide a basis for controlling the tip stall.

More experimental research is needed on the effect of the downstream volute. For wide range compressors, improvements might be made in surge margin if the volute distortion could be reduced over a wider operating range. The volute spoils much of the hard won gains in impeller efficiency by creating a circumferentially nonuniform flow off design. Some gains are possible in range if the compressor could be operated in a more axisymmetric manner as the impeller designer intended. The induced flow field asymmetry and the loss mechanisms inside this component at off-design is not well understood and both theoretical and experimental work should be carried out. A goal of such work would be to quantify the efficiency penalty from axisymmetric performance and losses associated with this diffusing component. This would be useful in predicting surge in practical systems where such volutes are common.

Another avenue of research is to investigate the performance of the impeller and vaneless diffuser arrangement with an axisymmetric downstream collection chamber or with a series of differently matched volutes. The axisymmetric performance can then be assessed independently of the downstream volute. If rotating stall is a strong player when the downstream collection chamber is axisymmetric, then it can be investigated. Such behavior may be more typical of aircraft engine applications.

Another area of effort involves improvements to the system dynamic model. One improvement would be to specify an axisymmetric curve in the program and incorporate some type of additional penalty for the circumferential flow distortion introduced by the volute. Basically this envolves calculating the flow distortion at volute off design conditions.

The model can also be used to investigate the effects that various forms of

external excitation present in a real system would have on surge behavior. Two main types of excitation exist in turbochargers installed on reciprocating engines. These include unsteady downstream throttling and variable torque drive. A parameter study of the importance of these forms of excitation on surge behavior would be useful for surge prediction in practical engine-turbocharger systems.

The stalling behavior of higher pressure ratio centrifugal compressor impellers and their associated pipe and vane diffusers is still a murky area deserving of some research effort. Particular attention should focus on the abruptness of the overall compressor characteristic in forward average flow. Such information is of importance for active control strategies to be implemented succesfully on practical high pressure ratio machines.

In such high pressure ratio aviation applications, it may be more sensible to attempt to actively control the source of the instability so as to stabilize the stage and gain some efficiency points as well. The success and practicality of any surge control strategy depends on knowing exactly where in the compression system control might be applied most effectively. For the compressor tested in this thesis, such control would naturally focus on the inducer tip stall which is the source of the instability. In analogy with medicine, this amounts to treating the cause of the disease rather than its symptoms.

REFERENCES

1. Abdel-Hamid, A.N., Haupt,U., and Rautenberg, M., "Unsteady Flow Characteristics in a Centrifugal Compressor with Vaned Diffuser"

2. Ball, C.L., "Fan and Compressor Research-An Outlook to the Future", MIT Gas Turbine Laboratory Seminar, 1983.

3. Bammert, K. and Rautenburg, M., "An Analysis of the Non-Steady and Non-Stable Flow Mechanisms in a Radial Compressor Impeller," ASME Paper No. 77-WA/GT, 1977.

4. Braembussche, R.V.D., "Rotating Stall in Vaneless Diffusers," von Karman Institute for Fluid Dynamics Technical Note 145, 1982.

5. Capece, V.R., "Investigation of Turbocharger Stall: I-Facility Design and Construction and Initial Performance Data," MIT GTL and PDL Report No. 165, June 1982.

6. Chen, G-T, "Active Control of Turbomachinery Instability-Initial Calculations and Results," MS Thesis, Department of Aeronautics and Astronautics, MIT, August 1987.

7. Chue, R.C., Hynes, T.P., Greitzer, E.M., Tan, C.S.,"Calculations of Inlet Distortion Induced Compressor Flowfield Instability," AGARD Conference Proceedings 400, "Engine Response to Distorted Flow", 1987.

8. Cumpsty, N.A., Private Communication.

9. Day, I.J., "Axial Compressor Stall," Ph.D. Thesis, Cambridge University Engineering Department, 1976.

10. Dean, R.C., "On the Unresolved Fluid Dynamics of the Centrifugal Compressor." in Advanced Centrifugal Compressors, ASME Gas Turbine Division, 1971, pp. 1-55.

11. Dean, R.C., "The Centrifugal Compressor," Creare Technical Note No. TN-183, 1973.

12. Dean, R.C. and Young, L.R., "The Time Domain of Centrifugal Compressor and Pump Stability and Surge," Journal of Fluids Engineering, March 1977.

13. Dean, R.C. and Young, L.R., "The Physics of Centrifugal Turbomachine Stage Stall, Surge and Stability," Creare TM-382A, 1975.

14. Den Hartog, J.P., Mechanical Vibrations, McGraw-Hill Book Company, New York, 1956, pp. 286-288.

15. Eastland, A.H.J., "Investigation of Compressor Performance in

Rotating Stall: I-Facility Design and Construction and Initial Steady State Measurements," MIT GTL and PDL Report No. 164, June 1982, pp. 95-97

16. Emmons, H.W., Pearson, C.E., and Grant, H.P., "Compressor Surge and Stall Propagation," ASME Transactions, Vol. 27, April 1955, pp. 455-469.

17. Emmons, H.W., Kronauer, R.E., and Rockett, J.A., "A Survey of Rotating Stall - Experiment and Theory," Journal of Basic Engineering, Transactions of ASME, Series D, 1959.

18. Filipenco, V., Private Communication

19. Fink, D.A., "An Experimental Investigation of Centrifugal Compressor Surge and Stall Phenomena in Turbochargers,", MIT MS Thesis, Department of Aeronautics and Astronautics, May 1984.

20. Flynn, P.F. and Weber, H.G., "Design and Test of an Extremely Wide Flow Range Compressor," ASME Paper No. 79-GT-80, 1979.

21. Fowler, H.S., "Experiments on the Flow Processes in Simple Rotating Channels," National Research Council of Canada Report No. ME-229, January 1969.

22. Frigne, P. and Braembussche, R.V.D., "Distinctions Between Different Types of Impeller and Diffuser Stall in a Centrifugal Compressor with Vaneless Diffuser," ASME Paper No. 83-GT-61, March 1983.

23. Gamache, R.N., "Forced Non-Recoverable Stall in Compression Systems," MIT GTL and PDL Unpublished Paper, 1983.

24. Gamache, R.N., Private Communication.

25. Greitzer, E.M., "Surge and Rotating Stall in Axial Flow Compressors, Part I: Theoretical Compression System Model," ASME Journal of Engineering for Power, Vol 98, No. 2, April 1976, pp. 190-198.

26. Greitzer, E.M., "Surge and Rotating Stall in Axial Flow Compressors, Part II: Experimental Results and Comparison with Theory," ASME Journal of Engineering for Power, Vol 98, No. 2, April 1976, pp. 199-217.

27. Greitzer, E.M., "Review - Axial Compressor Stall Phenomena," ASME Journal of Fluids Engineering, Vol. 102, June 1980, pp. 134-151.

28. Greitzer, E.M., "The Stability of Pumping Systems - The 1980 Freeman Scholar Lecture", Journal of Fluids Engineering, Vol. 103, June 1981, pp. 193-242.

29. Haldemann, Pinsley, Greitzer, and Epstein, Private Communication.

30. Harman, R.T.C., Gas Turbine Engineering Applications, Cycles, and Characteristics, Halsted Press Division of John Wiley and Sons, New York, 1981, pp. 65-76, 128-137.

31. Hill, P.G. and Peterson, C.R., Mechanics and Thermodynamics of Propulsion, Addison-Wesley, Massachusetts, 1970, pp. 282-294.

32. Horowitz, P. and Hill, W., The Art of Electronics, Cambridge University Press, Cambridge, 1980, p. 407.

33. Jansen, W., "Rotating Stall in a Radial Vaneless Diffuser," Transactions of ASME, December 1964, pp. 750-758.

34. Jansen, W., Carter, A.F., and Swarden, M.C., "Improvements in Surge Margin for Centrifugal Compressors," in Centrifugal Compressors, Flow Phenomena and Performance, AG28.

35. Japikse, D., "Radial Turbomachinery," ASME-Turbomachinery Course Notes, August 1978.

36. Johnston, J.P., "Radial-Flow Turbomachinery I-IV," Stanford University Lecture Notes.

37. Kammer, N. and Rautenberg, M., "An Experimental Investigation of Rotating Stall Flow in a Centrifugal Compressor," ASME Paper No. 82-GT-82, 1982.

38. Katz, W., Unpublished MIT UROP Report, 1984.

39. Kerrebrock, J.L., Aircraft Engines and Gas Turbines, MIT Press, Cambridge, Massachusetts, 1980, pp. 157-163.

40. Koff, S.G., "Stalled Flow Characteristics for Axial Compressors", MIT MS Thesis, Department of Mechanical Engineering, May 1983.

41. Koff, S.G., "A Control Volume Model of Rotating Stall in Multistage Axial Compressors", MIT Ph.D. Thesis, Department of Mechanical Engineering, September 1986.

42. Lancaster, D. TTL Cookbook, Howard W. Sams and Co., Inc., Indianapolis, Indiana, 1974.

43. Lavrich, P.L., "Time Resolved Measurements of Rotating Stall in Axial Flow Compressors," MIT Ph.D. Thesis, Department of Aeronautics and Astronautics, June 1988.

44. Lorett, J.A., and Gopalakrishnan, S.,"Interaction Between Impeller and Volute of Pumps at Off-Design Conditions," in Performance of Hydraulic Turbines and Pumps, ASME Winter Annual Meeting, November 1983.

45. Senoo, Y. and Kinoshita, Y., "Influence of Inlet Flow Conditions and Geometries of Centrifugal Vaneless Diffusers on Critical Flow Angle for Reverse Flow," in Centrifugal Compressor and Pump Stability, Stall and Surge, ASME Fluids and Gas Turbine Division, New York, 1976, pp. 157-166.

46. Shapiro, A.H., The Dynamics and Thermodynamics of Compressible Fluid Flow, Vol I, John Wiley and Sons, New York, 1953, pp. 73-111.

47. Sid, Michael, Unpublished MIT UROP Report.

48. Shearer, J.L., Murphy, A.T., and Richardson, H. H., Introduction to System Dynamics, Addison-Wesley, Reading, Massachusetts, 1971, pp. 296-322.

49. Stanitz, J.D. and Ellis, G.O., "Two-Dimensional Compressible Flow in Centrifugal Compressors with Straight Blades," NACA Report No. 954, 1950.

50. Tan, Choon, Private Communication.

51. Taylor, E.S., "The Centrifugal Compressor," in Aerodynamics of Turbines and Compressors, Princeton University Press, Princeton, New Jersey, 1964, pp. 553-586.

52. Toyama, K., Runstadler, P.W., and Dean, R.C., "An Experimental Study of Surge in Centrifugal Compressors," in Centrifugal Compressor and Pump Stability, Stall and Surge, ASME Fluids and Gas Turbine Division, York, 1976, pp. 69-89.

53. Whitfield, A., "Slip Factor of a Centrifugal Compressor and Its Variation with Flow Rate," Proc. Instr. Mech. Engrs., 188, 1974, pp. 415-421.

PHOTOGRAPHS

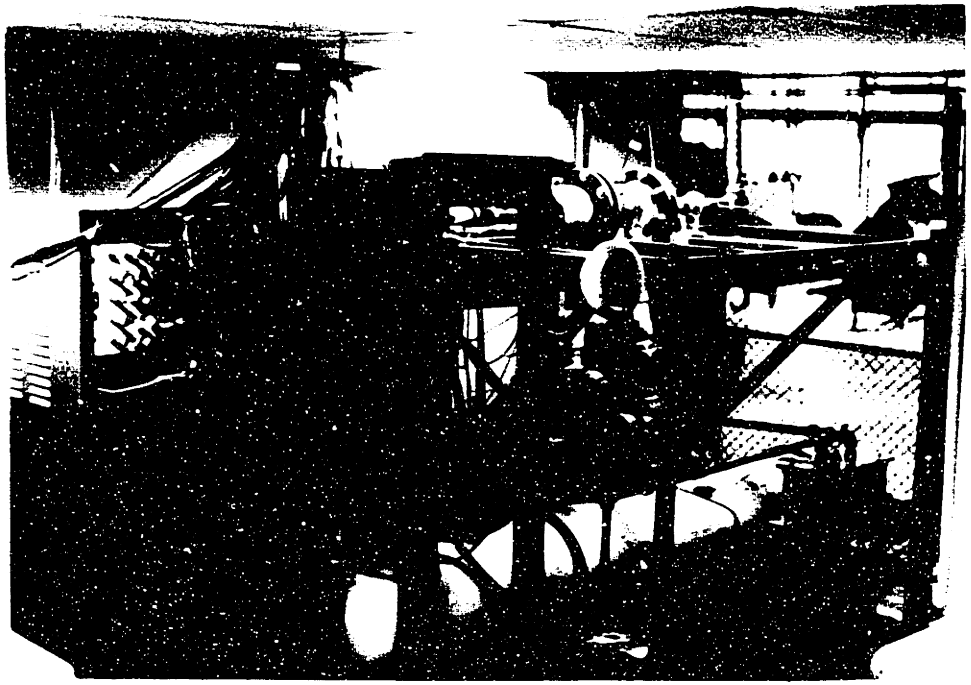

Photo 1 Overall Facility

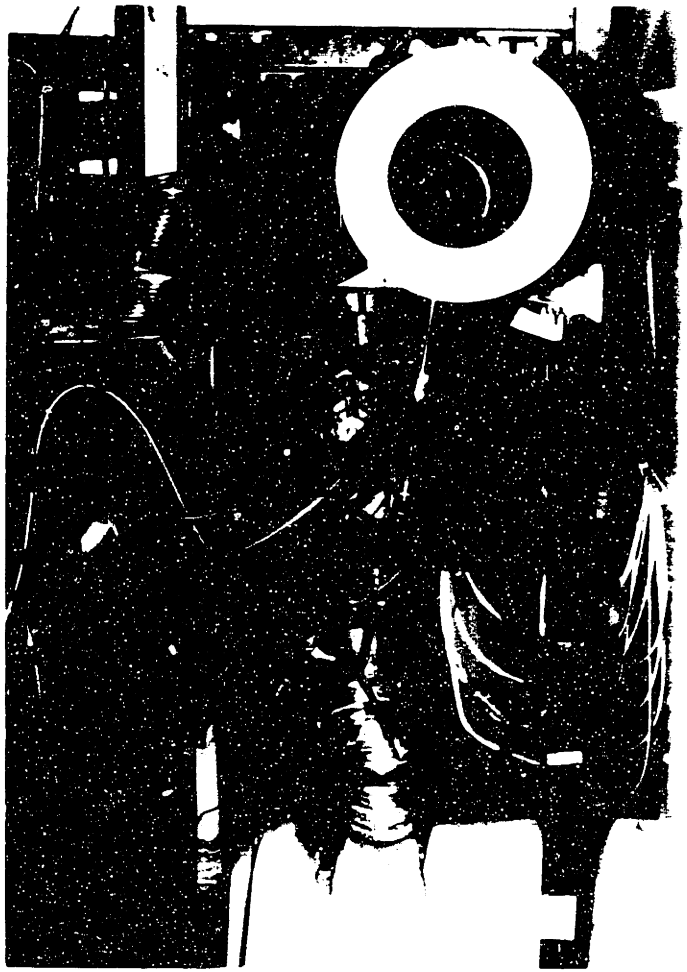

Photo 2 Small B System Throttling Arrangement

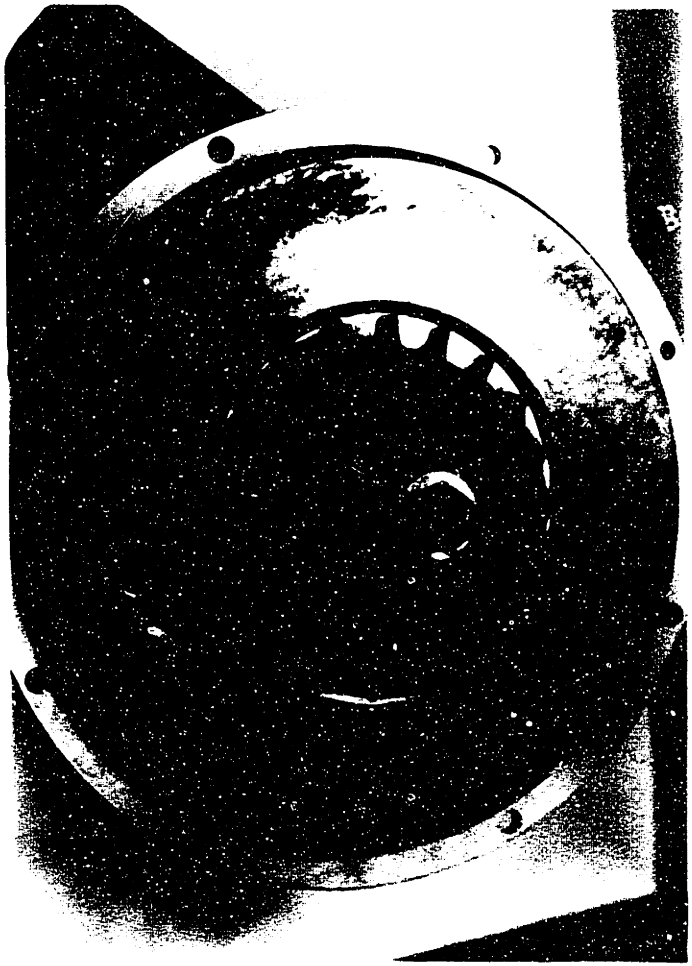

Photo 3 Impeller

Photo 4 Inlet Tongue Region Oil Streaks

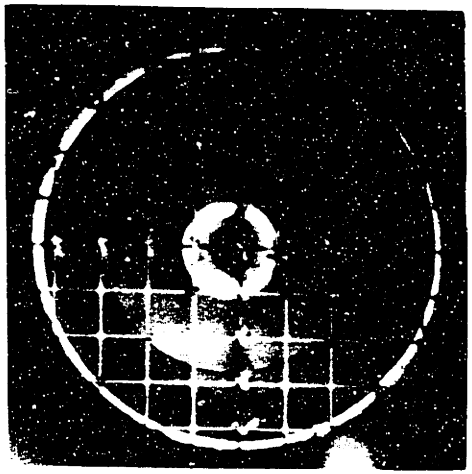

(a) No Swirl(ϕ = .125 @ 33K)

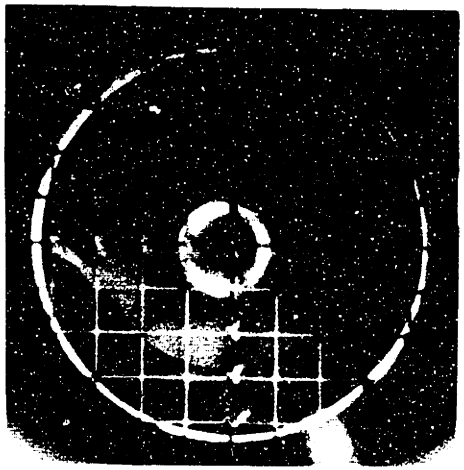

(b) Onset of Tip Swirl

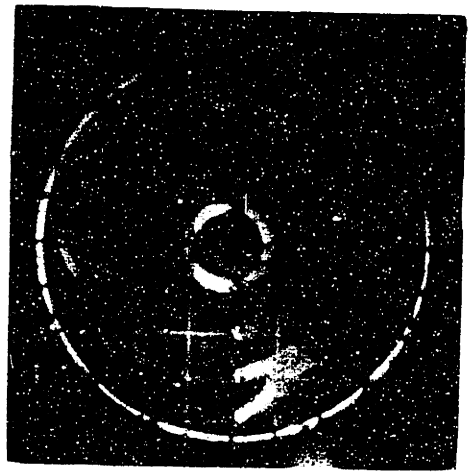

(c) Severe Overall Swirl(ϕ =.1 @ 33K)

Photos 5a-5c Inlet Flow Visualization

APPENDIX A

STABILITY AND ELECTRICAL ANALOGY OF COMPRESSION SYSTEM

For the simple compression system as shown in Fig. 5.1, the 1-D unsteady momentum equation for incompressible flow in the duct of length L is given by

$$\left(\frac{L}{A}\right)\frac{d\dot{m}_c}{dt} = \Delta P_c - \Delta P_p \tag{A.1}$$

Conservation of mass in the plenum is given by

$$\frac{d(\rho V_p)}{dt} = \dot{m}_c - \dot{m}_T \tag{A.2}$$

When mass flows are nondimensionalized by $\rho_o AcU$ and pressure differences are nondimensionalized by $.5\rho_o U^2$, Eq. A.1 becomes

$$\left\{\frac{2L}{U}\right\}\frac{d\Phi_c}{dt} = \widetilde{\Delta P}_c - \widetilde{\Delta P}_p \tag{A.3}$$

If the plenum process is isentropic, then

$$\frac{d\rho}{dt} = \frac{1}{kRT_p}\frac{dP}{dt} \tag{A.4}$$

Substituting Eq. A.4 into Eq. A.2, nondimensionalizing, and performing some algebra, Eq. A.2 becomes

$$\left\{\frac{V_p\ U}{a_p^2\ 2A}\right\}\frac{d\widetilde{\Delta P_p}}{dt} = \Phi_c - \Phi_T \qquad \text{(A.5)}$$

Eq. A.3, which is governs the flow in the duct, is analogous with the simple inductor relation given by Ldi/dt = del V. The quantity in brackets {2L/U} represents the inductance, the compressor flow coefficient represents the current, and the nondimensional pressure differences on the righthand side represents the voltage difference across the inductor. Similarly, Eq. A.5, which governs the behavior of the plenum, is analogous to the simple capacitor relation CdV/Dt = del i. The quantity in brackets $\{VpU/(2Aa_p^2)\}$ represents the capacitance, the plenum pressure rise coefficient represents the capacitor voltage, and the net flow into the plenum on the righthand side of Eq. A.5 represents the net inflow of current into the capacitor.

Letting L = {2L/U} and C = $\{VpU/(2Aa_p^2)\}$, then Eq. A.3 is

$$L\ \frac{d\Phi_c}{dt} = \widetilde{\Delta P_c} - \widetilde{\Delta P_p} \qquad \text{(A.6)}$$

and Eq. A.5 is

$$C\ \frac{d\widetilde{\Delta P_p}}{dt} = \Phi_c - \Phi_T \qquad \text{(A.7)}$$

If the interest is in perturbations around some equilibrium operating point, then

$$\Phi_c = \Phi_o + \delta\Phi_c \qquad \text{(A.8)}$$

$$\Phi_T = \Phi_o + \delta \Phi_T \tag{A.9}$$

$$\widetilde{\Delta P_c} = \widetilde{\Delta P_o} + \delta \widetilde{\Delta P_c} \tag{A.10}$$

and

$$\widetilde{\Delta P_p} = \widetilde{\Delta P_o} + \delta \widetilde{\Delta P_p} \tag{A.11}$$

where the o subscript represents the equilibrium condition of operation. If we introduce the compressor characteristic slope given by

$$C' = \frac{\delta \widetilde{\Delta P_c}}{\delta \Phi_c} \tag{A.12}$$

and throttle slope given by

$$T' = \frac{\delta \widetilde{\Delta P_p}}{\delta \Phi_T} \tag{A.13}$$

along with the relations given by Eq. A.8 through A.11 into Eq. A.6 and A.7, then via algebra

$$L \frac{d \delta \Phi_c}{dt} = C' \delta \Phi_c - \delta \widetilde{\Delta P_p} \tag{A.14}$$

and

$$C\frac{d\delta\widetilde{\Delta P}_p}{dt} = \delta\Phi_c - \frac{\delta\widetilde{\Delta P}_p}{T'} \tag{A.15}$$

To form a single second order equation describing the perturbations in massflow, Eq. A.14 and A.15 can be combined and differentiated. First Eq. A.14 is rewritten as

$$\delta\widetilde{\Delta P}_p = C'\delta\Phi_c - L\frac{d\delta\Phi_c}{dt} \tag{A.16}$$

This can be substituted into Eq. A.15 to give

$$\frac{d\delta\widetilde{\Delta P}_p}{dt} = \frac{1}{C}\left(\delta\Phi_c - \frac{C'}{T'}\delta\Phi_c + \frac{L}{T'}\frac{d\delta\Phi_c}{dt}\right) \tag{A.17}$$

If Eq. A.14 is differentiated, this is

$$L\frac{d^2\delta\Phi_c}{dt^2} = C'\frac{d\delta\Phi_c}{dt} - \frac{d\delta\widetilde{\Delta P}_p}{dt} \tag{A.18}$$

If Eq. A.17 is substituted into Eq. A.18 and some algebra is performed, then

$$\frac{d^2\delta\Phi_c}{dt^2} + \left(\frac{1}{CT'} - \frac{C'}{L}\right)\frac{d\delta\Phi_c}{dt} + \frac{1}{LC}\left(1 - \frac{C'}{T'}\right)\delta\Phi_c = 0 \tag{A.19}$$

If time in Eq. A.19 is nondimensionalized by a characteristic time constant given by

$$\tau = \sqrt{L\,C} \tag{A.20}$$

such that

$$dt = \tau\, d\tilde{t} \tag{A.21}$$

then Eq. A.19 can be rewritten as

$$\frac{d^2\delta\Phi_c}{d\tilde{t}^2} + \left(\frac{1}{\sqrt{\frac{C}{L}}\,T'} - \sqrt{\frac{C}{L}}\,C'\right)\frac{d\delta\Phi_c}{d\tilde{t}} + \left(1 - \frac{C'}{T'}\right)\delta\Phi_c = 0 \tag{A.22}$$

The behavior of this system is governed by the quantity $(C/L)^{1/2}$ for fixed values of C' and T'. If the original expressions for capacitance and inductance are substituted then

$$\left(\frac{C}{L}\right)^{1/2} = \left(\frac{\frac{V_p}{A}\,\frac{U}{2a_p^2}}{\frac{2L}{U}}\right)^{1/2} = \frac{U}{2a_p}\left(\frac{V_p}{AL}\right)^{1/2} \tag{A.23}$$

which is the B-parameter as defined in Eq. 1.1. Hence Eq. A.22 is identical to Eq. 1.6. Physically, then the B-parameter is a measure of the ratio of system capacitance to inductance. The system behavior is dependent on the B-parameter which controls this ratio.

For a characteristic equation $r^2 + A1r + A2 = 0$, stability requires $A1 > 0$ and $A2 > 0$. Hence the two stability conditions follow from Eq. A.22 are then

$$C' < T' \tag{A.24}$$

and

$$C' < \frac{1}{B^2 T'} \tag{A.25}$$

If Eq. A.6 and A.7 are written with time nondimensionalized, these are respectively

$$\tilde{L} \frac{d \Phi_c}{d \tilde{t}} = \widetilde{\Delta P_c} - \widetilde{\Delta P_p} \tag{A.26}$$

and

$$\tilde{C} \frac{d \widetilde{\Delta P_p}}{d \tilde{t}} = \Phi_c - \Phi_T \tag{A.27}$$

where the nondimensionalized inductance $\tilde{L}$ is simply

$$\tilde{L} = \frac{1}{B} \tag{A.28}$$

and the nondimensionalized capacitance $\tilde{C}$ is

$$\tilde{C} = B \tag{A.29}$$

The squareroot of the ratio of nondimensionalized capacitance to inductance is then

$$\left(\frac{\tilde{C}}{\tilde{L}}\right)^{1/2} = \left(\frac{B}{\left(\frac{1}{B}\right)}\right)^{1/2} = B \qquad \text{(A.30)}$$

The electrical circuit analogy for Eq. A.26 and A.27 are shown in Fig. A.1. The source is a current controlled voltage source which represents the compressor characteristic. The throttle is represented by the resistor R which at equilibrium has a value of $\tilde{\Delta}P_{po}/\bar{\Phi}_o$. Both the inductance(=1/B) and the capacitance(=B) depend on the B-parameter and hence the dynamic behavior of the system is determined by the magnitude of B.

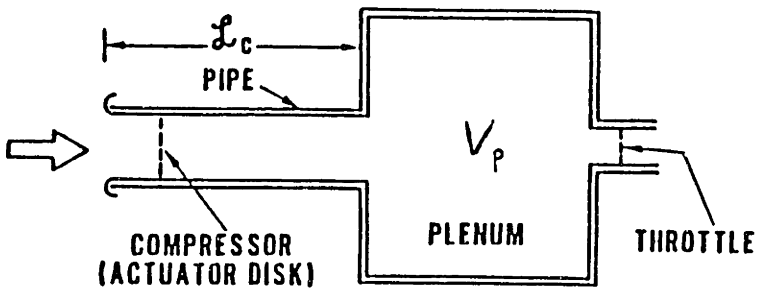

Compression system model

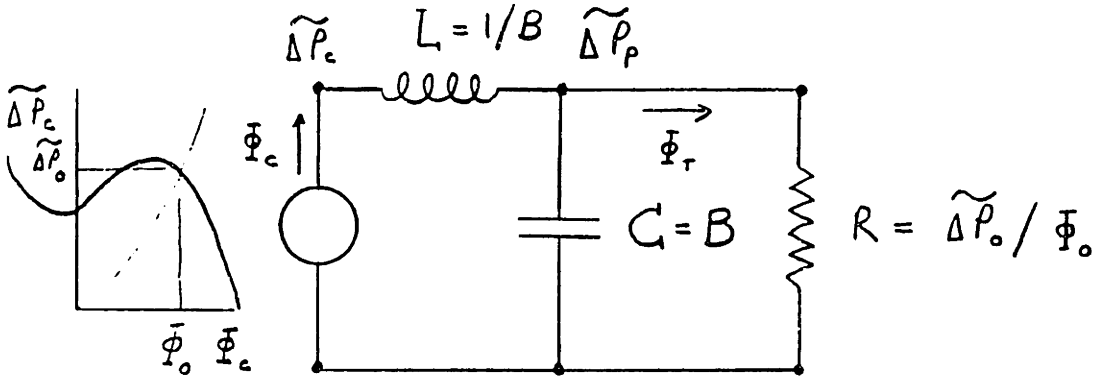

Compression system electrical analog

Fig. A.1 Compression System Electrical Analog

APPENDIX B TURBOCHARGER LABORATORY DRIVE

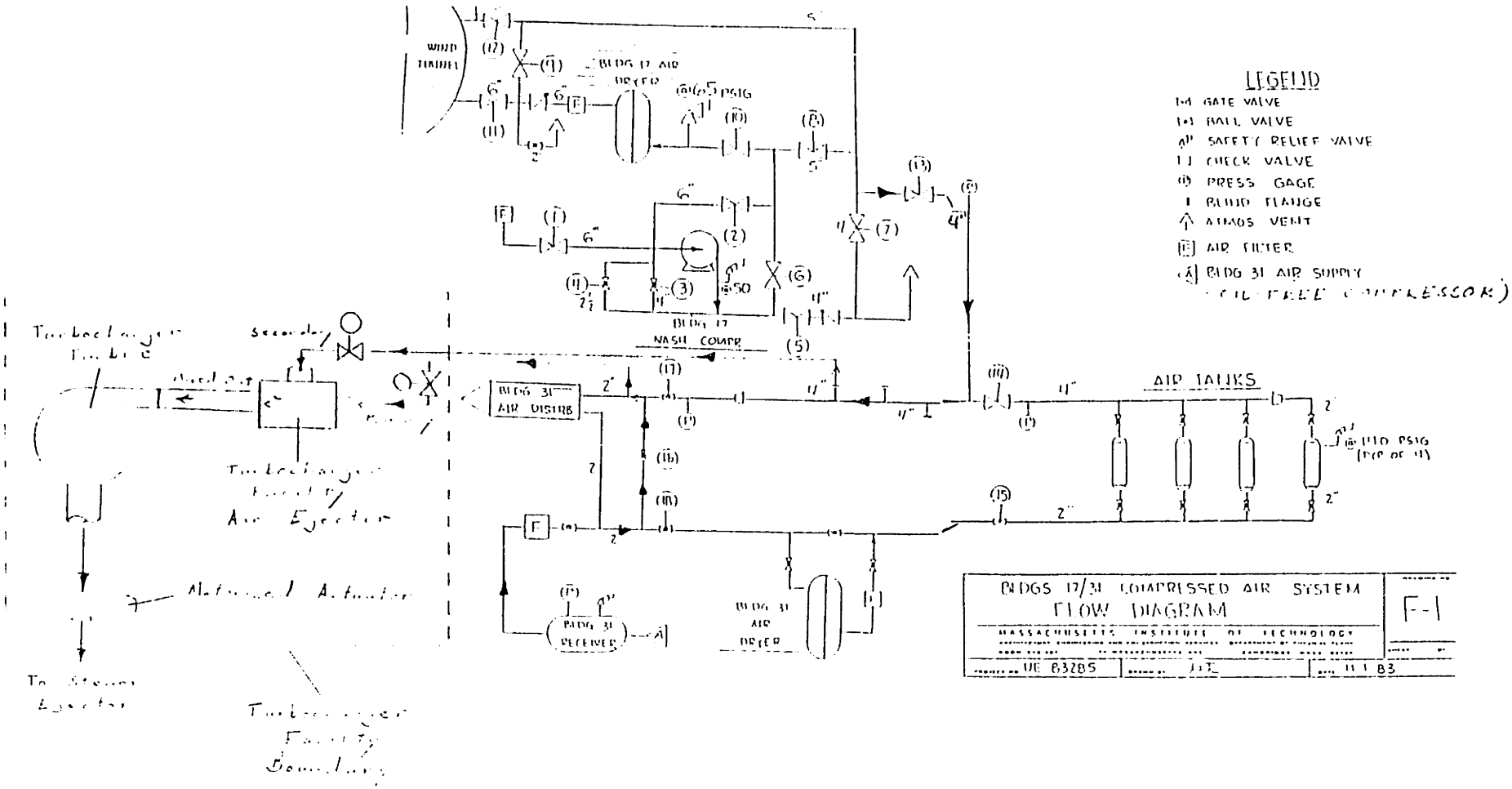

Fig. B.1 Small B System Drive Schematic

APPENDIX C COMPRESSOR HARDWARE FOR PRESSURE DISTORTION MEASUREMENT

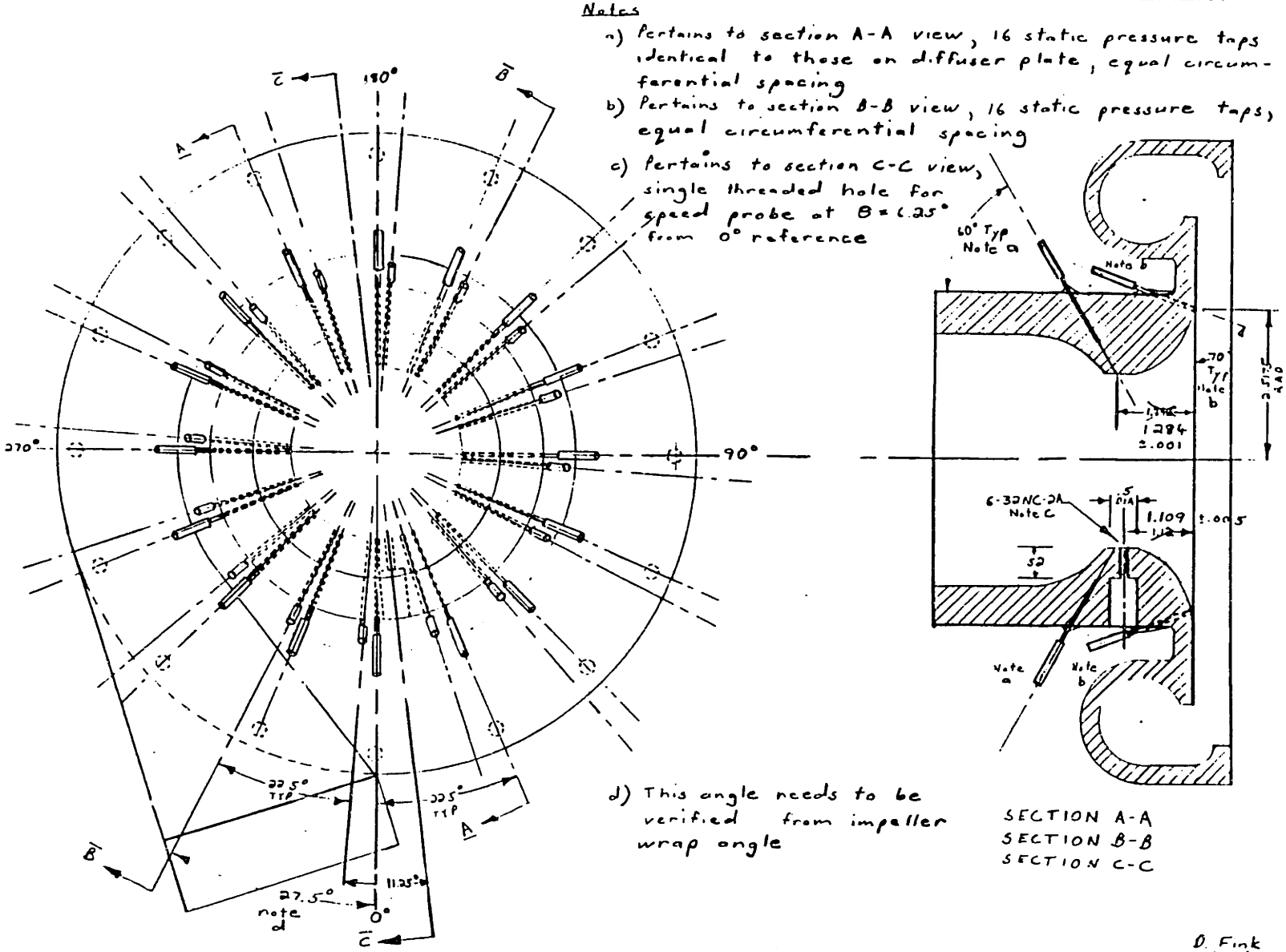

Fig. C.1 Compressor Case 2 for Circumferential Pressure Distortion Measurement

D. Fink 4/30/87

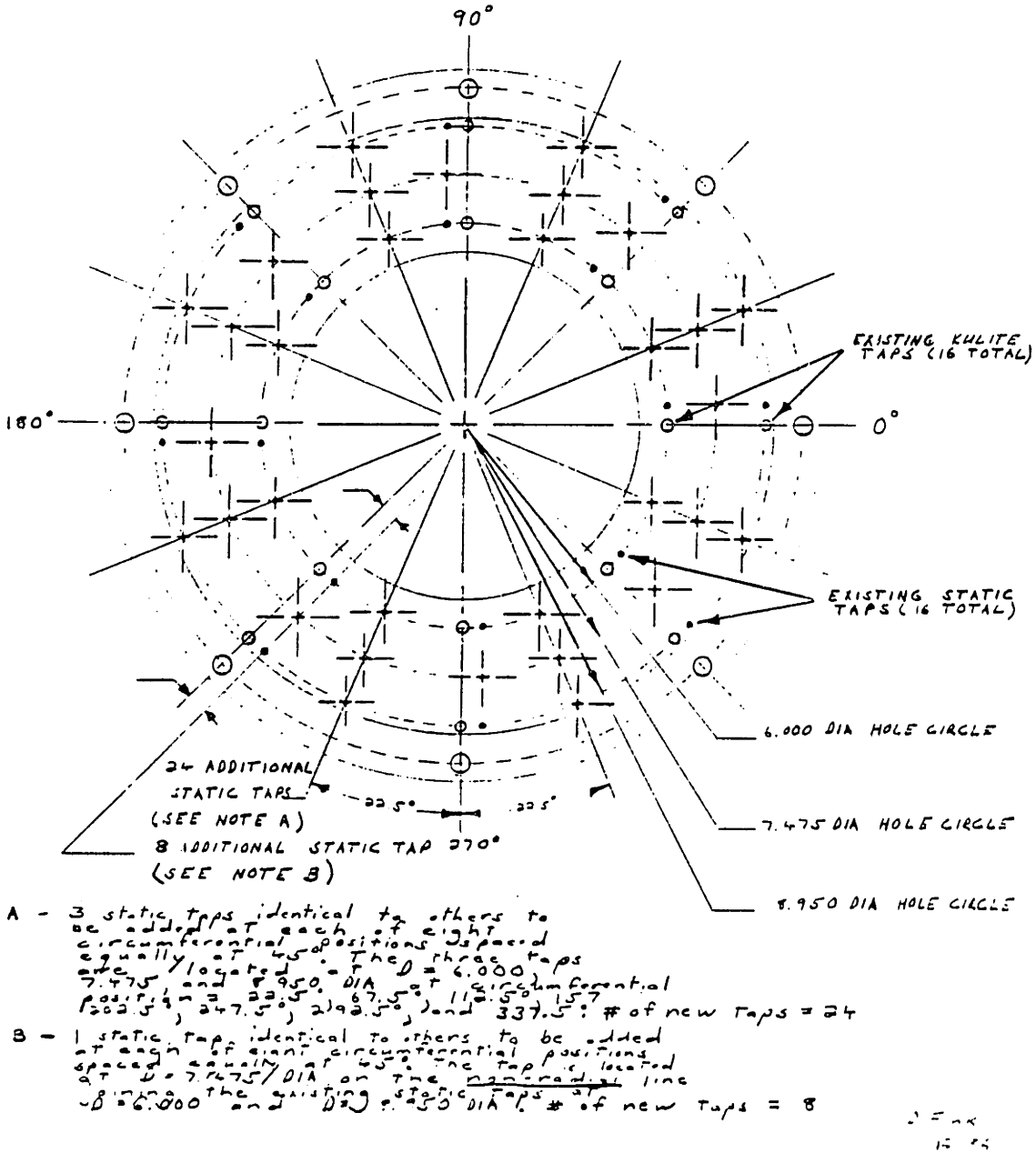

Fig. C.2 Diffuser Plate 2 for Circumferential Pressure Distortion Measurement

APPENDIX D

DATA ACQUISITION HARDWARE

A complete schematic of the data acquisition system is shown in Fig. D.1. The heart of the system is a Digital LSI-11/23 minicomputer which via the multiuser operating system RSX-11 operates several DRV-11 driver boards, the continuous to disc DT2752A A/D board, two RL02 hard discs, the DT2769 programmable clock, a GPIB parallel interface bus (IEEE-488), a Versatec, and several terminals.

The A/D used for the low response and time resolved data in this report is a Data Translation DT2752A 16 input DMA A/D board designed for use in both single sample mode or continuous to disc data acquisition mode. With the Data Translation software RSXLIB provided with this board, one is able to sample continuously at 50 KHz(3.125 KHz/channel over 16 channels). The sampled data are stored on an opened file on the RLO2 disc. Basically the DT2752A board siezes control of the 11/23 Q-bus temporarily and during that time writes data directly(via direct memory access which bypasses the CPU) and sequentially to each of eight predefined buffers setup in the computer internal memory. The CPU only functions to move the contents of each of these buffers when full to the open file on the RLO2 disc. RSX-11 system event flags signal the CPU that a buffer is full and ready to be transfered to the disc. The essential elements of the DT2752A architecture is shown in Fig. D.2. The system is currently limited to throughput rates of approximately 50 KHz.

The DT2769 programmable clock in the system serves two functions. First, it is used to set the sampling rate for the time resolved data. In this mode of operation, the output of the clock served as the input for the A/D external trigger. The clock also has a Schmidt trigger input whose state can be monitored by software. In a second mode of operation, the Scanivalve ready to read pulse was inputed to the Schmidt trigger to signal the A/D to sample the Scanivalve transducer voltage in single channel mode.

The Scanivalve is stepped remotely through an interface by one of the two DRV-11 boards (non-isolated DT-2768). The Scanivalve interface was built following an earlier lab design used by T. Eastland [15]. The DRV-11 board has two 40-pin connectors, computer output J1 and input J2. A schematic of this circuit appears in App. B of Fink[19]. A stepping pulse output from the computer at J1 actuates the

interface to step the Scanivalve. After the Scanivalve has stepped, the channel is read by the computer from J2 through the interface where it is presented as output from an optical encoder in the Scanivalve unit. Once the stepping pressure transient in the transducer has passed, the Scanivalve issues a ready to read pulse to the interface. This signal is used as input to the clock Schmidt trigger. Software continually monitors the state of the Schmidt trigger and when it is triggered, the A/D takes one or more samples of the Scanivalve transducer voltage.

The HP counter is used in remote mode and the low time averaged speed is obtained by reading the counter through the GPIB bus. For time resolved RPM information, the A/D samples the F/V output of the photo-optic speed sensor directly.

Temperatures on the K-type thermocouples are read using the μ MAC-4000 multiplexer. This device is operated via one RS-232 terminal line which is set up as a slave terminal in RSX-11. The terminal driver board DLV-11 was reconfigured via wire wrap jumpers to provide the proper number of stop bits (2) for operation as it is a non-standard setting.

The spectral data analysis is performed by an HP-3582A two-channel spectrum analyzer. Capabilities of this 25 kHz range analyzer include amplitude, phase, amplitude and phase transfer functions, coherence function and time functions. Various types of averaging can also be employed as well as various types of filter passband shapes. The desired high response probe for each of the two available spectral analyzer channels is selected in a manual switch box built for the purpose. The spectral analyzer is operated both manually and in remote operation with the GPIB. Remote mode is used currently to record the spectral data in a data file for later plotting and inspection.

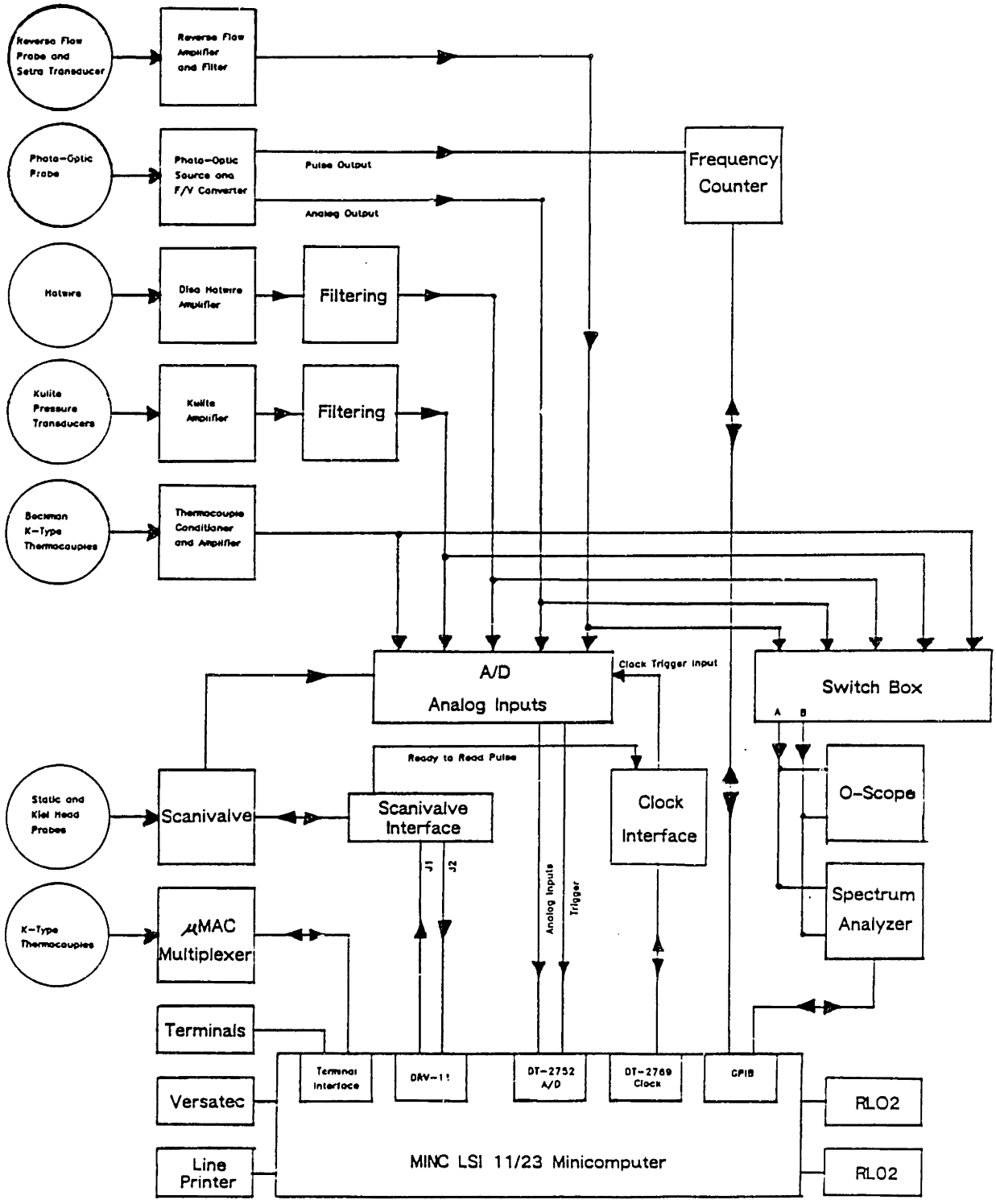

Fig. D.1 Data Acquisition Schematic

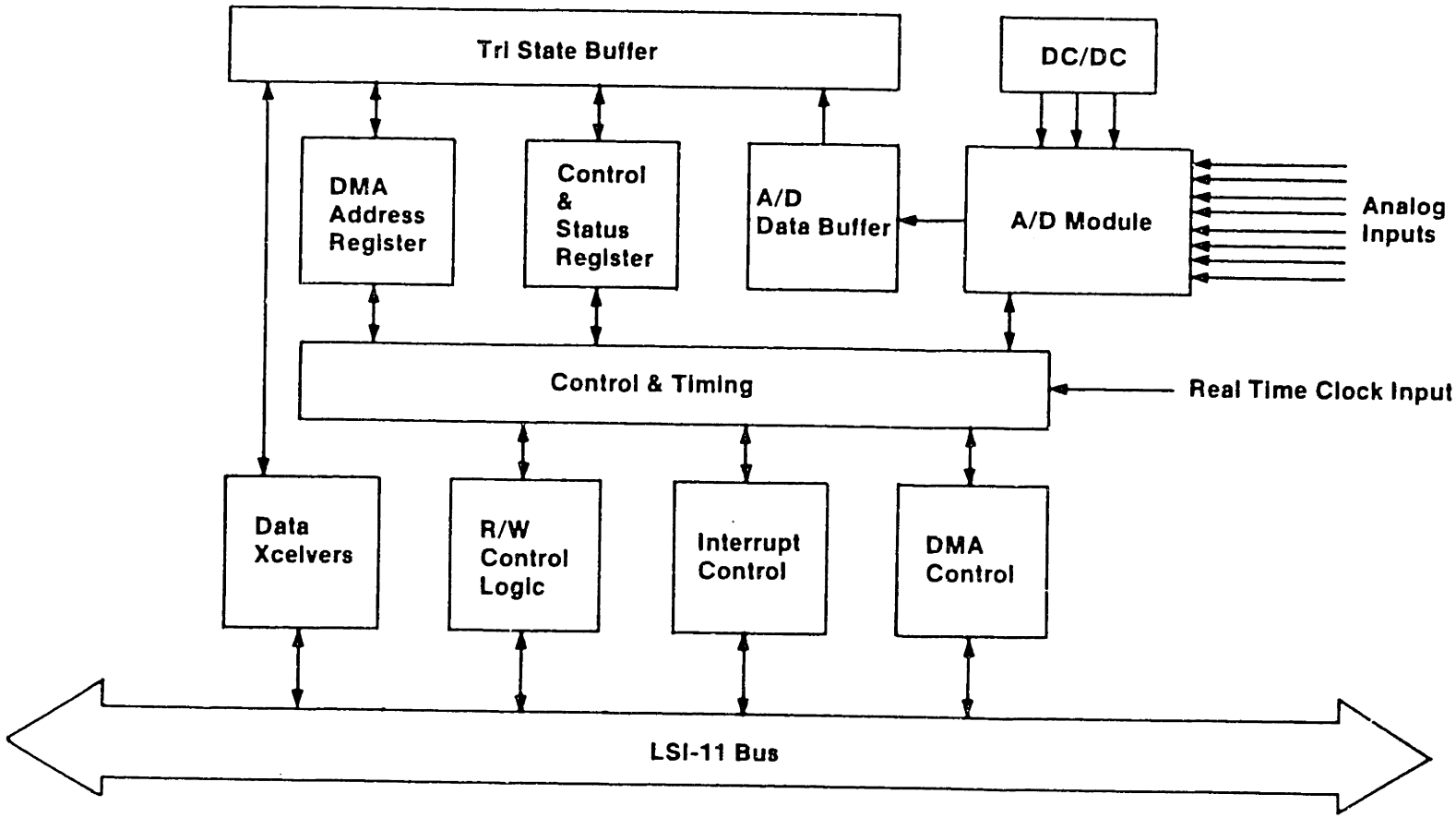

Fig. D.2 Direct to Disc Data Translation A/D System Schematic

Speed Sensor Probe Fixture Note d

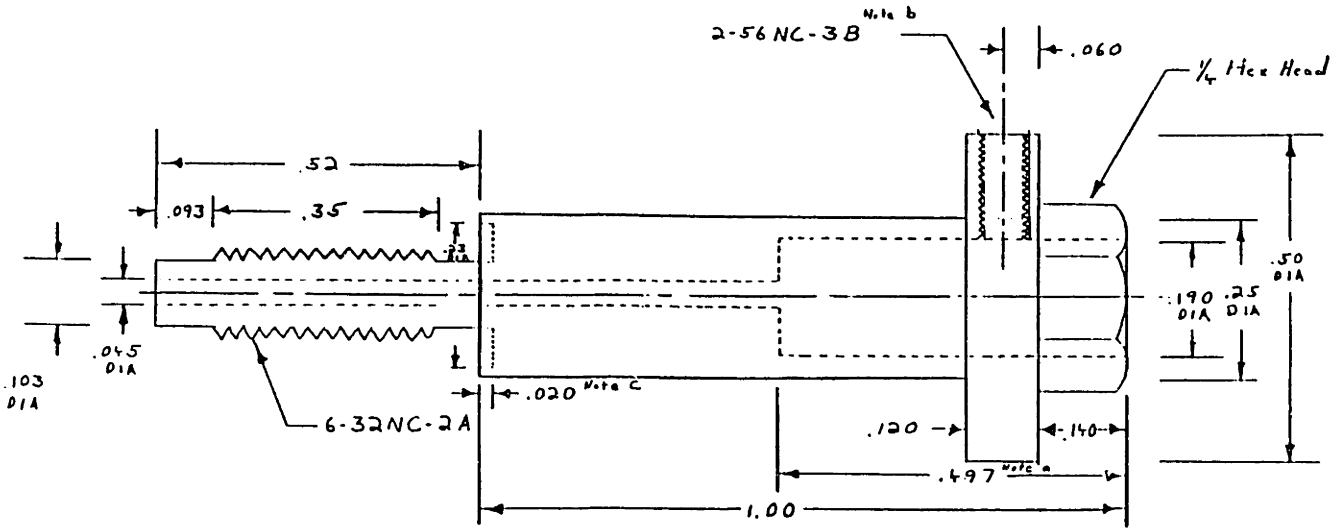

Notes

a) Includes .040 depth for Parker 2-002 O-Ring with .010 squeeze
b) For #2 1/8 long Unbrako self lock set screw
c) For Kulite XT-140 O-Ring
d) For Delon-Jenner E927 Reflective Scanner Fiber Optic Probe

D Fink

Fig. E.1 Speed Sensor Probe Fixture

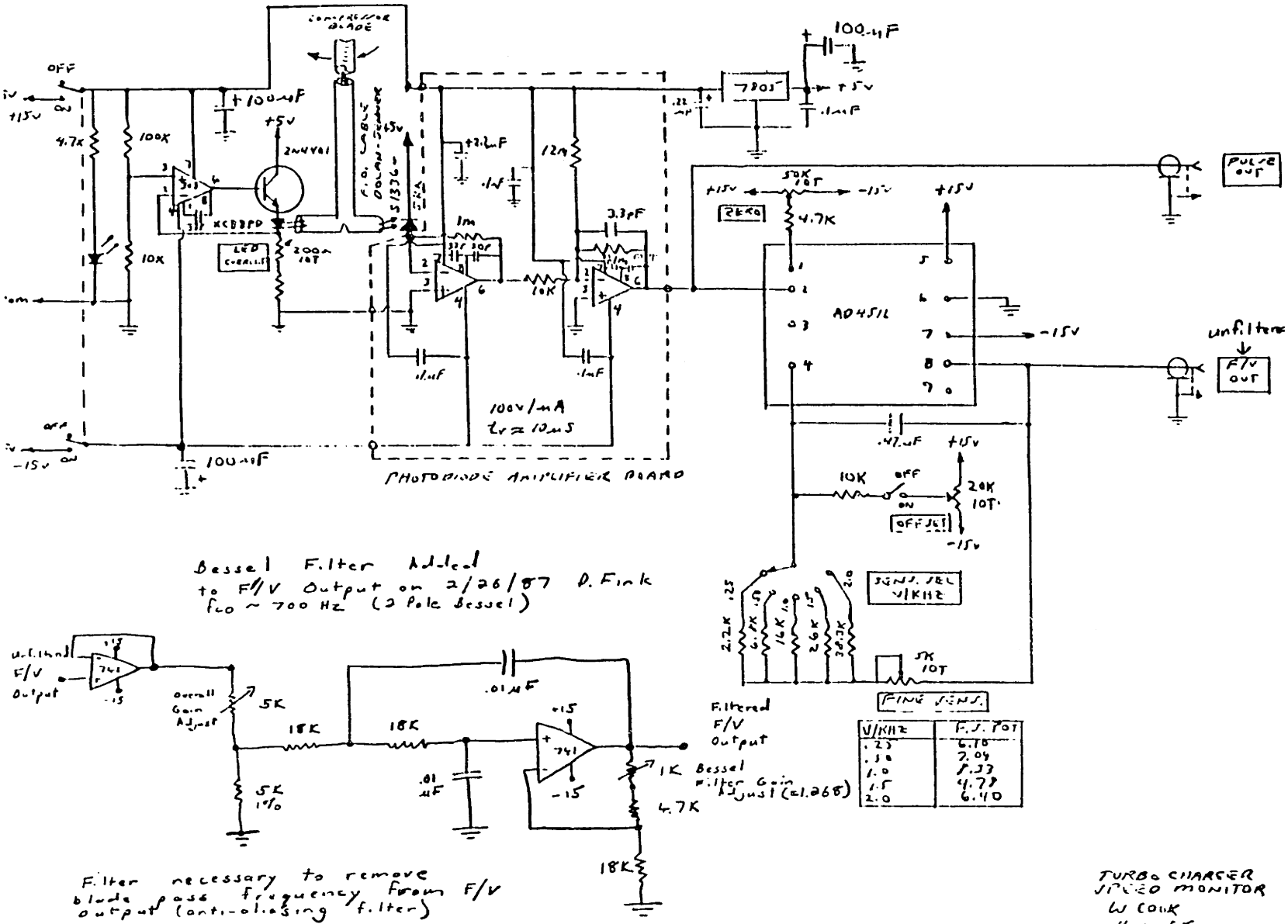

Fig. E.2 Transient Speed Electronics Schematic

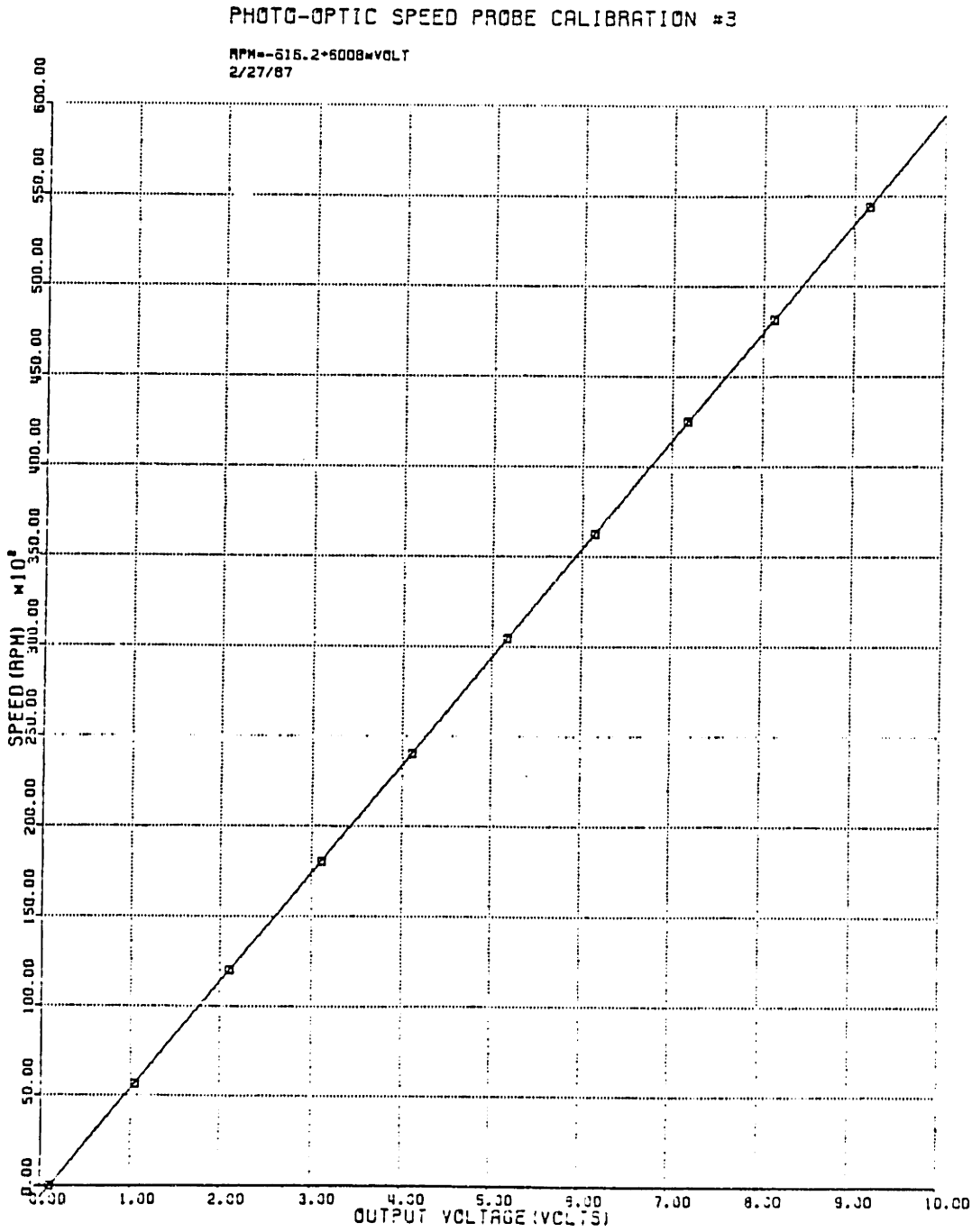

Fig. E.3 Photo Optic Speed Probe Calibration

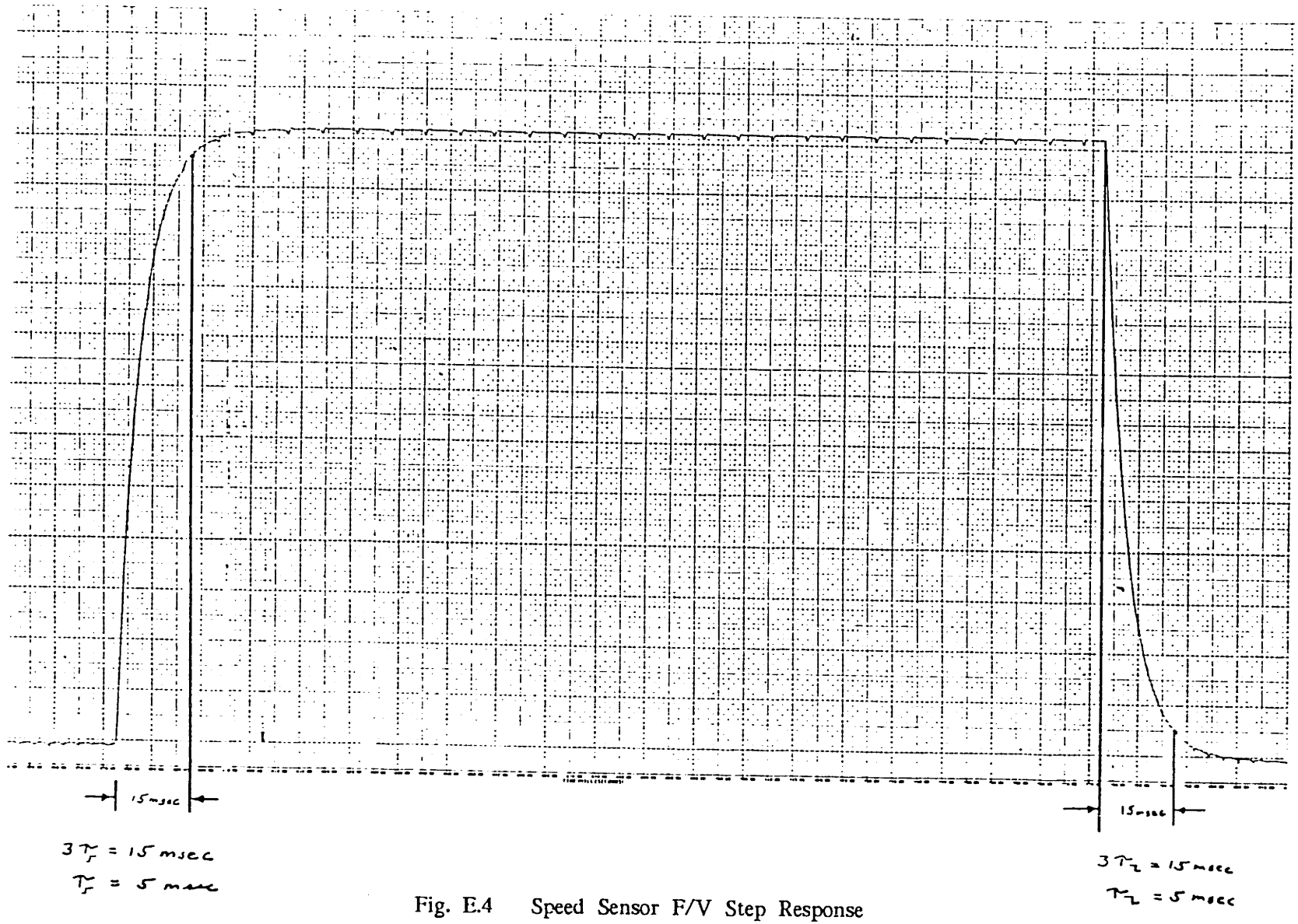

Fig. E.4 Speed Sensor F/V Step Response

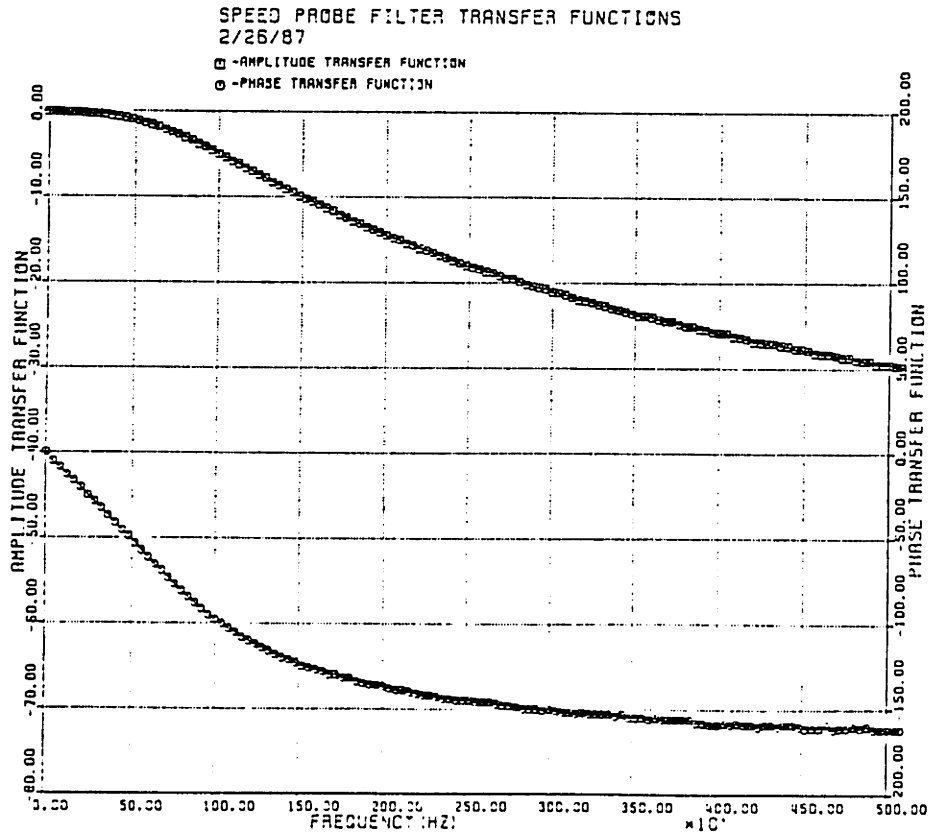

Fig. E.5 Speed Probe Filter Transfer Function

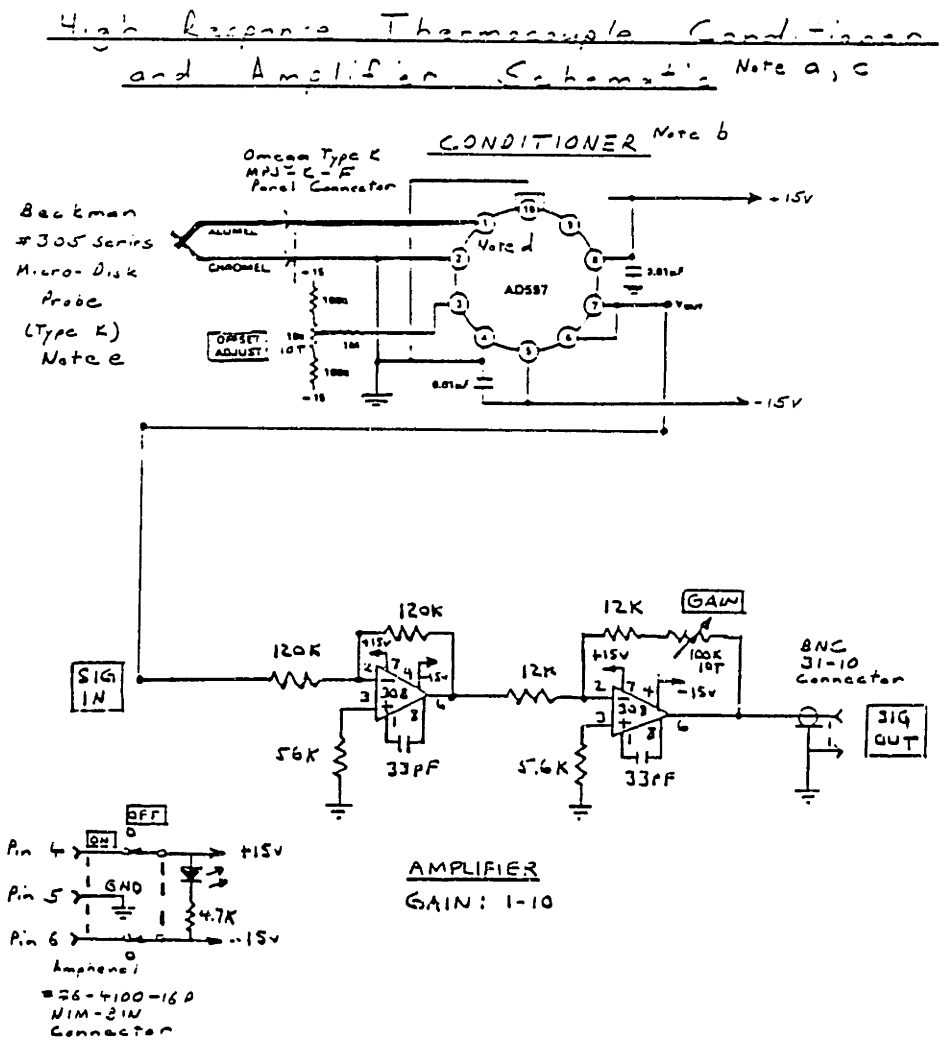

Fig. E.6 High Response Thermocouple Conditioner and Amplifier Schematic

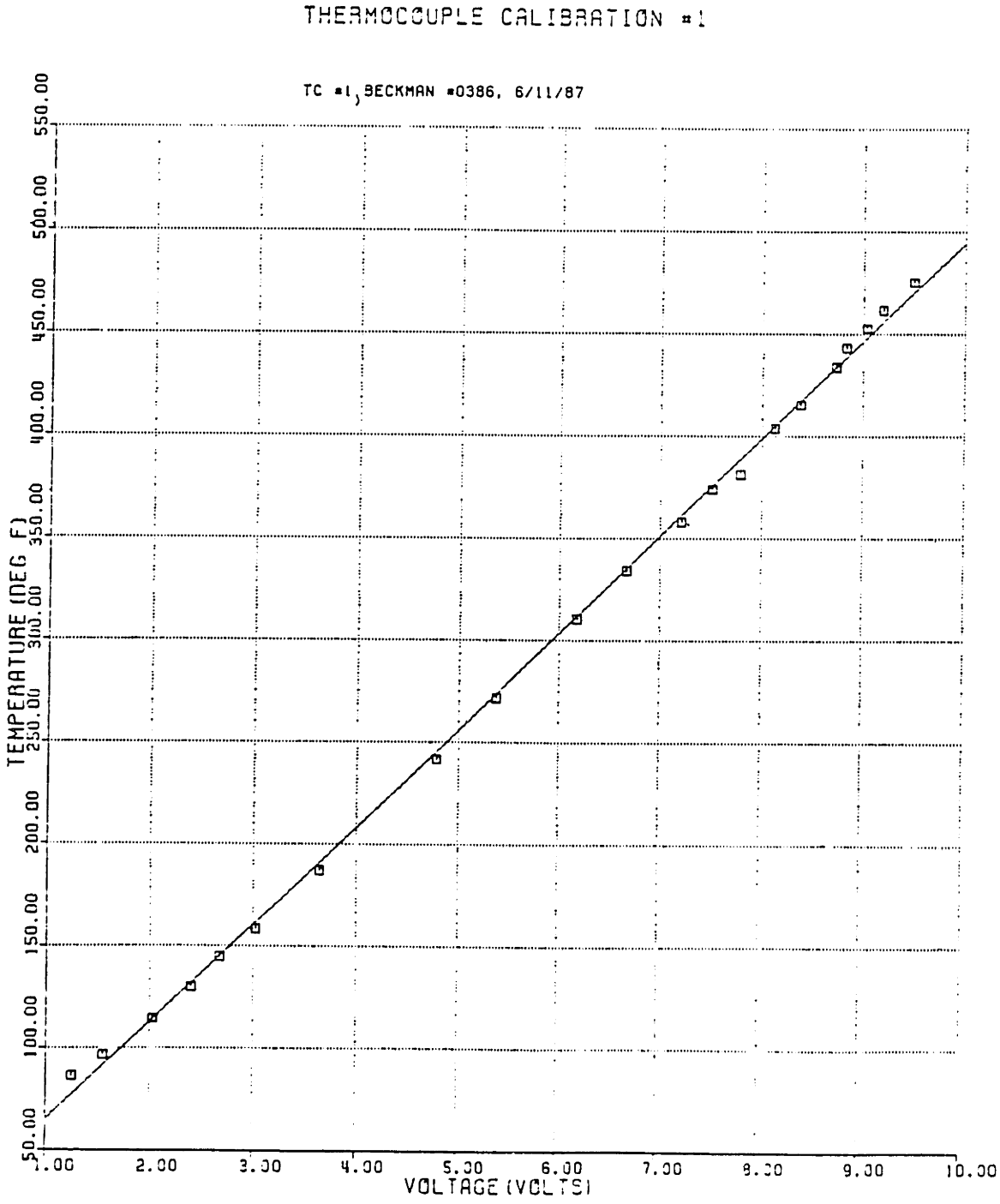

Fig. E.7 Typical High Response Thermocouple Calibration Curve

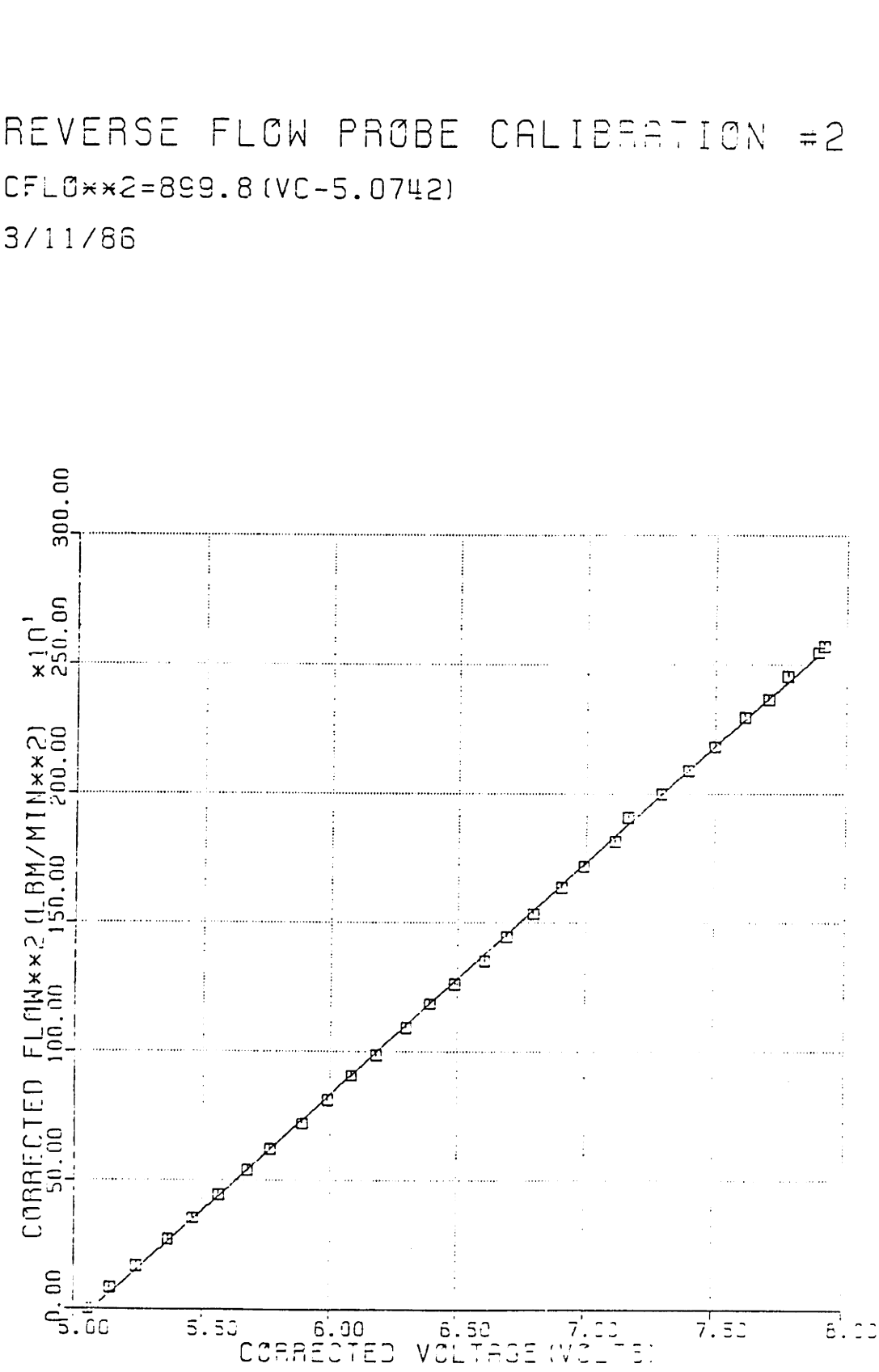

Fig. E.8 Typical Reverse Flow Probe Calibration Curve

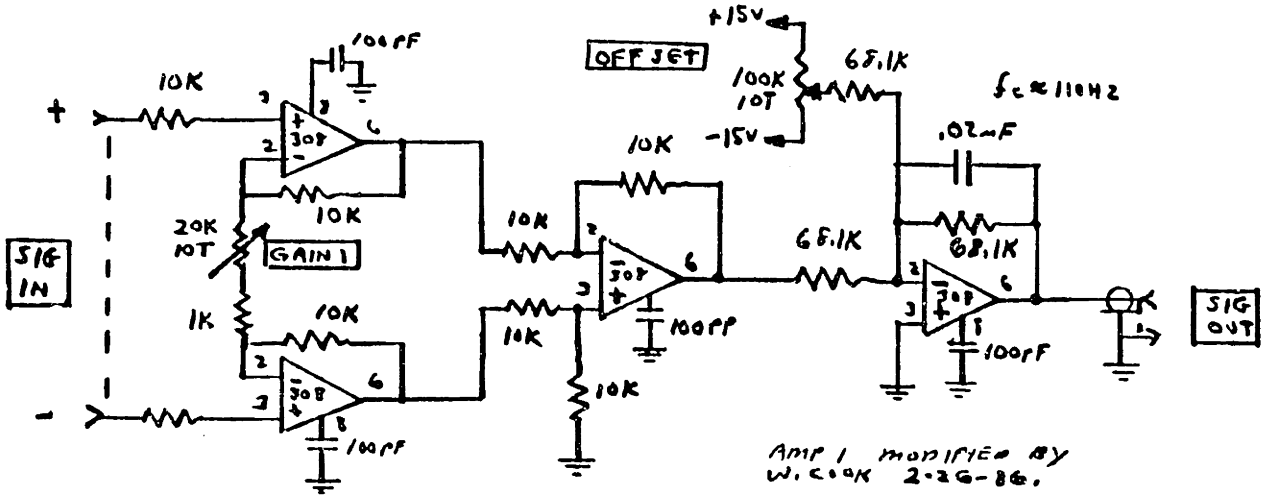

AMPLIFIER 1

Fig. E.9 Reverse Flow Probe Amplifier Schematic

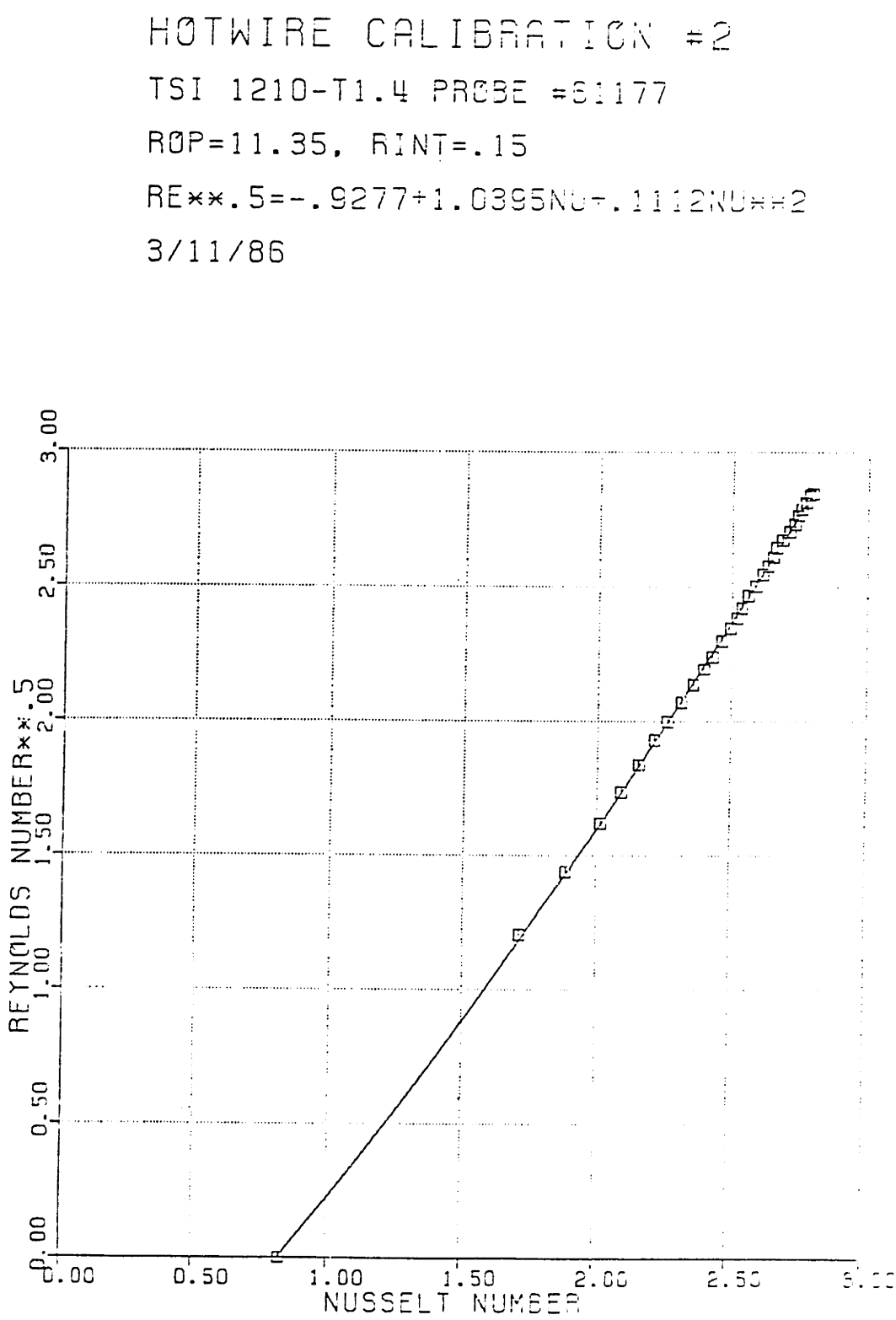

Fig. E.10 Typical Hotwire Calibration Curve

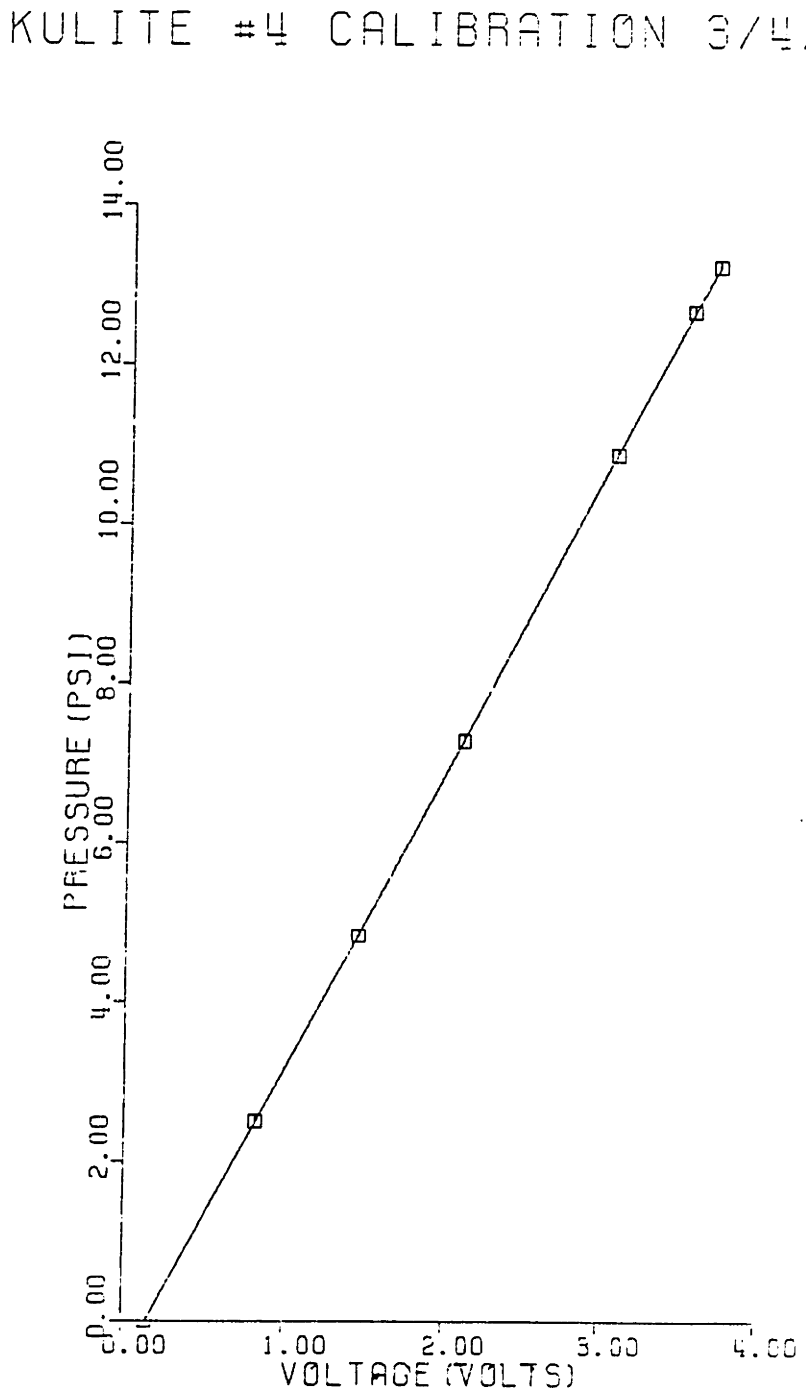

Fig. E.11 Typical Kulite High Response Pressure Transducer Calibration Curve

APPENDIX F

CALCULATION OF THE SLIP PARAMETER

The velocity triangle for flow exiting a centrifugal impeller is shown in Fig. F.1. The slip parameter is then defined as

$$\sigma = \frac{C_{\theta 2}}{U} \tag{F.1}$$

If there is no inlet swirl and no shroud friction then the slip parameter is equal to the work coefficient. But as shown in Fig. F.2, the work coefficient is seen to rise above 1 at low flows. For an impeller with radial exit blade angles, it is physically implausible for the flow to leave the rotor with an absolute tangential velocity above wheel speed.

Recirculation of hot gas in the tip clearance region or from stalled impeller channels could produce this effect. It can also be interpreted as a consequence of a significant amount of shroud friction existing in the compressor. Including shroud friction reduces the slip parameter. This is seen by looking at the control volume around the impeller shown in Fig. F.3. Writing conservation of angular momentum if shroud friction is included is then

$$\Gamma_c - \Gamma_f = \dot{m} r_T C_{\theta 2} \tag{F.2}$$

Written in terms of torque coefficients defined by $\tilde{\Gamma} = \Gamma / (\rho \omega^2 r_T^3 A_c)$, this is

$$\tilde{\Gamma}_c - \tilde{\Gamma}_f = \sigma \phi \tag{F.3}$$

Solving for slip parameter, we get then

$$\sigma = \frac{\tilde{\Gamma}_e - \tilde{\Gamma}_f}{\phi} = \psi_{work} - \frac{\tilde{\Gamma}_f}{\phi} \qquad \text{(F.4)}$$

Hence the term - $\tilde{\Gamma}_f / \phi$ represents the correction to the work coefficient due to control volume surface friction.

The friction torque was estimated by linear extrapolation of the torque coefficient curve shown in Fig. F.4 to shutoff. A value of friction torque coefficient of .020 was found in this extrapolation. Assuming this value to be constant and correcting the work coefficient data of Fig. F.2, the slip parameter was calculated and is shown in Fig. F.5. The slip was found to be nearly constant for $.07 < \phi < .50$ lying in a range of $.74 < \sigma < .82$. Busemann's correlation given by $1 - 2.4/N$ where N = Number of blades = 20 gives a slip value of .88 which is somewhat higher. At low flow coefficients, slip drops off sharply. In this analysis, at shutoff the correction approaches ∞. But at zero flow, in an ideal case, $\psi \to \infty$ as well so Eq. F.4 is still valid near shutoff. The data of Fig. F.2 does appear to approach shutoff in an asymptotic fashion towards ∞ but at very low flows, heat transfer violates the adiabatic assumption and limits the temperature rise.

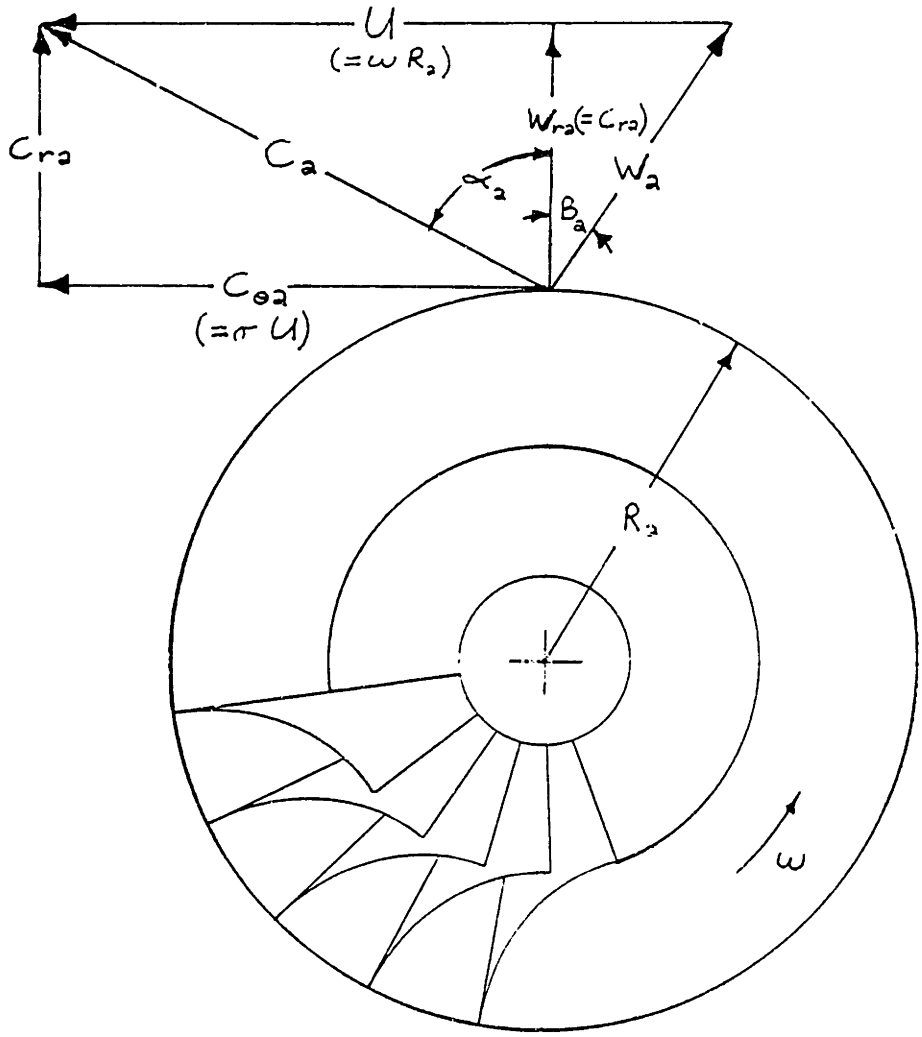

Fig. F.1 Vaneless Diffuser Velocity Triangle

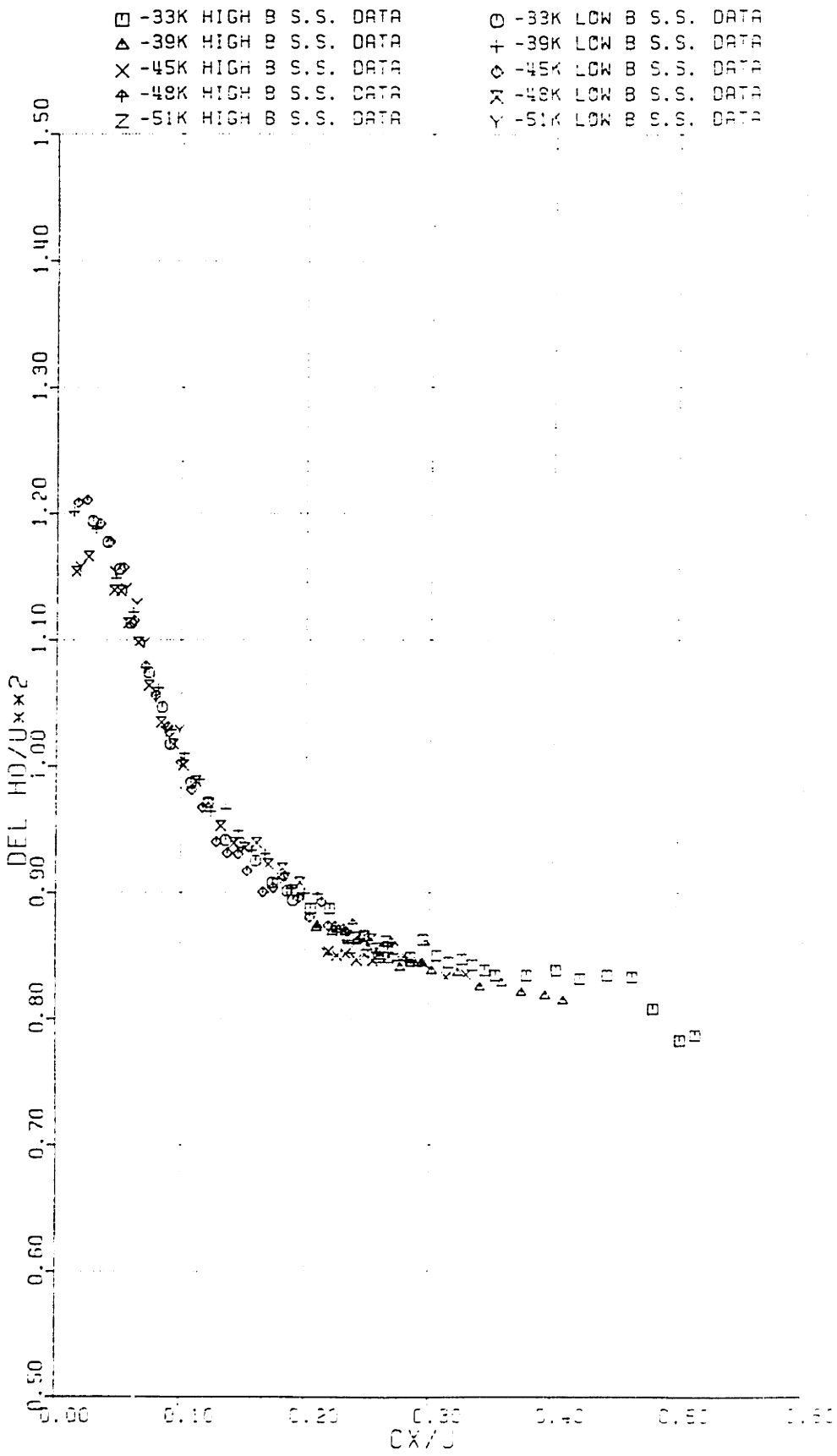

Fig. F.2 Compressor Work Coefficient vs Cx/U

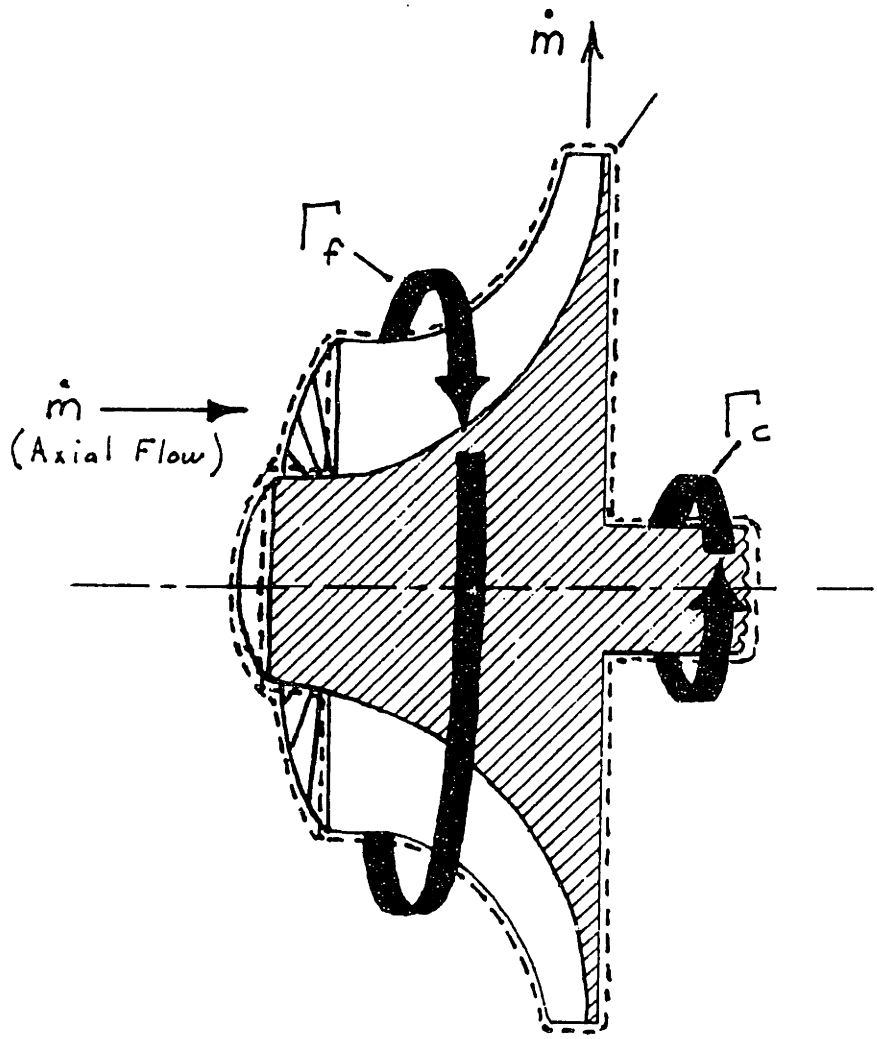

Fig. F.3 Control Volume of Compressor

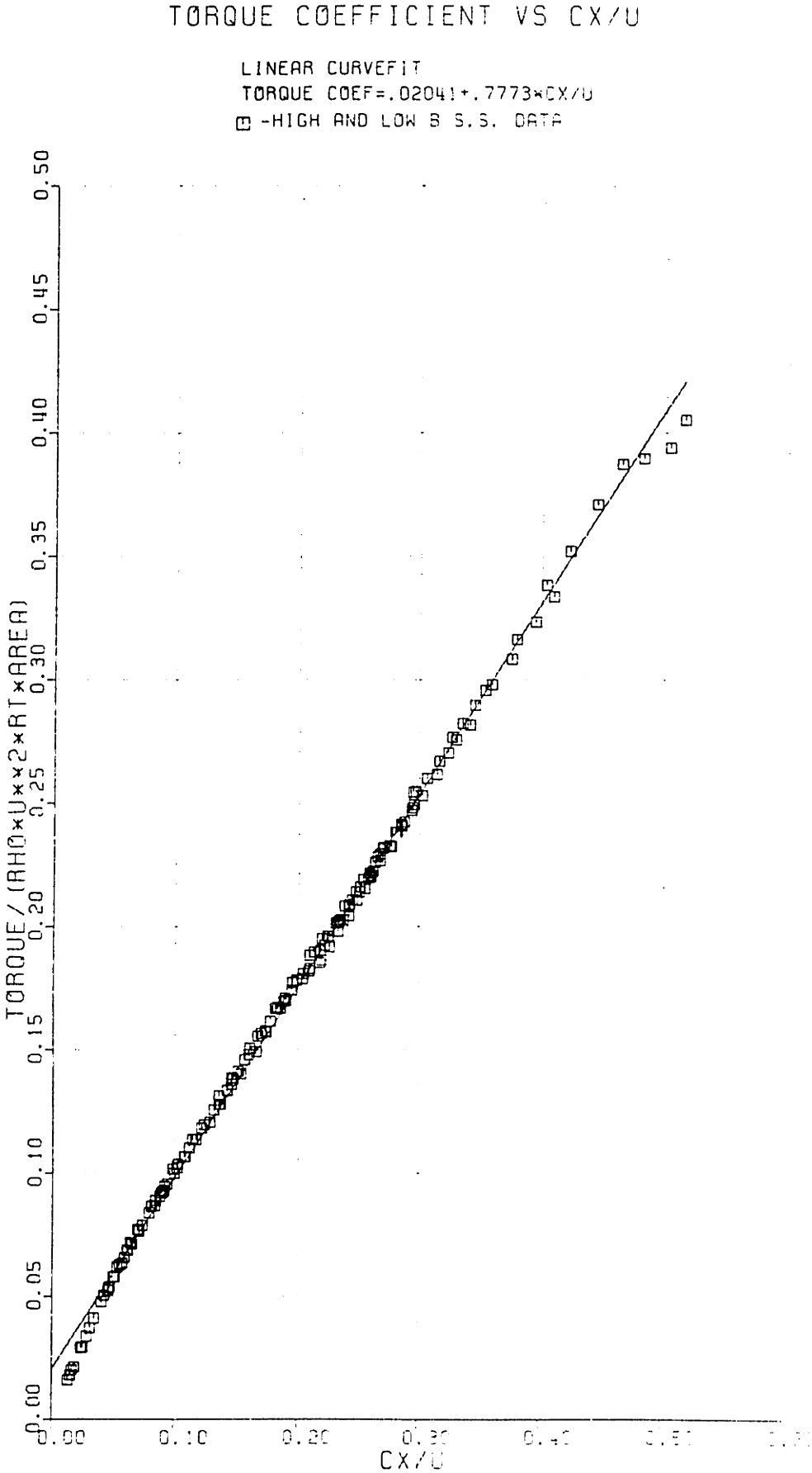

Fig. F.4 Compressor Torque Coefficient vs Cx/U

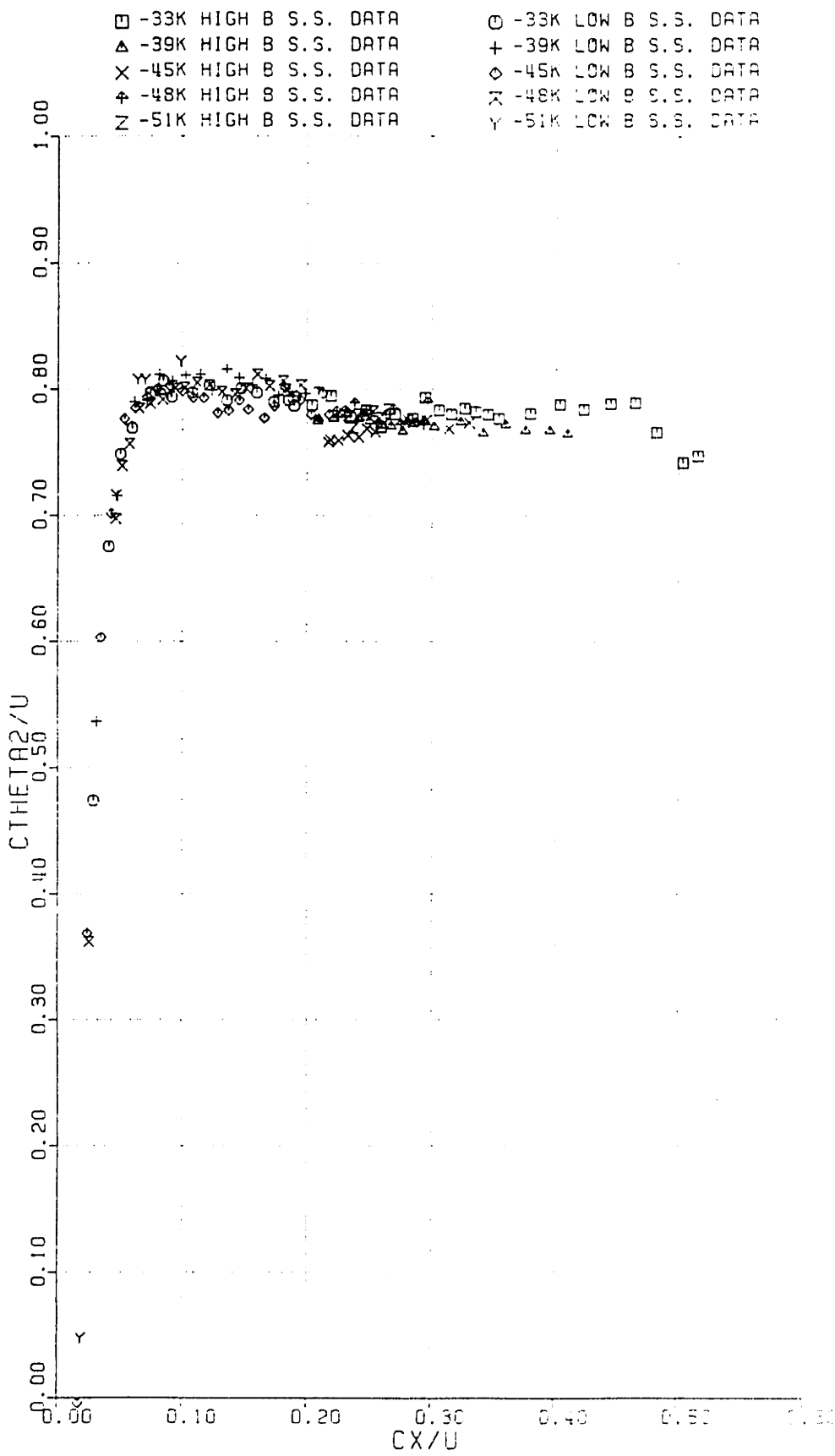

Fig. F.5 Compressor Slip Factor vs Cx/U

APPENDIX G

CALCULATION OF IMPELLER ABSOLUTE EXIT MACH NUMBER

The average impeller exit Mach number M can be found for an 2-D axisymmetric flow of an ideal gas if the flowrate $\dot{m}$, circumferential normal area Ar, static pressure P, total temperature To, tangential velocity C_θ, ratio of specific heats K, and gas constant R are known. Refering to the velocity diagram shown in Fig. F.1, mass continuity is

$$\frac{\dot{m}}{A_r} = \frac{P}{RT_o}\left(\frac{T_o}{T}\right)C_r \tag{G.1}$$

For adiabatic flow

$$c_p T_o = c_p T + \frac{C_\theta^2}{2} + \frac{C_r^2}{2} \tag{G.2}$$

or in terms of To/T

$$\frac{T_o}{T} = \frac{1}{\left(1 - \frac{C_\theta^2 + C_r^2}{2 c_p T_o}\right)} \tag{G.3}$$

Substituting Eq. G.3 into Eq. G.1 and substituting Cp = KR/(K-1), we arrive at

$$\frac{\dot{m}}{A_r} = \frac{P}{RT_o}\,\frac{C_r}{\left(1 - \frac{(K-1)}{2}\,\frac{(C_r^2 + C_\theta^2)}{KRT_o}\right)} \tag{G.4}$$

which can be solved for Cr since everything else is known. Letting X = Cr /

$(2CpT0)^{1/2}$, and performing some algebra a quadratic in X is found.

$$X^2 + bX + C = 0 \tag{G.5}$$

where

$$b = \sqrt{\frac{2}{k-1}}\ \frac{kP}{\dot{m}}\ \frac{A_r}{a_o} \tag{G.6}$$

and

$$C = \frac{(k-1)}{2}\left(\frac{C_\theta}{a_o}\right)^2 - 1 \tag{G.7}$$

The Mach number is then given by

$$M = \left\{\frac{2}{(k-1)}\left(\frac{1}{bX} - 1\right)\right\}^{1/2} \tag{G.8}$$

and the flow angle relative to the radial direction is given by

$$\alpha = \cos^{-1}\left\{X\left(\frac{1}{1-bX}\right)^{1/2}\right\} \tag{G.9}$$

In this analysis, the tangential velocity is required to find the flow Mach number and flow angle. This required a value of the slip parameter σ ($= C_\theta/U$) since wheel tip speed is known. The slip factor is estimated by the proceedure discussed

in App. F.

APPENDIX H

INDUCER MACH NUMBER CALCULATION AND LOSS ESTIMATE

For axial inlet flow at the inducer tip of radius R_1 with rotor speed of ω, the velocity diagram is shown in Fig. H.1. The relative velocity W_1 is given by

$$W_1^2 = C_{x1}^2 + (R_1\omega)^2 \tag{H.1}$$

Nondimensionalized by the inducer tip speed U_1, Eq. H.1 is

$$\frac{W_1^2}{U_1^2} = \phi_1^2 + 1 \tag{H.2}$$

where

$$\phi_1 = \frac{C_{x1}}{U_1} \tag{H.3}$$

The lefthand side of Eq. H.2 can be written as

$$\frac{W_1^2}{U_1^2} = \left(\frac{W_1^2}{kRT_1}\right)\frac{\left(\frac{T_1}{T_0}\right)}{\left(\frac{R_1}{R_2}\right)^2 M_{TO}^2} \tag{H.4}$$

where R_2 is the impeller tip radius and Mto is the impeller Mach index defined as

$$M_{TO} = \frac{U_2}{\sqrt{kRT_0}} \tag{H.5}$$

The temperature ratio To/T1 is related to the absolute axial Mach number Mx by

$$\frac{T_o}{T_1} = 1 + \frac{(K-1)}{2} M_{x1}^2 \qquad \text{(H.6)}$$

The square of the axial Mach number may also be written as

$$M_{x1}^2 = \left(\frac{C_{x1}}{a_1}\right)^2 = \left(\frac{C_{x1}}{U_1}\right)^2 \left(\frac{U_2}{a_0}\right)^2 \left(\frac{U_1}{U_2}\right)^2 \left(\frac{T_o}{T_1}\right) \qquad \text{(H.7)}$$

or

$$M_{x1}^2 = \phi_1^2 M_{TO}^2 \left(\frac{R_1}{R_2}\right)^2 \left(\frac{T_o}{T_1}\right) \qquad \text{(H.8)}$$

Substituting Eq. H.8 into Eq. H.6 and solving for the temperature ratio To/T1, then

$$\frac{T_o}{T_1} = \frac{1}{1 - \frac{K-1}{2}\left(\frac{R_1}{R_2}\right)^2 M_{TO}^2 \phi_1^2} \qquad \text{(H.9)}$$

Since

$$M_{1rel}^2 = \frac{W_1^2}{KRT_1} \qquad \text{(H.10)}$$

then by solving H.4 for the relative inlet Mach number and substituting Eq. H.2,

$$M_{1rel}^2 = (1+\phi_1^2)\left(\frac{T_0}{T_1}\right) M_{T0}^2 \left(\frac{R_1}{R_2}\right)^2 \tag{H.11}$$

is obtained. Substituting the temperature ratio expression of Eq. H.9 into H.11, this is

$$M_{1rel}^2 = \left\{ \frac{(1+\phi_1^2) M_{T0}^2 \left(\frac{R_1}{R_2}\right)^2}{1 - \frac{\kappa-1}{2}\left(\frac{R_1}{R_2}\right) M_{T0}^2 \phi_1^2} \right\} \tag{H.12}$$

The total to static pressure ratio in the relative frame is

$$\left(\frac{P_{01}}{P_1}\right)_{rel} = \left(1 + \frac{\kappa-1}{2} M_{1rel}^2\right)^{\frac{\kappa}{\kappa-1}} \tag{H.13}$$

The ideal inducer head coefficient, defined as

$$\psi_{ind} = \frac{\left(\frac{P_{01}}{P_1}\right)_{rel}^{\frac{\kappa-1}{\kappa}} - 1}{(\kappa-1) M_{T0}^2} \tag{H.14}$$

is then found by combining Eq. H.12 and H.13 with H.14 to yield

$$\psi_{ind} = \frac{\frac{1}{2}\left(\frac{R_1}{R_2}\right)^2 (1+\phi_1^2)}{1 - \frac{\kappa-1}{2}\left(\frac{R_1}{R_2}\right)^2 M_{T0}^2 \phi_1^2} \tag{H.15}$$

Eq. H.15 represents the ideal head recovery of the inducer. If all the dynamic head is lost in the inducer from tip stall, then this expression represents the head lost.

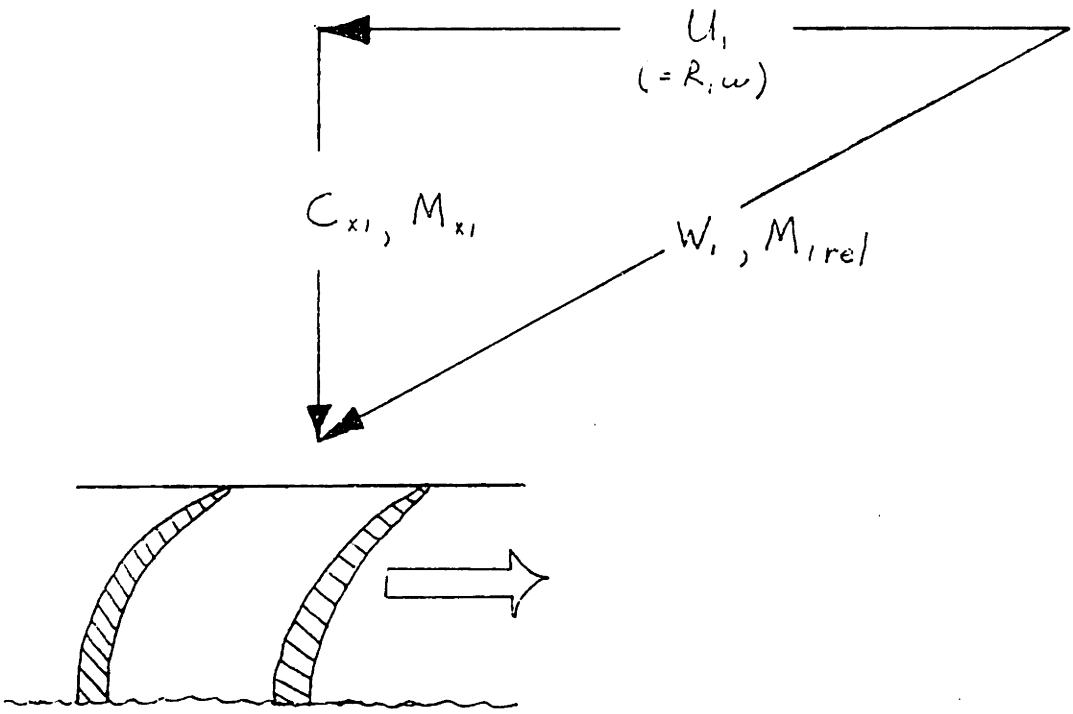

Fig. H.1 Inducer Tip Velocity Diagram